# A Scanning Tunnelling Microscopy study of $Bi_{1-x}Sb_x$ Nanostructures

A thesis submitted in partial fulfillment
of the requirements for the Degree of

Doctor of Philosophy in Physics
at
University of Canterbury

by

Ishan Vardhan Mahajan


Department of Physics and Astronomy
University of Canterbury
2017

'*The thesis is dedicated to the 'crazy ones'. The ones who 'believe'. The pathbreakers. The ones who persevere and never give up. No matter what!*

*'The ones who are 99.999% ultra high purity hard work, perseverance and mental strength'.*

*The good thing about science is that it's true whether or not you believe in it.*
*-Neil deGrasse Tyson.*

# Abstract

Topological Insulators promise a route to develop novel electronic devices with dissipation-less flow of electrons. Theoretical and experimental demonstration of topologically protected electronic states in a host of different materials has resulted in an exponential increase in the research undertaken in this field. The first experimentally verified 3-dimensional topological insulator, $Bi_{1-x}Sb_x$ exhibits a non-trivial topological phase, within the concentration range of $0.07<x<0.22$. The motivation for this project lies in exploring and understanding the impact of miniaturization on the topologically protected states of $Bi_{1-x}Sb_x$ alloys, when grown on a weakly interacting substrate like HOPG.

Studying the morphology of nanostructured $Bi_{1-x}Sb_x$ alloys on HOPG also provides a platform to investigate a transition from the ordered morphologies of pure Bi (110) islands to the fractal, disordered morphologies of Sb islands. Scanning Tunnelling Microscopy measurements are used to characterise the morphological and electronic properties of $Bi_{1-x}Sb_x$ islands. The morphology is similar to the wedding cake like profile of pure Bi (110) islands on HOPG, in which the formation of paired layers with thicknesses of 3, 5, 7 Monolayers (ML) is argued to result from a black-phosphorous like structure. Interesting outcomes include the presence of fingered 3 ML bases and irregular 5 ML stripes. An additional monolayer structure is also observed adjacent to the irregular 5 ML stripes and on top of large 3 ML bases in a select few islands as the Sb concentration is increased, referred to as the (3+1) ML region.

The experimentally acquired electronic spectra for each of the paired layers show similarity to the results obtained for pure Bi (110) islands on HOPG and are in good agreement with the corresponding DFT calculated band structures. Surprisingly, no noticeable difference in the band structures is observed as the Sb content is altered. The preliminary electronic spectra of the (3+1) ML region shows similarity to that of the 3 ML base and is indicative of a low density of states.

Distinct edge states are observed along the $Bi_{1-x}Sb_x$ island edges, particularly along the straight 7 ML stripe edges. The edge states are characterised by the presence of a distinct peak in the density of states around +0.1 V and observed as distinct, bright edges in the corresponding conductance maps near the Fermi level. In addition to the edge states, the observation of anomalous states in close proximity to the straight 7 ML edges and bright spots within the 5 ML regions are additional, interesting outcomes which merit future experimental studies.

# Contents

# 1 Introduction

Moore's law[1,2] predicts that the number of transistors incorporated inside an integrated circuit chip double every 18 months, a trend that has been observed unfailingly for over five decades and has been the benchmark for the semiconductor industry[3]. Realization of the Moore's law has been possible due to the continuous miniaturization of the incorporated transistor sizes. One of the key issues identified in the miniaturization process has been the fundamental feature size limit[4] of the semiconductor transistors, in addition to the undesirable practical problems like leakage currents and high resistance which increase with reduced dimensions. These issues have impeded the efficiency of electronic devices considerably and has therefore motivated intensive research in physical sciences, particularly in the field of 'Nanotechnology'[5].

Advancements in nanotechnology[5] have been instrumental in addressing the issue of fundamental feature size limits in semiconducting transistors. In addition, phenomenon like quantum size effects[6] become prominent at the nanoscale[7], allowing the possibility of tuning the material's electronic properties and create structures with desired electronic properties. In short, nanotechnology promises to change the face of research in the 21$^{st}$ century.

Research to look for replacements for the key component of present day transistors, has led to the discovery of a new class of matter called the 'Topological Insulators' (TIs)[8] in which the movement of electrons without backscattering promises the realization of resistance free electronic devices.

Figure 1-1 illustrates the lack of backscattering in a simple TI[9] by drawing an analogy with the movement of vehicles (electrons) on a highway (surface of a material). From everyday experience, it is well understood that movement of vehicles on narrow roads results in traffic jams and disruptions, whereas, a complete lack of traffic enables faster movement on freeways and highways. Normal conductors[6] and insulators can be considered to be analogous to narrow roads comprising a finite resistance, whereas TIs are like freeways in which the electrons can move without any disruption, i.e. without any backscattering.

Considering the potential of nanotechnology and TIs, their marriage can be imagined to address the challenges of the 21$^{st}$ century as well as open new vistas of research. The theme of this thesis is primarily centred around the amalgamation of the two research fields, i.e. developing an understanding of the morphological and electronic properties of the self-assembled, nanostructures

*Figure 1-1 A schematic demonstrating the situation in a topological insulator. Electrons are predicted to move without any backscattering, i.e. behave like vehicles moving on a highway. Image reproduced from[9].*

of the first 3-dimensional TI, i.e., $Bi_{1-x}Sb_x$[10-12]. The experiments are carried out in an Ultra-High Vacuum Scanning Tunnelling Microscope[13-15] (UHV-STM).

This chapter is divided into two parts, where the first part briefly discusses the key concepts of TIs and the second part discusses the key concepts related to 'self-assembly'[16,17].

## 1.1 Motivation

### 1.1.1 Dimensions in real space

To understand how the dimensions of a material affects the corresponding surface electronic states[6], the fundamental dispersion relations of a solid material need a brief mention. The lattice structure of a crystalline material produces a periodic potential which leads to an electronic band structure and is understood in terms of the corresponding energy-momentum dispersion relations. By modifying the charge carrier density or altering the spin orbit coupling (SOC), the surface electronic states associated can be engineered to intersect the Fermi level and in the process manipulate the material's ability to conduct.

The impact of a material's dimensions in real space on the corresponding surface electronic states is understood better by drawing an analogy[18] with the fictional, geometrical characters of the famous novel: Flatland[18]. Figure 1-2 demonstrates this analogy by showing different dimensions possible for a particular material in real space. Zero dimensional (0-D) materials represent the class of materials in which an electron's movement is restricted in all the directions (point land), a situation characteristic of quantum dots[19] and quantum corrals[20]. A one-dimensional material (1-D) represents the class of materials in which an electron's movement is possible in one dimension only, a situation

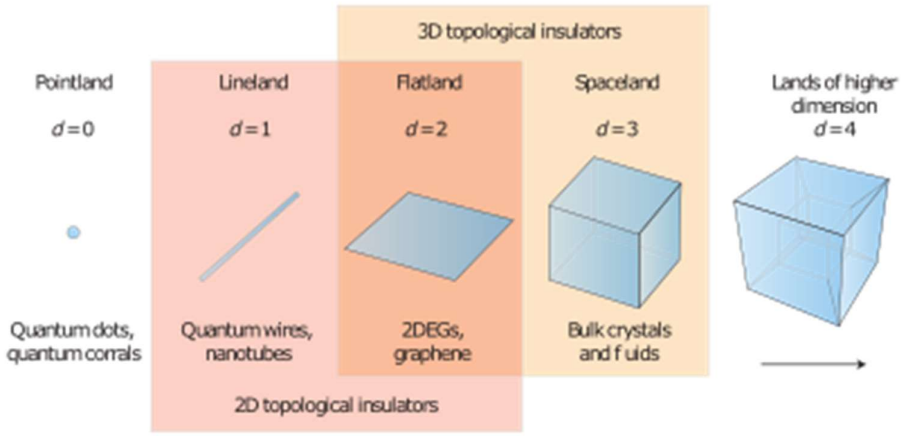


*Figure 1-2 Schematic drawings demonstrating different dimensions possible for objects in real space. Topologically protected states have been theoretically predicted and experimentally verified in 2-dimensional (flatland) and 3-dimensional materials (spaceland). Image reproduced from[18].*

characteristic of quantum wires, nanotubes[21] (line land). The two-dimensional (2-D) materials in which an electron's movement is possible in both the dimensions (flat land) represent exotic materials like graphene[22] and two-dimensional electron gases (2DEGs)[23]. Three dimensional materials like bulk crystals and fluids represent the class of materials in which an electron's movement is possible in all the three dimensions.

Research in the past[24] has focused on understanding the surface electronic states of the materials in isolation and their correlation with the dimensions of the materials remained missing. Therefore, an understanding of the impact of material's dimension (d) and the associated material boundary (d-1) on the corresponding surface electronic states is actively sought nowadays, particularly in the emerging field of TIs.

### 1.1.2 Topological Insulators

A topological insulator is a material that behaves as an insulator in its interior and has conducting states[25] on its surface. The electronic band structure of a typical topological insulator resembles that of an ordinary band insulator, with the Fermi level falling between the conduction and valence bands, but there are symmetry protected electronic states within the bulk energy gap that facilitate metallic conduction on the surface.

Figure 1-3 shows the band structure of a topological insulator, where, spin momentum locking[26] differentiates it from the band structure of a normal insulator. Fermi level crossings is a key concept that determines the topological nature of a material's surface electronic states as described in Ref[25]. An odd number of Fermi level crossings by the surface electronic states as seen in Figure 1-3 represent a non-trivial topological phase and an even number of Fermi level crossings represent a trivial topological phase, with graphene[24,27-37] being one such example of topologically non-trivial materials.

Figure 1-4 (a-b) demonstrates the link between the dimensions of a material and the associated topologically interesting electronic states by means of a schematic diagram. An example of a 2-D topological insulator (flatland) is shown in Figure 1-4 (a) showing the presence of electronic states along the material's edges, referred to as the 1-D edge states[18]. An example of a 3-D topological insulator is shown in Figure 1-4 (b) showing the presence of electronic states on one of the surface planes, which are called as the 2-D surface states[18]. Developing an in-depth understanding of the 2-D surface states and the 1-D edge states is possible nowadays with the advancements in the characterisation techniques like STM[13,14] and Angle Resolved Photoemission Spectroscopy (ARPES)[38] which has led to the realization of several novel TI materials.

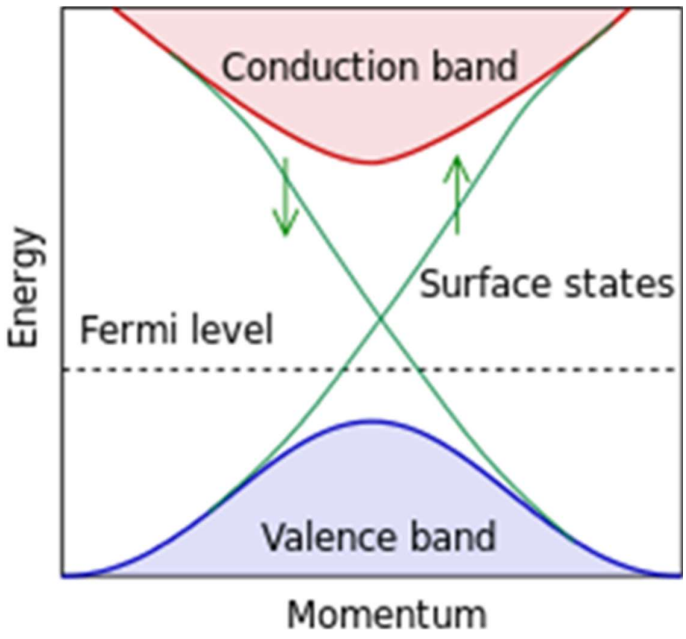


*Figure 1-3 Band structure of a topological insulator, in which the Fermi level within the bulk band gap is intersected by topologically protected surface states. Image reproduced from[25].*

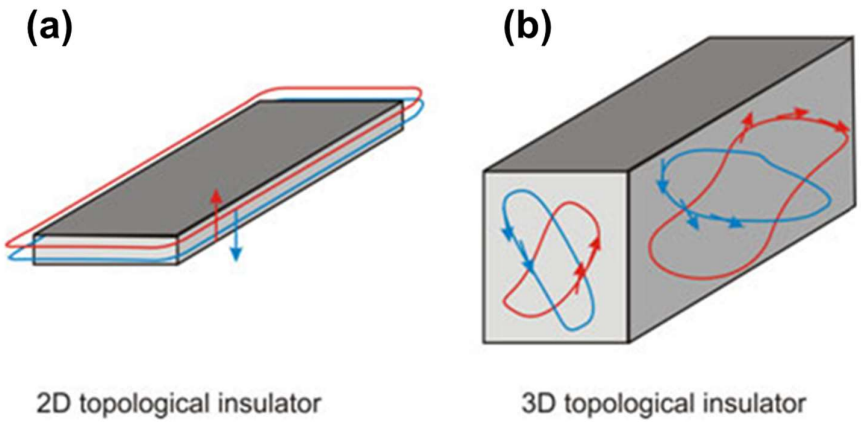


*Figure 1-4 (a) A schematic drawing showing a 2-D topological insulator with 1-D edge states. (b) A 3-D topological insulator showing the presence of 2-D surface states. Image reproduced from[18].*

### 1.1.3 Realization of Topological Insulators

HgTe/CdTe hetero-structures were the first class of 2-D TI to be predicted and experimentally verified[39,40]. The first material predicted[12] and experimentally verified[10,11] as a 3-D TI was $Bi_{1-x}Sb_x$ alloy, which is particularly interesting as a non-trivial topological phase is realized within the Sb (x) concentration range of $0.07<x<0.22$[10,12,41,42]. The two parent elements of $Bi_{1-x}Sb_x$ alloys, i.e. Bi and Sb have been observed to demonstrate topologically interesting properties as well, where pure Sb (111)[43,44] is a topological metal, in contrast to Bi[45] (110) and Bi[46,47] (111), both of which are 2-D TIs. The $Bi_2Se_3$[48,49] family alloys are the most extensively researched TIs due to the demonstration of a large band gap, a single Dirac surface state and a defined stoichiometry, all of which are essential requirements for identifying exotic topological phases. In addition, exotic new materials in which topologically protected states have been realized, include Weyl semimetals[50] indicating clearly that the field of TIs is growing at an exponential rate.

Out of all the classes of TI materials described above, $Bi_{1-x}Sb_x$ alloys are of particular interest as topologically protected surface states are observed within a certain ($0.07<x<0.22$) Sb concentration range. Moreover, a clear demonstration of topologically protected 1-D edge states in nanostructured $Bi_{1-x}Sb_x$ alloys is not reported till now and thus remains the motivation of the work undertaken during the course of this project. By undertaking this research, an answer is sought to the question-do the topologically protected states of 3-D $Bi_{1-x}Sb_x$ alloys survive at the nano-scale and manifest in the form of 1-D edge states?

The experiments conducted over the course of this project, build upon the knowledge and experience gained over the past few years on the growth of self-assembled nanostructures of Bi[51,52]

and Sb[53,54] on Highly Oriented Pyrolytic Graphite[55-57] (HOPG), a weakly interacting substrate. The next section therefore introduces a few key concepts related to the self-assembly processes, followed by brief discussions on the established morphologies of Bi and Sb nanostructures on HOPG.

## 1.2 Self assembly

Nanotechnology uses two types of approaches, i.e. the top-down and the bottom-up approaches[3,58]. The top-down approach comprises of techniques like lithography[3] and chemical etching[59] which provide a precise control on the nanostructures morphologies. The bottom-up approach comprises vapour deposition techniques like chemical vapour deposition[3] (CVD), physical vapour deposition[3] (PVD). Despite the lack of control, the bottom-up approach allows for the possibility of studying self-assembly[16] of atoms and consequently explore new nanostructure growth mechanisms.

Self-assembly of atoms on different types of substrates is known to result in the formation of diverse morphologies such as islands[17], rods[17,60] etc., providing a perfect playground to understand different growth mechanisms and thus, the basic mechanisms governing the growth of self-assembled nanostructures are discussed briefly in the next section.

### 1.2.1 Growth Mechanisms

Figure 1-5 shows a schematic diagram demonstrating the basic components of a self-assembly system, showing a substrate on which incoming atoms impinge. The impinging atom can land on different regions of the substrate, i.e. on a wide region (terrace) or at an inherent atomic defect, i.e. regions like a kink, step or a vacancy site. The impinging atom that gets adsorbed on the substrate

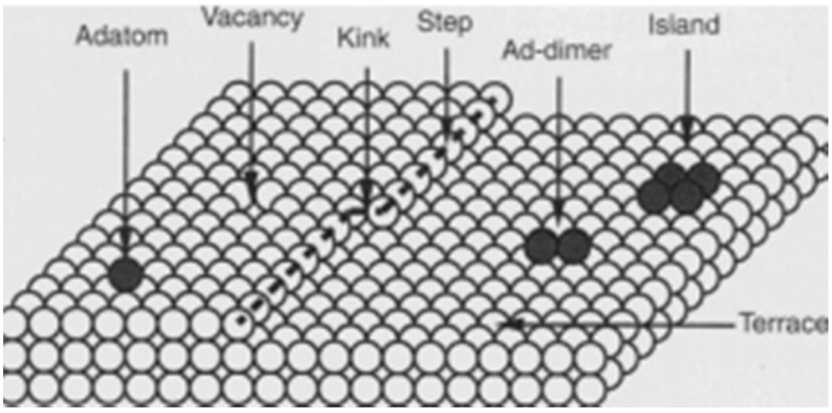


*Figure 1-5 Schematic diagram demonstrating the basic componenets of a simple self-assembled system. Image reproduced from[17].*

upon landing is called an adatom (adsorbed-atom). Two such adatoms joined together are called dimers and an aggregate of more than two adatoms is called an island.

Upon landing on the substrate, the atoms tend to move around on the substrate randomly, a phenomenon termed as surface diffusion[17], and is governed by the distance an adatom can move in between two nearest nucleation sites and the rate of adatom diffusion, described mathematically as:

$$D = a^2 k_s \quad (1)$$

where, $'D'$ is the surface diffusion coefficient, 'a' is the hopping distance between two nearest nucleating sites and $'k_s'$ is the site-to site hopping rate of an adatom. During the early stage of growth, a formation of larger structures like islands is seen due to higher adatom-adatom interaction. Subsequently, island nucleation increases, decreasing the average distance an adatom can travel before it encounters an existing island. At this stage of the growth, incoming adatoms tend to attach to the existing islands and refrain from forming any new islands.

#### 1.2.1.1 Substrate adatom interactions

Thin film growth depends on the dynamic interplay between the surface energies of adatoms and the underlying substrate. Specifically, three different types of surface energies are identified; the substrate surface energy i.e. $\gamma_S$ , the deposited surface free energy i.e. $\gamma_F$ and interface energy of the interface between substrate and film, i.e. $\gamma_I$. Figure 1-6 (a-c) shows three different thin film growth modes possible, based on different surface energy interactions. When the adatom-adatom interaction is greater as compared to that of the adatom-substrate interaction (Figure 1-6 (a)), three dimensional islands grow and is called the Volmer-Weber growth mode[61,62]. Metals adsorbing on weakly

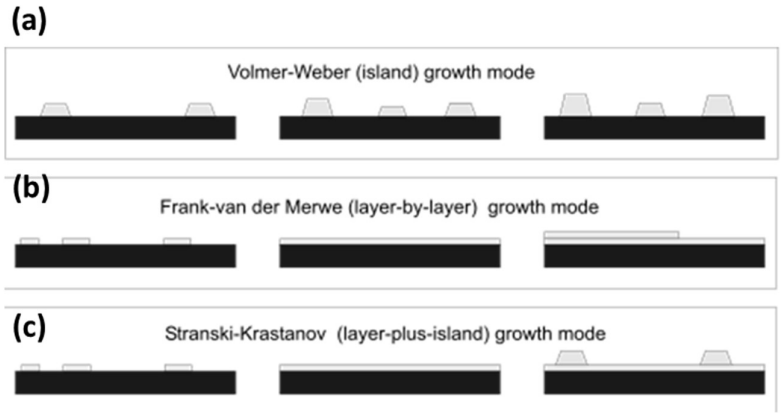


*Figure 1-6 (a-c) Schematic diagrams showing the different thin-film growth modes. Image reproduced from[54].*

interacting substrates like HOPG[63] and Mica[64] are typically known to demonstrate Volmer-Weber growth mode, expressed in the form of surface energies as:

$$\gamma_F > \gamma_S + \gamma_I \quad (2)$$

If the adatoms experience stronger interactions with the substrate as compared to the interactions amongst the adatoms, flat monolayer films grow (Figure 1-6 (b)), referred to as the Frank-van-der Merwe[65,66] growth mode. It is the primary growth mode of certain rare gases on HOPG[67] and expressed in terms of surface energies of the system as:

$$\gamma_F < \gamma_S + \gamma_I \quad (3)$$

The third type of growth mode referred to as Stranski-Krastonov[68] is depicted by the schematic diagram of Figure 1-6 (c) and is a combination of the two growth modes discussed above. It is characterised by the growth of atomically flat films along with three-dimensional islands. During the early stages of Stranski-Krastonov mode, Frank-der Merwe growth mode prevails and a switch to the Volmer-Weber growth mode happens under unfavorable growth conditions like increased strain in the system[69,70], for example, lattice mismatches[71]. Thus in Stranski-Krastonov mode, a subtle change is observed from film growth mode to island growth mode as the system's equilibrium shifts and it is expressed in surface energy terms as:

$$\gamma_F > \gamma_S + \gamma_I \quad (4)$$

The next two sections build upon the above discussions and discuss two methods of controlling the island morphologies by manipulating the experimental parameters (namely atomic flux and sample coverage)

#### 1.2.1.2 Atomic flux

Atomic flux is defined as the rate of arrival of atoms on a substrate and expressed in Å/s. A small change in atomic flux can significantly alter the growth dynamics as depicted by the schematic diagrams of Figure 1-7. The argument is verified by previous[54] room temperature studies on the growth of Bi and Sb islands which demonstrate clearly that small changes in atomic flux result only in subtle changes in the corresponding island morphologies. In contrast, previous[72] temperature dependent studies have shown considerable morphological changes with slight temperature changes.

The left panel of Figure 1-7 shows a low flux environment in which the arrival time of an adatom is less than the time needed for the aggregate's nucleation. In a low flux regime, few adatoms populate the substrate meaning that the time of arrival ($t_a$) for new atoms towards an already formed aggregate is greater than the time required ($t_c$) by the aggregate to incorporate the adatoms and stabilise. As a consequence, sufficient amount of time is available for the aggregate to form a compact shape. In

addition, with a few adatoms diffusing around on a substrate, there is a higher probability for the adatoms to bump into an already existing large aggregate. The dynamics are expressed in term of arrival times as:

$$t_a > t_c \tag{5}$$

The situation is different when the atomic flux is higher as depicted in the right panel of Figure 1-7. In a high flux regime, the substrate comprises greater number of adatoms, which implies that the arrival time ($t_a$) between adatoms is considerably reduced. The incoming adatoms are therefore, able to reach the islands' perimeter faster, preventing the island to acquire a smooth and compact morphology, instead the irregularities along the perimeters keep increasing. In addition, the higher number of adatoms allow the possibility for the formation of new islands. The dynamics are expressed in terms of arrival times as:

$$t_a < t_c \tag{6}$$

The formation of different island morphologies in the two flux regimes, thus indicates that altering the atomic flux presents an effective way to manipulate the final geometries.

#### 1.2.1.3 Sample coverage

The final shape of a self-assembled aggregate is expected to change when the amount of deposited material on a substrate is altered. The growth of a self-assembled aggregate is generally observed to proceed in three different stages as a function of sample coverage[73]. During the initial growth stage, collision of incoming adatoms leads to the formation of new islands and at some stage during the deposition process, the number of diffusing adatoms equals the number of nucleated islands and a critical island density value $N_c$[54] is reached. The second growth stage is characterized by

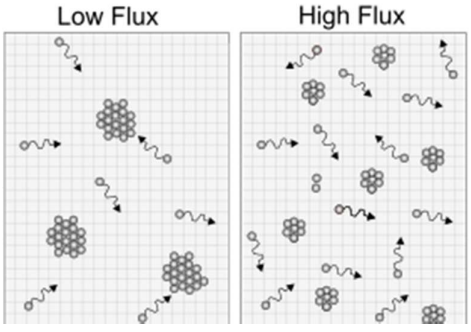


*Figure 1-7 Schematic diagrams showing the growth dynamics of self assembled aggregates in low and high flux environments. Image reproduced from[54].*

growth of new islands as the new incoming adatoms compete for nucleation and aggregation. The last stage of growth demonstrates coalescence of existing islands into larger islands, reducing the overall island density. The implications of coverage dependent growth are briefly explained later by discussing relevant examples of Bi island growth on HOPG as a function of material coverage (section 1.2.2.1.3).

The formation of self-assembled islands is tied to the overall free energy of a system, in particular to the dynamic interplay between the thermodynamically limited[74] and kinetically limited growth mechanisms, as briefly described in the next two sections.

#### 1.2.1.4 Thermodynamically limited growth

The general tendency of self-assembled nanostructures is to stabilize into energetically favourable geometries (i.e. thermodynamically stable), consistent with the tendency of any system to minimize the total free energy. As a rule of thumb, if the time interval between the arrival ($t_a$) of diffusing adatoms is higher than the time required for the island to coalesce ($t_c$), the resulting island will have a compact shape. In this scenario, the ample amount of time available for the island to incorporate the incoming adatoms allows it to attain an energetically favourable configuration. The thermodynamically limited growth is further aided by diffusion of the adatoms along the island's edges and is most prevalent in low flux environments, as evidenced by the formation of compact nanostructures[54].

The increased diffusion helps in smoothing out the island's perimeter, a process termed as edge diffusion[75,76] and is shown in Figure 1-8. The diagram in the left panel of Figure 1-8 shows an example of isotropic edge diffusion[75,77], resulting in the formation of a compact and hexagonal island shape.

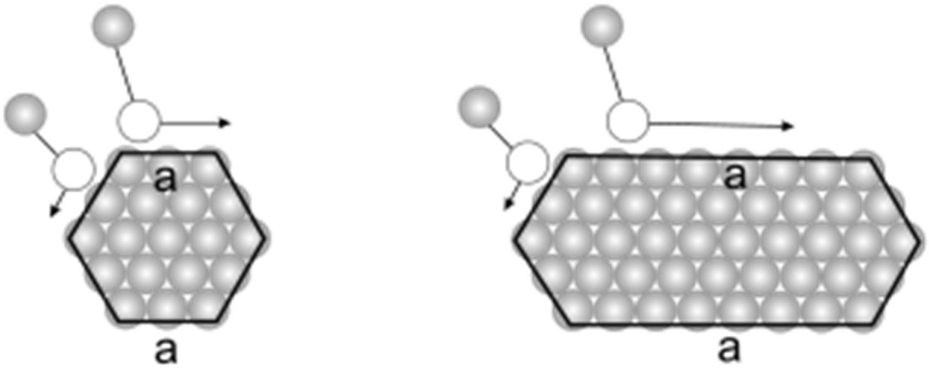


*Figure 1-8 An illustration of anisotropic edge diffusion along edges of an island. A difference in the diffusion barriers along a specific island edge can alter the geometry. A hexagonal island can transform into an elongated island as a result of anisotropic edge dffusion. Image reproduced from[54].*

The diagram on the right side of Figure 1-8 demonstrates the elongation of the same hexagonal island due to higher adatom diffusion along one edge (anisotropic). The discussion therefore, shows that in a thermodynamically limited growth regime, the relative rate of diffusion of adatoms along an island's edge and their diffusion across the substrate determines the final geometry of the aggregate.

#### 1.2.1.5 Kinetically limited growth process

During self-assembly processes[16,17], landing of atoms on a substrate leads to their consequent diffusion and the time of arrival of adatoms, ($t_a$), becomes the rate limiting step which determines the final island geometry. To account for this rate limiting step, Witten and Sanders put forward the diffusion limited aggregation (DLA)[78,79] model, which incorporates Eden's biological model of diffusion limited growth[80] and utilizes it to explain the fractal geometries observed in structures formed during thin film growth. In recent works[63,81], the DLA model is used to explain the formation of fractal geometries of Sb nanostructures on HOPG.

In a kinetically limited growth, the adatoms make random walks around on the substrate until encountered by an island and attach irreversibly to it. The process of adatom-island attachment continues further as more incoming adatoms approach from all the directions, particularly in a high local flux environment. As a consequence, an extension of the island's arms in a dendritic manner[82] is observed; a process comprising an irreversible attachment of adatoms to the island's outer boundaries. The extended island arms restrict any further movement of adatoms inside, eventually allowing the island to acquire a stable geometry.

Complementing the DLA growth model, kinetic Monte Carlo (KMC) simulations[78,79] further aid in understanding the formation of extremely large and fractal structures[80]. In these simulations, individual adatoms are allowed to perform random walks around large aggregates and the dynamics of the final aggregate's formation are observed. The simulations make it easy to observe the structural instabilities in a high local flux growth environment[81] and in the process enable a precise explanation of dendritic fingered patterns.

Mullins and Sekerka[83] explained the morphology evolution of large yet simple, circular islands into more complex, fingered islands under the presence of an external perturbation by simple schematic models, which are based on the impact of an external heat flow and diffusion of adatoms around circular aggregates. According to the schematic models, shapes of initial aggregates become irregular beyond a certain critical radius, causing a pronounced irregularity (Mullins-Sekerka instabilities) on the growth front. The demonstration of circular Sb islands' conversion into fingered islands[63,81] as a function of increasing adatom flux is explained primarily on the basis of Mullins-Sekerka type instabilities. In short, the discussion implies that both, the thermodynamic and

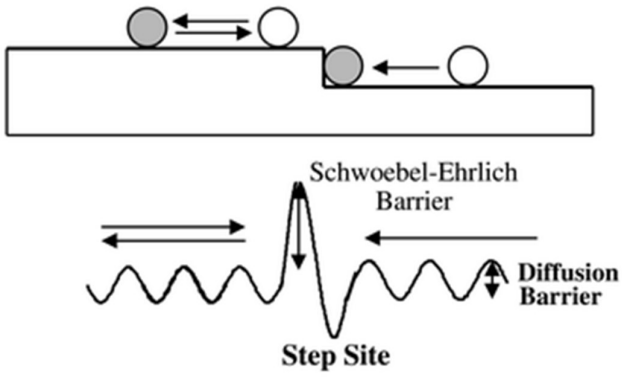


*Figure 1-9 A schematic diagram demonstrating the Ehrlich-Schwoebel (E-S) barrier at a substrate step edge. Image reproduced from[84].*

the kinetic growth models are intrinsic to a self-assembled system and the dynamic interplay between the two processes determines the final aggregate geometry.

The final morphology of the self-assembled aggregate is also governed by the nature of the underlying substrate as the substrates commonly used for the synthesis of self-assembled nanostructures often comprise of naturally occurring defects that disrupt the smooth diffusion of adatoms. An example of such defects are the step edges encountered on HOPG. The next section briefly discusses the implication of such substrate-defects on the movement of adatoms.

#### 1.2.1.6 Ehrlich-Shwoebel (E-S) barrier

The upper part of Figure 1-9 shows a schematic diagram depicting an adatom diffusing across the lower terrace of a substrate and encountering a naturally occurring step edge. The lower part of Figure 1-9 shows the higher energy barrier that the adatom experiences near the step edge, due to the stronger bonding of the adatom with the lower terrace. This higher energy barrier is referred to as the Ehrlich-Shwoebel (E-S) barrier[84,85].

The adatoms have to overcome the E-S barrier when climbing down from an upper terrace or while climbing up to an upper terrace of the substrate. There are two possible scenarios during an adatom's encounter with a step edge, i.e., the adatom can either replace an existing adatom on the adjoining terrace or occupy a vacant lattice space. The two scenarios differ depending on the nature of the substrate being studied as well as the nature of the adatoms. Precise knowledge of E-S barriers

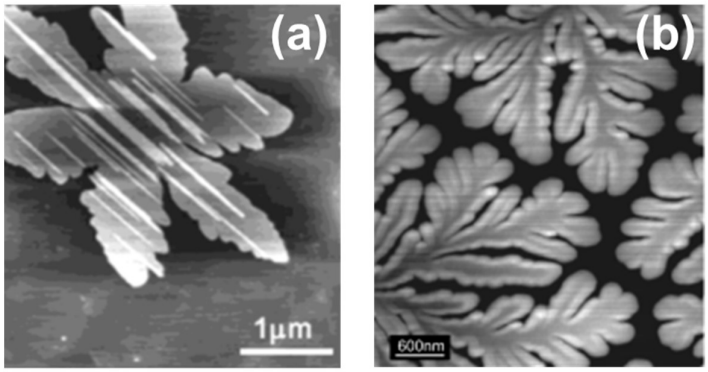


*Figure 1-10 Atomic force microscope (AFM) images of (a) Pure Bi (110) island on HOPG, showing a star like shape. (b) Pure Sb islands on HOPG showing fingered growth. Images reproduced from[54].*

prevalent in a self-assembled system can enable the synthesis of different morphologies of nanostructures with a precise control over the final nanostructure geometry.

### 1.2.2 Self-assembled Bi and Sb nanostructures

This section reviews the morphologies of self-assembled Bi and Sb nanostructures, which are the main focus of this thesis. It is well understood[51,52,86,87] that weak interaction forces on substrates like HOPG allow for high mobility of adatoms that enables the formation of variety of different nanostructure morphologies[51,52,54] such as islands and nanorods. An example is shown in Figure 1-10 (a-b), where (a) is the representative AFM image of pure Bi (110) island on HOPG and (b) is the representative AFM image of pure Sb islands on HOPG. A brief discussion on the morphology of Bi (110) islands on HOPG is presented first and is followed by brief discussions on the morphologies of Sb islands on HOPG.

#### 1.2.2.1 Bi (110) island growth on HOPG

Low coverage growth of pure Bi nanostructures on HOPG reveals[51,52,86,87] that growth of islands and nanorods (via homogeneous nucleation[52,77]) dominates in low coverage regimes. Two distinct types of morphologies are observed depending on the location of islands on HOPG, where small, compact islands are observed to form along the step edges and large islands are observed to form on wide terraces[52]. The mechanisms governing the step edge nucleated island morphologies are discussed first, followed by a discussion on terrace nucleated islands.

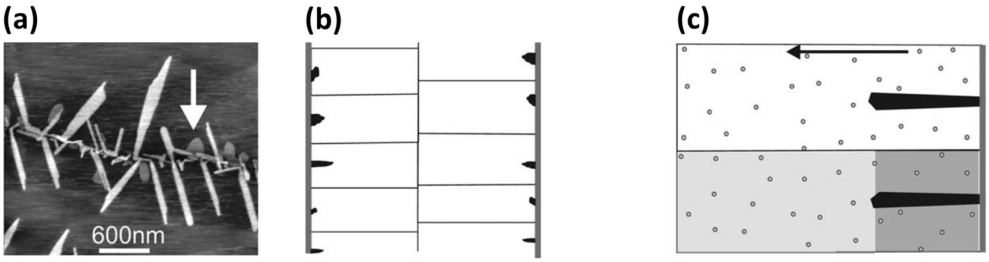


*Figure 1-11 (a) Representative AFM image of step edge nucleated Bi islands at a low sample coverage (b) Schematic diagram showing the capture zones along HOPG step edges highlighting the diffusion fields. (c) Schematic diagram showing final island geometries. Images reproduced from[51].*

#### 1.2.2.1.1 Step edge growth

Step edges on HOPG formed as a result of cleaving the top-most surface[51,54] act as naturally occurring traps (nucleation centres) for the adatoms and as a consequence show a higher island density[51,54]. A combination of mechanisms like the local adatom flux and competitive adatom capture[88] determine the final island geometries.

Figure 1-11 (a) shows a representative AFM image of step edge nucleated Bi islands on HOPG[51], characterised by a high density of rod like islands. The white arrow indicates the presence of a small, round Bi island, representing the smaller, compact Bi island geometries. The high density of rod like islands in the AFM image indicate that the diffusion of adatoms in between HOPG step edges is restricted and results in a competition amongst the islands for incoming adatoms, referred as competitive adatom capture[88]. It is illustrated in the schematic diagrams of Figure 1-11 (b-c), where (b) shows a decrease in the diffusion field around the initial islands and the black lines demarcate the capture zones for the incoming adatoms. The 'diffusion field' above refers to areas of different adatom density on a substrate. The movement of adatoms takes place from a high (large substrate terrace) to a low (island edges) diffusion field region, analogous to the charge movement in an electric field.

The decrease in the diffusion field in each of the capture zones in Figure 1-11 (b), thus, results in the number of adatoms attaching along the perimeter of aggregates to reduce, preventing any lateral expansion. The probability of adatoms attaching at the tip of the aggregate, therefore, increases in such a scenario and the final island geometries are more elongated as shown in Figure 1-11 (c).

#### 1.2.2.1.2 Growth on wide substrate terraces

Defect free regions i.e. wide terraces on HOPG offer a perfect playground to study the impact of homogeneous[77] nucleation of adatoms. Terrace nucleated islands have an isotropic diffusion field

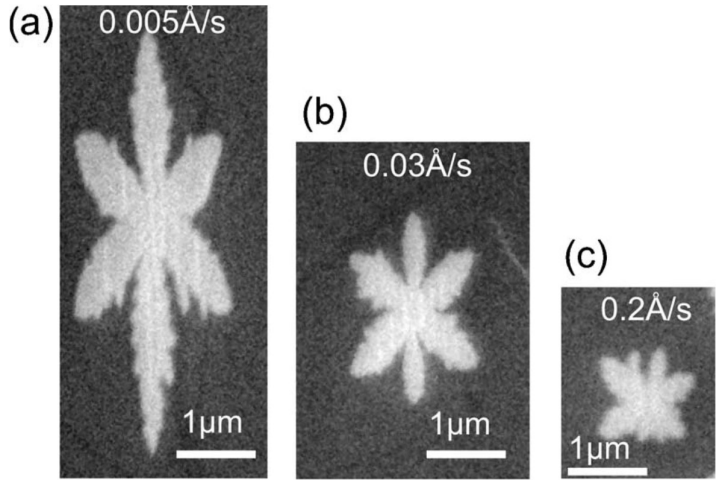


*Figure 1-12 (a-c) Representative SEM images of terrace nucleated Bi (110) aggregates showing the evolution in morphology with flux (indicated on the images); coverage is fixed at 1 ML. Image reproduced from[52].*

around them which tends to increase the average size of the islands as adatoms approach islands from all the directions. The formation of terrace nucleated islands is explained primarily on the basis of established models of DLA[79]. In addition, extension of the island's perimeters into the diffusion field leads to the formation of small protrusions which extend as more adatoms arrive and eventually start forming ordered shapes, as evidenced by the star shaped Bi islands (Figure 1-12 (a-c)) on large HOPG terraces[52].

Figure 1-12 (a-c) demonstrates the impact of increasing sample coverage on the Bi (110) island shapes on wide HOPG terraces by representative Scanning Electron Microscopy[89] (SEM) micrographs. Figure 1-12 (a) is an SEM micrograph of a large, six-pointed star shaped Bi island grown in a low atomic flux regime. As the atomic flux is gradually increased, the mean size of the Bi islands decreases as evidenced by the SEM micrograph of Figure 1-12 (b) and the SEM micrograph of Figure 1-12 (c) shows that as the atomic flux is increased further, irregularity along the island's perimeter increases with a simultaneous decrease in the island's mean size. The irregularities (dendritic features) along the island perimeters are explained as a result of the higher local adatom flux prevalent on the wide substrate terraces.

Building on this knowledge, the next two sections discuss how the Bi (110) island morphologies on HOPG evolve when the experimental parameters (atomic flux and the sample coverage) are manipulated.

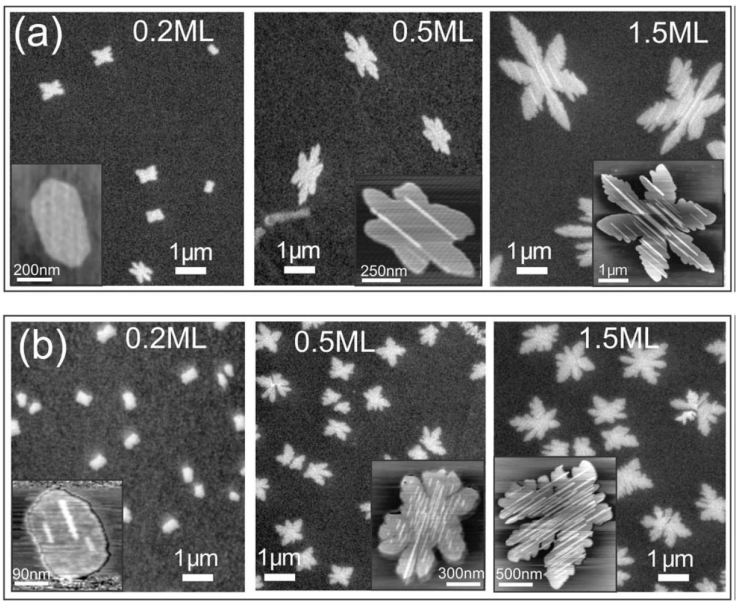


*Figure 1-13 Representative SEM images showing the variation in Bi (110) island morphology with increasing coverage for (a) The low flux (F=0.005Å/s) regime and (b) The high flux (0.2Å/s) regime. The coverage is indicated on each SEM image. The insets are higher resolution AFM images. Image reproduced from[52].*

#### 1.2.2.1.3 Coverage dependence

This section presents the coverage dependent growth characteristics of Bi along the step edges and large terraces (discussed first) of HOPG. Figure 1-13 (a-b) shows the evolution in morphology of Bi (110) islands as a function of sample coverage, where, Figure 1-13 (a) is representative of the low flux regime (F=0.005 Å/s) growth dynamics. The presence of small and isolated Bi islands, devoid of stripes at an average coverage of 0.2 ML are seen first and as the average coverage is increased to 0.5 ML, star shaped Bi islands start to appear. Eventually, an increase in the average coverage up to 1.5 ML causes the star shaped islands to develop irregularities along the island perimeters along with a simultaneous increase in the stripe density.

Figure 1-13 (b) is representative of the high flux regime (0.2 Å/s) growth dynamics showing the presence of small Bi islands (~90 nm) at a low sample coverage of 0.2 ML first. An increase in the coverage up to 0.5 ML causes the Bi islands to develop irregular perimeters and an increase in the stripe density. The trend continues and the irregularities along the island perimeters increase significantly with coverage increase up to 1.5 ML. Overall, the size of Bi islands tends to increase as the coverage is increased in both the flux regimes. The only noticeable difference being that the

shapes of the Bi islands are more defined in the low coverage regime as compared to that in the high flux regime.

The growth of Bi (110) islands along the step edges of HOPG[51] show a similar growth pattern (i.e. increase in the mean area) with increasing sample coverage. Figure 1-14 shows representative SEM micrographs of step edge nucleated Bi (110) islands as a function of sample coverage, where, at low sample coverages (0.2 ML), small islands are observed but as the sample coverage is gradually increased to 0.7 ML, needle like island morphologies are observed more frequently, which is a result of competitive adatom capture. The needle like morphologies develop into larger islands as the average coverage is increased to 1.5 ML, consistent with the general impact of increasing coverage on island morphologies.

#### 1.2.2.1.4 Flux dependence

This section discusses the evolution in the morphology of Bi islands on HOPG as a function of incoming atomic flux on large HOPG terraces as well as on the HOPG step edges. The morphologies on wide HOPG terraces are discussed first, followed by a discussion on the step edge nucleated morphologies.

Figure 1-15 (a-b) shows representative SEM images of Bi (110) islands on large HOPG terraces, grown in different flux regimes. Figure 1-15 (a) shows a compact island morphology which is representative of the island shapes in low flux regimes and Figure 1-15 (b) shows a star shaped Bi

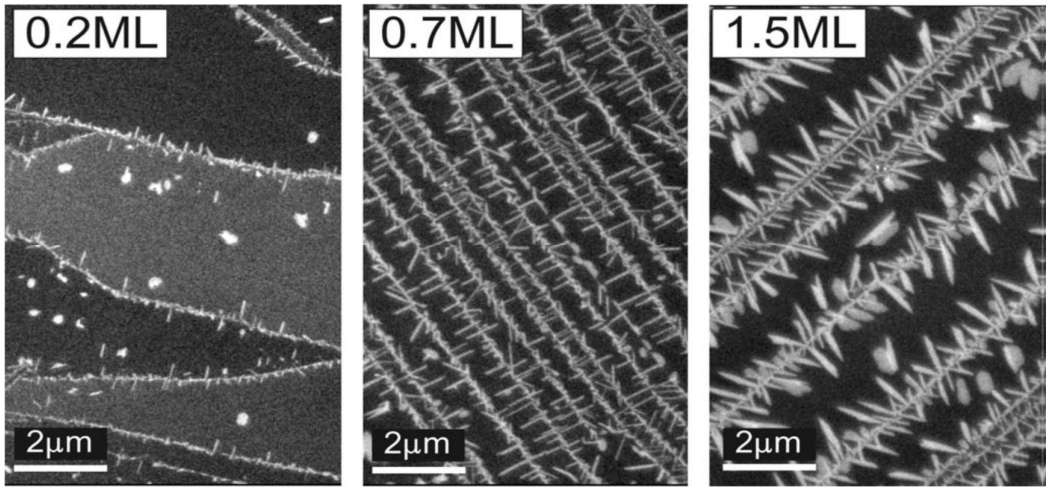


*Figure 1-14 Representative SEM images showing the evolution in the morphology of Bi (110) islands as a function of coverage in the low flux regime. The sample coverage is indicated on the SEM images, with the flux held constant at 0.005 Å/s. Image reproduced from[51].*

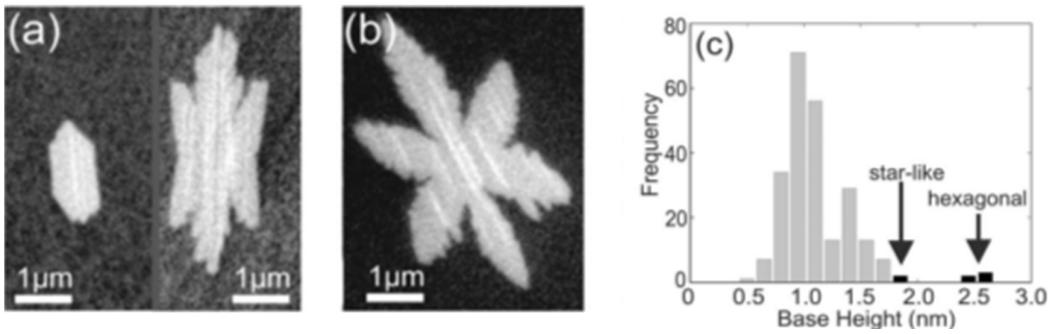


*Figure 1-15 Representative SEM images showing the evolution in island morphology with increasing flux at a constant coverage. (a) Shows compact, hexagonal Bi islands at F=7×10$^{-4}$ Å/s. (b) Star shaped Bi island at F= 0.2Å/s (c) Histogram of island base heights for the 7×10$^{-4}$ Å/s flux (black bars), where the Bi island types (starlike or hexagonal) are indicated in the plot. Image reproduced from[52].*

island which is representative of island shapes in the higher flux regimes. An increased irregularity along the island perimeters can be easily identified in Figure 1-15 (b). These two island morphologies show different height distributions for the bases as evidenced by the histogram in Figure 1-15 (c). Star-like Bi island bases (high flux regime) are characterized by an average height of ~2 nm, while the compact and hexagonal island bases (low flux regime) are characterized by an average height of ~2.5 nm.

Figure 1-16 shows the flux dependent evolution in the morphologies of Bi (110) islands along the HOPG step edges by means of representative SEM images (coverage is kept constant at 1.5 ML). The low flux regime (7×10$^{-4}$ Å/s) is characterised by the growth of elongated nanorods which sparsely populate the substrate surface. A slight increase in the atomic flux up to approximately 0.03 Å/s causes the width of nanorods to increase and an increase in the flux to approximately 0.2 Å/s causes the length of the nanorods to decrease with an overall increase in the island density.

The next section builds on the above discussion on the morphology of Bi islands on HOPG and discusses the morphology of Bi islands on other substrates.

#### 1.2.2.2 Growth of Bi on other substrates

Growth of Bi islands on different substrates like Mica[90], Molybdenum disulphide[90] ($MoS_2$), Si[91] (111) is being undertaken actively nowadays to look for interesting, new physics and also to draw parallels with the growth pattern of Bi islands on HOPG. The key difference in all these cases is the nature of interaction of the substrate with Bi adatoms, where growth on Mica is characterized by the presence of oblong Bi nanostructures[90](low flux) whose elongation decreases as the flux is increased.

In addition to the different island shapes, a lack of stripes characterises Bi nanostructures on Mica as compared to the typically observed striped Bi[54] (110) islands on HOPG. Bi island growth on Si[91] (111) on the other hand, shows the presence of large islands with stripes, similar to the growth on HOPG.

Bi on $MoS_2$[90] also reveals a growth pattern similar to that observed for Bi/HOPG system, but with a comparatively higher density of 2-dimensional islands. One of the key results emerging out of the investigations of Bi islands on $MoS_2$ is the average thickness at which the transition of Bi (110) to Bi (111) oriented islands takes place. The transition occurs between average sample coverage of 7 and 15 ML for Bi (110) islands on $MoS_2$ as compared to approximately 12 ML as reported in Ref[54] for Bi (110) islands on HOPG. A stronger substrate-island interaction for Bi/$MoS_2$ system as compared to Bi/HOPG system is speculated to be the reason for different transition thicknesses for both the cases[92].

Having discussed the morphology of Bi islands in considerable detail, the morphology of self-assembled Sb[81] nanostructures on HOPG ,which are observed to form fractal[80] islands are briefly discussed next.

#### 1.2.2.3 Sb nanostructures on HOPG

Growth of Sb nanostructures on HOPG[93] at room temperature reveals a growth pattern that is similar to that of naturally occurring structures like snowflakes[94]. The tendency of Sb is to form branched and fractal islands[81] on HOPG which lack a defined and compact geometry. The measurement of taller heights[54] by AFM[95] confirms the 3-dimensional nature (Volmer-Weber growth mode) of Sb islands on HOPG in contrast to the 2-dimensional growth mode of Bi (110) islands on HOPG[52,54,87]. The morphology study of Sb islands on HOPG[54,63,81] as a function of incoming atomic flux

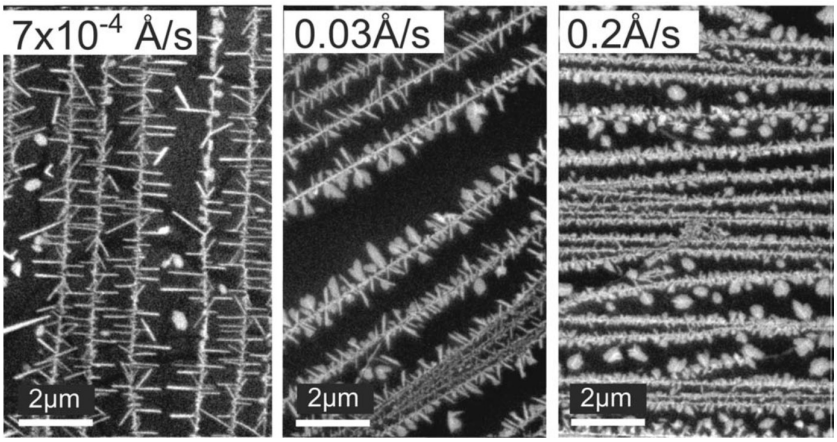


*Figure 1-16 Representative SEM images showing the evolution in the shape of step-edge nucleated Bi (110) islands as a function of flux. The flux is indicated on the images, the coverage is held constant at 1.5 ML. Image reproduced from[51].*

and the average sample coverage reveals a dynamic interplay between compact and branched morphologies. The discussion in the next two sections is kept short and restricted to the Sb morphology evolution, firstly, as a function of the atomic flux and then as a function of sample coverage.

#### 1.2.2.3.1 Flux Dependance

Figure 1-17 (a-c) shows representative SEM micrographs[54] demonstrating the morphology evolution of Sb islands on HOPG as a function of the incoming atomic flux. Figure 1-17 (a) shows the growth of Sb islands in a low atomic flux regime (0.005 Å/s) where small, compact islands decorate the HOPG step edges and larger islands occupy a small fraction of the HOPG terrace. Figure 1-17 (b) demonstrates the evolution in the island morphology in a higher flux regime (0.03 Å/s) clearly demonstrating increased branching along the island perimeters. Figure 1-17 (c) is representative of the highest flux regime (2 Å/s) studied and reveals a marked increase in the island density. In addition, two different types of island morphologies can be identified here, i.e. small and compact island morphologies along the step edges and branched island morphologies on the wide terraces.

The transition of smaller, compact Sb islands into larger and branched islands as a function of increasing flux is understood in terms of the dynamic interplay between the arrival time of atoms, i.e. $t_a$ and the time required for their subsequent incorporation into the aggregate, i.e. $t_c$. In a low flux regime few Sb adatoms populate the substrate which means that $t_a$ of new atoms towards any island is greater than $t_c$ required by the island to incorporate the atoms and stabilize the final island shape. As a consequence, sufficient time is available for the island to stabilize into a compact shape as observed near the step edges in Figure 1-17 (c).

The situation is opposite in higher flux regimes as the substrate comprises of higher number of atoms diffusing on HOPG, which means that the arrival time ($t_a$) of Sb atoms is considerably reduced. The incoming Sb atoms are therefore able to reach the islands' perimeter faster and in the process modify the perimeters and the island is unable to develop a smooth and compact morphology. The irregularities along the island perimeters, instead keep increasing as evidenced by the branched Sb island morphologies of Figure 1-17 (c).

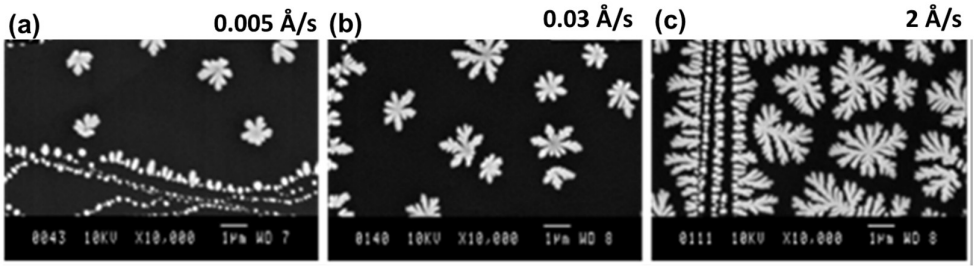


*Figure 1-17 (a-c) Representative SEM micrographs of Sb on HOPG as a function of increasing flux (coverage held constant at 10 ML). Image reproduced from[54].*

#### 1.2.2.3.2 Coverage dependant growth

Figure 1-18 (a-c) shows the evolution in the morphology of Sb islands on HOPG as a function of the average sample coverage. Figure 1-18 (a) shows the growth of small Sb islands at a low sample coverage of 5 ML, clearly showing that the Sb islands occupy only a small fraction of the substrate surface. Figure 1-18 (b) demonstrates an increased branching on the terrace nucleated Sb islands as the sample coverage is increased slightly to 10 ML. The step edge nucleated Sb islands, although, are again relatively compact and devoid of branching. Figure 1-18 (c) demonstrates a noticeable increase in the mean size of the terrace nucleated Sb islands as the sample coverage in increased to 40 ML and as a consequence a large fraction of the substrate gets occupied by islands. In addition, step edge nucleated and terrace nucleated islands show pronounced irregularity around the islands' perimeters. Overall an increase in the mean Sb island size and island branching is observed as a function of average sample coverage, consistent with other studies of Sb islands on HOPG[63,81].

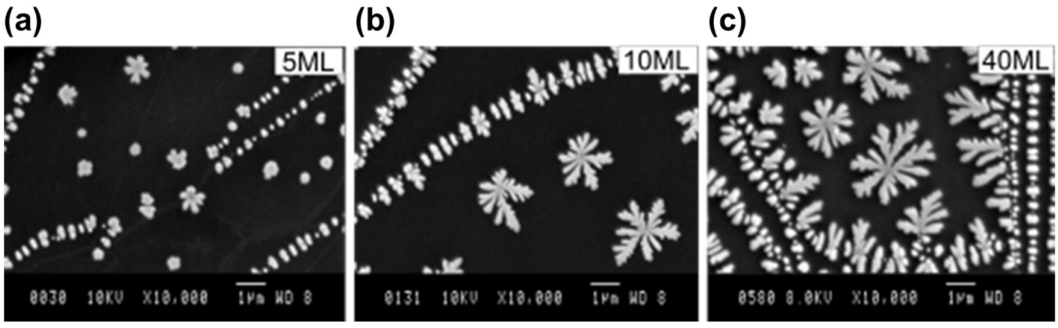


*Figure 1-18 (a-c) Representative SEM images of Sb islands on HOPG as a function of increasing coverage. The flux is kept constant at 0.03 Å/s. Image reproduced from[54].*

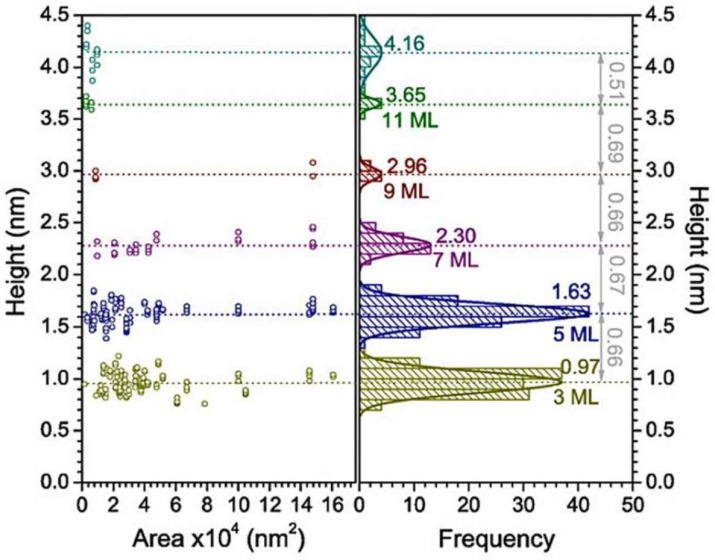


*Figure 1-19 The statistical height distribution of paired layers of Bi (110) islands on HOPG. The heights do not change as a function of island area as demonstrated by the area dependant chart shown alongside. Image reproduced from[99].*

The information presented on the discussion of self-assembled morphologies of pure Bi (110) and pure Sb islands on HOPG enables an understanding of the STM results[96-99] reported for pure Bi (110) islands on HOPG (next section).

### 1.2.3 STM on pure Bi (110) islands on HOPG

Investigations[96-99] of the morphology of Bi islands (section 1.2.2.1) on HOPG by STM reveals several interesting phenomena. Firstly, the height measurements (Figure 1-19) of the stripes[99] reveal a paired layer growth pattern along with the presence of an unusually taller island base, speculated to be a result of an additional 1 ML (3.3 Å) high wetting layer. Figure 1-19 shows that the average heights of 3 ML bases is 0.97 nm and the subsequent layers increases in paired layer manner,

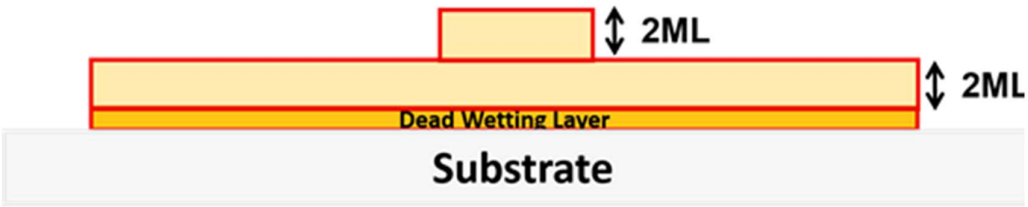


*Figure 1-20 A schematic diagram showing the wedding cake like morphology for Bi (110) islands on HOPG.*

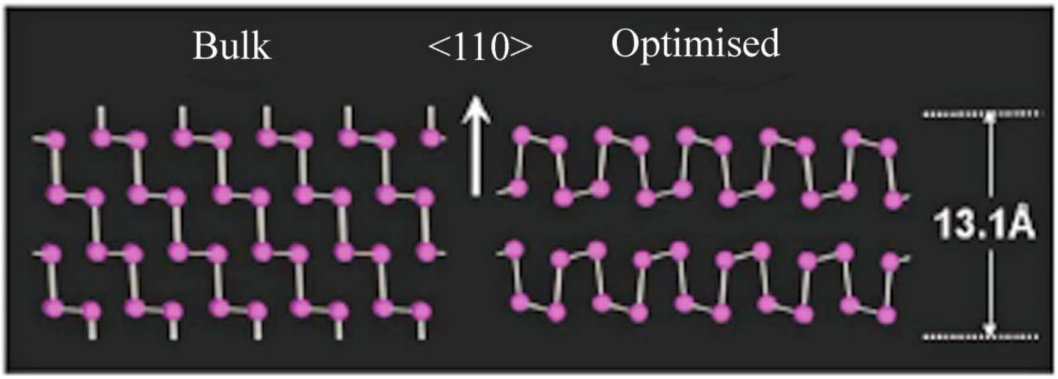


*Figure 1-21 The left panel shows a side view of Bi (110) phase with an unrelaxed bulk structure, comprising of four monolayers. The right panel shows the calculated atomic structure of the same Bi (110) phase after structural optimization. The optimized structure is analogous to the 'puckered layer structure' of black phosphorus. Image reproduced from[91].*

evidenced by distinct histogram peaks at 1.65 nm (5 ML), 2.30 nm (7 ML), 2.96 nm (9ML). Figure 1-20 demonstrates the paired layer geometry for a typical Bi (110) island on HOPG by means of a schematic diagram in which the wetting layer (yellow) and the consequent paired layers (light red) demonstrate a wedding cake like geometry. The presence of wetting layer is not well understood, but it does not alter the electronic properties of the paired layers as demonstrated in Ref[98]. Paired layer formation is argued to be a manifestation of black phosphorous (BP) like allotrope formation (Figure 1-21) and is on the same lines of the argument given in Ref[91] for Bi island growth on Si (111).

The right panel in Figure 1-21 shows the optimised BP like atomic rearrangement, which is achieved by the rotation of every second bond, resulting in the saturation of the dangling bonds from the (110) surface of the bulk structure (left panel). This configuration, therefore, results in the formation of 'paired layers' which are 2 ML thick and results in Bi (110) islands with a bilayer increment.

The other key result to have emerged out of the STM investigations is the demonstration[98] of lateral quantum size effects[6,100] (QSE) in the [001] lattice direction. Figure 1-22 shows the statistical width distribution on different thicknesses of Bi (110) islands on HOPG. The periodicity in the measured widths is evidenced by distinct, regularly occurring histogram peaks at 15 nm (3 ML), 6 nm (5 ML) and 4 nm (7 ML) in Figure 1-22. The periodicity in the measured widths is used to estimate the associated Fermi wavelengths for 3, 5 and 7 ML high thicknesses. A statistical measurement of island widths enables the calculation of the associated Fermi wavelengths by the equation:

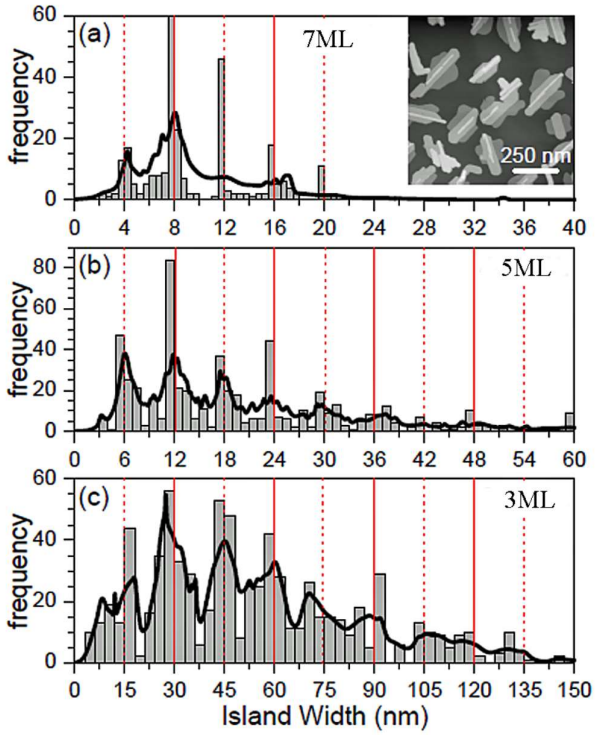


*Figure 1-22 Statistical width analysis on paired layers of pure Bi (110) islands on HOPG. Periodicity in the widths of different island thicknesses is understood to manifest due to quantum size effects. The Fermi wavelength $\lambda_F$ and $\lambda_{F/2}$ are indicated by solid and dashed vertical lines respectively. Measured $\lambda_F$ are 8 nm, 12 nm and 30 nm for 7, 5 and 3 ML thick islands respectively. Inset shows the typical Bi islands on HOPG. Image reproduced from[98].*

$$w = \frac{n\lambda_F}{2} \tag{7}$$

Where, w denotes the width of the corresponding island region and $\lambda_F$ denotes the corresponding Fermi wavelength. Figure 1-23 shows a schematic diagram which demonstrates the presence of quantized values of Fermi wavelengths[6] of the paired layers on Bi[98] (110) islands. This quantized expression of Fermi wavelengths is argued to arise due to a periodicity in the widths of a specific paired layer, analogous to the standing wave formation in a simple closed organ pipe[6,101]. The associated Fermi wave vector[6] can therefore, be estimated from the calculated widths and used[98] to correlate the experimental results to the theoretical calculations.

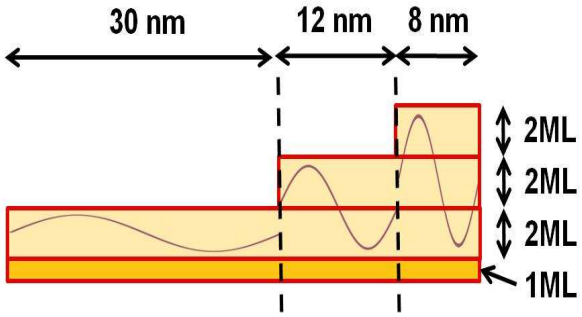


*Figure 1-23 A schematic diagram showing quantized Fermi wavelength values estimated for Bi (110) islands on HOPG, due to an observed periodicity in the island widths.The figure shows the calculated Fermi wavelength values for 3 ML, 5 ML and 7 ML.*

## 1.3 Questions addressed in this thesis

There are three major questions, addressed by STM investigations carried during this project:

- How does the morphology of $Bi_{1-x}Sb_x$ islands on HOPG evolve as a function of Sb concentration?
- How does the local density of states (LDOS) of the paired layers of $Bi_{1-x}Sb_x$ islands evolve as a function of Sb concentration?
- Do $Bi_{1-x}Sb_x$ islands demonstrate the presence of edge states?

## 1.4 Structure of thesis

Chapter 2 describes the crystal structure of the key materials (Bi, Sb and HOPG) along with the description of the experimental setup and the characterisation technique used during the project.

Chapter 3 describes the morphology of $Bi_{1-x}Sb_x$ islands by analysing the RT-STM images with an emphasis on the island morphology evolution as a function of Sb concentration.

Chapter 4 describes the 50 K Scanning Tunnelling Spectroscopy (STS) results acquired on the paired layers of $Bi_{1-x}Sb_x$ islands with an emphasis on understanding the reproducibility of dI/dV features by spectral histograms.

Chapter 5 describes the conductance maps acquired on the edges of the paired layers of $Bi_{1-x}Sb_x$ islands along with the analysis of the corresponding edge dI/dV spectra.

Chapter 6 The major conclusions of the project and the outlook for future experiments is briefly discussed.

# 2 Experimental Description

The chapter describes the materials, experimental setup and techniques used during the project. The crystal structures of the two key elements, pure Bi, Sb and the substrate (HOPG) used in the project are discussed first, followed by a description of the experimental setup, i.e. the Ultra-High Vacuum Variable Temperature Atomic Force Microscope (UHV-VT AFM)[102] setup. The setup description includes a brief description of the methodology adopted for HOPG surface cleaning. After setup description, the chapter discusses the key characterisation technique used in the project, i.e. STM and is concluded with a brief demonstration of the data processing and analysis methodology.

## 2.1 Materials

This section briefly describes the bulk crystallographic structure of Bi, Sb (evaporant materials) followed by that of the substrate (HOPG).

### 2.1.1 Bismuth and Antimony

Bi and Sb are group V semimetals[6] with a rhombohedral (A7) crystal structure[103], out of which Bi is especially interesting for studying quantum size effects[6] due to the low concentrations of charge carriers, small effective masses, large Fermi wavelengths up to 40 nm and large mean free paths[103,104]. The unit cells of both the materials (Bi and Sb) comprise of two atoms per unit cell with the corresponding lattice parameters in the rhombohedral system:

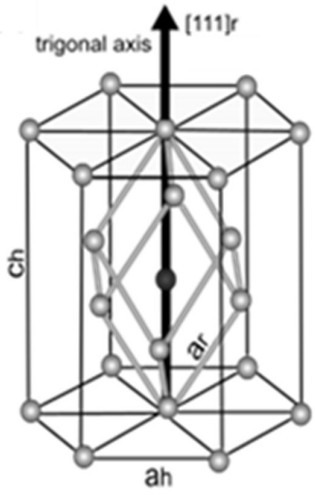


*Figure 2-1. A rhombohedral unit cell comprising of a two atom basis, inscribed inside a hexagonal system. The central atom is shaded dark and the [111] direction is denoted. Image reproduced from[54].*

- Bi: $a_r$= 4.75 Å, $\alpha_r$=57.14°
- Sb: $a_r$= 4.51 Å,$\alpha_r$=57.7°

Figure 2-1 shows a rhombohedral unit cell, used for describing the crystal structures for both Bi and Sb. Each unit cell comprises two atoms, which are bonded to three nearest atoms within the same layer by strong covalent bonds and to the atoms in the adjacent layers by weak bonds. The central atom inside the unit cell of Figure 2-1 is shaded dark to show clear distinction from the atoms at the edges of the unit cell. It is emphasized that all the key crystallographic notations used in the project are described by the rhombohedral indexing system[6].

### 2.1.2 HOPG

HOPG comprises stacked carbon-carbon sheets, bonded by Van-der Vaal forces, causing it to be a weakly joined material. Figure 2-2 (a) shows the hexagonal crystal structure of HOPG[105] in which the stacking sequence of the C-C layers is observed to repeat after every two layers. The accepted value of the average distance between two adjacent C-C layers is approximately 3.4 Å (denoted in Figure 2-2 (a)).

Figure 2-2 (b) shows the top surface of the HOPG crystal structure along the vertical trigonal-axis in which dashed lines denote the interlayer weak bonds and dark lines denote the intralayer strong bonds (1.42 Å). Upon cleaving (section 2.2.5), the weak interlayer bonds of HOPG break first and leave a smooth and flat HOPG surface in the process. HOPG is available in different grades, like the SPI-1 or ZYA (calibration quality) grade which exhibits a low mosaic angle (a measure of the ordered nature of

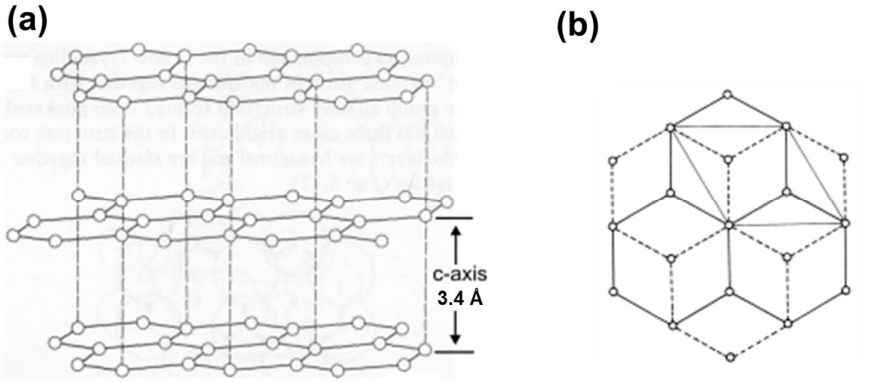


*Figure 2-2 (a) Shows the crystal structure of graphite, in which the broken lines indicate weak bonds between successive graphite sheets and the solid lines indicate the strong bonds within a layer (b) Shows the top surface of a single graphite sheet, viewed along the trigonal-axis. Images reproduced from[105].*

HOPG), whereas, grades like the SPI-2 (ZYB) and SPI-3 (ZYH) comprise of considerably high mosaic angles and are not suitable for experiments in which the requirement of high-quality substrates is essential. All the experiments performed during this project are performed on the SPI-1 grade of HOPG to prevent any substrate induced contamination. In addition, the HOPG surface is manually cleaved in atmospheric conditions (section 2.2.5) to further remove contaminants prior to deposition.

## 2.2 Experimental setup: UHV VT AFM

The UHV VT-AFM setup consists of two main chambers, i.e. the main Scanning Probe Microscopy (SPM) chamber, and the Fast Entry Lock (FEL) chamber. The key components of both the chambers are explained in this section, with the key components of the main SPM chamber explained first, followed by a description of the FEL. The description is followed by discussion of UHV pumping in the VT-AFM.

### 2.2.1 Main SPM chamber

Figure 2-3 shows the front view (photograph) of Omicron UHV-STM/AFM setup in which the key components are labelled using black arrows. The region labelled as the SPM vacuum chamber essentially comprises two regions, the vapour deposition region (Knudsen Cells (section 2.2.1.3)) and the characterisation region (microscope assembly (section 2.2.1.1)). The main microscope assembly is housed on the SPM base plate (section 2.2.1.1) and is capable of operating at extremely low-pressure values (~$10^{-11}$ mbar). Such low-pressure values are attained by continuous pumping by an Ion getter pump (I-G pump) and three titanium sublimation pumps[106,107] (TSPs) operating in tandem, all of which are explained in section 2.2.3.

The part labelled as the manipulator in Figure 2-3 refers to an extended, movable arm consisting of a place holder used for holding samples and tip holders during sample preparation and deposition processes (section 2.2.1.4). The part labelled as the wobble stick is a UHV compatible arm with a pincer at the front which is used for clamping and moving the sample and tip holders inside the setup. The view ports have glass shields that enable observation of all the internal components of the setup. A continuous flow cryostat[102] for low temperature (50 K) experiments is housed at the backside of the SPM base plate (next section).

In addition, the setup comprises of a quartz crystal microbalance (section 2.2.1.6) used for the estimation of the vapour atomic flux from the Knudsen cells. A carousel for parking 6 sample plates/tips at a given point of time is located inside the setup, increasing the setup's efficiency. The back side (not shown in Figure 2-3) of the UHV AFM setup comprises of a Fast Entry Lock (FEL) used for exchange of samples. The FEL is discussed in more detail later in section 2.2.2.

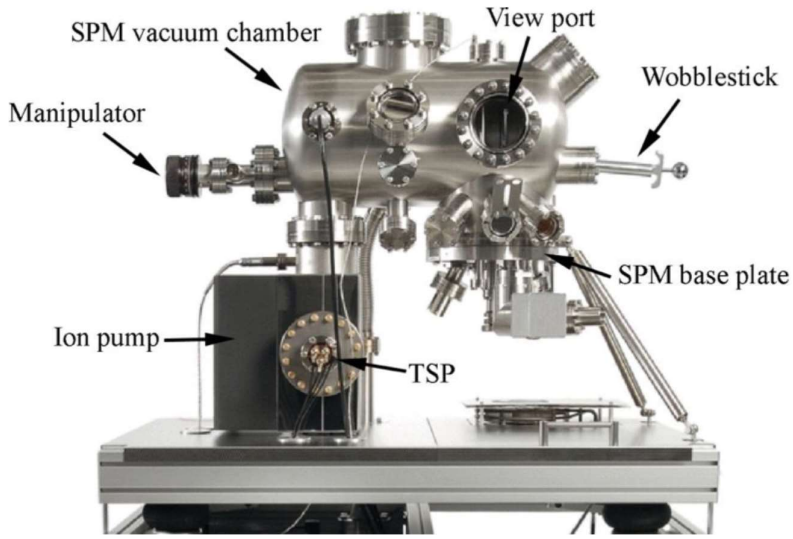


*Figure 2-3 Photograph of the Omicron VT AFM setup used during the project. Image reproduced from[102].*

#### 2.2.1.1 SPM Base plate-microscope assembly

Figure 2-4 shows front view of the schematic diagram of SPM microscope assembly housed on the SPM base plate, surrounded by four spring columns. Copper plates used for intercepting vibrations of the suspension system by means of a current damping mechanism surround the whole SPM base plate. The exchange of sample and tip holders on the microscope assembly is enabled by locking the whole spring suspension system using a push-pull motion (PPM) feedthrough. The LHe flow cryostat (section 2.2.1.2) indicated in the schematic diagram is attached to the sample stage by means of a copper braid to establish a thermal connection between the sample stage and cryostat.

The most important component of the SPM assembly, i.e. the piezoelectric scanner is housed inside the SPM base plate (shown in Figure 2-5) as well. The scanner is primarily responsible for controlling the movement of a sharp metallic tip on the surface of a sample by adjusting the feedback loop. The schematic diagram of the piezoelectric scanner in Figure 2-5, shows that the scanner comprises an additional inner electrode inside the main scanner tube, where the inner surface of the tube allows for the vertical displacement (z) of the scanner and the lateral motion (x and y) is enabled by the outer electrode. The loading head of the scanner is protected by a radiation shield and comprises of tiny magnets that hold the AFM and STM tip holders together.

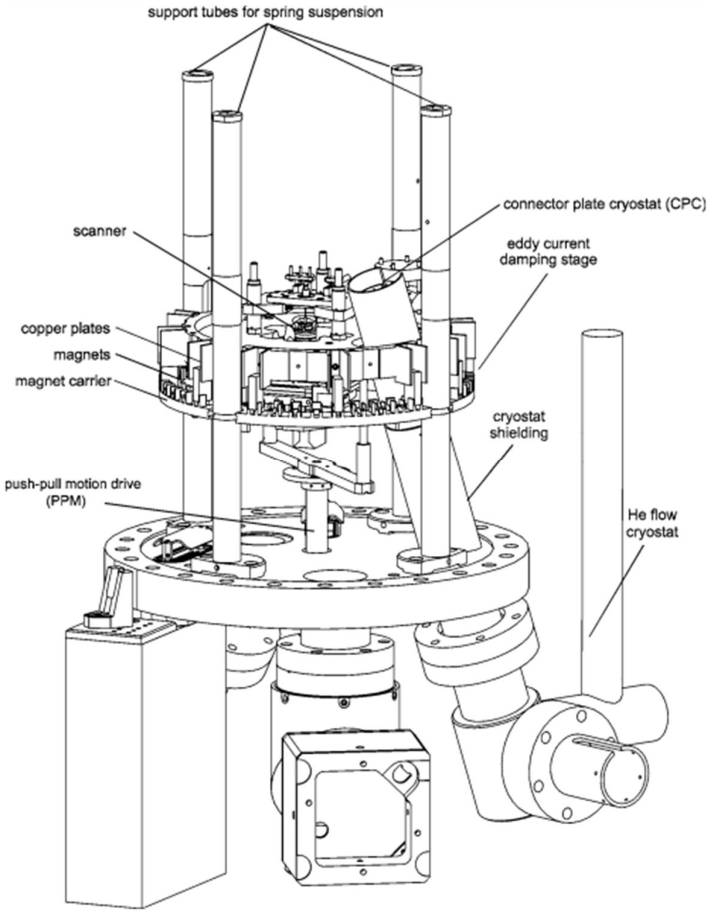


*Figure 2-4 A schematic diagram of the scanning probe microscope assembly housed inside the Omicron VT AFM setup. Image reproduced from[102].*

The piezoelectric scanner design[102] allows precise and controlled movement of the attached STM tips/AFM cantilevers in x, y and z directions by expansion and contraction in response to an externally applied bias voltage. The scanner has a maximum scan range of about 10 µm in the two lateral directions (x and y) and a limit up to ~1.5 µm in the vertical direction (z). The key concept governing the motion of the piezoelectric scanner is the natural response of piezoelectric materials[108] to externally applied voltages. A net z-displacement due to the contraction and expansion of the piezoelectric scanner's tube takes place as different bias voltage is applied. In principle, different feedback loop settings can be used for a precise control over the movement of the scanner. The piezoelectric scanner can be operated either in constant height or constant current setting mode during the image acquisition process, both of which are explained later in section 2.3.2.

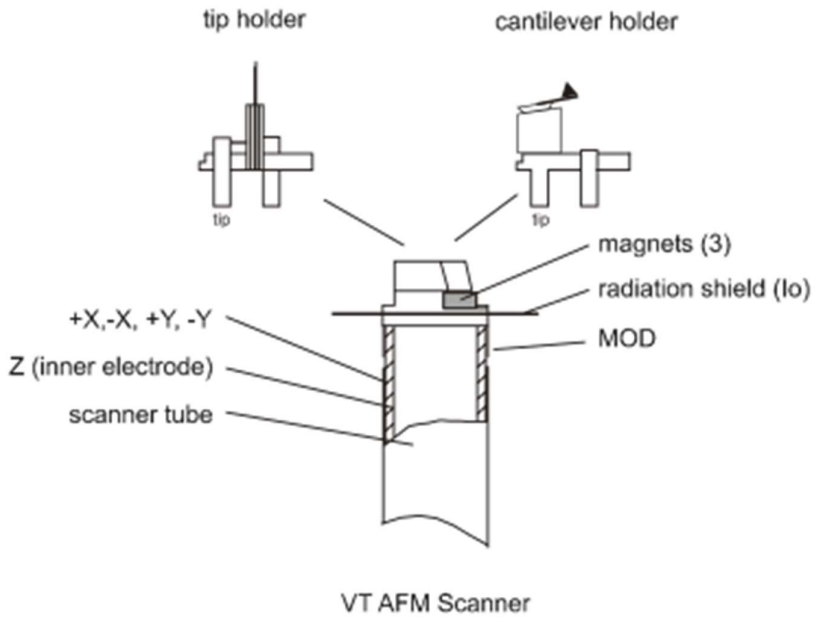


*Figure 2-5 A schematic diagram of the piezoelectric scanner. Image reproduced from[102].*

#### 2.2.1.2 Flow Cryostat: 50 K temperature measurements

STM measurements, in particular, tunnelling spectroscopy experiments, are more stable at low temperatures as thermal drift and fluctuations in the movement of the STM tip are considerably reduced. The use of liquid nitrogen ($LN_2$) and liquid helium (LHe) through the continuous flow cryostat enables the stabilization of the VT-AFM setup at cryogenic temperatures. Cooling down of the setup by using $LN_2$ makes it possible to achieve working temperatures of approximately 100 K, whereas cooling down of the setup by LHe allows the working temperatures to be stabilized at much lower (~50 K) values.

Figure 2-6 shows the schematic diagram of the experimental setup arrangement during the low temperature LHe measurements. As can be seen in the schematic diagram, the inlet of the flow cryostat is connected to LHe Dewar via a cryogenic liquid transfer tube (siphon) that consists of a needle valve (A) to monitor LHe flow through the whole system. The outlet of the cryostat is connected to the LHe rotary pump via a pressure control block that consists of a fine needle valve (B) and coarse valve (bypass) for controlling the flow of LHe within the setup arrangement. The whole setup arrangement allows steady maintenance of cryogenic temperature values (~50 K) as a result of continuous pumping of LHe through the flow cryostat. The next two sections describe flushing of He line prior and one of the cooling down protocols.

#### 2.2.1.2.1 Flushing of the He line

In order to make sure that there are no leaks within the LHe setup, flushing of the line is initiated by keeping valve A, B and the bypass closed initially. To start the flushing process, the helium pump (rotary) is switched on, simultaneously with the opening of the bypass valve located on the pressure control block. During this time, the pressure display at the control block is closely monitored and as the pressure reaches a value below 150 mb, the bypass valve is closed.

A good estimation of leakage in the He line is done by monitoring the control block pressure for about one minute. A steady value of the pressure on the control block indicates that the He line is devoid of any leakages. After this step, valve A is opened until the pressure reaches approximately a value of 1 bar and thereafter observed again for about a minute. On the attainment of a steady pressure value, valve A is closed. The bypass valve is opened again to allow the pressure on the control block to reach approximately 50 mB and closed again. The steps described above are repeated about 6-8 times to ensure no leaks are present in the He line. Thereafter, preparations are initiated for cooling down of the whole setup.

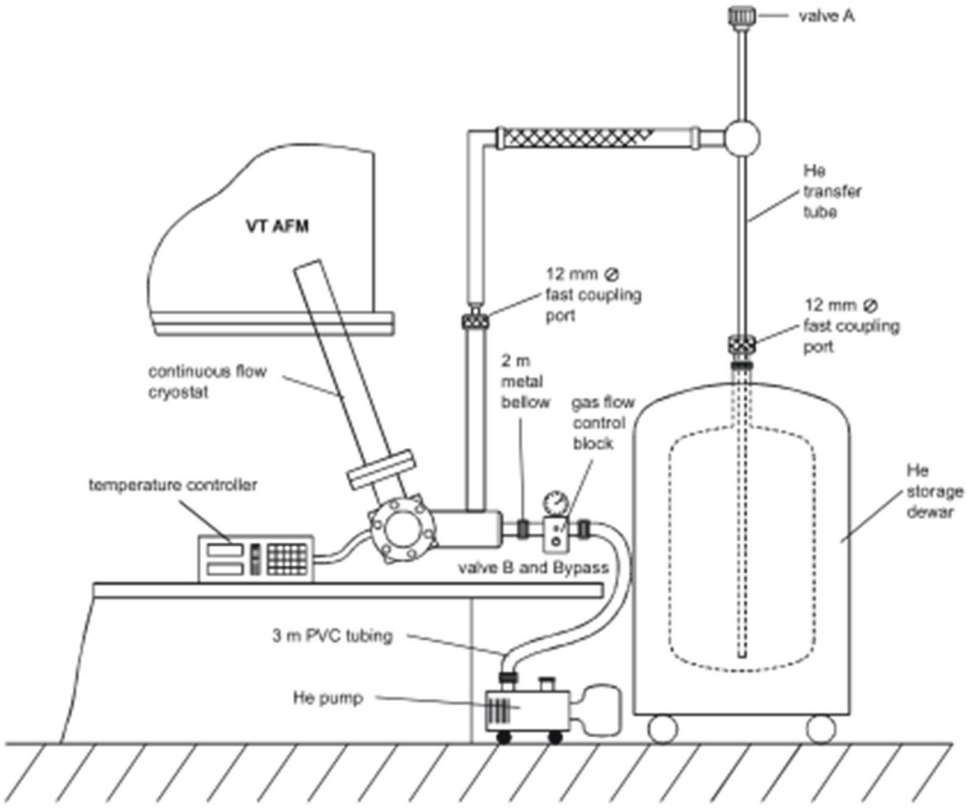


*Figure 2-6 A schematic diagram showing the experimental arrangement for the low temperature (50 K) measurements in the Omicron VT-AFM setup. Image reproduced from[102].*

#### 2.2.1.2.2 Cooling down and warming up protocols

On completion of the flushing process, one of the standard[102] (slow and fast) cool down procedures can be initiated. The slow cool down protocol is described in this section as it is the protocol used for LHe measurements during the project. The protocol involves closing down of the bypass valve first and setting the fine valve 'B' to approximately 8 mm, which allows attainment of steady temperatures up to ~50 K. Lastly, valve 'A' is opened partly to allow a sufficient flow of LHe through the setup.

On completion of LHe experiments, a simple warming up procedure is followed in which the rotary pump is switched off first and the valve 'B' is closed thereafter to allow the pressure in control block to reach approximately 1000 mB. Valve 'A' is closed after this step to prevent any flow of LHe from the dewar. The siphon is then lifted out of the dewar and the cryostat opening is closed by a plug to avoid any unwanted ice formation.

### 2.2.1.3 Knudsen Cells

Standard vapour evaporation techniques like chemical vapour deposition[3] (CVD), physical vapour deposition[3] (PVD) and molecular beam epitaxy[3] (MBE) make use of crucibles which can be heated up to extremely high temperatures (~1500° C) and in the process, enable evaporation of materials with a high melting point materials conveniently. The standard Knudsen cell (Figure 2-7) used in the VT-AFM setup is designed for evaporation of materials at operating temperatures up to approximately 1000° C. Such high temperatures are attained by thermal radiation of the PBN (Pyrolytic Boron Nitride) crucible (labelled in Figure 2-7) placed inside the Knudsen cell. The temperature of the


*Figure 2-7 A photograph of a standard Knudsen cell used in an Omicron VT AFM setup. Image reproduced from[102].*

PBN crucible is measured by the direct contact of the crucible head by a chromel/alumel (type K) thermocouple[109].

A reliable measurement of the crucible's temperature and consequently the atomic flux of the evaporated material is possible only when a stable temperature is maintained throughout the whole length of the crucible. The stability in the temperature of the crucible is achieved by allowing continuous movement of water in an integrated water cooling shroud around the crucibles (indicated in Figure 2-7). The flux of the water through the shrouds is usually greater than 30L/hr to allow a quick dissipation of heat developed as a result of high crucible temperatures.

To avoid any impurity contamination of the crucible materials, it is important that certain precautions are followed. First and foremost, filling up of the crucibles should always be performed in an extremely clean environment, preferably under a laminar airflow[110] chamber. Secondly, lint-free gloves and grease free tweezers are considered essential while holding the crucible during the filling up process.

#### 2.2.1.4 Manipulator

The preparation of samples by vapour deposition in the VT-AFM setup is enabled by placing substrates inside a vacant holding space at the tip of a long UHV compatible arm called the manipulator. The presence of an internally integrated heater unit inside the manipulator's head is used to control the temperature of the sample placed on the manipulator head. The effective temperature of the manipulator's head can be varied from 25° C to 900° C by ramping power of the integrated sample heater. The manipulator head can be heated up in two different ways, i.e. resistive (used for samples like HOPG) and direct heating (used for samples like Silicon) methods.

In addition to this inbuilt heating facility, the manipulator can be moved in x, y, z directions and rotated by ±180° (Θ). The capture of incoming vapour beams from the Knudsen cells is facilitated by this four-dimensional rotation facility of the manipulator. The standard settings of the manipulator used during deposition of the different elements (Bi and Sb) simultaneously during the preparation of an alloy, the settings shown in Table 2-1 are used.

#### 2.2.1.5 Wobble Stick

Figure 2-8 shows a schematic diagram of the UHV compatible wobble stick housed inside the setup, primarily used for moving samples and tip holders inside the main SPM chamber. The wobble

| x | y | z | Θ |
|---|---|---|---|
| 13 cm | 14.4 cm | 45.8 cm | 150° |

*Table 2-1 Standard settings of the manipulator during a typical material deposition process.*

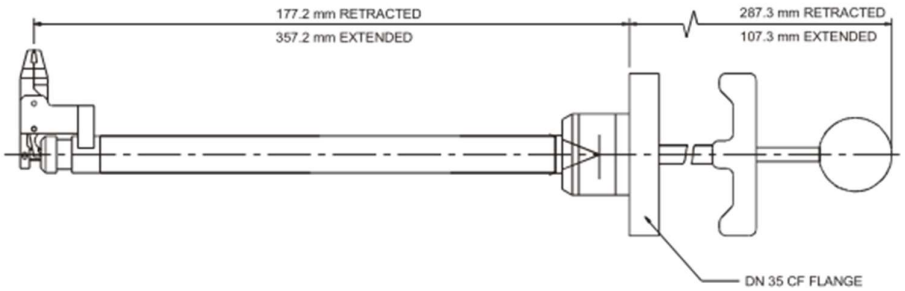


*Figure 2-8 A schematic diagram of the wobble stick fitted inside the UHV-VT AFM setup, primarily used for moving samples and tip holders insde the main SPM chamber. Image reproduced from[102].*

stick has a double action pincer at the front, which means that both the jaws at the front are movable and can be used to grab hold of a different sample and tip holders. The knob fitted on the extreme right is pressed tightly against the handle to open the jaws and grab the sample plates and tip holders. The whole wobble stick assembly allows efficient movement inside the system as it can be moved in three different directions, i.e. linear motion in the z-plane, angular motion in the x-y plane along with the pincer grip motion.

#### 2.2.1.6 Quartz monitor: Flux measurement

The development of high-quality thin films requires precise estimation of the atomic flux of the evaporated materials. Moreover, estimating the atomic percentages of the constituent materials of thin films is considered a good research practice. The VT-AFM comprises of a quartz crystal micro balance[111] (Sycon STM-100) housed inside the main SPM chamber used for the measurement of atomic flux, both prior to and after the deposition process. A retractable flange holds the quartz microbalance in its designated port. The quartz crystal is protected from any radiation damages by the continuous circulation of water through the attached water pipes.

The Sycon STM-100 makes use of the resonant frequency of the quartz micro balance to determine the mass of any deposited film on it. A slight change in the resonant frequency of the micro balance due to the deposition of additional mass is utilized to estimate the deposited film's total thickness. A reliable interpretation of the measured atomic flux although requires a systematic calibration of the quartz microbalance. The calibration comprises of three major factors that tend to affect the process significantly, namely the material density, material Z factor and tooling factor. Each of these factors is briefly explained in the next few subsections.

#### 2.2.1.6.1 Density Determination

The accuracy in the measurement of film thickness is accomplished routinely by using the literature value of material's bulk density. To estimate the density of an unknown material, a simple protocol is followed in which a substrate is placed adjacent to the crystal sensor to align the substrate and sensor with the incoming evaporant beam. Once, the position of the substrate and the crystal is aligned, the instrument density is set to the bulk density value of the material. After the above described processes, approximately 5000 Å of material is deposited both on the crystal sensor and the substrate. The substrate is eventually removed and taken out from the main SPM chamber and the deposited film's thickness is measured in an ambient AFM setup.

#### 2.2.1.6.2 Z-factor

The Z-factor includes information about the density and shear modulus of the quartz crystal and the deposited film. A common practice is to use the accepted literature values of Z-factors. For materials, whose Z-factor values are not available, a calibration deposition similar to that employed for the density determination method is employed. Once the parameters are setup, a thicker film is deposited and used for calibration purposes in an ambient AFM setup.

#### 2.2.1.6.3 Tooling Determination

The position of quartz micro balance inside the main SPM chamber is not ideal, as it is not positioned directly in front of either of the Knudsen cells. To account for this difference in the microbalance's position w.r.t the Knudsen cells, a suitable calibration method referred to as tooling determination can be followed. The substrate is placed in the sample holder position of the manipulator and a thicker film (~5000 Å) is deposited using either the bulk or the calibrated density and Z-factor values and the tooling parameter is set to 100%. Once the film is deposited, the substrate is taken out of the chamber and the film thickness is measured in an ambient AFM setup. The tooling factor, thereafter can be estimated by:

$$Tooling\ \% = 100 \times \frac{measured\ substrate\ thickness}{estimated\ substrate\ thickness} \tag{8}$$

### 2.2.2 Fast Entry Lock: FEL

The FEL chamber is primarily used to transfer sample plates/tip holders inside the main SPM chamber. The FEL is isolated from the main SPM chamber by means of a gate valve which prevents

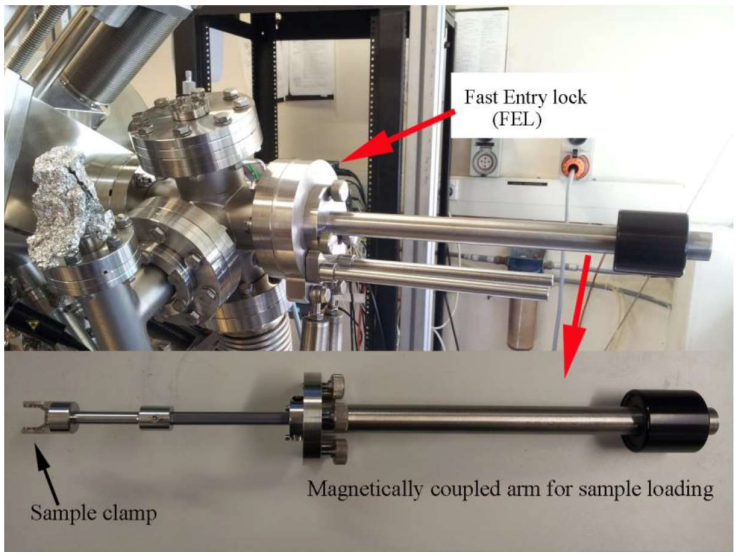


*Figure 2-9 A photograph showing the side view of the VT-AFM setup, consisting of the FEL used for transferring sample/tip holders to the main SPM chambler by means of a magnetically coupled arm.*

any break in the setup's vacuum and consists of a magnetically coupled transporter arm (Figure 2-9) which is used for sample transfers by clamping the samples at the front. It is important to note that the sample is loaded onto the manipulator arm in atmospheric conditions and immediately after sample loading process, the FEL is pumped down to approximately $10^{-8}$ mbar (reached in approximately 2 hours after starting the turbo molecular pump (section 2.2.3.3)). On reaching this pressure value, the gate valve between the FEL and main SPM chamber is opened to transfer the sample without breaking vacuum between the two chambers.

### 2.2.3 UHV Pumping

UHV conditions (~$10^{-11}$mbar) in any experimental setup are achieved by continuous pumping by an Ion-Getter Pump (IGP) and Titanium Sublimation Pumps (TSPs) operating in tandem and the process is complemented by preliminary pumping by a Turbo Molecular Pump (TMP). The key components of all these three different pumps are discussed briefly followed by a descriptions of their working mechanism.

#### 2.2.3.1 Ion-getter pump (IGP)

The IGPs form an intricate component of any UHV apparatus in which the working experimental conditions need to have low pressures (<$10^{-6}$ mbar). The IGPs are the cleanest and most efficient

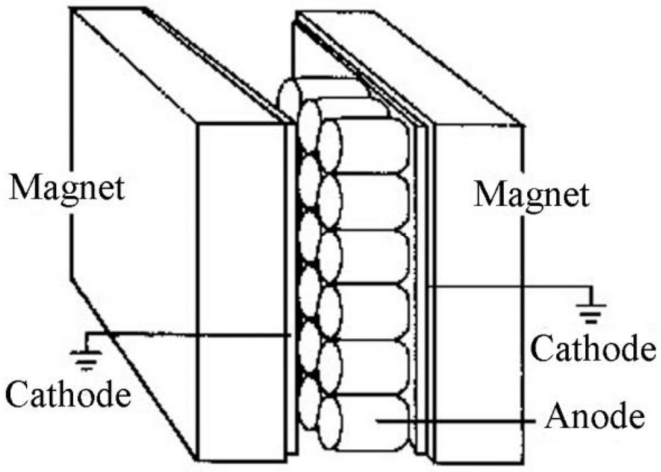


*Figure 2-10 A schematic diagram of an ion-getter pump, showing the key components.*

pumps used to attain UHV conditions, a fact attributed primarily to their unique mechanical arrangement and working mechanisms.

Figure 2-10 shows a schematic diagram of an IGP, showing the presence of an anode, a cathode within the main enclosure which is enclosed by two permanent magnets. The non-presence of any moving parts inside the IGPs makes them an ideal candidate for vacuum sealed systems that require a reliable and long-term operation. In addition, IGPs operate without any vibrations and agitation, resulting in minimum power consumption. All these capabilities of the IGPs allow a diverse range of applications to be possible and thus form an integral part of scientific apparatus such as particle accelerators[112], mass spectrometers[113] and high-resolution microscopy techniques[89]. The IGPs work by capturing the randomly moving residual gas particles inside the UHV chambers by converting them into solid compounds and permanently binding within the I-G pump setup. This binding of the gas particles inside the IGPs allows maintenance of stable vacuum conditions for longer time durations.

#### 2.2.3.1.1 Mechanism

The external power source that controls the working of an IGP allows the application of a positive bias on the anode, which creates an electron cloud within the setup. The applied positive bias to the anode alters the charged particles' velocity and density, affecting the overall pressure. The permanent magnets around the IGP setup induce a strong magnetic field and force the residual charged particles within the electron cloud to move in spiral orbits. During this process, neutral particles in the electron cloud are ionised as they collide with electrons of sufficiently high energy.

These collisions tend to free up more electrons, increasing electron cloud's density and ionising other gas particles in the process. Upon the collision of ions, a few of the ionized particles react with the cathode, leaving other neutral particles in free motion. This interaction distributes the cathode material throughout the IGP setup, thus providing fresh cathode material for interaction with the residual particles.

The eventual removal of residual particles from the UHV chamber thus depends on the type of gas species as well as on the type of cathode material used inside the IGP. These two factors play a vital role in the overall pressure maintained by the IGP.

#### 2.2.3.2 Titanium Sublimation Pumps (TSPs)

Titanium (Ti) is a common getter material, which forms a key component of the Titanium Sublimation Pumps (TSPs) commonly used in UHV setups. TSPs work by chemisorption of residual charged particles in a UHV chamber on the evaporated titanium metal surface. A standard TSP evaporates Ti, which condenses on the colder internal surface of the IGP, forming a chemically active Ti layer. The residual gas molecules which are in perpetual motion due to the action of the I-G pump are captured as they collide with the titanium film surface. After consecutive cycles of Ti filament evaporation, the initially adsorbed gas molecules get covered (buried) by a fresh layer of evaporated Ti and this burial process contributes to the removal of residual charged particles.

The TSP assembly installed in the Omicron VT-AFM setup is shown in Figure 2-11. The main TSP assembly comprises a UHV compatible flange housed inside the IGP within the main SPM chamber. At

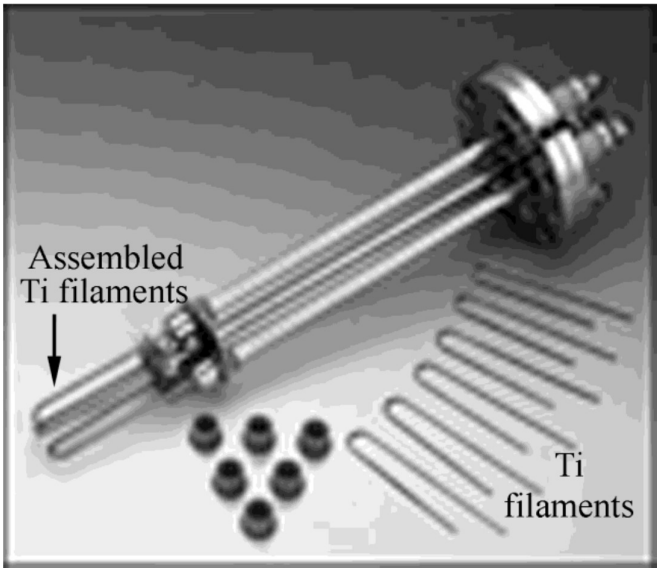


*Figure 2-11 Photograph of titanium sublimation pumps used in the UHV AFM system.*

any given point of time, the TSP assembly is capable of holding together three different Ti filaments. Individual Ti filaments are shown alongside the main TSP assembly in Figure 2-11. Efficient pumping by a TSP pump is possible only when sufficiently high pumping speeds and low interval times between subsequent evaporation cycles are used.

Importantly, the pumping speed of TSPs is directly proportional to the chemically active surface of the filaments, where the typical time intervals of Ti filament evaporation can be tuned anywhere between 8 to 32 hours. A common practice is to operate the TSPs in conjunction with the IGPs and evaporate Ti for short bursts, with each evaporation cycle lasting for approximately one minute.

#### 2.2.3.3 Turbo Molecular Pump

A Turbo Molecular Pump (TMP) works on the same working principle as that of an airplane's turbine. A standard TMP comprises rotor and stator disks. Stators are fixed discs that contain the same blades as that of the rotors, but both of them are oriented in opposite directions. Figure 2-12 shows a lateral view of a standard TMP which demonstrates the presence of a rotor-stator combination. Once the blades of the TMP start to spin at an approximate RPM (revolutions/minute) of 20000-90000, then the residual charged particles present inside the setup are imparted a slight momentum on collision with rotating blades. This continuous rotation of rotor-stator pair drives the gas particles towards the pump exhaust and eventually removed from the setup.

A TMP usually works in tandem with a rotary pump. A rotary pump aids in attaining pressures up to approximately $10^{-3}$ mbar and once, the overall pressure reaches approximately $10^{-3}$ mbar, the TMP is switched on and allowed to pump away the residual charged particles. At such high pressures (~$10^{-3}$ mbar), the gas flow is generally referred to as molecular flow, which means that the gas particles

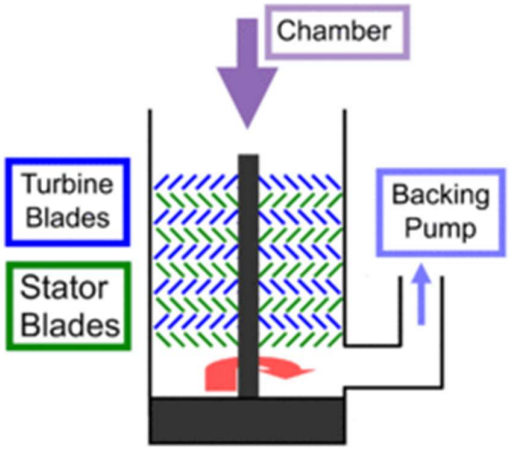


*Figure 2-12 Schematic diagram of a turbo-molecular pump (TMP).*

are relatively free to move around within the SPM chamber and to a good approximation demonstrate a regime of minimum interaction. During this minimum interaction regime, TMP imparts enough momentum to each of the charged particles independently and propels them towards the pump exhaust. This propulsion mechanism creates an efficient pumping environment within the setup.

Once turned on, the TMP can work for long durations of time and reduce the system pressures until saturation is reached. Saturation of the pumping mechanism takes place between the pressure range ($10^{-6}$-$10^{-8}$) mbar and is attributed to two major reasons. The first reason is desorption of residual gas particles from the high vacuum seals and bearings, a phenomenon which increases significantly at lower pressure values. The gas desorption effect thus increases the overall setup pressure by counteracting the pumping effect of the TMP. The other reason causing the saturation of pressure is the presence of any unwanted leaks around the vacuum seals. Such leaks become increasingly significant at lower pressure values, due to the pressure difference between the outside and inside of the setup.

The TMP incorporated within the VT-AFM is primarily used for pumping down of the FEL (section 2.2.2) chamber, apart from creating high vacuum conditions before a bake out session. In spite of the efficient pumping capabilities of all the pumps described in this section, UHV experimental setups are prone to contamination as a result of unwanted charged particles and therefore, require high-temperature bake outs after few months of continuous operation.

### 2.2.4 Baking of VT-AFM

To remove contaminants from UHV chambers, regular baking at sufficiently high temperatures (~150° C) is considered important. The standard protocols followed before, during and after a standard bake-out session on the VT-AFM setup are outlined in the next two sections.

#### 2.2.4.1 Pre-bake out protocol

Before a high-temperature bake-out is initiated on the VT-AFM setup, the vent valve is checked and tightly closed to avoid any unwanted leaks. The turbo molecular pump attached to the FEL is switched on and allowed to pump the whole chamber to low pressures preferably to the order of low $10^{-5}$ mbar. This step is performed with the gate valve completely open to allow effective pumping of the whole SPM chamber. In the meantime, all the magnetic parts (three) attached to the setup are removed to prevent any temperature induced damage to the magnets. Thereafter, the remaining cables are carefully removed except the cable connecting the Ion gauge to the SPM controller unit.

The fibre optic cable attaching the laser unit of the AFM preamplifier requires special attention, due to the cable's fragility, therefore, all efforts should be made to not apply any undue and extra

pressure while removing it. The components of the UHV chamber that contain any rubber inlets, like the cryostat inlet valve, are inspected and any rubber components are carefully removed.

Once, all the cables are removed, the attached water pipes used for maintaining equilibrium temperatures around the two Knudsen cells and the quartz micro balance are removed. Removal of any residual water from the vacant Knudsen cell ports and water pipe inlets is further accomplished by blowing a jet of compressed air.

As a last precautionary measure, the STM bench table is inspected for the presence of any plastic or rubber remnants lying around, which are consequently removed, if found. After a careful inspection of the STM bench table, all the vacant pins and viewports (glass) are covered by small aluminium foil pieces to minimize unwanted thermal expansion and charge accumulation during the high-temperature bake out session. The final step includes covering the setup with a dedicated bakeout frame. The IGP is then switched off, before initiating a standard bake out session at 150° C for a duration of 24-48 hours.

#### 2.2.4.2 Post bakeout Protocol

Once the bake out reads successful on the SPM controller unit, all the cabling is attached back and sufficient time (~6 hours) is allowed for the setup to cool down to room temperature. Once the system has cooled down, each of the TSP filaments is degassed at least three times for durations of 1 minute each. The degassing procedure is continued until each of the TSP filament shows a reduction in the release of contaminants. Once all the pumps have been sufficiently degassed, the manipulator arm in the main chamber is degassed at approximately 90 W for 16 hours (preferably overnight). During the manipulator degassing process, an empty Tantalum (Ta) sample plate is used to cover the integrated heater to avoid radiative damage to nearby components in the setup. The last step comprises of closing the gate valve between the main SPM chamber and FEL to prevent a back flow of contaminants in the main SPM chamber.

### 2.2.5 Substrate: HOPG preparation

The weak bonding within the interlayers of HOPG allows a simple cleaning (cleaving) method to be followed, in which the top most layer of HOPG is removed. The cleaving process is generally not uniform and thus results in the formation of unwanted graphite flakes and step edges. The average height of an HOPG step edge can vary slightly although an accepted value of the step edge height is ~3.3 Å. The HOPG cleaving process comprises of pressing the HOPG sample (10×10) mm by an adhesive tape and pulling off the adhesive tape quickly. This peel off procedure can be rather abrupt and the

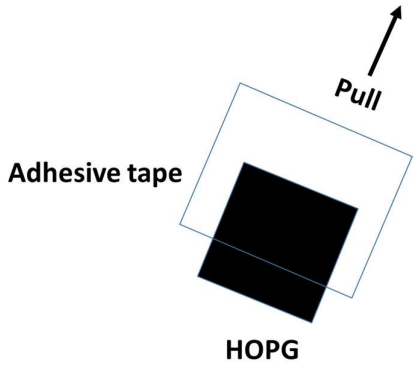


*Figure 2-13 The cleaving of an HOPG sample by pulling off the top most layer by means of an adhesive tape.*

final result can vary depending upon the peel off direction. Generally, the cleaving procedure enables removal of a thin graphite flake and the procedure is continued until a smooth and flat HOPG surface is obtained.

Once, a smooth and flat surface is obtained, the cleaved HOPG sample is immediately loaded into the VT AFM setup via the FEL and transferred to the main SPM chamber once low enough ($10^{-8}$ mbar) pressure is achieved. After transferring the cleaved HOPG sample into the main SPM chamber, the wobble stick is used to hold it and place it safely in the designated holding place on the manipulator's head and subjected to overnight (~16) hours of resistive annealing, which results in a clean, contamination free HOPG sample.

Having described all the key components of the experimental setup, working of the STM is discussed in the next section.

## 2.3 Scanning Tunnelling Microscope

Quantum tunnelling[7] has been understood since the early days of quantum mechanics and was first realized in planar junctions[114]. In principle, quantum tunnelling allows the movement of electrons between two conducting samples without the samples coming in actual contact. Figure 2-14 shows a schematic diagram demonstrating electron tunnelling between two conducting samples (i.e. a sample and an STM tip) as they are brought within quantum tunnelling regime[6]. The sample and STM tip are assumed to be as ideal metals in which the electrons are filled up to their respective Fermi levels ($E_F$) and electrons can be made to tunnel through the vacuum barrier gap (eV) on the application of an external bias voltage. The work function is denoted by $\Phi$ and on the application of an external bias, electrons can tunnel from the occupied energy levels of the material with the higher Fermi level to

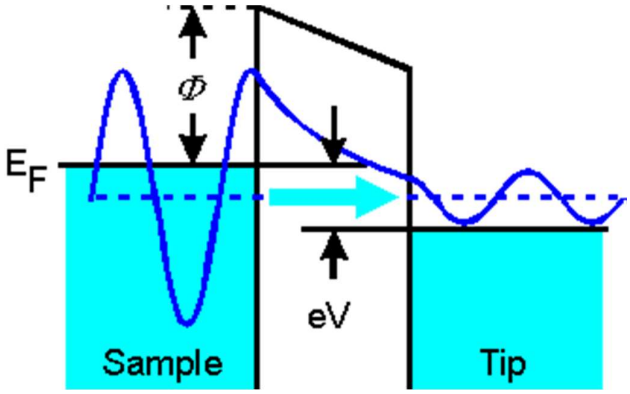


*Figure 2-14 A schematic diagram demostrating electron tunneling as two metallic samples (substrate and STM tip) are brought within the tunnelling regime.*

the unoccupied energy levels of the material with the lower Fermi level. As can be seen in Figure 2-14, the electron wave function decays exponentially across the vacuum barrier gap during the tunnelling process.

The practical demonstration of electron tunnelling across a vacuum barrier in a prototype STM was used to reveal the atomic arrangement of Si (111) by Rohrer et al[13-15]. The STM uses a piezoelectric scanner which monitors the precise movement of a sharp metallic tip attached to it. Figure 2-15 shows a schematic diagram demonstrating a simple prototype of an STM that works on the principle of quantum tunnelling between two metal electrodes (i.e. a conducting tip and a conducting sample) placed within the tunnelling regime.

To develop an understanding of the experimental results obtained via STM, the mathematical equations governing electron tunnelling between two conducting electrodes (sample and tip) are described, where tunnelling current from sample to tip, and that from the tip to sample at energy ε is explained by the following equations:

$$I_{sample-tip}=-2e\frac{4\pi^2}{h}|M|^2\left(\rho_s(\in).f(\in)\right).(\rho_t(\in -eV).[1-f(\in -eV)]) \quad (9)$$

$$I_{tip-sample}=-2e\frac{4\pi^2}{h}|M|^2\left(\rho_t(\in -eV).f(\in -eV)\right).(\rho_s(\in).[1-f(\in)]) \quad (10)$$

where, |M| is the tunnelling matrix element, $\rho_s(\in)$ and $\rho_t(\in)$ are the DOS of the sample and the tip respectively, and ƒ (ε) is the Fermi function. The STM measures both of these contributions, therefore summing the above two equations and integrating over all energies gives the following:

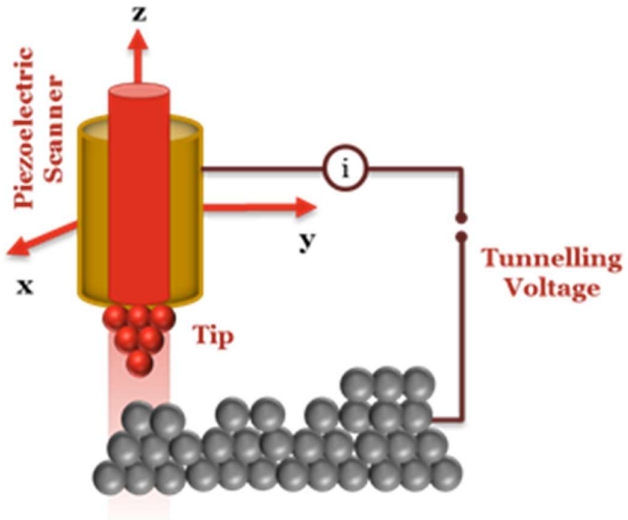


*Figure 2-15 A schematic diagram demonstrating the interaction between a piezoelectric scanner and a substrate. A sharp STM tip at the top of the scanner is used to measure tunnelling current.*

$$I = 2\frac{-4\pi^2 e}{h}\int_{-\infty}^{+\infty} |M|^2 \rho_s(\in)\rho_t(\in -eV)[f(\in)[1-f(\in -eV)] - f(\in -eV)[1-f(\in)]]d\in \tag{11}$$

The experiments conducted at low temperatures (~4K) do not have any thermal broadening, which reduces the above equation to:

$$I \approx -2e\frac{4\pi^2}{h}\int_0^{eV} |M|^2\rho_s(\in)\rho_t(\in -eV)d\in \tag{12}$$

in an ideal situation, the density of states of the STM tip, i.e. $\rho_t$ is considered to be energy independent, which renders $\rho_t(\in -eV) \sim \rho_t(0)$. Using this approximation, the equation above reduces to:

$$I \approx -2e\frac{4\pi^2}{h}\rho_t(0)\int_0^{eV} |M|^2\rho_s(\in)d\in \tag{13}$$

The energy independence[115] of |M| allows the rearrangement of the equation by taking it out of the integral of the equation and written as:

$$I \approx -\frac{8e\pi^2}{h}|M|^2\rho_t(0)\int_0^{eV} \rho_s(\in)d\in \tag{14}$$

At this stage, an assumption is considered that the vacuum barrier between the sample and the tip is a simple square barrier[115], allowing the WKB[115] approximation to be applied to the matrix element, which is given by:

$$|M| \approx e^{-4\frac{\pi s\sqrt{2m\Phi}}{h}} \tag{15}$$

where m is the electron's mass, s is the width of the vacuum barrier and ϕ is the local barrier height, which comprises of the tip and sample work functions. The STM tunnelling current can, therefore, be approximated to:

$$I \approx -\frac{4e\pi^2}{h} e^{\frac{-\pi s\sqrt{8m\Phi}}{h}} \rho_t(0) \int_0^{eV} \rho_s(\in) d \in \tag{16}$$

The tunnelling current is proportional to the sample's density of states within the energy range (0 to E) eV. The derivative of the above equation thus yields an approximate relation between the STM tunnelling current and the sample's density of states:

$$\frac{dI}{dV} \propto \rho_s\,(\mathrm{eV}) \tag{17}$$

Where, $\frac{dI}{dV}$ refers to the sample's differential conductance, implying that the measured differential conductance of a sample by an STM tip effectively measures the sample's density of states.

The process of tunnelling between an STM tip and a sample on the application of different bias values is summarized in Figure 2-16 (a-c) by a schematic diagram, where Figure 2-16 (a) depicts the situation without the presence of the second electrode and without the application of any external bias. The black circles represent the electrons of a sample, which occupy the energy levels up to $\mathcal{E}_F$ (Fermi level) , Ψ represents the sample's work function and the energy level of vacuum denoted by $\mathcal{E}_{vac}$. Figure 2-16 (b) demonstrates the situation when an STM tip comes in tunnelling regime of the sample, where the red circles represent the electrons within the STM tip up to the Fermi level. As seen in Figure 2-16 (b), electron tunnelling is not observed without the application of an external bias voltage. The application of a negative bias to the sample pushes the Fermi level of the sample higher

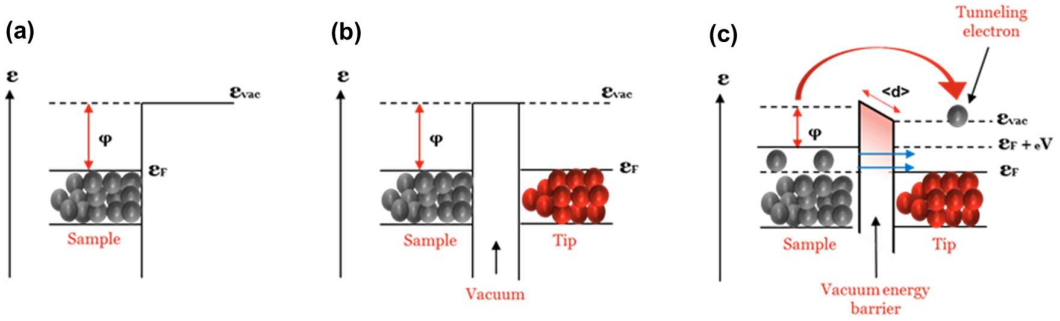


*Figure 2-16 (a) Shows a schematic diagram indicating the Fermi level of a sample. (b) Demonstrates the alignment of energy levels of the sample as it comes in contact with a sharp STM tip. (c) demonstrates the phenomenon of electon tunnelling between the sample and the tip on the application of a finite bias value.*

and initiates the process of electron tunnelling from the occupied states of the sample to the unoccupied states of the STM tip (Figure 2-16 (c)).

The ability of an STM tip to effectively measure the tunnelling current highlights STM's versatility as a surface characterisation technique, and is further enabled by the preparation of atomically sharp STM tips (next section).

### 2.3.1 STM tip preparation

Electrochemically etched tungsten (W) tips are routinely used for high-resolution STM measurements. The preparation of extremely sharp tungsten tips by a simple electrochemical etching procedure makes it a preferred choice for STM measurements. These tips are obtained by dipping a small diameter of the metallic wire into an alkaline electrolyte solution alongside a counter electrode. Once the experimental system is set up, a small voltage between the two electrodes is applied until the wire's tip dissolves, forming a sharp apex[116]. Apart from this advantage of obtaining atomically sharp tips in a single step, one drawback of using tungsten tips is the rapid contamination of the etched tip due to tungsten's poor resistance to oxidation. Therefore, to avoid such tip contamination, it is considered essential to immediately transfer the freshly etched STM tips into the FEL for continuous pump down.

Platinum-Iridium (Pt/Ir) is another material (alloy) used for preparing STM tips as Pt is highly resistant to oxidation and the tiny fraction (10%) of Iridium makes it a relatively hard material. Standard Pt/Ir tips are prepared by cutting a fresh piece of Pt/Ir wire grabbed with pliers at an acute angle with a pair of regular scissors. All the results acquired during this project are obtained by preparing atomically sharp Pt/Ir STM tips.

### 2.3.2 STM Imaging

The imaging process in a typical STM experiment involves raster scanning of the STM tip on the surface of a sample, resulting in the generation of a 3-dimensional image. There are two different STM imaging methods are used for image acquisition, the constant height mode and the constant current mode, both of which are explained in the next two sections.

#### 2.3.2.1 Constant height mode

Figure 2-17 (a) shows a schematic diagram of the constant height mode employed during an STM image acquisition process. In constant height mode, the vertical position of the piezoelectric

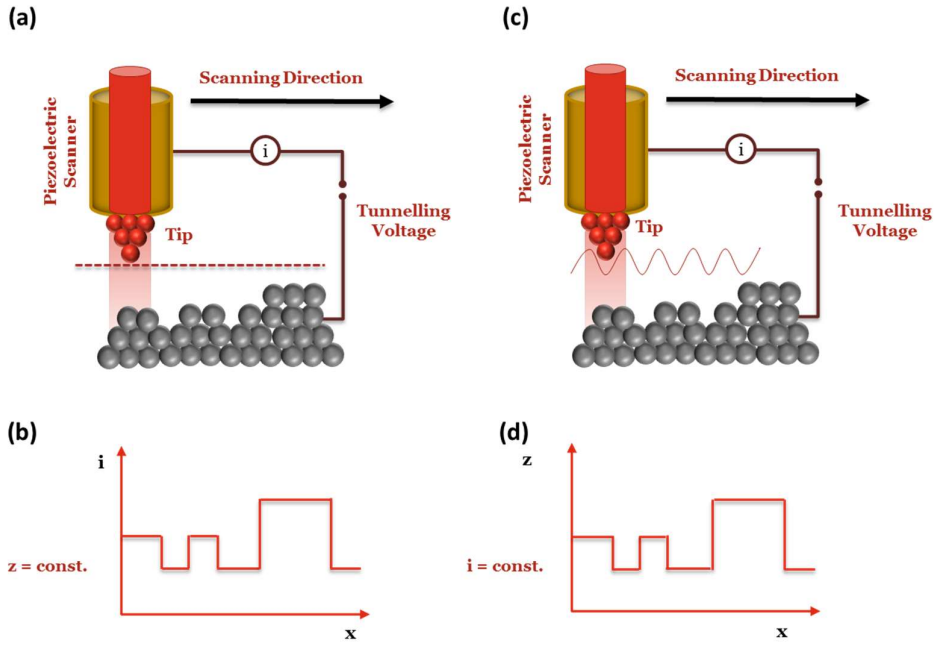


*Figure 2-17 Demonstrates the different STM operating modes (a) Constant height mode (b) Corresponding line profile (c) Constant current mode (d) Corresponding line profile.*

scanner is fixed, enabled by choosing a low value of the feedback loop (PID). As the distance of the piezoelectric scanner is maintained at a constant height above the sample surface, local variations in the tunnelling current are used to map the final image. The corresponding line profile (plotted as a function of position) for the constant height mode is shown in Figure 2-17 (b). The line profile precisely demonstrates the local current variations present within a sample. The constant height mode works well for surfaces which are atomically flat because the interaction of the STM tip with an abrupt surface can result in a tip crash.

#### 2.3.2.2 Constant current mode

Figure 2-17 (c) shows a schematic diagram of the constant current mode routinely used during standard STM image acquisition processes. In the constant current mode, a constant value of the tunnelling current is maintained throughout the measurement process and is used to control the vertical movement of the STM tip on the sample surface. Variations in the geometry and the LDOS of a sample surface give rise to different tunnelling current values, therefore to maintain a constant value of the current, the scanner moves vertically (±z) by a proportional amount and prevents the tip from crashing on the sample surface.

The corresponding line profile in Figure 2-17 (d) demonstrates the height variations in the vertical axis, plotted as a function of the position (x). The lateral (x-y) movement of the STM tip on the surface of the sample, therefore, enables the measurement of local height variations, which allows measurement of LDOS of the region and generation of a 3-dimensional image.

### 2.3.3 Scanning Tunnelling Spectroscopy (STS)

Scanning Tunnelling Spectroscopy[115,117] (STS) allows an in-depth understanding of the region's electronic structure by measuring tunnelling current spectra at energies up to several electron volts, both in occupied and unoccupied sample states regions[115]. In a typical STS measurement, the feedback loop (which fixes the tip-sample distance) is switched off, and the current response (I(V)) of the sample is measured as a function of the voltage sweeps (± V). The current response provides information about the integral of the sample's DOS (section 2.3) and the first order differential I(V) with respect to the applied V provides information about the surface LDOS (section 2.3). The acquired tunnelling current response I(V) is numerically differentiated to extract LDOS of the sample in Current Imaging Tunnelling Spectroscopy[115] (CITS) mode. More advanced STS techniques involve the usage of a lock-in amplifier[118] to directly map the LDOS (dI/dV) by modulating the applied voltage (dV) and measuring the change in current (dI). All the STS measurements performed in this project are done in the CITS mode (next section).

#### 2.3.3.1 Current Imaging Tunnelling Spectroscopy (CITS)

CITS is a tunnelling spectroscopy technique in which I(V) spectra are recorded at every pixel (2-dimensional grid) of an STM image as a function of continuous voltage sweeps. The image of the selected sample region is recorded along with the I(V) spectra at each pixel of the grid. Numerical differentiation of I(V) spectra is done manually afterward to generate corresponding dI/dV spectra. The CITS process, in principle, generates two different results, the first being the dI/dV spectra and the second being the 3-dimensional LDOS (conductance) maps. Each LDOS map (slice) provides information about the LDOS of the material at a specific bias.

It is important to note that in order to avoid any abrupt movement of the piezoelectric scanner during the I(V) acquisition process, the feedback loop is turned off and a predefined value of the gap voltage ($V_t$) and set point current ($I_t$) keeps the tip-sample distance constant throughout the measurement. In a standard CITS measurement, the STM tip moves to the first pixel of the chosen sampling grid and records a single I(V) spectra with the feedback loop switched off and thereafter

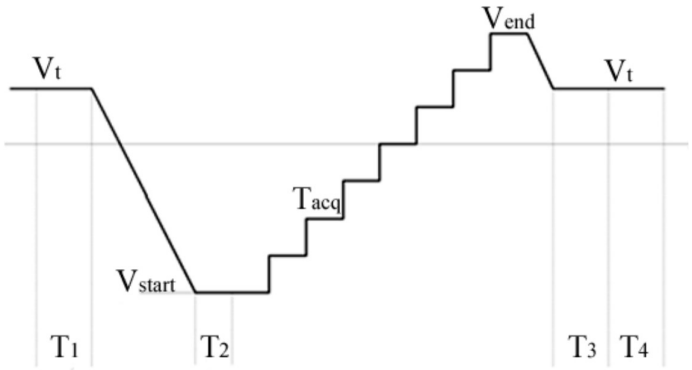


*Figure 2-18 A schematic drawing showing the time distributions involved during acquisition of a single I(V) spectrum in a standard CITS measurement. The different time intervals ($T_1$, $T_2$, $T_3$ and $T_4$) are shown here. Image reproduced from[102].*

scans through the sample to acquire the topography with the feedback loop switched on. The acquisition process of a single I(V) spectra is demonstrated in Figure 2-18 by a suitable schematic diagram. Once the region for CITS data set acquisition is selected, the STM tip waits for a time $T_1$ with the feedback loop switched on. The feedback loop switches itself off after the time interval $T_1$ and prepares itself for the acquisition of the I(V) spectra within the specified Bias range (±x) V. The first step involves ramping up of the gap Voltage ($V_t$) to the first value of the specified bias range (i.e. $V_{start}$). This ramping up step is called the slew rate.

After this voltage ramping step, the STM tip stabilizes on the sample surface by waiting for an additional time $T_2$ (initial delay) and starts the acquisition of the first I(V) spectra. Generally, a larger initial delay ($T_2$) allows for the stabilization of the STM tip and measurement of stable current. Thereafter, the I(V) acquisition process is initiated, as each data point is measured during a predefined acquisition time ($T_{acq}$).The $T_{acq}$ time interval comprises of averaged values of a number of I(V) measurements which is defined as:

$$Data\ point = \frac{\sum_1^{oversampling\ factor} single\ measurement}{oversampling\ factor} \tag{18}$$

Figure 2-19 demonstrates the time distribution within the $T_{acq}$ i.e. the time interval, clearly depicting that a slight change in the oversampling factor can be used to determine the final value of the data point. The same set of parameters (oversampling) are used to acquire individual data points until the voltage attains the final value (i.e. $V_{end}$) as shown previously in Figure 2-18.

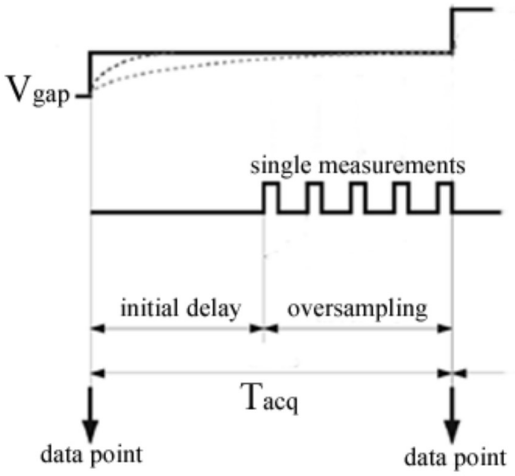


*Figure 2-19 A schematic diagram demonstrating oversampling during the acquisition of a single data point in a CITS measurement. Image reproduced from[102].*

After the acquisition of the last data point in the I(V) spectra, the voltage is set back to the gap voltage ($V_t$) and the feedback loop remains off for an additional short time interval, i.e. $T_3$, allowing the STM tip to stabilize itself. During the last time interval i.e. $T_4$, the feedback loop is switched on again and the tip scans over the pixel to acquire the surface topography. This complete procedure records a single I(V) curve and used each time a CITS experiment is conducted. The typical time interval settings used during the CITS measurements shown in this thesis are:

$T_1$ = 100 µs

$T_2$= 300 µs

$T_3$= 200 µs

$T_4$= 200 µs

The raw CITS data sets are generally noisy due to the interaction of the STM tip with the sample surface and therefore, require post filtering in order to extract reliable information about the surface LDOS. The CITS processing protocol and methodologies adopted on CITS data sets shown in this thesis are outlined in the next section.

## 2.4 CITS processing techniques

The quality of raw I(V) spectra acquired during CITS measurements is adversely affected by the STM equipment noise[119] and tip-sample interaction[97,115]. Extraction of reliable information from noisy I(V) spectra requires post processing by means of simple signal processing techniques. Primarily, two different processes, i.e. (median and moving average) filters are used to process the raw I(V) spectra

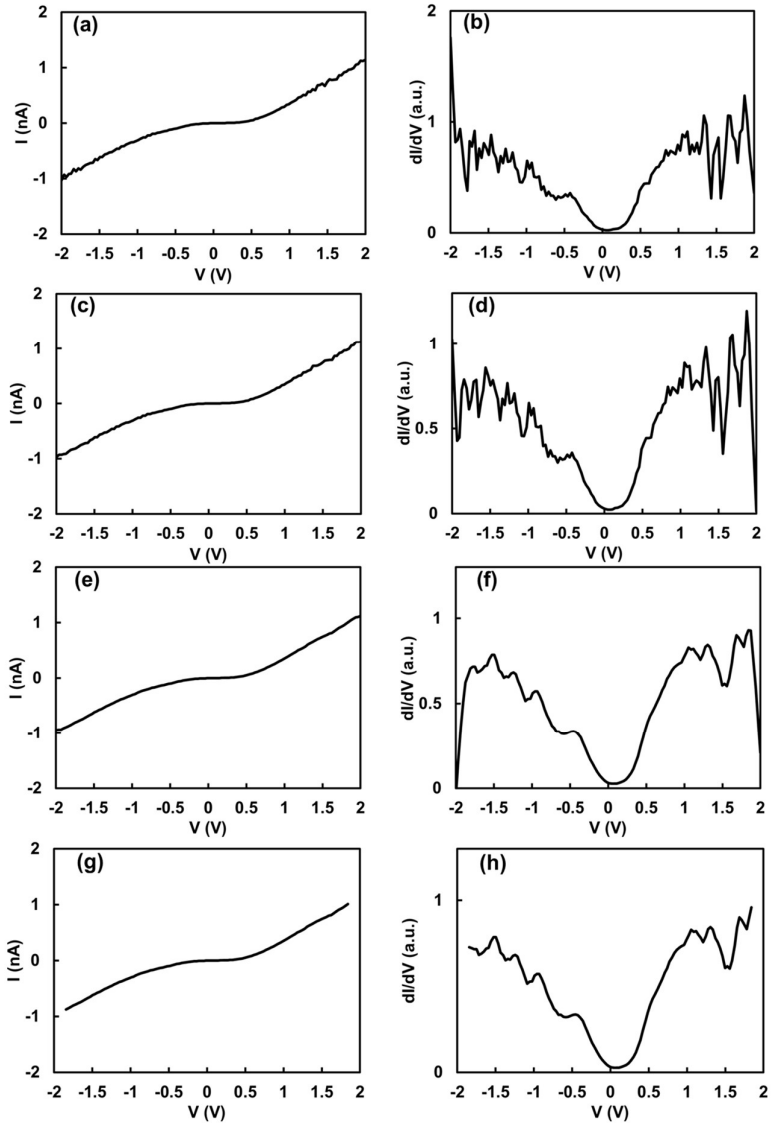


*Figure 2-20 (a) A raw I(V) spectrum extracted from a 50 K CITS dataset (±2 V) acquired on a $Bi_{0.87}Sb_{0.13}$ island. (b) Shows the corresponding numerically differentiated dI/dV spectrum. (c) The raw I(V) spectrum shown in (a) is processed by using a five-point median filter. (d) Shows the corresponding dI/dV spectrum. (e) The I(V) spectrum is further smoothened by the application of a five point moving average filter. (f) Shows the resulting dI/dV spectrum. (g) Inconsistent points at the end of each spectrum are manually removed. (h) Shows the final dI/dV spectrum.*

acquired during CITS measurements. The filtered I(V) spectra are then numerically differentiated to obtain the corresponding dI/dV spectra. These two signal filtering processes are briefly explained in

the next section, followed by a demonstration of the data processing methodology employed on the CITS datasets in this thesis.

### 2.4.1 Median and moving average filters

Median and moving average filters are widely[120,121,122] used as image filtering techniques for the removal of experimental noise. The median filter comprises a window that works by moving through each data point, analysing nearby data points (depending on the window size) and replacing the values by the median (middle) value, whereas a moving average filter is an unweighted arithmetic mean of 'N' data points of a signal that 'slides' along through the whole dataset. Median filtering is particularly useful in the removal of anomalous spikes present in experimentally (CITS) acquired I(V) spectra, without altering the spectra's overall shape. The disadvantage of both the filtering techniques is the inconsistent modification of the addition of the edge points of the filtered I(V) spectra, which have to be manually removed.

### 2.4.2 Demonstration of CITS data processing methodology

This section is divided into two parts, where the first part demonstrates the impact of median and moving average filters on a raw, individual I(V) spectrum and the second part demonstrates the reproducibility of filtered dI/dV spectra by extracting spectral histograms[123] from small, defect free areas of 5 ML thick regions of different CITS datasets.

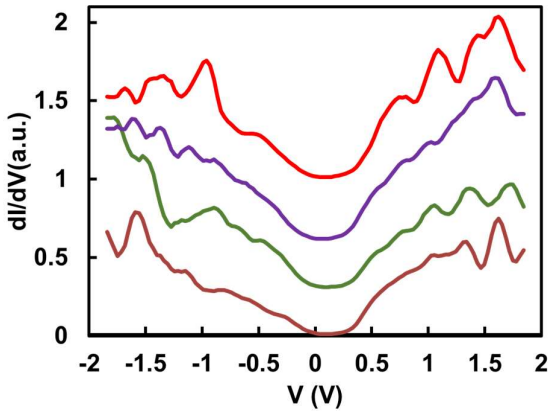


*Figure 2-21 Four individual dI/dV spectra which have been processed in accordance with the I(V) filtering protocol described in Figure 2-20 (a-h). Each of the spectra is vertically offset by equal amounts (+0.2) for clarity. As can be seen, the spectra are devoid of any anomalous spikes but the positions of the key dI/dV features (local maxima and shoulders) appears to vary.*

#### 2.4.2.1 I(V) filtering protocol

Figure 2-20 (a) shows an individual I(V) spectrum extracted from a 50 K CITS dataset of a $Bi_{0.87}Sb_{0.13}$ island in which low-intensity current spikes near higher bias values are noticeable. Figure 2-20 (b) shows the corresponding numerically differentiated (dI/dV) spectrum which retains the noise due to current spikes, a result, seen in the form of anomalous, high intensity dI/dV peaks. In accordance with the previous section's brief explanation, a median filter (five-point window) is applied on the raw I(V) spectrum of Figure 2-20 (a).

The impact of a five-point median filter on the raw [I(V) and dI/dV] spectra is shown in the two plots of Figure 2-20 (c) and (d) respectively. As seen clearly, the overall shapes of I(V) and dI/dV spectra are not affected by the application of median filter, although the anomalous current spikes are removed, resulting in a slight reduction of the dI/dV peak intensities. A moving average filter (five-point window) is then applied as shown in Figure 2-20 (e) and (f).

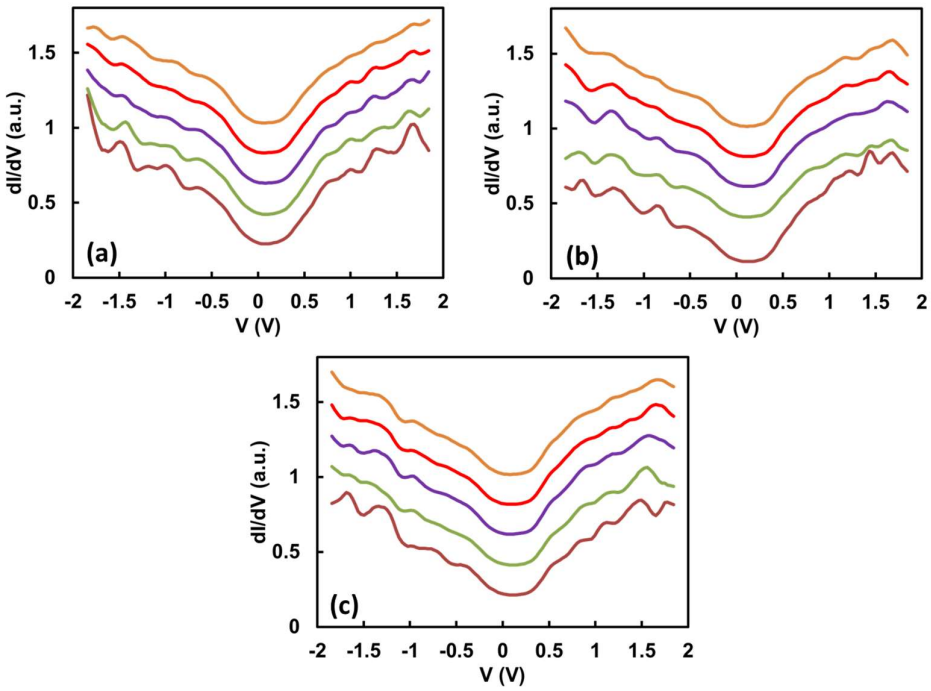


*Figure 2-22 (a-c) Show plots of vertically offset dI/dV spectra extracted from three different areas (5 ML) within a CITS dataset of a $Bi_{0.87}Sb_{0.13}$ island. All the dI/dV spectra in each of the plots are vertically offset by equal amounts (+0.2) for clarity. The different colours of the spectra represent dI/dV spectra obtained with different spatial averaging values. The spectra are shown in increasing order of spatial averaging: (4, 8, 16, 32, 64) from bottom to top.*

At first, it is difficult to identify any noticeable difference in the I(V) spectrum of Figure 2-20 (e) as compared to the one shown in Figure 2-20 (c), but the dI/dV spectrum in Figure 2-20 (f) clearly demonstrates impact of the moving average filter. The last step in the filtering process comprises manually removing points from the ends of the filtered I(V) spectrum (Figure 2-20 (g)). The final dI/dV spectrum (Figure 2-20 (h)) therefore contains well-defined dI/dV features (local maxima and shoulders).

Figure 2-21 demonstrates the spatial variations in the filtered CITS data set by means of four vertically offset, individual dI/dV spectra. The dI/dV spectra are acquired from four different areas (within 5 ML) of a CITS dataset and are pre-processed in accordance with I(V) filtering protocol described above. As seen clearly, each of the four dI/dV spectra are devoid of any anomalous spikes, although variations in the positions of the key features (local maxima and shoulders) are noticeable. This variation therefore, highlights the need of implementing spatial averaging to effectively distinguish the reproducible dI/dV features.

Figure 2-22 (a-c) demonstrates the impact of different amounts of spatial averaging on the filtered dI/dV spectra, where (a-c) correspond to spectra taken from three different areas within one CITS dataset. The dI/dV spectra (dark red) at the bottom of each of the three plots are a result of spatially averaging 4 individual dI/dV spectra, followed by spatially averaged (i.e. 8, 16, 32 and 64) dI/dV spectra from bottom to top. As, can be identified, spatial averaging of eight individual dI/dV spectra is considered optimum for a coherent analysis of the dI/dV spectra, without compromising on the feature's intensities.

#### 2.4.2.2 Spectral histograms

Spectral histograms[123] are a statistical analysis tool used to analyze the distribution of local maxima and shoulders of a large number of dI/dV spectra in CITS datasets. Spectral histograms are representative of the local maxima and shoulders present in all the dI/dV spectra associated with the area of interest within a CITS dataset. Analysis by a spectral histogram thus allows checking the reproducibility of the dI/dV spectra of a specific CITS dataset, in addition to checking the reproducibility of different CITS datasets.

Two different CITS datasets of $Bi_{0.87}Sb_{0.13}$ islands are shown in this section to demonstrate analysis by spectral histograms. After establishing the usefulness of spectral histograms, a comparison with the dI/dV spectra associated with the selected areas of interest is shown. The section is concluded by comparing the spectral histograms of $Bi_{0.87}Sb_{0.13}$ islands with the spectral histograms reported[124] for pure Bi islands. All the analysis shown in this section is restricted to defect free and sufficiently large regions within the 5 ML thick stripes and bases.

Figure 2-23 shows the topography (explained in detail in chapter 3) of a $Bi_{0.87}Sb_{0.13}$ island acquired simultaneously during a 50 K CITS measurement. The island comprises of a flat 3 ML base and a 5 ML region on top. The large area coverage of the 5 ML region allows comparison of spectral histograms associated with different areas of the 5 ML region to check the reproducibility of the dataset. Five different areas of interest (A, B, C, D and E) are marked on top of the 5 ML stripe. The sizes of regions A, B and C are kept same which represent approximately 500 individual dI/dV spectra, whereas regions D and E are larger and represent approximately 800 individual dI/dV spectra.

The spectral histograms corresponding to each of the five different areas along with the sum of each of the five histograms are shown in Figure 2-23. The solid black lines drawn on top of each of the histograms are indicative of the major histogram peaks noted for pure Bi (see Figure 3.11 in Ref[124]). The comparison between $Bi_{1-x}Sb_x$ and pure Bi CITS datasets is done primarily as the two electronic band structures are expected to be in reasonable agreement owing to the similar electronic structures of Bi and Sb. The position of the black lines is not altered intentionally to check the reproducibility of

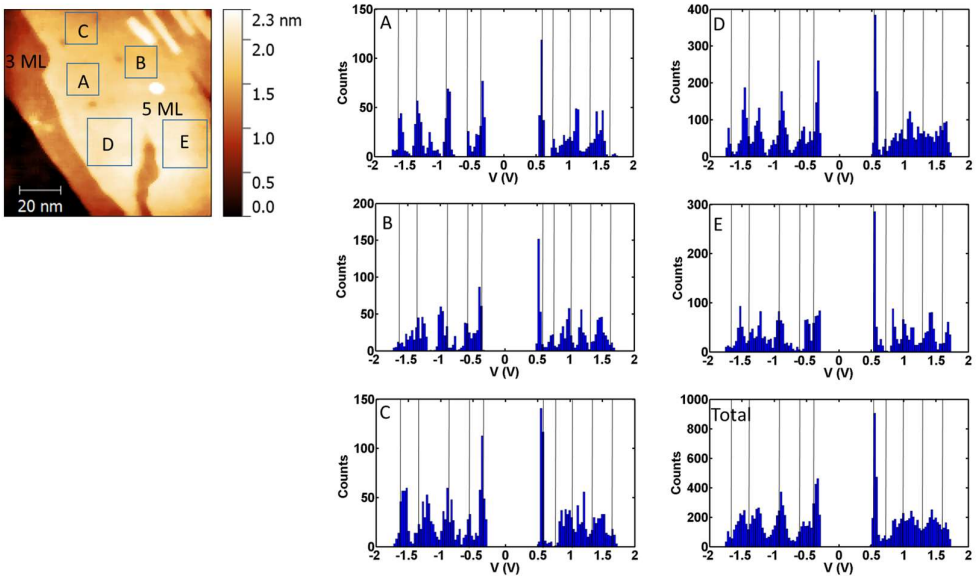


*Figure 2-23 Topography of a $Bi_{0.87}Sb_{0.13}$ island with a 3 ML high base, acquired simultaneously during a 50 K CITS measurement. The five different areas (A, B, C, D and E) marked on the 5 ML stripe represent areas from where spectral histograms are extracted from and shown here. The labels on each of the five histograms indicate the respective areas of analysis, with the histogram at the bottom right corner representing the sum of all the individual five histograms. The black lines on top of each histogram indicate positions of the major histogram peaks as observed and reported for pure Bi[124] islands on HOPG. The positions of the black lines are not altered for consistency. Experimental parameters: ±2V, 1 nA.*

the dI/dV features and eventually develop a reliable method of distinguishing real dI/dV features from experimental artefacts.

There are five major peaks each in the positive as well as negative bias regions for all the five chosen areas. The histogram peaks in the negative bias region are in reasonable agreement, in particular, the first major histogram peak at -0.4 V. On the positive bias region, apart from the first major peak at +0.5 V, agreement between rest of the histogram peaks is not straightforward and in general highlights the spatial variations in the features of dI/dV spectra.

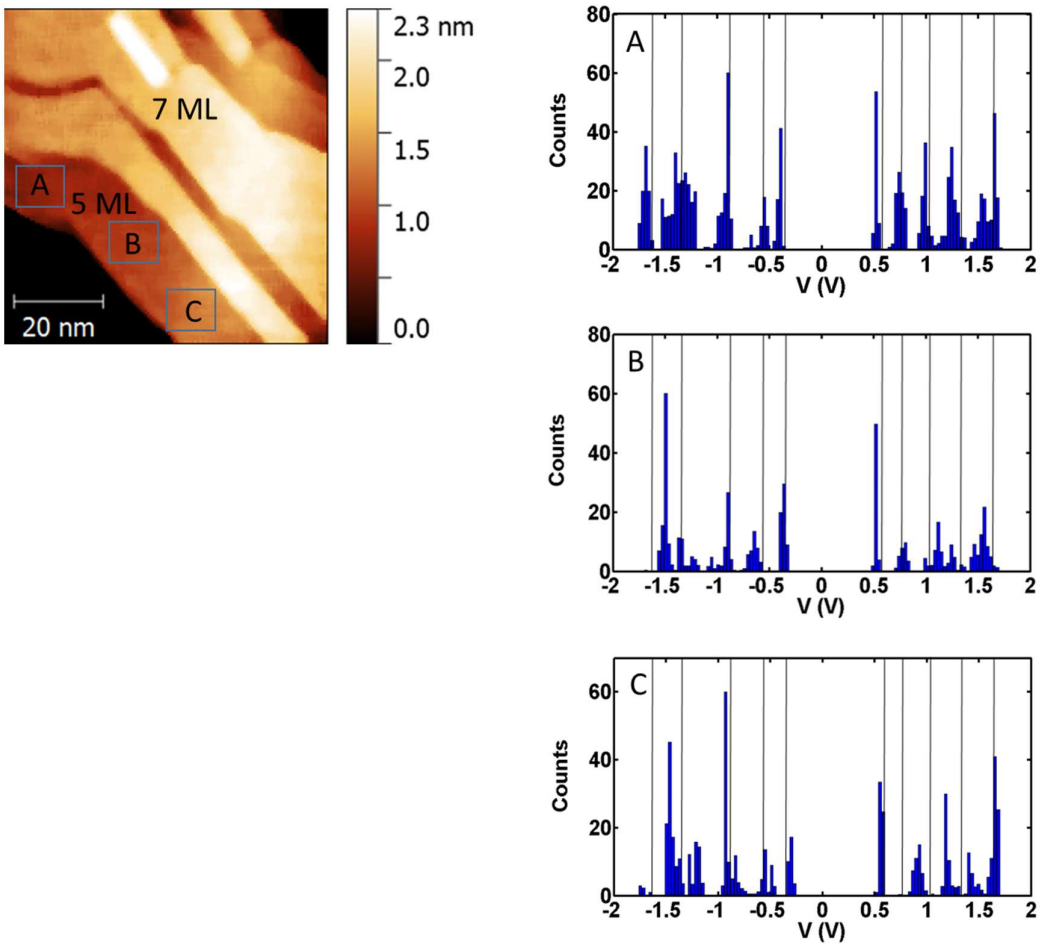


*Figure 2-24 Topography of a $Bi_{0.87}Sb_{0.13}$ island with a 5 ML high base, acquired during a 50 K CITS measurement. The three different blue squares (A, B and C) marked on the 5 ML base represent areas from where spectral histograms are extracted from and shown here. The labels on each of the three histograms indicate the respective areas of spectral histogram analysis. The black lines indicate positions of the major histogram peaks and their positions are kept consistent with that of the previous dataset to demonstrate dataset reproducibility. Experimental parameters: ±2V, 1 nA.*

The last histogram at the bottom right corner of Figure 2-23 represents total of all the five areas of interest. A good agreement, in particular, between the first two major histogram peaks at -0.4 V and +0.5 V and the solid black lines is seen. In addition, the next two peaks on each of the regions (i.e. positive and negative bias) also demonstrate a good agreement with the black lines. A similar analysis of three different areas (5 ML) of a different 50 K CITS dataset is shown in Figure 2-24. The topography image, acquired simultaneously with I(V) spectra during the 50 K CITS measurement comprises a $Bi_{0.87}Sb_{0.13}$ island with a flat 5 ML high base and two 7 ML stripes on top. Three defect free areas (A, B and C) are marked on the 5 ML base which are chosen for analysis of the corresponding spectral histograms. As can be seen clearly from the three spectral histograms, the major histogram peaks show a good agreement with the black lines drawn on top. Overall, the general agreement between the positions of the major histogram peaks of the two CITS datasets described in Figure 2-23 and Figure 2-24 highlight the reproducibility of 5 ML dI/dV spectra features.

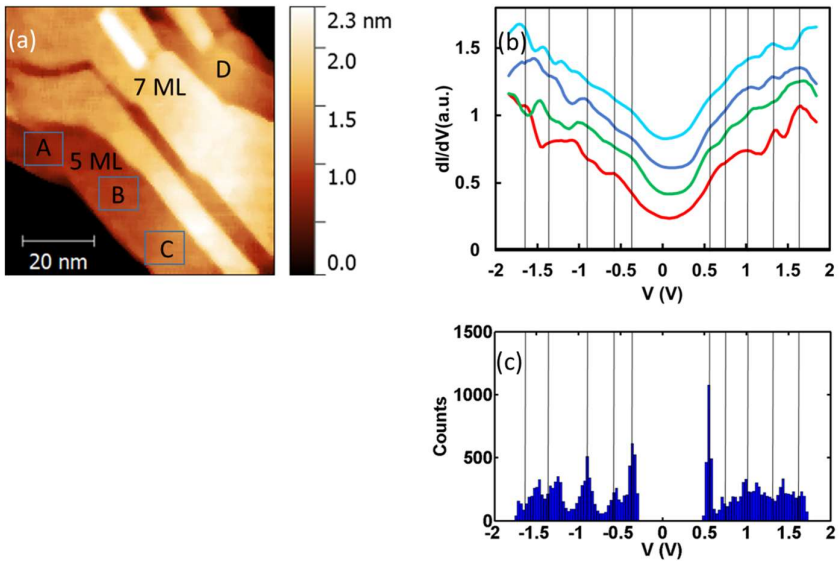


*Figure 2-25 (a) Topography of the $Bi_{0.87}Sb_{0.13}$ island shown earlier in Figure 2-24. The areas (A, B and C) are marked along with an additional area D on the top right corner. (b) The representative dI/dV spectra of regions A, B, C and D are shown by vertically offseting each of the spectra by equal amounts (+0.2). (c) The spectral histogram shown below the dI/dV spectra plot is a result of addition of eleven different spectral histograms corresponding to three different 50 K $Bi_{0.87}Sb_{0.13}$ CITS datasets. The black lines drawn on top of the dI/dV spectra and the spectral histogram are kept at the same positions as described earlier for Figure 2-23 and Figure 2-24. Experimental parameters: ±2V, 1 nA.*

Having established that the spectral histograms are an effective method to demonstrate reproducibility of the key features of the dI/dV spectra, a comparison between representative dI/dV spectra of the three marked regions of Figure 2-24 and a spectral histogram which is a result of addition of eleven different spectral histograms corresponding to three different CITS datasets is shown in Figure 2-25 (a-c). As can be seen, the black lines largely align well with the shoulders and local maxima of the dI/dV spectra shown in Figure 2-25 (b). Moreover, the alignment of black lines with the first three peaks in Figure 2-25 (c) further reinforces the effectiveness of using spectral histograms for CITS analysis. Having established that the spectral histograms demonstrate a good

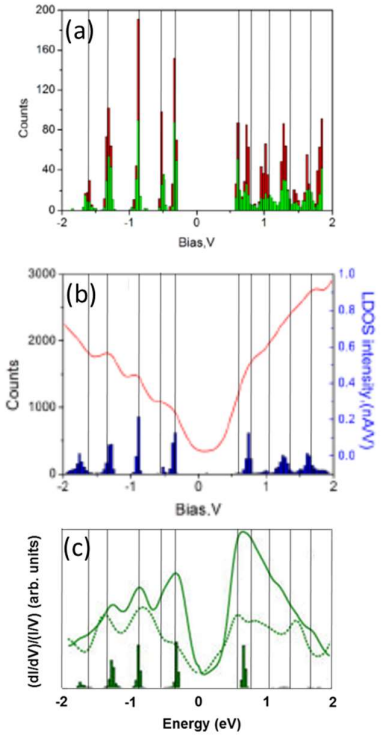


*Figure 2-26 (a) Spectral histograms demonstrating the presence of local moxima and shoulders within a small region of a CITS dataset obtained on a 5 ML thick pure Bi island, reproduced from[124]. The red histograms originate from a selected region on a 5 ML Bi stripe and the green histogram represents the sum total counts of five different regions on the same 5 ML stripe. (b) Representative 5 ML dI/dV spectra plotted along with the corresponding spectral histogram, reproduced from[124]. (c) Representative experimental (solid green) normalized dI/dV spectra of a 5 ML thick pure Bi island and DFT calculated spectra (dashed green), with the major STS features (local maxima and shoulders) highlighted by corresponding spectral histograms, reproduced from[98]. Important to note-(b) and (c) are shifted by approximately 60 mV to allow an agreement with the positions of the spectral histogram peaks observed for $Bi_{0.87}Sb_{0.13}$ islands.*

agreement with the key features of the dI/dV spectra of $Bi_{0.87}Sb_{0.13}$ islands, a brief analysis of the dI/dV results and spectral histograms reported[124] for 5 ML thick regions of pure Bi islands on HOPG is shown in Figure 2-26 (a-c). Figure 2-26 (a) is a spectral histogram corresponding to a small area within a 5 ML region of a pure Bi island grown on HOPG (see Figure 3.11 (b) in Ref[124]). Figure 2-26 (b) shows a representative 5 ML dI/dV spectra of a pure Bi island plotted along with the corresponding spectral histogram (see Figure 3.12 (e) in Ref[124]). Figure 2-26 (c) shows a representative normalized dI/dV spectra of a pure Bi island along with the corresponding spectral histogram (see Figure 3 (a) in Ref[98]). The black lines drawn in Figure 2-26 (a) are the same as those in Figure 2-23, Figure 2-24 and Figure 2-25 except that they have been shifted by approximately 60 mV to the right in Figure 2-26 (b) and Figure 2-26 (c).

The comparison between the spectral histograms of 5 ML thick regions of $Bi_{0.87}Sb_{0.13}$ and pure Bi islands reveals that the key dI/dV features are the same, except for shifts in feature's positions by approximately 60 mV, which can be attributed to the doping effect of the Sb. Spatial variations in dI/dV spectra are inherent to both $Bi_{0.87}Sb_{0.13}$ as well as Bi CITS datasets and the agreement between the spectra for alloy islands and pure bismuth islands is surprising, a result that will be discussed in more detail in chapter 4. Having discussed the features' general agreement, there are instances where the lines do not align well with the LDOS features, in particular on the positive bias. Such instances of misalignment are difficult to understand in a CITS data set and therefore, measurements are spatially averaged on different regions to reach a conclusion. It is important to note that a 60 mV shift is applied to all the lines drawn on the experimental normalized dI/dV spectra of $Bi_{1-x}Sb_x$ alloys discussed in chapter 4 as a better agreement is observed with the LDOS features.

#### 2.4.2.3 Feenstra Normalization

Although the tunnelling transmission probability |M| is not easy to quantify as |M| increases monotonically as a function of the tip-sample bias and affects the consistent analysis of the dI/dV spectra features at higher bias values. Feenstra et al[125,126] demonstrated that the dependency of |M| on the tip-sample spacing and the applied bias tends to cancel out as a result of a simple normalization procedure. The Feenstra normalization comprises division of the acquired dI/dV by the averaged I/V values as shown here:

$$\rho_s \propto \frac{\left[\frac{dI}{dV}\right]}{\left[\frac{I}{V}\right]} \tag{19}$$

Equation (19) shows that the normalized conductance (ratio) is directly proportional to the LDOS ($\rho_s$) of the sample and provides an effective method for analysing the sample LDOS as the

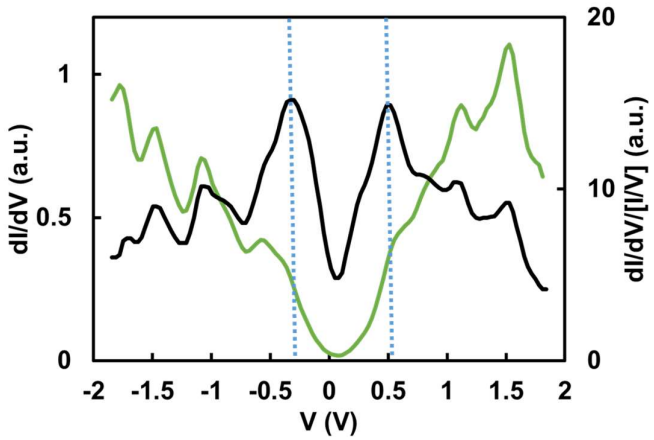


*Figure 2-27 The green dI/dV spectra (primary vertical axis) is a result of spatially averaged 8 individual curves and obtained after implementing the I(V) filtering protocol described earlier in Figure 2-20 (a-h). Feenstra normalization enhances the respective features (shoulders and local maxima) as seen in the black dI/dV/[I/V] spectra (secondary vertical axis).*

impact of tip-sample distance and the applied bias on the final dI/dV spectra is ruled out. Figure 2-27 shows a plot demonstrating the impact of Feenstra normalization procedure on a filtered and spatially averaged dI/dV spectra. The green dI/dV spectra (primary vertical axis) is a filtered dI/dV spectra (spatially averaged 8 curves) corresponding to a 5 ML region of a $Bi_{0.87}Sb_{0.13}$ island. The equivalent Feenstra normalized spectra (black) is plotted on the secondary vertical axis in which the major features (local maxima and shoulders) are emphasized, in particular the two features at +0.5 V and -0.3 V (indicated by dashed blue lines). Importantly, the plots demonstrate that positions of the major features of the dI/dV spectra are not altered, rather only emphasized clearly by the implementation of the Feenstra normalization procedure.

The Feenstra normalization procedure is applied only on the dI/dV spectra acquired in higher bias range (±2 V), which consists of all the results shown later in chapter 4. The CITS results acquired in lower bias range of ±0.4 V and ±1 V are not Feenstra normalized and shown as dI/dV spectra, which comprises all the results shown later in chapter 5.

## 2.5 Experimental details

Commercially available HOPG (SPI-1) is used as a substrate in all the experiments during the project. HOPG is cleaved in the atmosphere, then loaded into the UHV system and annealed at 450° C for approximately 16 hours (overnight) to remove contaminants prior to deposition. After the substrate has cooled down to room temperature, high purity bismuth (99.999%) and antimony

(99.999%) are evaporated from separate PBN crucibles simultaneously. 2 ML thick coverage samples of $Bi_{1-x}Sb_x$ alloys are prepared by evaporating the two materials onto HOPG, with the Bi flux maintained at ~0.01 Å/sec and three different flux values for Sb ($8.3\times10^{-4}$ Å/s, 0.0018Å/s and 0.0036 Å/s) to obtain different concentrations of $Bi_{1-x}Sb_x$ islands. Three different $Bi_{1-x}Sb_x$ concentration (x=0.06, 0.13 and 0.24) sample series are prepared and studied during the project. The Sb flux values are much lower than those used in section 1.2.2.3 to investigate Sb nanostructures on HOPG, therefore, it is expected that the morphology of $Bi_{1-x}Sb_x$ alloys is governed by Bi (higher flux) and not Sb. Furthermore, to account for the fact that the amount of evaporated material is not desorbed from the HOPG surface, atomic flux readings as measured by the quartz monitor are calibrated by depositing higher coverages of Bi and Sb on SiN (Silicon Nitride) substrates, and consequently measuring the average material thickness in an ambient AFM. The flux calibration method is exactly same as employed in Refs[54,124], which have clearly demonstrated that at room temperature, the amount of evaporated material is in good agreement with the deposited material coverage on HOPG.

STM images of $Bi_{1-x}Sb_x$ islands (Chapter 3) are acquired at room temperature (R-T) and all the CITS measurements are carried out at 50 K. The RT-STM images are acquired with a 256 x 256 pixels resolution and all the CITS measurements are acquired with a 128×128 pixels resolution. The STM tips used in these experiments are Pt-Ir tips, with the typical scanning parameters used during STM imaging being $V_t$ = +0.8 V and $I_t$ = 10 pA.

The average scan size for CITS measurements varied between 30-100 $nm^2$ and island topography images of the area of interest are recorded simultaneously with the I(V) spectra, within the 3.3 nA/800 Hz range (preamp settings). The tunnelling current is kept constant at 1 nA during the CITS measurements, where each I(V) spectra consists of 128 data points. These settings result in a single CITS measurement to take approximately 45-60 minutes to complete.

## 2.6 Summary

The bulk crystallographic structure of the three key materials used during the course of this project, i.e. Bismuth (Bi), Antimony (Sb) and the substrate, HOPG, which is followed by a description of all the key components of the Omicron VT AFM setup, with a subsection describing the HOPG cleaving procedure. Thereafter, the fundamental concepts of the characterisation technique used during the project, i.e. STM is described in considerable detail, with emphasis laid on the two imaging modes (constant height and constant current) and the spectroscopy mode (CITS). The chapter is concluded by description of the CITS data filtering methodology employed for analysis of the CITS data acquired on $Bi_{1-x}Sb_x$ islands.

# 3 Morphology of $Bi_{1-x}Sb_x$ islands on HOPG

This chapter discusses the growth of nanostructured $Bi_{1-x}Sb_x$ alloys on HOPG and their subsequent morphological characterisation by SEM and STM. The preparation of $Bi_{1-x}Sb_x$ nanostructured alloys is done by simultaneous evaporation of the two elements (Bi and Sb) in the UHV-STM system. Presence of a small percentage of Sb in $Bi_{1-x}Sb_x$ nanostructures is expected to have a noticeable impact on the island morphologies as compared to those of pure Bi (110) nanostructures[51,52,54,81] on HOPG.

The general morphology characteristics of $Bi_{1-x}Sb_x$ nanostructures are discussed first by comparing with the morphologies of pure Sb and pure Bi (110) nanostructures on HOPG. The SEM results are shown in the next section, which provide the first evidence for the large scale, general morphology characteristics.

## 3.1 Morphology comparisons: Sb, Bi, $Bi_{1-x}Sb_x$ on HOPG

### 3.1.1 Large scale morphologies: SEM

Figure 3-1 (a-c) are SEM micrographs of pure Sb[54], pure Bi[52] and $Bi_{1-x}Sb_x$ nanostructures grown on HOPG respectively. Figure 3-1 (a) shows fingered (red arrow) islands of pure Sb on HOPG. Figure 3-1 (b) shows the growth of striped (white arrow), star shaped islands of pure Bi (110) islands on HOPG. Figure 3-1 (c) shows $Bi_{1-x}Sb_x$ alloy islands on HOPG which are characterised by fingers (red arrow) as well as stripes (white arrow) on top of the base. The irregularity in the shape of the alloy islands is reminiscent of the fractal and finger like growth of Sb islands[54,63,81,127] on HOPG, while the striped

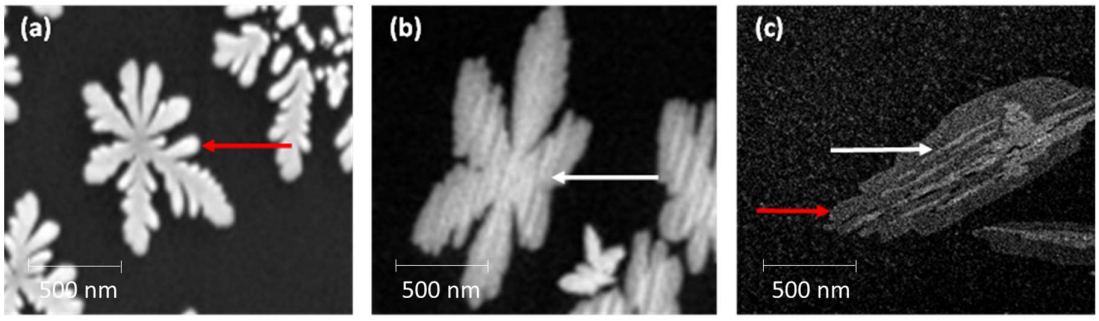


*Figure 3-1 SEM micrographs of (a) Pure Sb islands (0.01 Å/s) on HOPG showing a fingered growth, reproduced from[54]. (b) Pure Bi (110) star shaped islands on HOPG (0.005 Å/s), characterised by ordered and striped island growth, reproduced from[52]. (c) $Bi_{0.06}Sb_{0.94}$ islands on HOPG, characterised by fingered island bases with irregular stripes on top.*

morphology indicates the BP[91] (section 1.2.3) like growth mode similar to that observed for pure Bi[98,99,124] (110) islands.

The SEM results of $Bi_{1-x}Sb_x$ islands, therefore, give the impression that the presence of small amounts of Sb into Bi, alters islands' morphology slightly, indicating that $Bi_{1-x}Sb_x$ islands have signatures of both Bi (striped) and Sb (fingered) island growth modes. These subtle differences in the island morphologies are understood better by higher resolution imaging by STM (next section).

### 3.1.2 Higher resolution images: STM

Figure 3-2 (a-c) shows representative higher resolution STM images of pure Sb, pure Bi (110) and $Bi_{1-x}Sb_x$ islands grown on HOPG. Figure 3-2 (a) is an STM image of a terrace nucleated, fingered pure Sb island on HOPG. Small fingered protrusions (white arrows) and a taller structure characterise the island's shape, complementing the previously shown, large scale SEM micrograph of Figure 3-1 (a). The morphology is in good agreement with the well-established, previously reported fingered, morphology of 3-dimensional Sb islands[54,63,81] on HOPG. Figure 3-2 (b) shows an STM image of a terrace nucleated pure Bi (110) island on HOPG. The striped morphology of the Bi island (black arrows) confirms the ordered and defined geometry observed previously for Bi[51,52,87,99] (110) islands and is in general consistent with the morphology characteristics shown in the larger scale SEM micrograph of Figure 3-1 (b).

Figure 3-2 (c) shows STM image of a $Bi_{0.87}Sb_{0.13}$ island, which has characteristics of both pure Bi and pure Sb islands. A fingered island base (white arrows) and a striped morphology (black arrows) confirm the intuition of a hybrid (Bi and Sb) morphology for the $Bi_{1-x}Sb_x$ alloy islands. Owing to their similarity, The morphology of $Bi_{1-x}Sb_x$ islands is compared in more detail with that of pure Bi islands in the next section.

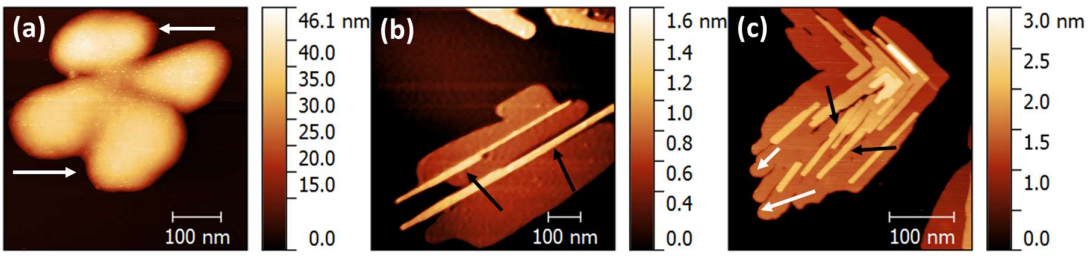


*Figure 3-2 (a) RT-STM image showing a tall, fingered pure Sb island grown on HOPG (b) RT-STM image showing a pure Bi (110) island on HOPG with a distinct striped morphology (c) RT-STM image of a $Bi_{0.87}Sb_{0.13}$ island, showing morphological characteristics of pure Sb (fingered growth) as well as morphological characteristics of pure Bi (striped growth). Imaging parameters: +0.8 V, 10 pA.*

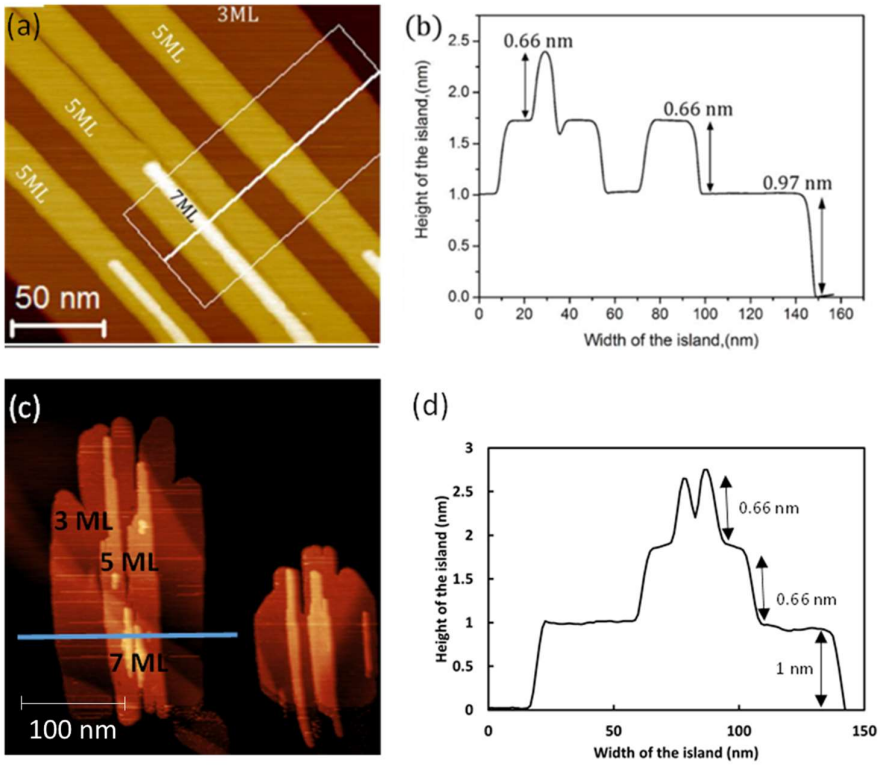


*Figure 3-3 (a-b) RT-STM image of a pure Bi island on HOPG (reproduced from[124]) with its corresponding profile showing a wedding cake like structure is compared with a (c) RT-STM image and (d) profile of a $Bi_{0.87}Sb_{0.13}$ island on HOPG highlighting a similar wedding cake like structure. Imaging parameters: +0.8V, 50 pA.*

### 3.1.3 Detailed comparison of $Bi_{1-x}Sb_x$ with pure Bi (110) morphology: STM

Figure 3-3 (a) shows an STM image of a pure Bi (110) island[124] grown on HOPG, with the corresponding line profile drawn across the island in Figure 3-3 (b). It is compared with an STM image of a $Bi_{1-x}Sb_x$ island grown on HOPG, shown in Figure 3-3 (c). A line profile across the $Bi_{0.87}Sb_{0.13}$ island is shown in Figure 3-3 (d), which corresponds to the blue line drawn in Figure 3-3 (c). Both the islands are observed to grow with a 'wedding cake' like structure and the striped pattern on top of the atomically flat bases is similar as well. The line profiles indicate that the height distribution of $Bi_{0.87}Sb_{0.13}$ islands follows the same pattern as observed for pure Bi[99](110) islands. This observation is confirmed by a statistical height analysis of the $Bi_{1-x}Sb_x$ islands, shown in Figure 3-4. $Bi_{1-x}Sb_x$ island bases show a peak height at 1.05 nm and the stripes on top of the base lead to two peaks in the histogram at 1.65 nm and 2.3 nm. These heights are comparable to the heights (section 1.2.3) observed for pure Bi[99] (110) islands on HOPG.

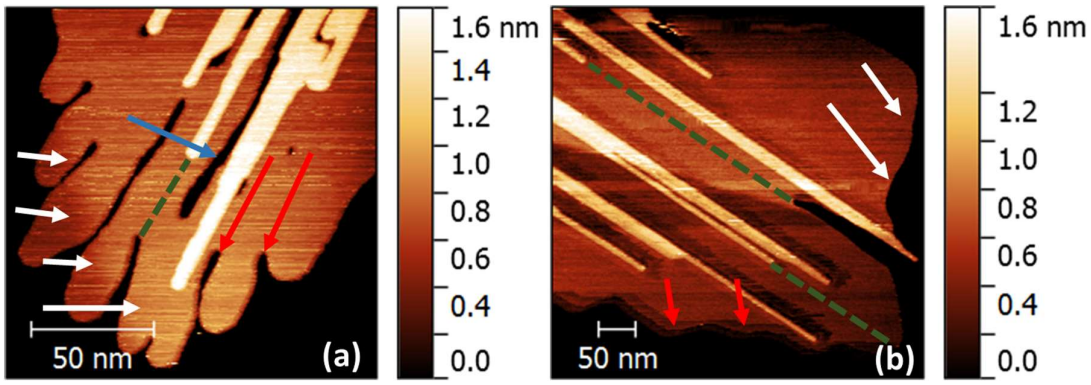


*Figure 3-5 (a) RT-STM image of a $Bi_{0.87}Sb_{0.13}$ island showing finger-like splitting at the tip of the base, in addition to the notches at the base. (b) RT-STM image of a fingerless pure Bi (110) island on HOPG having well defined stripes which align with the kinks at the base. Imaging parameters: (+0.8 V, 10 pA)*

A monolayer of Bi (110) is 0.33 nm high, hence a height of 1.05 nm approximately corresponds to a 3 ML high base. The 3 ML high bases comprise of paired layers on top of a dead wetting layer (section 1.2.3) as observed for pure Bi[98,99] (110) islands on HOPG. A BP[91] like growth is argued as the reason for paired layer growth for stripes on pure Bi (110) islands and the similarity in the heights for the two systems indicates a similar, 'BP' like growth mode for $Bi_{1-x}Sb_x$ islands. From here on in the thesis, 3 ML refers to a height of 1.05 nm for $Bi_{1-x}Sb_x$ islands, with subsequent paired layer growth at 1.63 nm (5 ML) and 2.3 nm (7 ML).

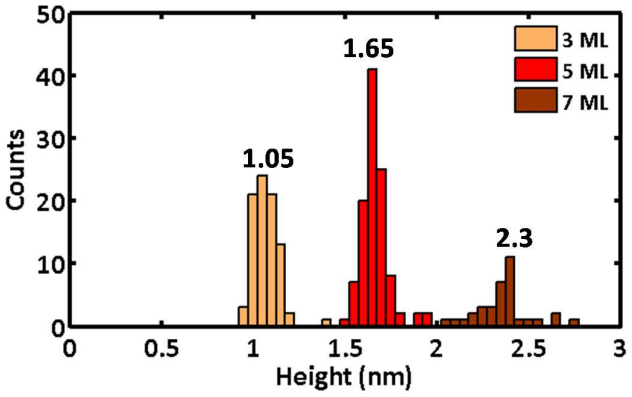


*Figure 3-4 A plot showing the statistical height analysis for $Bi_{1-x}Sb_x$ islands. Island bases show a peak height of 1.05 nm and a peak height of 1.63 nm and 2.3 nm is observed for the consequent stripes on top. The height distribution is in agreement with the height distribution reported[98] for pure Bi (110) islands on HOPG.*

Although, the basic morphology of both the islands in Figure 3-3 (a-d) is similar, i.e. 'wedding cake like', there are significant differences in the alloy and pure Bi (110) morphology owing to the presence of Sb, as highlighted in Figure 3-5 (a-b). The influence of Sb is clear in the base of the $Bi_{1-x}Sb_x$ island (Figure 3-5 (a)) in the form of fingers (white arrows) and trenches (blue arrow). The distinct finger like patterns (white arrows) in the base of $Bi_{1-x}Sb_x$ island in Figure 3-5 (a) show an asymmetry and a lateral expansion, which is different to the fingerless (white arrows) base of the pure Bi (110) island shown in Figure 3-5 (b). Red arrows in Figure 3-5 (a) point towards the notches in the base of $Bi_{1-x}Sb_x$ island, which are different to the kinks (red arrows in Figure 3-5 (b)) in the base of the pure Bi (110) island, although, for both the islands shown in Figure 3-5 (a-b), the stripes tend to align with the kinks and notches present in the two bases respectively (highlighted by green dashed lines).

These comparisons again reveal that the morphology characteristics of $Bi_{1-x}Sb_x$ islands on HOPG is a mix of pure Bi (110) and pure Sb island growth modes. The similarities of the $Bi_{1-x}Sb_x$ islands to the pure Bi[97-99] (110) islands however, indicates a similar lattice structure and therefore, attempts to understand the $Bi_{1-x}Sb_x$ morphology at the atomic level are discussed next.

### 3.1.4 Lattice structure comparisons of Bi and $Bi_{1-x}Sb_x$

Figure 3-6 (a) shows a 50 K STM image of a $Bi_{1-x}Sb_x$ island. The black rectangle marks the region of 5 ML stripe, where atomic resolution is obtained and shown in Figure 3-6 (b). Black arrows in Figure 3-6 (b) point towards inherent defects in the lattice structure of $Bi_{1-x}Sb_x$ and such defects are not reported in pure Bi atomic resolution images[124]. The lattice constant is determined by Fourier transforming the atomically resolved images and one such example is shown in the FFT of Figure 3-6 (c). The lattice constant is estimated to be (0.49±0.01×0.45±0.01) $nm^2$, similar to the experimentally

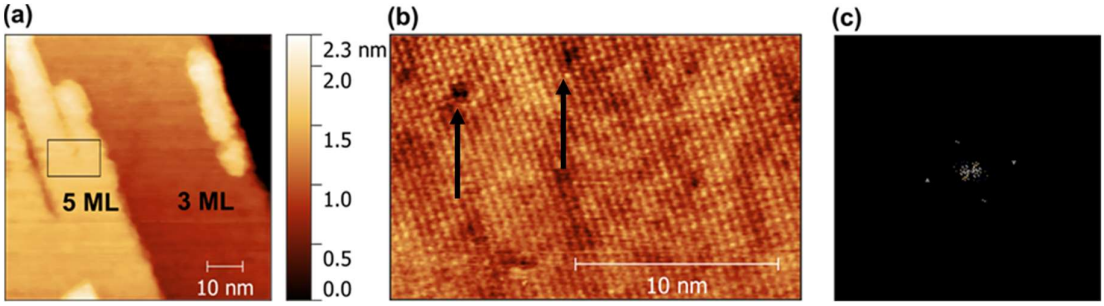


*Figure 3-6 (a) 50 K STM image of a $Bi_{0.87}Sb_{0.13}$ island (-0.9 V, 100 pA, LT-STM) on which atomic resolution is obtained on the region marked by a black rectangle. (b) Shows atomically resolved STM image (-0.9 V, 1 nA) of the region marked on 5 ML stripe in (a). (c) Shows FFT of the STM image shown in (b).*

verified lattice constant (0.48 ± 0.03 x 0.46 ± 0.02) $nm^2$ of pure Bi[96-99,124], indicating that $Bi_{1-x}Sb_x$ islands grow with a similar rectangular unit cell with two atoms per unit cell. The similarity in the two lattice structures indicates a similar fast growth [$\bar{1}$10] direction as observed for pure Bi[99] (110) islands. From the preliminary results, it can be said that the presence of Sb does not alter the $Bi_{1-x}Sb_x$ lattice structure significantly.

The discussion till now shows that Sb introduces changes in the form of fingered bases and irregular stripes in $Bi_{1-x}Sb_x$ islands, but the lattice structure remains similar to that of pure Bi[99,124] (110) islands on HOPG. These interesting, new morphological characteristics of $Bi_{1-x}Sb_x$ islands on HOPG are discussed by means of higher resolution STM imaging in the next section.

## 3.2 Detailed Investigations: $Bi_{1-x}Sb_x$ islands' morphology

This section is divided into two parts, each of which discusses the heights and shapes of different types of $Bi_{1-x}Sb_x$ islands on HOPG. The island heights on the basis of island's location on HOPG are discussed first and thereafter a discussion is pursued on the interesting and irregular $Bi_{1-x}Sb_x$ island shapes.

### 3.2.1 3 ML and 5 ML high $Bi_{1-x}Sb_x$ island bases

Figure 3-7 (a-b) shows two RT-STM images acquired on different locations of HOPG on the same $Bi_{0.87}Sb_{0.13}$ sample. The STM image shown in Figure 3-7 (a) comprises 5 step edges (white arrows) on HOPG showing growth of smaller (~100 nm), compact islands. Figure 3-7 (b) shows a wide HOPG terrace, devoid of the HOPG step edges, where fingered, large (~400 nm) islands are observed. Height measurements show that the compact islands, as seen in Figure 3-7 (a) are generally 5 ML high and the fingered islands seen in Figure 3-7 (b) are 3 ML high. A statistical height analysis for $Bi_{1-x}Sb_x$ island

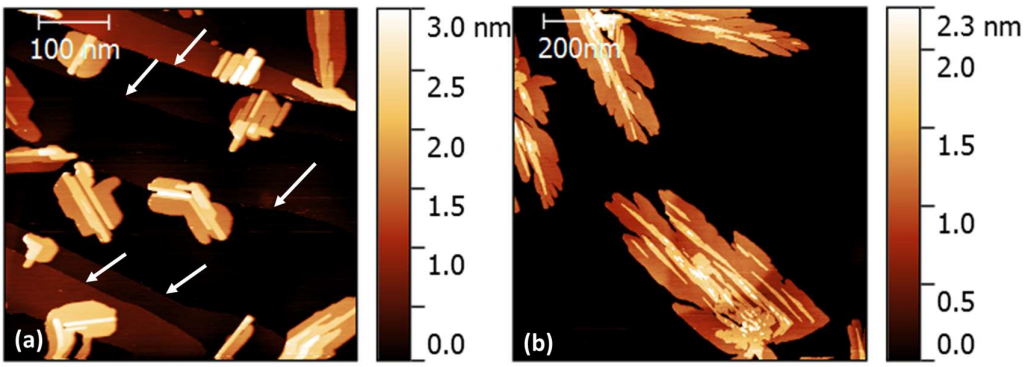


*Figure 3-7 (a) RT-STM image of step edge nucleated $Bi_{0.87}Sb_{0.13}$ islands, which exhibit a compact morphology (b) RT-STM image of terrace nucleated $Bi_{0.87}Sb_{0.13}$ islands, which exhibit fingered and irregular morphologies. Imaging parameters: +0.8 V, 10 pA.*

bases is shown in Figure 3-8 to complement the above observations. The peak at 1.1 nm characterizes 3 ML high base $Bi_{1-x}Sb_x$ islands and the peak at 1.65 nm characterizes 5 ML high base $Bi_{1-x}Sb_x$ islands.

It is well understood that for self-assembled Bi[51] islands, a low local adatom flux results in a slower growth process and the formation of taller, thermodynamically stable[51,54,90] shapes. The taller (5 ML high) islands in Figure 3-7 (a) nucleating along the HOPG step edges are explained similarly to the pure Bi (110) islands[52,87] that nucleate at the step edges. A low local adatom flux on closely spaced step edges means that thermodynamic effects dominate over kinetic effects and the islands have more time to rearrange into taller structures, and is consistent with the previously reported[54] results on Bi and Sb nanostructures.

The lower heights of larger, fingered $Bi_{1-x}Sb_x$ islands shown in Figure 3-7 (b), on the other hand, are explained similarly to the heights of large, star shaped Bi islands growing on wide HOPG terraces[52,54,87]. A high local adatom flux leads to a faster island growth which prevents the formation of taller islands. The different shapes of the 3 ML and 5 ML base $Bi_{1-x}Sb_x$ islands are discussed in more detail in the next section.

### 3.2.2 Shapes of $Bi_{1-x}Sb_x$ islands: Compact and irregular geometries

Figure 3-9 (a) shows a higher resolution RT-STM image of a small and compact 5 ML base $Bi_{0.87}Sb_{0.13}$ island and Figure 3-9 (b) shows a higher resolution RT-STM image of a 3 ML base $Bi_{0.87}Sb_{0.13}$ island, which is characterized by an irregularity along the base as well as on the stripes. The 5 ML base island shows well defined protrusions in the base (blue arrow in Figure 3-9 (a)), while irregular, asymmetric fingers decorate the 3 ML base island (blue arrow in Figure 3-9 (b)).

In contrast, the white arrows in both, Figure 3-9 (a) and (b) point towards the two different types of stripes. The stripes on the 5 ML base island in Figure 3-9 (a) show a regular and ordered geometry as compared to the irregular shape of the stripes on the 3 ML base island in Figure 3-9 (b).

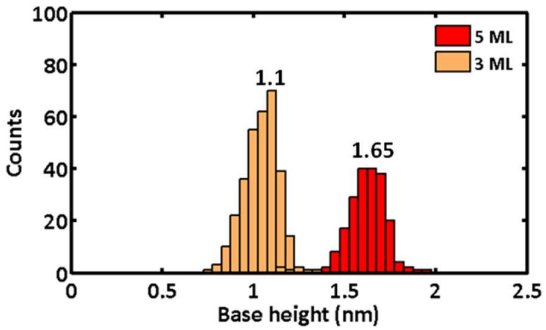


*Figure 3-8 A plot showing statistical height analysis on the $Bi_{1-x}Sb_x$ island bases. Two different island base heights can be seen. A peak at 1.1 nm corresponds to the 3 ML high islands and a peak at 1.65 nm corresponds to the 5 ML base islands.*

Despite these morphology differences, the overall morphology of these two islands remains similar (i.e. wedding cake like).

These observations point towards essentially two different kinds of basic $Bi_{1-x}Sb_x$ island shapes. The different shapes are explained on the basis of two competing mechanisms, namely edge diffusion and the incoming local adatom flux. For step edge nucleated islands, which grow in a low local flux environment, edge diffusion of adatoms dominates[51], thus resulting in the formation of compact islands as shown in Figure 3-7 (a) and Figure 3-9 (a). On wide HOPG terraces, the quicker arrival of incoming adatoms as compared to edge diffusion, destabilizes the islands[52,54,81] and the result is an irregular, anisotropic geometry (Figure 3-9 (b) and Figure 3-7 (b)).

Pure Bi[51,52,54,98,99] (110) islands on HOPG show an ordered growth morphology, therefore Sb is the primary reason for the irregularity in the $Bi_{1-x}Sb_x$ islands (bases and fingers). The discussion on the different $Bi_{1-x}Sb_x$ shapes is taken forward by focusing on the irregularity present in the island bases in the next section.

#### 3.2.2.1 Irregular $Bi_{1-x}Sb_x$ bases: Finger development

Figure 3-10 (a) shows an RT-STM image of a $Bi_{0.87}Sb_{0.13}$ island having a fingered growth at the tip of the island base, with a white square marking the fingered region. Figure 3-10 (b) is a higher resolution RT-STM image of the fingered region, marked by the white square in Figure 3-10 (a). The lateral expansion and asymmetry of the fingers is highlighted by the double sided purple arrows in Figure 3-10 (b). Fingered growth is observed routinely on pure Sb islands[54,63,81] on HOPG and not for

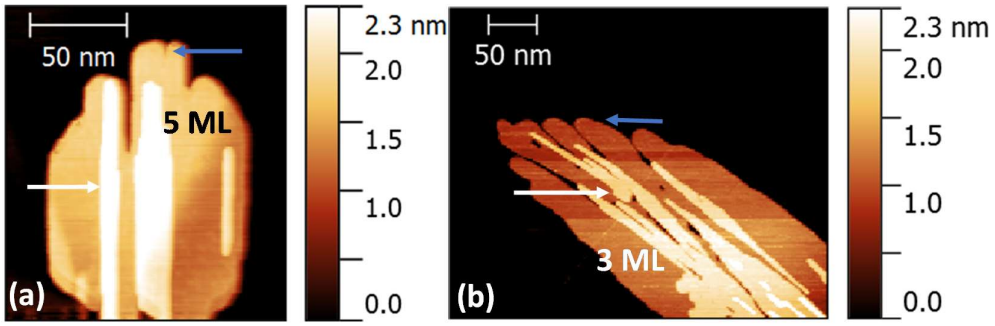


*Figure 3-9 (a) RT-STM image of a 5 ML base $Bi_{0.87}Sb_{0.13}$ island showing a compact shape of the base and the stripes above. (b) RT-STM image of a 3 ML base $Bi_{0.87}Sb_{0.13}$ island showing an irregular shape of the base and the stripes on top of it. Imaging parameters: +0.2 V, 10 pA.*

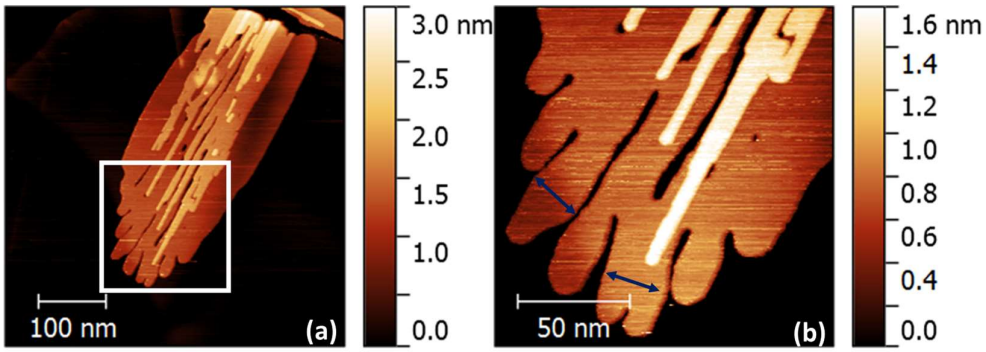


*Figure 3-10 (a) RT-STM image of a $Bi_{0.87}Sb_{0.13}$ island, which shows finger-like protrusions in the island base. (b) Shows a higher resolution RT-STM image of the fingered region marked in (a). Imaging parameters: (+0.8 V, 10 pA, RT-STM)*

pure Bi[51,54,87,98,99,124] (110) islands on HOPG, which indicates that the origin of these finger-like patterns at the tip of $Bi_{1-x}Sb_x$ island bases is most likely due to the presence of Sb. Taking a cue from the explanation of fingered Sb islands[54,81], Mullins Sekerka[83] like instabilities are expected to play a pivotal role in explaining these morphological features.

Mullins Sekerka like instabilities owe their origin to the diffusion of incoming material or the impact of heat flow across the aggregate. As it is shown in the Hele Shaw[83] experiments, the initial circular shape of the liquid (glycerine) develops small protrusions which eventually form finger like instabilities, when a fresh liquid is injected into it. A dynamic interplay between surface tension and the pressure gradient is the major cause of the instabilities in the circular shape of the liquid drop. The fingered patterns in the Sb islands on HOPG[54,63] owe their origin to an analogous effect of the adatom diffusion field, which tends to destabilize the initial stable island morphology. The destabilizing effects are not observed as frequently for smaller islands which have a more stable and compact morphology due to higher edge diffusion of adatoms which nullify the impact of the diffusion field. A high adatom diffusion field around the islands explains the origin of the $Bi_{1-x}Sb_x$ base fingers shown in Figure 3-10 (a-b).

As shown earlier in Figure 3-9 (b), the irregularity in the shape of 3 ML base $Bi_{1-x}Sb_x$ islands can also be seen along the stripe edges. The next subsection discusses briefly, the irregular 5 ML stripes on top of 3 ML $Bi_{1-x}Sb_x$ island bases.

#### 3.2.2.2 Irregular stripes: 5 ML stripe bulges

Figure 3-11 (a-b) shows RT-STM images of two $Bi_{0.87}Sb_{0.13}$ islands that exhibit the formation of irregular 5 ML stripes on one side of the islands, indicated by white arrows. The general morphologies of both the islands are similar to the typical $Bi_{1-x}Sb_x$ morphologies described earlier in section 3.1.2.

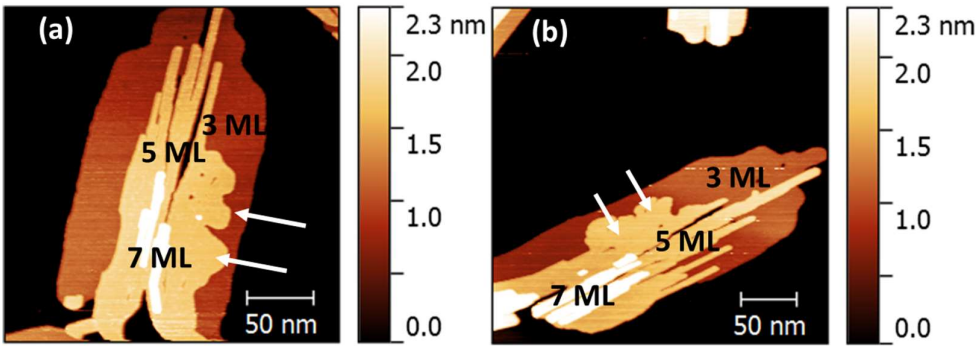


*Figure 3-11 (a-b) RT-STM images of two $Bi_{0.87}Sb_{0.13}$ islands with a 3 ML high base, showing the presence of irregular 5 ML stripes in the form of bulges (white arrows). Imaging parameters: +0.2V, 50 pA.*

Each of the two islands comprise a flat 3 ML high base, irregular 5 ML stripes and small 7 ML stripes on top. The areas of interest, i.e. the irregular 5 ML stripes are focused upon for imaging in both the islands by means of higher resolution RT-STM images in Figure 3-12 (a-b).

The reason to image the two 3 ML high $Bi_{0.87}Sb_{0.13}$ islands is primarily to study the peculiar one-sided bulging of the 5 ML stripes, as highlighted by the blue arrows in Figure 3-12 (a-b). A ball and stick model in the inset of Figure 3-12 shows a hybrid bulk/BP like structure which has previously been proposed as one of the schematic models for the 5 ML stripes of pure Bi[97] (110) islands on HOPG. The

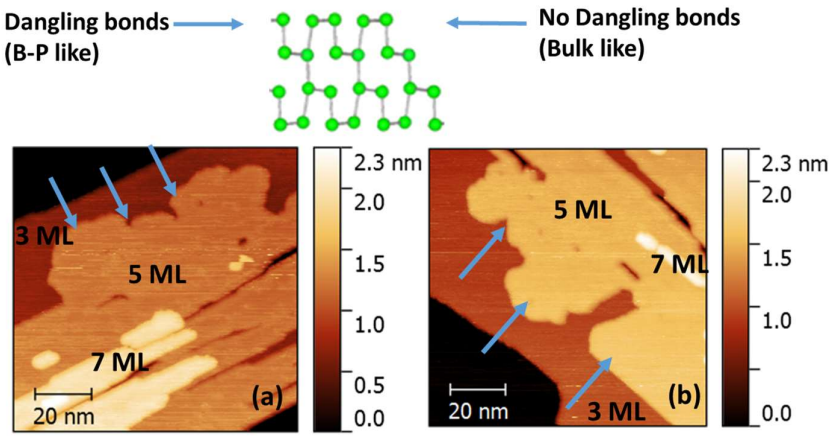


*Figure 3-12 (a-b) Higher resolution RT-STM images of the 5 ML bulging stripes of two $Bi_{0.87}Sb_{0.13}$ islands. The blue arrows indicate the incoming adatoms. A ball and stick model (hybrid bulk/BP like structure) reproduced from[97] is shown on top highlighting the asymmetry along the two edges. Imaging parameters: +0.2V, 50 pA.*

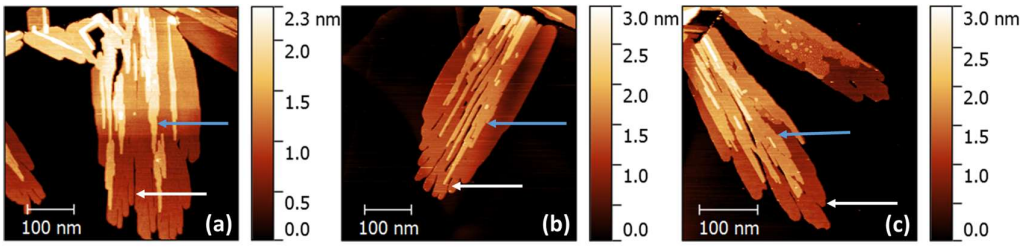


*Figure 3-13 (a) RT-STM image of a 3 ML base $Bi_{0.94}Sb_{0.06}$ island. (b) RT-STM image of a 3 ML base $Bi_{0.87}Sb_{0.13}$ island showing an increase in the coverage of the island base by the 5 ML stripes. (c) RT-STM image of a $Bi_{0.76}Sb_{0.24}$ shows a significant increase in the irregularity and the area occupied by the stripes on top of the base. Imaging parameters: +0.2 V, 50 pA.*

hybrid schematic model has the features of bulk Bi lattice structure (no dangling bonds) along one 5 ML stripe edge and BP like structure (dangling bonds) along the other stripe edge as highlighted by blue arrows and is speculated to cause the expansion of 5 ML stripes along one side of the islands. The incoming adatoms will have more probability of attaching to the 5 ML stripe edge with dangling bonds and expand it laterally as compared to the 5 ML stripe edge without dangling bonds.

Having discussed the key features of $Bi_{1-x}Sb_x$ islands, the next section discusses the change in the islands' morphologies as a function of Sb concentration.

## 3.3 Concentration dependent study of $Bi_{1-x}Sb_x$ islands

$Bi_{1-x}Sb_x$ sample series with three different Sb (x) concentrations (x=0.06, 0.13 and 0.24) are prepared and intuitively, a co-existence of striped and fingered island morphologies is expected, irrespective of the Sb content. Representative STM images of $Bi_{0.94}Sb_{0.06}$, $Bi_{0.87}Sb_{0.13}$ and $Bi_{0.76}Sb_{0.24}$ islands are shown in Figure 3-13 (a), (b) and (c) respectively. The scale of the three images is kept

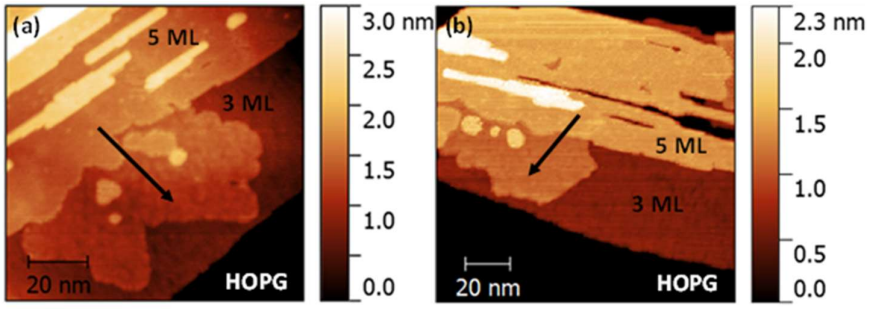


*Figure 3-14 (a-b) RT-STM images of $Bi_{0.76}Sb_{0.24}$ islands showing the presence of an additional monolayer region (black arrows) having nucleated adjacent to the irregular 5 ML stripe edges and on top of the 3 ML bases. Imaging parameters: (+ 0.2 V, 100 pA, RT-STM).*

similar to allow comparison of the difference in the morphology of $Bi_{1-x}Sb_x$ islands as a function of Sb content. The irregular geometry of the islands is evidenced in Figure 3-13 (a-c) and indicated by white and blue arrows, which point towards fingered bases and irregular stripes respectively. The striped nature of the islands in Figure 3-13 (a-c), confirms that the $Bi_{1-x}Sb_x$ islands retain the wedding cake like structure up to x=0.24 and is reminiscent of the growth mode of pure Bi[97-99,128] (110) islands. The fingered bases in all the three islands are reminiscent of the fingered Sb[54,63] islands on HOPG, clearly highlighting the impact of Sb.

The STM image of $Bi_{0.94}Sb_{0.06}$ island shown in Figure 3-13 (a) reveals a low coverage of the stripe area, which increases slightly for the $Bi_{0.87}Sb_{0.13}$ island shown in Figure 3-13 (b). This trend continues, with a substantial increase in the area coverage by the stripes on the $Bi_{0.76}Sb_{0.24}$ island in Figure 3-13 (c). These observations are speculated to result from an overcoming of the (E-S)[84] barrier along the island edges by the incoming adatoms with increasing Sb content and is one of the important results of the concentration dependent study and is discussed in more detail in section 3.4.

In addition to the increase in the coverage of 5 ML stripes as a function of Sb content, the other key result emerging out of the concentration dependant study is the presence of an additional region adjacent to the irregular 5 ML stripes and on top of 3 ML bases as shown in Figure 3-14 (a-b) in which, two RT-STM images of different $Bi_{0.76}Sb_{0.24}$ islands, with a 3 ML high base are shown. Black arrows in Figure 3-14 (a-b) indicate the additional region, which clearly grows differently to the paired layers and is identified as one of the most interesting findings during the course of this project, because such structures are not observed in the STM images of pure Bi[98,99] (110) islands. It is emphasized that the

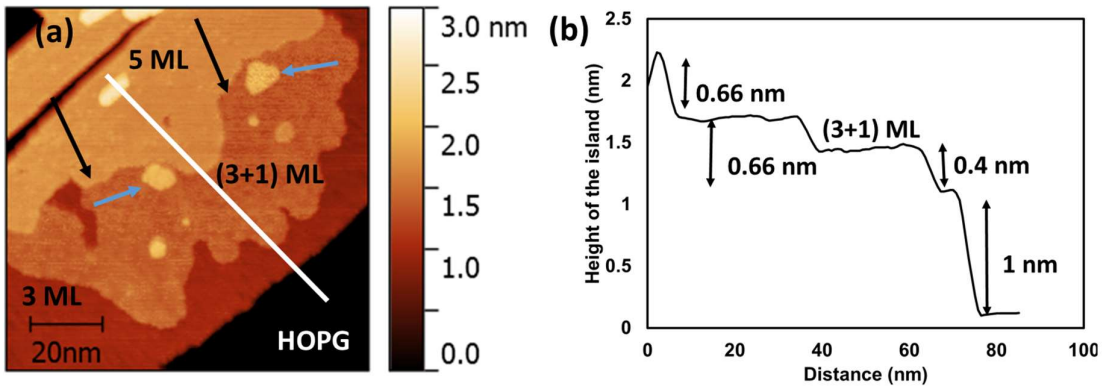


*Figure 3-15 (a) Higher resolution RT-STM image of a $Bi_{0.76}Sb_{0.24}$ island comprising a (3+1) ML region. Black arrows indicate the irregular edges of irregular 5 ML stripes and blue arrows indicate the growth of small islands (overlayers) on top of (3+1) ML. (b) A height profile of the (3+1) ML region, corresponding to the white line drawn across (3+1) ML in (a). Imaging parameters: (+0.2 V, 10 pA).*

| Concentration of alloy | Number of islands with (3+1) ML (STM) | Total islands imaged(STM) | Percentage of (3+1) ML observed |
|---|---|---|---|
| 6 % | 3 ± 2 | 219 | 1 % |
| 13 % | 12 ± 3 | 251 | 5 % |
| 24% | 16 ± 4 | 148 | 11 % |

*Table 3-1 Table demonstrating the probability of locating a (3+1) ML region on a $Bi_{1-x}Sb_x$ island as a function of Sb concentration.*

additional monolayer region is observed to nucleate on top of the 3 ML base $Bi_{1-x}Sb_x$ islands and adjacent to the irregular 5 ML stripe edges, hence it is referred to as (3+1) ML region from here on in the thesis.

### 3.3.1 (3+1) ML

The discoveries of 2-D materials like graphene[33,129], silicene[130], germanene[131] has motivated researchers all over the world to pursue in-depth morphological investigations of such 2-dimensional nanostructures as they present an opportunity of exploring novel morphological and electronic properties. Moreover, the physisorbed[132,133] monolayers of molecules and atoms provide an excellent platform for the fundamental study of surface atoms' diffusion and Moiré Patterns[128,134] at the nanoscale. Therefore, the presence of the (3+1) ML regions on $Bi_{1-x}Sb_x$ islands provides a good platform to study the above mentioned properties in more detail by means of higher resolution STM imaging.

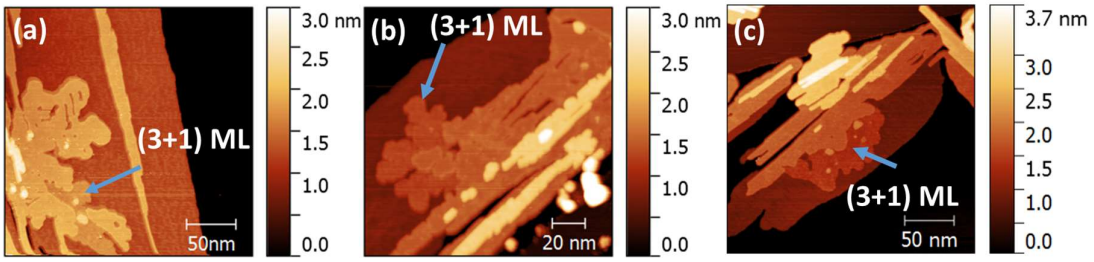


*Figure 3-16 (a) RT-STM image of a $Bi_{0.94}Sb_{0.06}$ island comprising a (3+1) ML region, identified to occupy a small region on top of the 3 ML base. (b) RT-STM image of a $Bi_{0.87}Sb_{0.13}$ island, showing a larger area coverage of the (3+1) ML region. (c) RT-STM image of a $Bi_{0.76}Sb_{0.24}$ island, showing the highest coverage of the (3+1) ML region. Imaging parameters (a-c): (+0.2 V, 10 pA).*

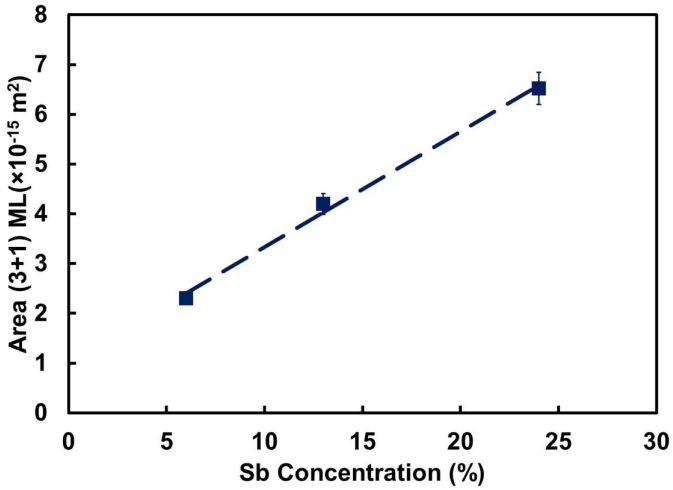


*Figure 3-17 A plot showing the area occupied by the (3+1) ML regions on $Bi_{1-x}Sb_x$ islands as a function of Sb content in the samples, where the dashed blue line is a linear trendline demonstrating the increase in the (3+1) ML area as a function of Sb content.*

Figure 3-15 (a) is a higher resolution RT-STM image of a $Bi_{0.76}Sb_{0.24}$ island comprising a (3+1) ML region nucleated on top of the 3 ML base, observed to grow with an irregular geometry. The non-uniform lateral spread of the (3+1) ML region renders it fundamentally different from the 5 ML and 7 ML stripes observed on $Bi_{1-x}Sb_x$ islands. Blue arrows on Figure 3-15 (a) point towards the additional, small islands (over layers) formed on top of (3+1) ML. Black arrows in Figure 3-15 (a) point towards the irregularity of the 5 ML stripe edge, speculated to be the regions of nucleation of the (3+1) ML, indicating a stronger affinity of the incoming adatoms along the irregular 5 ML stripe edges.

Figure 3-15 (b) shows a height profile of the (3+1) ML region which corresponds to the white line drawn across the island in Figure 3-15 (a). In addition, the impact of Sb content on the formation of (3+1) ML is supported by the numbers shown in Table 3-1 which indicate that the probability of finding a (3+1) ML region on a $Bi_{1-x}Sb_x$ island increases as a function of Sb concentration. Only 1 % (3/210) $Bi_{0.94}Sb_{0.06}$ islands and 5 % (12/259) of $Bi_{0.87}Sb_{0.13}$ islands show evidence for the presence of (3+1) ML regions. A substantial increase to 11 % (16/148) of $Bi_{0.76}Sb_{0.24}$ islands showing the presence of (3+1) ML region, clearly indicates that the presence of the (3+1) ML is directly proportional to the amount of Sb content in the samples.

The (3+1) ML region is speculated to form due an increase in the up-diffusion of incoming adatoms across the 3 ML base edges with increasing Sb concentration, probably facilitated by a low E-S barrier[84] along the 3 ML $Bi_{1-x}Sb_x$ base edges. Pure Sb is known previously to form taller, 3-dimensional islands which is much in contrast to the flat 2-dimensional Bi islands, which is in itself

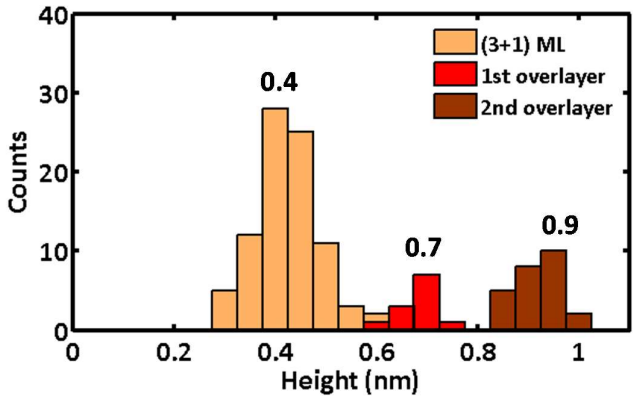


*Figure 3-18 A plot showing height analysis on (3+1) ML regions and the small islands, referred to as overlayers. The overlayers are identified to have different heights and therefore called as 1st and 2nd overlayers. All heights are measured with respect to the 3 ML island base.*

suggests that Sb has a lower E-S barrier on HOPG and is therefore able to overcome the barrier along the 3 ML base edges of alloys and facilitate the formation of the (3+1) ML regions.

The affinity of the (3+1) ML for the irregular 5 ML stripe edges is argued on the basis of additional dangling bonds along irregular edges, which increase the probability of incoming adatoms to nucleate. The different morphology of the (3+1) ML regions is understood in more detail by corresponding area coverage and heights analysis (next section).

### 3.3.2 Area coverage and heights of (3+1) ML

Figure 3-16 (a-c) shows RT-STM images of $Bi_{1-x}Sb_x$ islands with different Sb concentrations, where (a) represents $Bi_{0.94}Sb_{0.06}$ (b) represents $Bi_{0.87}Sb_{0.13}$ and (c) represents $Bi_{0.76}Sb_{0.24}$ islands. The blue arrows point towards the (3+1) ML regions in each of the three images. As can be identified by looking at the images, the area occupied by the (3+1) ML is smaller for $Bi_{0.94}Sb_{0.06}$ island in (a) as compared to the comparatively larger areas occupied for both the $Bi_{0.87}Sb_{0.13}$ and $Bi_{0.76}Sb_{0.24}$ islands, as seen in (b) and (c) respectively. This observation is verified in Figure 3-17 by a plot of the (3+1) ML area as a function of Sb concentration for different $Bi_{1-x}Sb_x$ islands, in which each data point represents an average of five different (3+1) ML regions. The plot clearly shows that with increasing Sb content in the islands, the area coverage of the (3+1) ML region increases linearly, supporting the earlier observation of larger (3+1) ML areas for $Bi_{0.87}Sb_{0.13}$ and $Bi_{0.76}Sb_{0.24}$ islands in Figure 3-16 (b) and Figure 3-16 (c) respectively. The area coverage analysis also indicates an increase in the up diffusion of incoming adatoms as Sb concentration is increased.

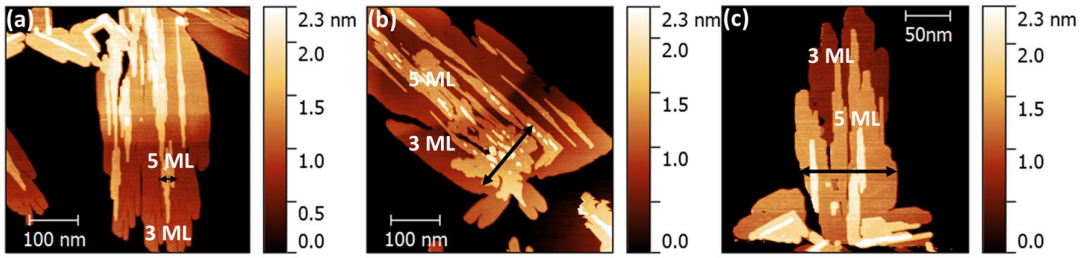


*Figure 3-19 (a-c) shows three different RT-STM images showing different area coverage by the 5 ML stripes on top of the 3 ML bases, where (a) is a $Bi_{0.94}Sb_{0.06}$ island with the least amount of 5 ML stripe area coverage. (b) is a $Bi_{0.87}Sb_{0.13}$ island showing a comparitively larger 5 ML stripe coverage. (c) is a $Bi_{0.86}Sb_{0.24}$ island base showing the highest 5 ML stripe area coverage. Imaging parameters: +0.2 V, 50 pA.*

A height analysis of the (3+1) ML and the small overlayers growing on top of it is shown in Figure 3-18 in which a histogram peak at 0.4 nm for (3+1) ML regions and two more histogram peaks at 0.7 nm ($1^{st}$) and 0.9 nm ($2^{nd}$) for the subsequent over layers is identified. Since the small islands on top of the (3+1) ML increase by 0.3-0.4 nm each time, it is speculated that the small circular overlayers could be individual layers with approximate thickness of 0.33 nm. In this manner, the (3+1) ML could be a single $Bi_{1-x}Sb_x$ monolayer with approximate thickness of 0.33 nm (measured 0.4 nm). The (3+1) ML could be (111) oriented as the morphology in general, is different to the island paired layers. Similarly, the (3+1) ML regions could be (110) oriented films with a bulk-rhombohedral lattice, as evidenced by the lack of paired layer formation and nucleation of circular islands on top. Although, a lack of atomic resolution images on the (3+1) ML regions prevents a confirmation of the above two hypothesis and will be the focus of future experiments.

The (3+1) ML region is fragile, hence, acquisition of atomically resolved STM images of the (3+1) ML is difficult. Moreover, during each attempt to acquire atomic resolution images, either the STM tip would lose sharpness or disrupt (3+1) ML's overall shape.

## 3.4 Stripe/Base area ratio: Different E-S barriers

Figure 3-19 shows representative STM images of (a) $Bi_{0.94}Sb_{0.06}$ (b) $Bi_{0.87}Sb_{0.13}$ and (c) $Bi_{0.76}Sb_{0.24}$ islands. As it is emphasized by the lateral arrows drawn across 5 ML regions, the area occupied by the 5 ML stripes on top of each of the three island bases is observed to increase with increasing Sb concentration. To confirm this observation, the ratio of area occupied by the 5 ML stripes and the area of the island bases is analysed for different Sb concentration samples and shown in Figure 3-20. The analysis is done separately for 5 ML stripes which grow on top of 3 ML base $Bi_{1-x}Sb_x$ islands and 7 ML

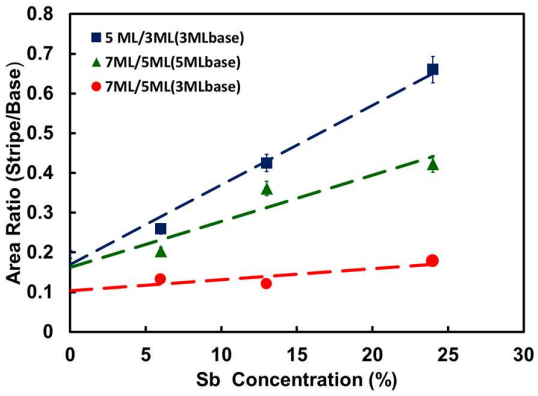


*Figure 3-20 Plot showing the change in ratio of area occupied by the stripes (5 ML and 7 ML) on top of the island bases (3 ML and 5 ML) as a function of Sb concentration. The dashed lines represent the trend lines.*

stripes which grow on top of 5 ML and 3 ML base $Bi_{1-x}Sb_x$ islands. Each dataset represents the average area ratio for 15 $Bi_{1-x}Sb_x$ islands.

The area ratio of 5 ML/3 ML (blue) in Figure 3-20 increases significantly as a function of Sb concentration, implying that with increasing Sb concentration, higher number of adatoms are able to climb up across the 3 ML bases by overcoming the E-S[84] barrier. A similar trend is observed for the area ratio of 7ML stripes on 5 ML bases (green), indicative of a similar overcoming of the E-S barrier across the edges of the 5 ML high bases. On the other hand, no noticeable change is observed in the ratio of (7 ML/5 ML) stripes for islands with a 3 ML base (red) as a function of Sb concentration, implying that 7 ML stripes on top of 3 ML base $Bi_{1-x}Sb_x$ islands are more likely to be formed by direct impingement, rather than due to adatoms climbing across the island edges.

In addition, the stripe/base (5 ML/3 ML) ratio is plotted as a function of the island base area for different concentration $Bi_{1-x}Sb_x$ islands and is shown in Figure 3-21, where green, blue and black data series represent $Bi_{0.94}Sb_{0.06}$, $Bi_{0.87}Sb_{0.13}$ and $Bi_{0.76}Sb_{0.24}$ islands respectively. As evidenced by the three data series, the 5ML/3ML ratio increases as expected with increasing Sb concentration, tentatively indicative of the area-independent nature of the result.

This section is concluded by stating that the area coverage of the stripes, in particular of the 5 ML stripes on top of the 3 ML $Bi_{1-x}Sb_x$ bases increases as a function of Sb concentration indicating an increase in up-diffusion of adatoms across the 3 ML $Bi_{1-x}Sb_x$ island bases. In addition, preliminary analysis indicates that the results are independent of the island base area. It is clarified here that no measurable increase in sample coverage is observed for 3 ML base $Bi_{1-x}Sb_x$ islands as a function of Sb concentration by means of STM images.

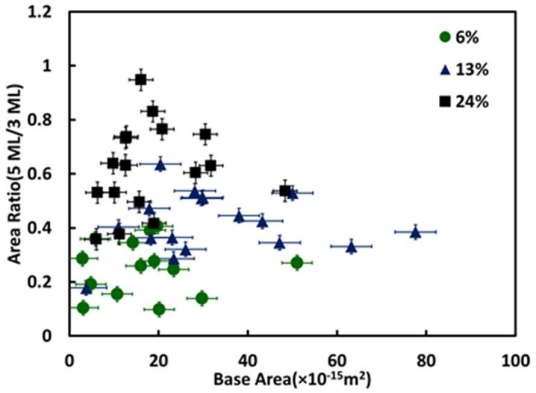


*Figure 3-21 Plot showing variation in area ratio for 5ML/3ML regions as a function of island base area for different concentration $Bi_{1-x}Sb_x$ samples, where green, blue and black represent $Bi_{0.94}Sb_{0.06}$, $Bi_{0.87}Sb_{0.13}$ and $Bi_{0.76}Sb_{0.24}$ islands respectively.*

The distinct morphological characteristics of $Bi_{1-x}Sb_x$ islands, in particular, the presence of fingered island bases, irregular 5 ML stripes and (3+1) ML regions motivates the study of the islands' morphology as a function of the sample coverage, primarily to identify interesting, new growth patterns like the (3+1) ML. In addition, previous[54] investigations of pure Bi (110) islands on HOPG system demonstrate a growth orientation transition from Bi (110) to Bi[51,54,87] (111) islands at a critical higher sample coverage of 12 ML. In addition, Bi[46,135,136] (111) and $Bi_{1-x}Sb_x$[137] (111) islands are interesting candidates for exploration of topologically protected electronic states. The next section thus, briefly describes the preliminary STM results obtained on a higher coverage (12 ML) $Bi_{0.87}Sb_{0.13}$ sample.

## 3.5 Higher coverage growth: Preliminary results

Figure 3-22 (a-b) shows two higher RT-STM images of a 12 ML $Bi_{0.87}Sb_{0.13}$ sample in which islands are seen to occupy a major portion of HOPG. Importantly, it can be seen that the islands retain the wedding cake like morphology (blue arrows), irrespective of the increased sample coverage, although the stripes show a slight irregularity as indicated by the black arrows. Clearly, no transition to (111) oriented islands is seen in the preliminary STM images of higher coverage $Bi_{0.87}Sb_{0.13}$ sample. The number of stripes on top of each of the islands, although is observed to increase significantly and speculated to have the same growth mechanism as reported for higher coverage pure Bi[87] (110) islands on HOPG.

To understand the morphology characteristics of 12 ML high $Bi_{0.87}Sb_{0.13}$ islands in more detail, future studies will be focused on preparation of different Sb concentration samples, with an emphasis on identifying the key morphological similarities and differences with the low coverage samples. Apart

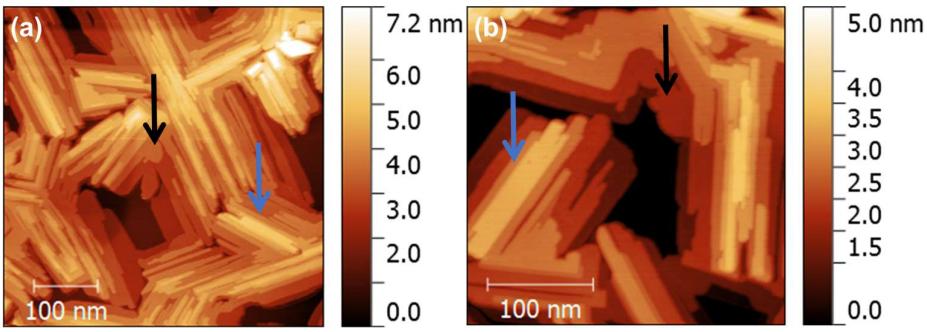


*Figure 3-22 (a-b) RT-STM images of $Bi_{0.87}Sb_{0.13}$ islands in a higher coverage (12 ML) sample. As seen, a large portion of HOPG is covered by islands, which essentially demonstrate the typical wedding cake morphology (blue arrows) identified in the 2 ML coverage samples, in addition to the irregular shapes of stripes (black arrows). Imaging parameters: +0.2 V, 10 pA.*

from the possibility of engineering new geometries of $Bi_{1-x}Sb_x$ islands at higher coverage, 50 K CITS measurements will be focused upon in considerable detail as topologically interesting electronic states similar to that reported[137] for Bi (111) islands can be mapped and studied.

## 3.6 Summary

The morphology characteristics of $Bi_{1-x}Sb_x$ islands on HOPG have been studied by STM as a function of Sb concentration, (x=0.6, 0.13 and 0.24). The islands demonstrate irregularity in the 3 ML high bases (fingered protrusions), similar to the fingered growth of Sb[54,63,81] islands on HOPG. The stripes show an irregular morphology, in particular, the 5 ML stripes, which are speculated to act as nucleation centres for incoming adatoms, resulting in the formation of an additional region. The precise location of the additional region is used to refer it as the (3+1) ML region, an interesting result as such regions are not usually observed for pure Bi[98,99](110) islands on HOPG. The Sb concentration dependent study reveals an increased probability of locating (3+1) ML regions as the Sb concentration is increased.

Having described the key morphological characteristics of $Bi_{1-x}Sb_x$ islands in this chapter, the electronic properties of the paired layers for the low coverage samples are described in detail in the next chapter and concluded with a brief description of the preliminary results obtained on the (3+1) ML regions.

# 4 Electronic properties of $Bi_{1-x}Sb_x$ islands on HOPG

The lattice periodicity of crystalline materials leads to an electronic band structure[6] which comprises of occupied and unoccupied energy levels[3]. The first order numerical derivative (dI/dV) of experimentally measured tunnelling current as a function of the applied bias voltage is equivalent[115] to the LDOS of the material (section 2.3.3). The LDOS can be measured in an STM when tunnelling current is acquired as a function of the applied bias in the scanning tunnelling spectroscopy (STS) mode. The STS results can thereafter be compared with the DFT[138] calculated LDOS for comparison and a detailed analysis.

All the STS results presented in this chapter are acquired in the CITS (section 2.3.3.1) mode at 50 K in the bias range of ±2 V with a set point current of 1 nA. The acquired I(V) spectra are filtered and processed with the methodology described in section 2.4 and numerically differentiated to obtain the final dI/dV spectra which are shown as Feenstra[139,140] normalized [dI/dV/(I/V)] (section 2.4.2.3) spectra.

The representative 50 K CITS results are shown for each of the paired layers, i.e., 3 ML, 5 ML and 7 ML of $Bi_{1-x}Sb_x$ islands as a function of Sb concentration and compared with the corresponding DFT calculated LDOS. It is emphasized that the experimentally acquired spectra of 3 ML, 5 ML and 7 ML thick regions of $Bi_{1-x}Sb_x$ islands are compared with the DFT calculated LDOS of 2 ML, 4 ML and 6 ML thick free-standing slabs of $Bi_{1-x}Sb_x$ ultra-thin films, due to the presence of a 1 ML (3.3 Å) high wetting layer (section 1.2.3) beneath the island bases.

The chapter is divided into two parts, where the first part discusses the DFT calculated band structures and corresponding LDOS of 2 ML, 4 ML and 6 ML thick, free-standing slabs of $Bi_{1-x}Sb_x$ , Bi ultra-thin films, with an emphasis on the impact of different Sb concentrations (x=0, 0.12, 0.24) on the band structures.

The second part of the chapter discusses in detail, the experimental LDOS of 3 ML, 5 ML, 7 ML regions and briefly, that of the (3+1) ML regions of $Bi_{1-x}Sb_x$ islands. The representative spectral histograms[123] for each of the three different $Bi_{1-x}Sb_x$ concentrations are shown alongside the representative spectra of the paired layers to demonstrate data sets' reproducibility, in accordance with the methodology outlined earlier in section 2.4.2.

## 4.1 Electronic band structures

### 4.1.1 DFT Calculated band structure diagrams and LDOS spectra: Bi and $Bi_{1-x}Sb_x$

The DFT[138] calculated band structures for three different thicknesses (2, 4 and 6) ML for pure Bi[98,124] and $Bi_{1-x}Sb_x$ free-standing slabs are presented and discussed in this section. The band structures are obtained from first-principles calculations using HGH (Hartwigsen-Goedecker-Hutter)-type

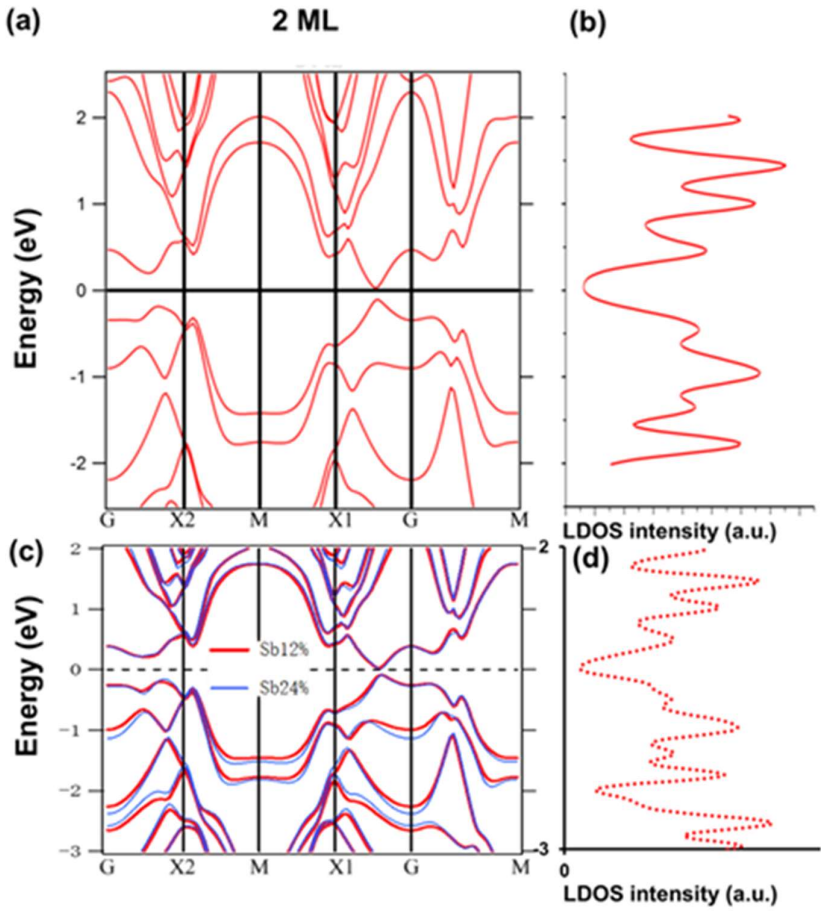


*Figure 4-1 (a) Band structure diagram of a 2 ML thick, free-standing slab of pure Bi ultra-thin films, reproduced from[124]. (b) Corresponding calculated 2 ML LDOS, reproduced from[124]. (c) Band structure diagrams of 2 ML thick, free standing slabs of $Bi_{0.88}Sb_{0.12}$ (red) and $Bi_{0.76}Sb_{0.24}$ (blue) ultra-thin films. (d) Corresponding calculated 2 ML LDOS of $Bi_{0.88}Sb_{0.12}$ ultra-thin films.*

pseudopotentials and a plane-wave basis set[141]. All the band structure calculations are performed on relaxed, free-standing slabs (i.e. no effect of the substrate is included) in the presence of spin-orbit coupling[142]. The final calculated density of states is a result of integration over the entire Brillouin zone and the methodology adopted is the same as that adopted for the results reported[98] for pure Bi ultra-thin films. Specific details about the positions of the locals and the variations in the LDOS from an atom to atom can be found in the similarly performed DFT calculations discussed in previously published reports[98,141]. All the DFT calculations were performed by Guang Bian at University of Illinois, Urbana Champagne, USA as a part of this study. The band structures of pure Sb are not explored yet and discussed in this work, although, the band structure of Sb (110) can be found in Ref[143].

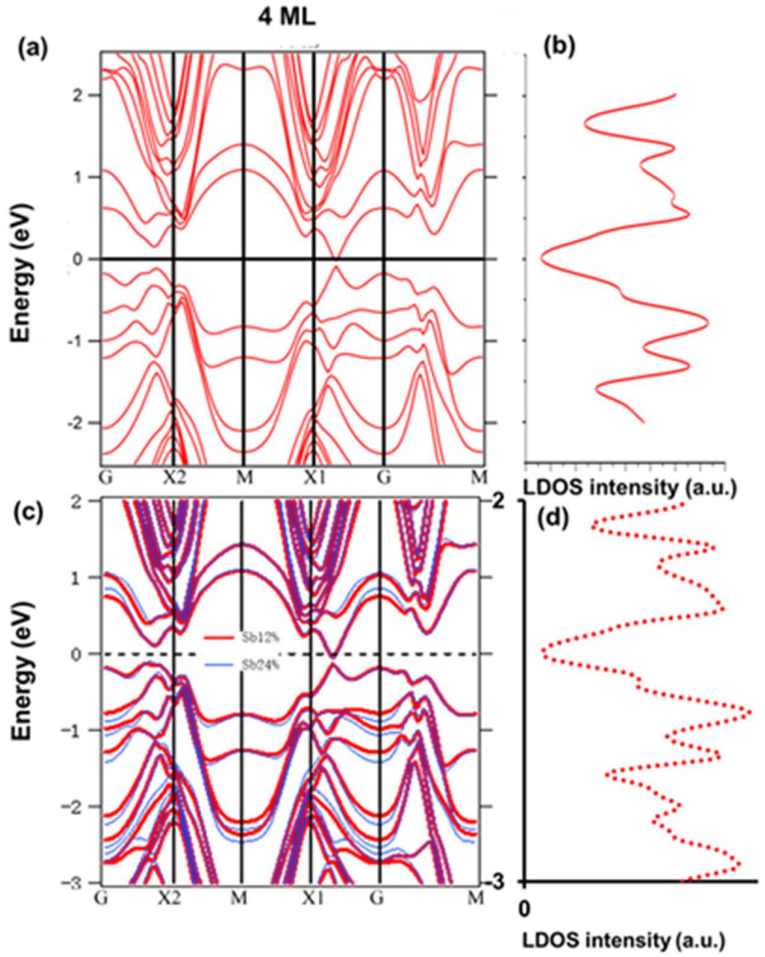


*Figure 4-2 (a) Band structure diagram of a 4 ML thick, free standing slab of pure Bi ultra-thin films, reproduced from[124]. (b) Corresponding calculated 4 ML LDOS, reproduced from[124]. (c) Band structure diagrams of 4 ML thick, free standing slabs of $Bi_{0.88}Sb_{0.12}$ (red) and $Bi_{0.76}Sb_{0.24}$ (blue) ultra-thin films. (d) Corresponding calculated LDOS of 4 ML thick $Bi_{0.88}Sb_{0.12}$ ultra-thin films.*

Figure 4-1, Figure 4-2 and Figure 4-3 show band structure calculations of pure Bi and $Bi_{1-x}Sb_x$ for x=0.12 (red) and 0.24 (blue) for 2, 4 and 6 ML free standing respectively. For simplicity, the calculated LDOS spectra are shown only for $Bi_{0.88}Sb_{0.12}$ ultra-thin film slabs.

#### 4.1.1.1 2 ML

The band structure diagram and the corresponding calculated LDOS spectrum for 2 ML thick, pure Bi[98,124] free-standing slabs are shown in Figure 4-1 (a-b). The horizontal black line drawn in (a) denotes the Fermi level[144] and the electronic bands in the positive and negative energy values represent the unoccupied and occupied energy levels respectively in which only a few bands are

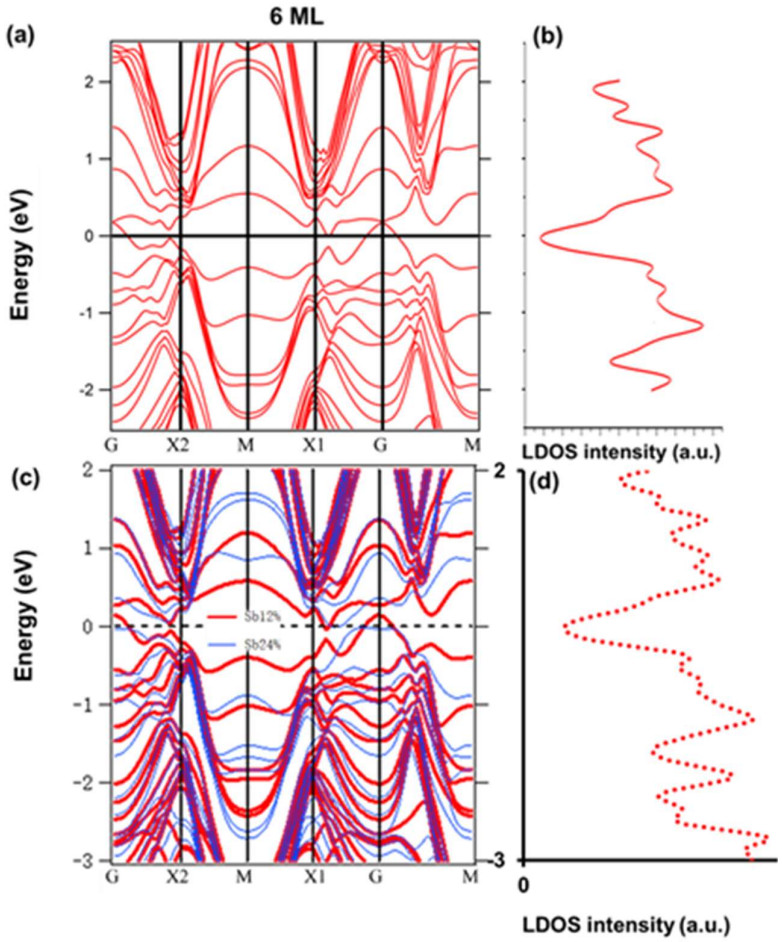


*Figure 4-3 (a) Band structure diagram of a 6 ML thick, free standing slab of pure Bi ultra-thin films, reproduced from[124]. (b) Corresponding calculated LDOS, reproduced from[124]. (c) Overlaid band structures of 6 ML thick, free standing slabs of $Bi_{0.88}Sb_{0.12}$ (red) and $Bi_{0.76}Sb_{0.24}$ (blue) ultra-thin films. (d) Corresponding calculated LDOS spectrum of a 6 ML thick slab of $Bi_{0.88}Sb_{0.12}$ ultra-thin films.*

observed near the Fermi level. Figure 4-1 (b) shows a clear valley in the calculated LDOS near the Fermi level, corresponding to the small band gap in Figure 4-1 (a). The calculated LDOS in Figure 4-1 (b)) clearly shows the presence of four distinct peaks in the negative bias region and three distinct peaks in the positive bias region, within the energy range of ±2 V.

Figure 4-1 (c) shows the band structure diagram of 2 ML thick, free-standing slabs of $Bi_{1-x}Sb_x$ (x=0.12 (red) and x=0.24 (blue)). It becomes immediately clear from Figure 4-1 (c) that the two band structures (x=0.12 and 0.24) of $Bi_{1-x}Sb_x$ ultra-thin films are similar to each other as well as to the band structure of pure Bi, shown in Figure 4-1 (a). The similarity therefore, indicates that an increase in the

concentration of Sb (from x=0 up to x=0.24) does not alter the band structure of $Bi_{1-x}Sb_x$, which is further highlighted by similarity between the LDOS spectra of Figure 4-1 (d) and Figure 4-1 (b).

#### 4.1.1.2 4 ML

The DFT calculated band structure diagram and the corresponding calculated LDOS spectrum of 4 ML thick, free-standing slabs of pure $Bi^{124}$ ultra-thin films are shown in Figure 4-2 (a-b) where (a) is the band structure diagram and (b) is the corresponding calculated LDOS.

One of the identifiable differences in the 4 ML band structure diagram (Figure 4-2 (a)) as compared to the 2 ML band structure (Figure 4-1 (a)) is the increase in number of bands. Figure 4-2 (b) shows the corresponding calculated LDOS, in which two distinct local maxima and a shoulder are present in the negative bias region, in addition to two distinct local maxima in the positive bias region within the bias range of ±2 V.

Figure 4-2 (c-d) shows the band structure diagrams and LDOS of 4 ML thick slabs of $Bi_{1-x}Sb_x$ (x=0.12 (red) and x=0.24 (blue)). It is clear that there is no significant change in the band structure of $Bi_{1-x}Sb_x$ as the Sb concentration is increased from x=0.12 to x=0.24 and agrees rather well with that of pure Bi (Figure 4-2 (a-b)).

#### 4.1.1.3 6 ML

The DFT calculated band structure diagram and the calculated LDOS spectrum of 6 ML thick, free-standing slabs of pure $Bi^{124}$ ultra-thin films are shown in Figure 4-3 (a-b), where (a) is the band structure diagram and (b) is the corresponding calculated LDOS.

Figure 4-3 (a) clearly shows that the number of electronic bands in either of the regions (i.e. positive and negative bias regions) have increased as compared to those observed for 2 ML and 4 ML band structures, apart from two distinct Fermi level crossings. In addition, the corresponding calculated LDOS in Figure 4-3 (b) shows the presence of four distinct local maxima in both the regions (i.e. positive and negative bias) within the energy range of ±2 V.

Figure 4-3 (c-d) show the band structure diagrams and corresponding LDOS spectra of 6 ML thick, free-standing slabs of $Bi_{1-x}Sb_x$ (x=0.12 (red) and x=0.24 (blue)), in which again, no significant change is noticed as the Sb concentration is increased from x=0.12 to x=0.24, with remarkable similarity with the calculated band structure and LDOS of pure Bi (Figure 4-3 (a-b)).

## 4.2 Experimental LDOS

This section presents experimental dI/dV spectra for the different thicknesses of $Bi_{1-x}Sb_x$ islands, i.e. 3 ML, 5 ML, 7 ML and (3+1) ML. Each of the figures demonstrating the experimental results for 3,

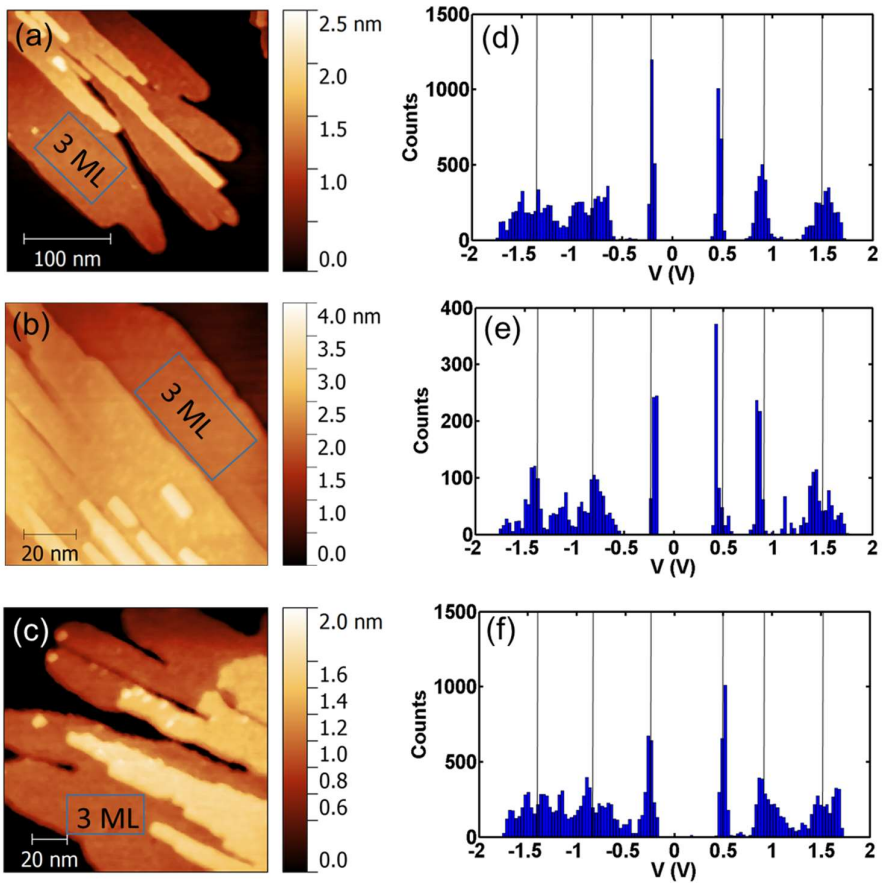


*Figure 4-4 Topographies of (a) $Bi_{0.94}Sb_{0.06}$ (b) $Bi_{0.87}Sb_{0.13}$ and (c) $Bi_{0.76}Sb_{0.24}$ island acquired simultaneously with the I(V) spectra duirng 50 K CITS measurements. The areas of interest for spectral histogram analysis on the 3 ML bases are marked by blue rectangles. The representative spectral histograms of 3 ML bases corresponding to each of the three different concentrations are shown in (d-f), where (d) represents $Bi_{0.94}Sb_{0.06}$ (e) represents $Bi_{0.87}Sb_{0.13}$ and (f) represents $Bi_{0.76}Sb_{0.24}$ spectral histograms. The black lines drawn on top of the spectral histograms represent the major dI/dV features observed for 3 ML high bases of pure Bi islands and are consistent with the methodology described in section 2.4.2.2. Experimental parameters: ±2 V, 1 nA.*

5 and 7 ML in this section comprise four different curves, i.e. the Feenstra normalized dI/dV spectra of pure Bi (orange) extracted from[98], Feenstra normalized dI/dV spectra for $Bi_{0.94}Sb_{0.06}$ (green), $Bi_{0.87}Sb_{0.13}$ (blue) and $Bi_{0.76}Sb_{0.24}$ (black). Each of the final spectra is vertically offset by an equal amount (+0.1) for clarity. Solid black vertical lines drawn on top of each of the plots indicate positions of major dI/dV features reported[124] for pure Bi regions of the same thickness, with the methodology being similar as outlined in section 2.4.2.2. In addition to the different dI/dV spectra (Figure 4-5, Figure 4-7 and Figure 4-9), three additional figures (Figure 4-4, Figure 4-6 and Figure 4-8) show the corresponding

island topographies and spectral histograms (section 2.4.2.2). As far as possible, the dI/dV spectra and spectral histograms are acquired from islands with large, defect free areas to enable extraction of reasonable number of counts for the spectral histograms. Blue rectangles are drawn on each of the islands to mark the areas from where the spectral histograms are extracted.

### 4.2.1 3 ML

Figure 4-4 (a-c) shows the STM images of 3 ML $Bi_{1-x}Sb_x$ islands. Each of the image is for a different Sb concentration, where (a) is a $Bi_{0.94}Sb_{0.06}$ island (b) is a $Bi_{0.87}Sb_{0.13}$ island and (c) is a $Bi_{0.76}Sb_{0.24}$ island. The corresponding spectral histograms are shown in Figure 4-4 (d-f). There are three distinct (+0.5 V, +0.9 V, and +1.5 V) peaks in the positive bias region in each of the three histograms, which are clearly at the same energies as the black lines, indicating that the spectral histogram peaks are in the same

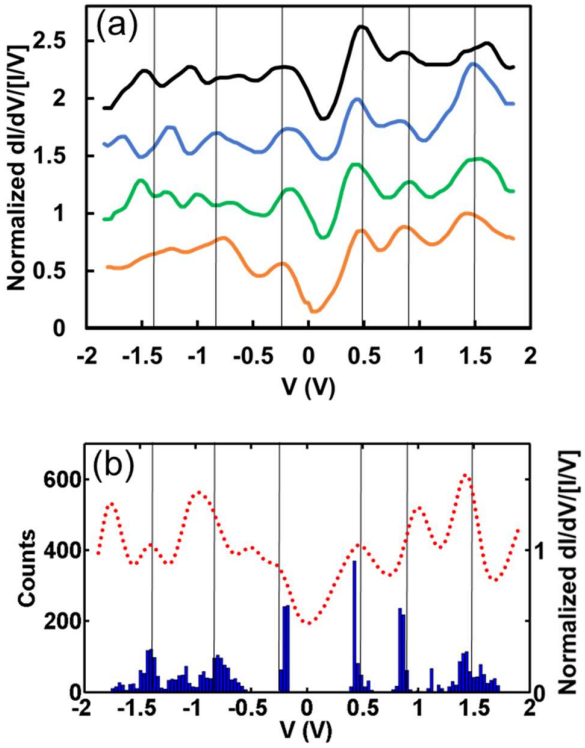


*Figure 4-5 (a) Representative, experimentally acquired dI/dV spectra (Feenstra normalized) for 3 ML bases of pure Bi[98] (orange) and $Bi_{1-x}Sb_x$ islands, where green, blue and black spectra represent $Bi_{0.94}Sb_{0.06}$, $Bi_{0.87}Sb_{0.13}$ and $Bi_{0.76}Sb_{0.24}$ spectra respectively. Each of the spectra is vertically offset (+0.1) for clarity. (b) Shows the DFT calculated LDOS spectrum (red dashed) of 2 ML thick slab of $Bi_{0.88}Sb_{0.12}$ ultra-thin films along with the representative spectral histogram for 3 ML thick bases of $Bi_{0.87}Sb_{0.13}$ islands denoting the energy positions of the key dI/dV features (local maxima and shoulders). Experimental parameters: ±2 V, 1 nA.*

position as for pure Bi[98,124] islands. At negative bias, the major histogram peaks are also in similar positions as they are for pure Bi[98,124] islands.

Figure 4-5 (a) shows that the experimental dI/dV spectra for pure Bi and the representative spectra for each of the three different $Bi_{1-x}Sb_x$ concentrations are in good agreement and in general, with increasing Sb concentration, no significant change in the 3 ML dI/dV features is observed. Moreover, Figure 4-5 (b) shows a good agreement between the major features of the DFT calculated 2 ML LDOS spectrum (red dashed) and peaks of the 3 ML spectral histogram, clearly indicating the similarity between experimental and calculated LDOS. The agreement of the black lines and the calculated LDOS, although is not perfect, as the features in the calculated LDOS appear slightly shifted.

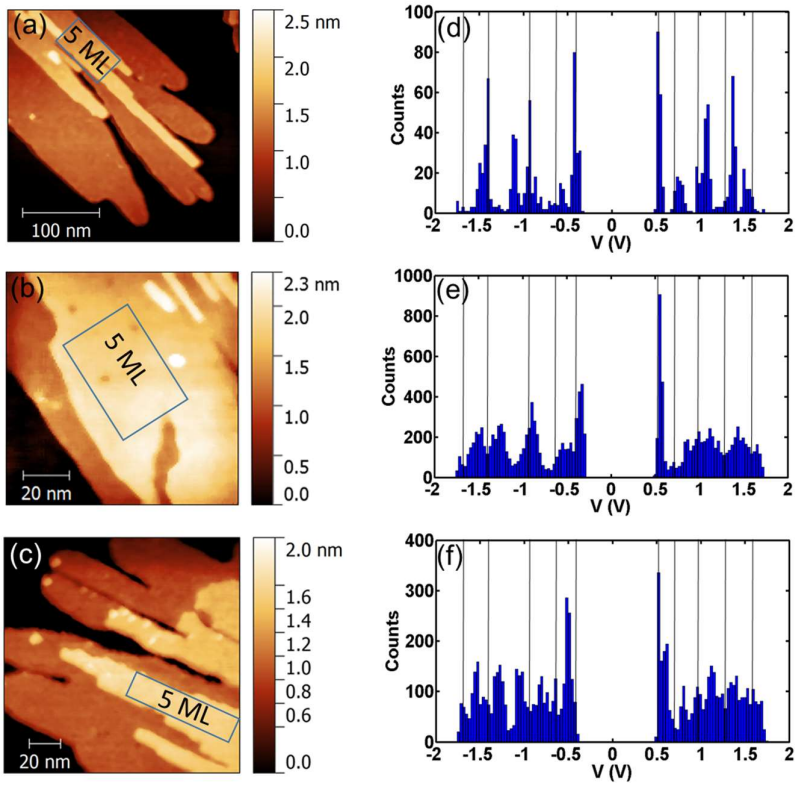


*Figure 4-6 Topographies of (a) $Bi_{0.94}Sb_{0.06}$ (b) $Bi_{0.87}Sb_{0.13}$ and (c) $Bi_{0.76}Sb_{0.24}$ islands acquired simultaneously with I(V) spectra duirng 50 K CITS measurements. The areas of interest and analysis of spectral histogram analysis on the 5 ML stripes are marked by blue rectangles. The representative spectral histograms of 5 ML stripes corresponding to each of the three different concentrations are shown in (d-f), where (d) represents $Bi_{0.94}Sb_{0.06}$ (e) represents $Bi_{0.87}Sb_{0.13}$ and (f) represents $Bi_{0.76}Sb_{0.24}$ spectral histograms. The black lines drawn on top of the spectral histograms represent the major peaks observed for 3 ML high bases of pure Bi islands and are consistent with the methodology described in section 2.4.2.2. Experimental parameters: ±2 V, 1 nA.*

### 4.2.2 5 ML

Figure 4-6 (a-c) shows STM images of 5 ML $Bi_{1-x}Sb_x$ islands for different Sb concentrations. The corresponding spectral histograms are shown in Figure 4-6 (d-f) in which the first two peaks at +0.5 V and -0.5 V on positive and negative bias demonstrate a good agreement with the black lines on top, marking the peaks in the pure Bi data. Additional histogram peaks on each of the bias regions which although, are reproducible, demonstrate slight variations in their positions.

Figure 4-7 (a) shows that representative dI/dV spectra for 5 ML thick regions of pure Bi and the three different $Bi_{1-x}Sb_x$ concentrations are in good agreement. The agreement between the major features of the calculated 4 ML LDOS (red dashed spectrum) and the spectral histogram shown in

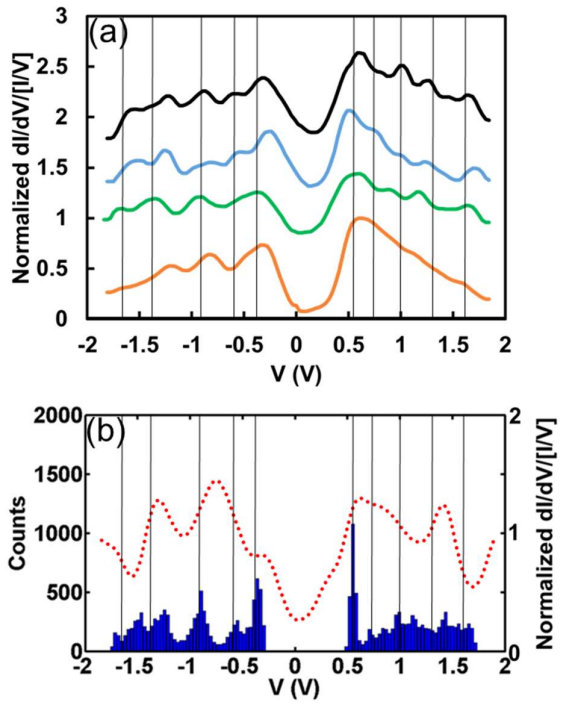


*Figure 4-7 (a) Representative, experimentally acquired dI/dV spectra (Feenstra normalized) for 5 ML regions for $Bi^{98}$ (orange) and $Bi_{1-x}Sb_x$ islands, where green, blue and black represent $Bi_{0.94}Sb_{0.06}$, $Bi_{0.87}Sb_{0.13}$ and $Bi_{0.76}Sb_{0.24}$ spectra respectively. Each of the spectra is vertically offset (+0.1) for clarity. (b) Shows the DFT calculated LDOS spectrum for 4 ML thick slab of $Bi_{0.88}Sb_{0.12}$ ultra-thin films (red dashed) along with the representative spectral histogram of 5 ML stripes of $Bi_{0.87}Sb_{0.13}$ islands, denoting the energy positions of the key dI/dV features (local maxima and shoulders). Experimental parameters: ±2 V, 1 nA.*

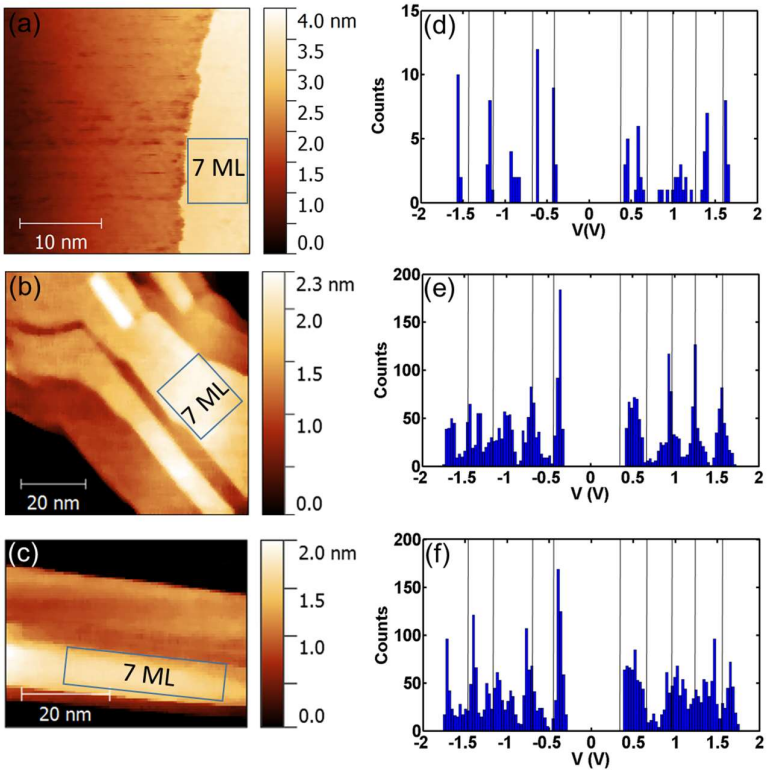


*Figure 4-8 Topographies of (a) $Bi_{0.94}Sb_{0.06}$ (b) $Bi_{0.87}Sb_{0.13}$ and (c) $Bi_{0.76}Sb_{0.24}$ islands acquired simultaneously with I(V) spectra during 50 K CITS measurements. The areas of interest of spectral histogram analysis on the 7 ML stripes are identified and marked by blue rectangles. The representative spectral histograms of 7 ML stripes corresponding to each of the three different concentrations are shown in (d-f), where (d) represents $Bi_{0.94}Sb_{0.06}$ (e) represents $Bi_{0.87}Sb_{0.13}$ and (f) represents $Bi_{0.76}Sb_{0.24}$ spectral histograms. The black lines drawn on top of the spectral histograms represent the major peaks observed for 7 ML high stripes of pure Bi islands and consistent with the methodology described in section 2.4.2.2. Experimental parameters: ±2 V, 1 nA.*

Figure 4-7 (b) is not perfect, as the LDOS features appear to be shifted, but in general, the plot demonstrates a pattern similar to that observed for 5 ML regions of pure Bi[98,124](110) islands.

### 4.2.3 7 ML

Figure 4-8 (a-c) shows the STM images of $Bi_{1-x}Sb_x$ islands comprising 7 ML stripes. The corresponding spectral histograms are shown in Figure 4-8 (d-f) which have smaller number of counts as compared to each of the two other thicknesses (3 ML and 5 ML) due to the narrower widths of 7 ML stripes. In spite of the lower counts, a reasonable agreement is observed between the positions of histogram peaks and the previous data for pure Bi (black lines).

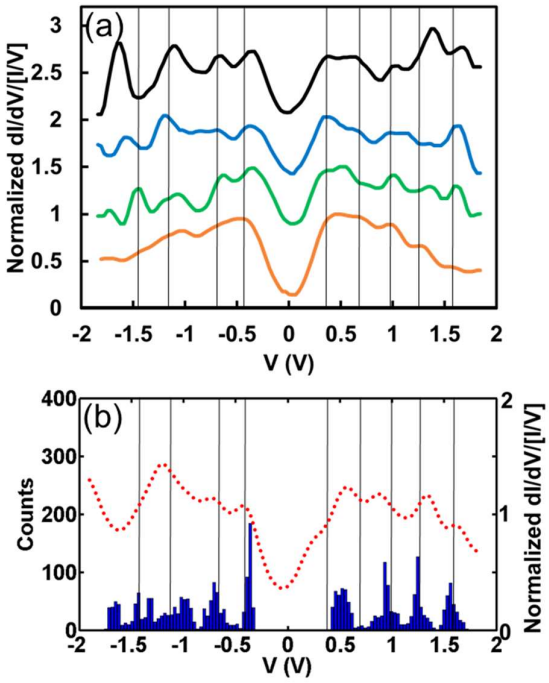


*Figure 4-9 Experimentally acquired dI/dV spectra (Feenstra normalized) for 7 ML stripes of Bi[98] (orange) and $Bi_{1-x}Sb_x$ islands, where green, blue and black represent $Bi_{0.94}Sb_{0.06}$, $Bi_{0.87}Sb_{0.13}$ and $Bi_{0.76}Sb_{0.24}$ spectra respectively. The spectra are vartically offset (+0.1) for clarity. (b) Shows the DFT calculated LDOS spectrum for 6 ML thick slab of $Bi_{0.88}Sb_{0.12}$ ultra-thin films (red dashed) along with the representative spectral histogram of 7 ML stripes of $Bi_{0.87}Sb_{0.13}$ islands, indicating energy positions of the key dI/dV features (local maxima and shoulders). Experimental parameters: ±2 V, 1 nA.*

Figure 4-9 (a) shows representative dI/dV spectra for 7 ML stripes of the three different $Bi_{1-x}Sb_x$ concentrations and pure Bi[98,124], which are again, very similar in their overall shape. Moreover, agreement of the features amongst each of the spectra and with the black lines is rather good. The similarity therefore, highlights both the reproducibility and similarity of the 7 ML spectra features as a function of Sb concentration. Figure 4-9 (b) furthermore, shows that the features of the calculated 6 ML LDOS (red dashed spectrum) align well with the peaks of the 7 ML spectral histogram, while, the agreement with the black lines is not perfect and there are slight shifts in the peak positions as compared to the results obtained for pure Bi[97,123].

### 4.2.4 (3+1) ML

This section briefly discusses the experimental spectra for (3+1) ML thick regions. The previous discussion of (3+1) ML regions in section 3.3.1 showed that the probability of finding a (3+1) ML region increases as the Sb content is increased and that the (3+1) ML regions are therefore, most frequently observed on $Bi_{0.76}Sb_{0.24}$ islands. Therefore, the discussion is restricted to the preliminary 50 K CITS results acquired on $Bi_{0.76}Sb_{0.24}$ islands.

Figure 4-10 (a) shows the STM image of a $Bi_{0.76}Sb_{0.24}$ island in which the distinct (3+1) ML region can be seen. The morphology of the island in Figure 4-7 (a) is consistent with the typical $Bi_{0.76}Sb_{0.24}$ island morphologies described earlier in chapter 3 and therefore, not described in more detail here. The red and black square represent the areas from where dI/dV spectra are extracted for the (3+1) ML and 3 ML region. Both the spectra are Feenstra normalized and shown in Figure 4-10 (b) with a vertical offset for clarity.

The 3 ML spectrum (black) is similar to that for the $Bi_{0.76}Sb_{0.24}$ spectrum shown in Figure 4-10 (a). The (3+1) ML spectrum shows a striking similarity to the spectrum of the underlying 3 ML base. The CITS results on (3+1) ML region are preliminary and corresponding band structure calculations are required for an in depth analysis. In principle, subtraction of the 3 ML spectrum from that of the (3+1)

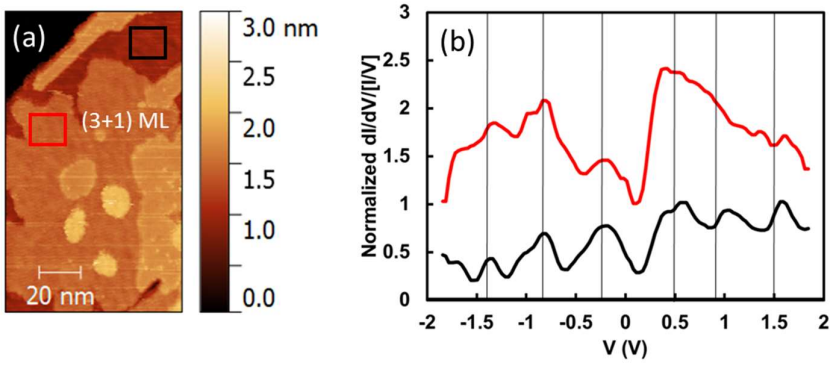


*Figure 4-10 (a) Topography of a $Bi_{0.76}Sb_{0.24}$ island, comprising a (3+1) ML region. The image is acquired simultaneously with I(V) spectra during a 50 K CITS measurement. (b) Experimentally acquired dI/dV spectra (Feenstra normalized) for 3 ML (black) and (3+1) ML (red) regions for a $Bi_{0.76}Sb_{0.24}$ island. The black lines drawn on top of the plot represent the key features of 3 ML bases of pure Bi and are consistent with the methodoly described in section 2.4.2.2. The (3+1) ML spectrum is vertically offset for clarity. Experimental parameters: ±2 V, 1 nA.*

ML might allow the representative spectrum to be obtained. However, the quality of the spectra would need to be improved in order to allow such analysis.

## 4.3 Summary

The experimental dI/dV spectra are similar for all the Sb concentrations (x=0.06, 0.12 and 0.24) for each of the typical thicknesses, i.e. 3 ML, 5 ML and 7 ML observed in $Bi_{1-x}Sb_x$ islands, in addition to being similar to the previously reported[98,124] dI/dV spectra of pure Bi (110) islands. Apart from the similarity in the experimental results, the DFT-calculated LDOS are in good agreement with all the experimental spectra for each of the three $Bi_{1-x}Sb_x$ island concentrations (x=0.06, 0.13 and 0.24) as demonstrated by the corresponding spectral histograms.

# 5 Edge states of $Bi_{1-x}Sb_x$ islands on HOPG

3-D TIs such as $Bi_{1-x}Sb_x$[10-12,42,137] are host to robust surface electronic states and currently, TIs are being explored by researchers all around the world to develop smart electronic devices and minimize the energy loss. Miniaturization of 3-D TIs into 2-D TIs is expected to result in the realization 1-D edge states. In this context, there are two key questions that need to be answered, firstly, is it possible to observe the edge states and secondly, how robust are the edge states to atomic buckling and surface reconstructions?

Edge states can be thought of as pathways for the electron to move in an insulating region and correspond to the semi-classical skipping orbits observed along the edges of a typical Hall-bar[6,7]. STM and ARPES have been used to investigate edge states in a number of materials[32,60,135,136,145-151] with evidence of topologically protected edge states reported in materials like HgTe[39,40], $Bi_2Te_3$[152,153].

STM is a surface sensitive technique and allows for extraction of localized information of the topography and LDOS of the surface, providing the right framework for studying the edge states of $Bi_{1-x}Sb_x$ islands. Experimental[45,124] evidence of unusually higher conductance along the edges of pure Bi (110) islands on HOPG[124] further motivates an in-depth study of the edges of $Bi_{1-x}Sb_x$ islands. In addition, the morphology of $Bi_{1-x}Sb_x$ islands (Chapter 3) allows the possibility of understanding the characteristics of edge states as a function of the paired layers.

This chapter first discusses STM results on the different edges of $Bi_{1-x}Sb_x$ islands in considerable detail, with suitable evidence presented to highlight the higher edge conductance (brighter edges) and followed by two subsections (5.6 and 5.7) in which preliminary results on anomalous electronic states and bright spots are briefly discussed.

## 5.1 Bright island edges: STM images

Figure 5-1 (a) shows a RT-STM image of a $Bi_{0.87}Sb_{0.13}$ island, acquired with a low tip-sample bias (+0.2 V) in which a 5 ML base with bright edges is identified. The island has a wedding-cake-like structure, typical of $Bi_{1-x}Sb_x$ islands on HOPG (Chapter 3) and comprises two 7 ML stripes on top of the 5 ML high base. A white arrow in Figure 5-1 (a) indicates the bright edge of the 5 ML base, but similar brightness along the 7 ML stripe edges is difficult to identify in Figure 5-1 (a). When the same island is imaged with a higher tip-sample bias (+0.6 V), similar bright 5 ML base edges are not observed.

Additionally, bright, spot-like features at different regions inside the 5 ML base region in Figure 5-1 (a) are seen and one such region of bright spots is encircled black. Such bright spots are not observed inside the 5 ML base region in Figure 5-1 (b) when imaging is done with a higher (+0.6 V) tip-sample bias. The observation of bright spots inside 5 ML regions of $Bi_{1-x}Sb_x$ islands will be discussed in more detail in section 5.7.

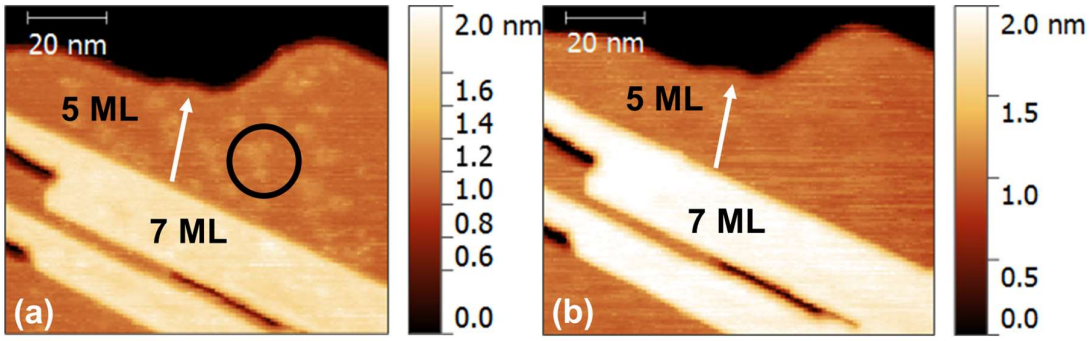


*Figure 5-1 (a) RT-STM image of a 5 ML base $Bi_{0.87}Sb_{0.13}$ island showing unusual bright edges, when the imaging is done at a low tip-sample bias (+0.2 V, 10 pA). (b) RT-STM image of the same $Bi_{0.87}Sb_{0.13}$ island on which the bright 5 ML base edges are not seen, when the imaging is done at a higher tip-sample bias (+0.6 V, 10 pA).*

Unusually bright edges of Bi[45] (110) islands on HOPG and Ni, Cu[154] islands have been previously reported and explained on the basis of edge reconstructions[155] and charge transfer from the STM tips. As the STM essentially maps the LDOS[115] at lower tip-sample bias, a higher LDOS along the $Bi_{1-x}Sb_x$ island edges might explain the observation of brighter edges in Figure 5-1 (a). The presence of edge reconstructions along the edges of $Bi_{1-x}Sb_x$ islands is verified by obtaining atomic resolution STM images.

Figure 5-2 (a) shows a RT-STM image of a 3 ML base $Bi_{0.87}Sb_{0.13}$island. The black rectangle highlights the 5 ML stripe edge, where atomic resolution is obtained and is shown in Figure 5-2 (b) in which it is clearly seen that the edge is characterized by a hump-like feature. A line profile of the blue line of Figure 5-2 (b) is shown in Figure 5-2 (c), emphasizing the hump like feature clearly. The slight

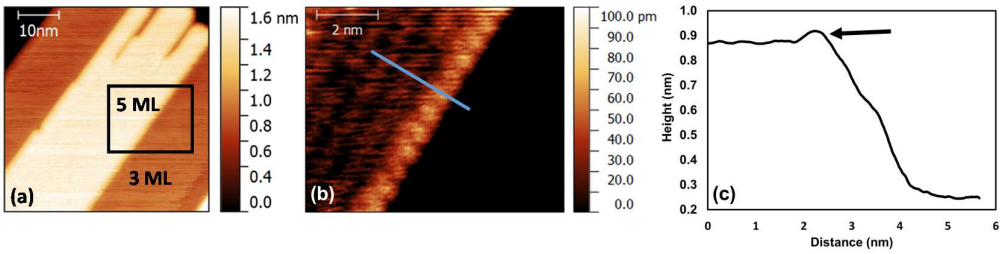


*Figure 5-2 (a-b) RT-STM image of a $Bi_{0.87}Sb_{0.13}$ island with a 3 ML base on which atomic resolution on the 5 ML stripe edge is obtained (+0.8 V, 50 pA). (b) Atomically resolved STM image of the 5 ML stripe edge showing a different atomic arrangement (+0.1 V, 800 pA) (c) A line profile across the 5 ML stripe edge of (b), highlighting the edge protrusion.*

increase in the height of the edge is thus indicative of a different edge atomic arrangement as compared to the atomic arrangement in the bulk of the 5 ML stripe and will be focused upon in future studies by acquiring better quality atomic resolution images.

Additional LDOS features are usually observed along the edges of nanostructured islands, as reported in Ref[45], therefore, CITS measurements which allow for a better understanding of the LDOS by means of dI/dV spectra are pursued and the results are shown in the next section.

## 5.2 CITS on $Bi_{1-x}Sb_x$ island edges

CITS measurements allow for studying of dI/dV spectra along with the generation of conductance maps at different bias simultaneously. This section consists of two subsections; with the first section (5.2.1) depicting the distinct $Bi_{1-x}Sb_x$ edge states observed in the CITS conductance maps and section 5.2.2 describing the dI/dV spectra corresponding to the edge states.

### 5.2.1 Edge states in CITS conductance maps

During CITS acquisition process, current maps at different bias [I(V)] are generated along with the topography of the region[115]. Thus, numerical differentiation of the current maps allows for the studying of conductance maps at different bias [dI/dV (V)] along with the topography of the region. A direct comparison between the islands' topography and the corresponding conductance maps allows for a quicker understanding of the varying conductance inside a $Bi_{1-x}Sb_x$ island. Representative conductance maps of $Bi_{1-x}Sb_x$ islands with a 3 ML and 5 ML base along with the corresponding island topographies are presented in this section, with the discussion on 5 ML base $Bi_{1-x}Sb_x$ islands presented first.

#### 5.2.1.1 Edge states on $Bi_{1-x}Sb_x$ islands with a 5 ML base

Figure 5-3 (a-b) shows a 50 K CITS dataset acquired on a $Bi_{0.87}Sb_{0.13}$island with a 5 ML base. The topography of the island is shown in Figure 5-3 (a) with the corresponding conductance map at 120 mV shown in Figure 5-3 (b). The island topography in Figure 5-3 (a) is similar to the wedding cake like island geometry shown in Chapter 3 with two 7 ML stripes and an additional 9 ML stripe on top of the 5 ML base. There is a slightly disordered and complex region at the top right corner of the image which is ignored in this analysis. Three squares (blue, black, green) mark different regions along the 7 ML stripe edge from where the corresponding dI/dV spectra are extracted and discussed later in section 5.2.2.

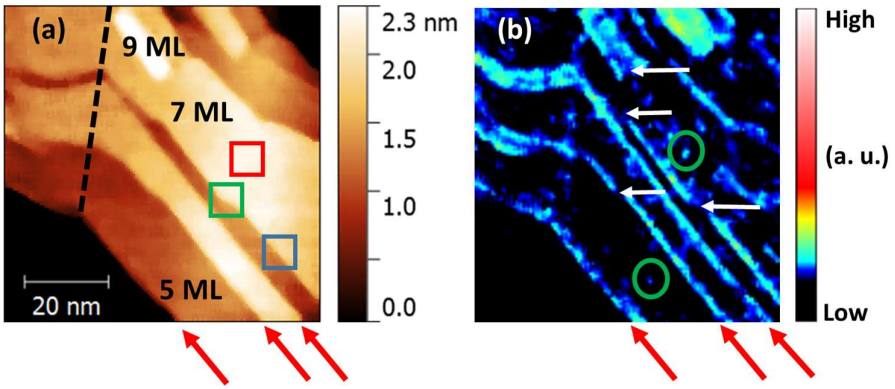


*Figure 5-3 (a) STM image showing topography of a 5 ML base $Bi_{0.87}Sb_{0.13}$ island acquired during a 50 K CITS measurement (-2V, 1 nA). (b) Corresponding conductance map at 120 mV, in which higher conductance along the 7 ML stripes and 5 ML base edges is noted.*

The edges of the 5 ML base, 7 ML and 9 ML stripes are fairly straight, except for regions in where the edges are curved and where kinks are present. The top left corner of the image is dominated by stripes which are curved; which is probably because of a grain boundary[156] and is indicated by the black dashed line in Figure 5-3 (a). In the remainder of this section, the analysis is restricted to the non-disordered regions of 5 ML and 7 ML edges as indicated by the red arrows in Figure 5-3 (b).

The edge states appear in the conductance map (Figure 5-3 (b)) as brighter when compared to the dark interior of the respective structures. At first sight (red arrows), the edge states appear to be continuous along the topographic edges of 5 ML, 7 ML and 9 ML stripes in Figure 5-3 (b). However, in fact, the observed behaviour is more complex. At the grain boundary (black dashed line), the edge states follow the curved 7 ML stripe edges but the edge states seem to disappear at kinks (white arrows) on the edges of 7 ML stripes and at the lower curved end of the 9 ML stripe (note that the edge states appear to follow the curvature of the upper end of this structure). The missing edge states along the facetted regions of the 7 ML stripe edges are discussed in more detail in section 5.2.2.2. Apart from the edge states; there are a few additional bright spots observed inside the 5 ML base and the 7 ML stripe, with two such spots encircled green. These spots are most commonly observed inside 5 ML stripes; better examples and further discussion of which are presented in section 5.7.

Figure 5-3 (b) showed a single conductance map at 120 mV, but Figure 5-4 shows conductance maps for a wider range of voltages. No edge states are seen along the island edges in the conductance maps of (-205 mV) and (-120 mV) in Figure 5-4 (a-b). With increasing bias (-80 mV), faint edge states are seen on the 5 ML and 7 ML stripes in (Figure 5-4 (c)). This trend continues and stronger edge states

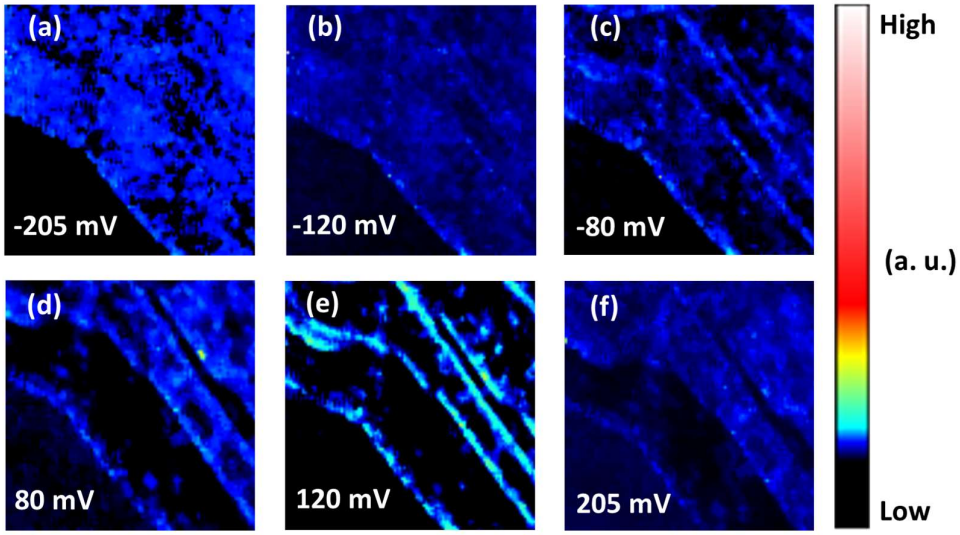


*Figure 5-4 (a-f) The corresponding conductance maps at different bias for the CITS dataset shown in Figure 5-3. Distinctly higher 7 ML stripe edge conductance is observed within a certain bias range and peaks at approximately 120 mV.*

are seen in the next two conductance maps of 80 mV and 120 mV in Figure 5-4 (d) and Figure 5-4 (e) respectively. The last conductance map at 205 mV in Figure 5-4 (f) shows that the stripe and base edge states are no longer seen distinctly. The 120 mV conductance map in Figure 5-4 (e) shows the highest edge conductance with a peak in the corresponding dI/dV spectra and is discussed in section 5.2.2.

#### 5.2.1.2 Edge states on $Bi_{1-x}Sb_x$ islands with a 3 ML base

Figure 5-5 (a-b) shows a 50 K CITS dataset acquired on a 3 ML base $Bi_{0.87}Sb_{0.13}$island. Figure 5-5 (a) shows the island topography with the corresponding conductance map at 120 mV in Figure 5-5 (b). The 3 ML base island also has two 5 ML stripes and one 7 ML stripe on top. Figure 5-5 (a) shows that the edges of the stripes are fairly straight, except for the kinks (white arrows) along the 7 ML stripe edges. Kinks (white arrows) also mark the 3 ML base edge and a grain boundary in the underlying graphite runs through across the 3 ML base, seen as a bright feature (labelled with blue arrow) in the topography image.

The darker region (green arrow) inside the 5 ML stripe in Figure 5-5 (b) is indicative of lower conductance, whereas, higher conductance inside the 3 ML base is noted by a non-uniformity and is attributed to noise during the data acquisition. This non-uniformity is different to the higher conductance related to the bright spots mentioned earlier corresponding to the 5 ML base CITS data set of Figure 5-3 (a-b). Similar to the discussion of Figure 5-3 (a-b), at first sight, the edge states (red

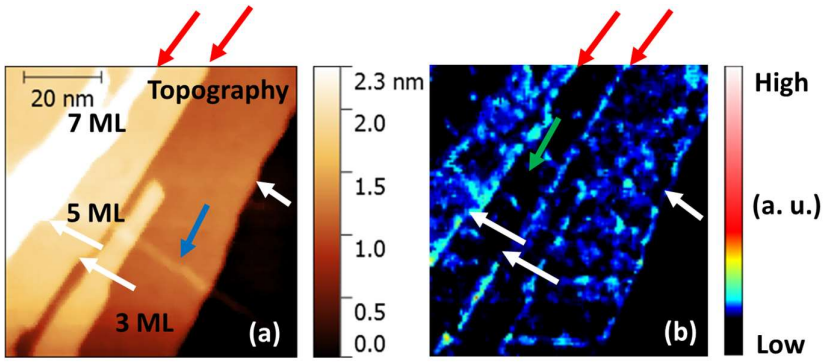


*Figure 5-5 (a) Topography of a 3 ML base $Bi_{0.87}Sb_{0.13}$ island acquired during a 50 K CITS measurement. (-2 V, 1 nA) (b) Corresponding conductance map at 120 mV showing higher conductance along the 5 ML and 7 ML stripe edges.*

arrows) appear to be continuous and seem to follow the topographic edges of 5 ML and 7 ML stripes in Figure 5-5 (b) and again, there are missing edge states at kinks (white arrows in Figure 5-5 (b)).

The discussion shows that the 7 ML stripe edges show higher intensity of conductance as compared to the 5 ML stripe and 3 ML base edges and therefore, from here on, a detailed discussion on the 7 ML stripe edge states is presented first and is followed by brief discussions on 5 ML (section 5.5.2) and 3 ML edge states (section 5.5.3). The 7 ML edge states are understood in more detail in terms of the corresponding dI/dV spectra in the next section.

### 5.2.2 dI/dV spectra

The CITS measurements, as described in chapter 4, allow for the extraction of dI/dV spectra from a specific region of an island and this allows an understanding of the edge states' LDOS. Figure 5-6 shows a comparison between three different dI/dV spectra, corresponding to the straight 7 ML stripe edge region (blue), bulk 7 ML stripe region (red) and facetted 7 ML stripe region (green) as marked in Figure 5-3 (a).

The black arrow in Figure 5-6 indicates a distinct peak around +0.1V in the dI/dV spectrum corresponding to the straight 7 ML stripe edge, a feature not present in the other two spectra. The +0.1V dI/dV feature is consistently observed for edge states of 7 ML stripes, however, in Figure 5-6, the feature is weak because of the large bias range (±2 V) of this particular dataset. The +0.1 V feature is observed more clearly in a smaller bias range (±0.4 V) as presented in the next two sections.

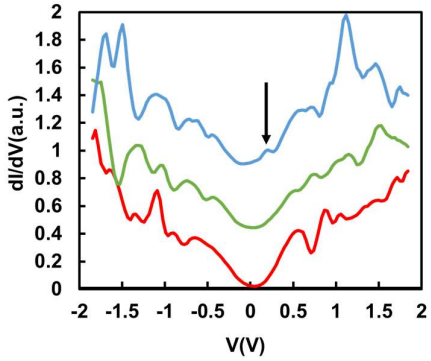


*Figure 5-6 A comparison between the dI/dV spectra corresponding to the straight 7 ML stripe edge region (blue), a facetted 7 ML stripe region (green) and the bulk 7 ML stripe region (red). All the spectra are vertically offset (+0.2) for clarity and are extracted from the regions marked in Figure 5-3 (a) by coloured squares.*

#### 5.2.2.1 Regular and straight 7 ML $Bi_{1-x}Sb_x$ stripe edges

Figure 5-7 (a) shows the STM image of a $Bi_{0.76}Sb_{0.24}$ island with a 5 ML base and 7 ML stripes covering majority of the island base. The 5 ML base has fairly straight edges separated by kinks (white dots). The 7 ML stripes also have fairly straight edges, apart from two kinks indicated by green dots. Figure 5-7 (b) depicts topography of the 7 ML stripe region acquired during a ±0.4 V CITS measurement at 50 K. Blue, green and black squares mark the regions on the straight 7ML stripe edge from where corresponding dI/dV spectra [spatially averaged 8 curves] are extracted and shown later in Figure 5-8 (a). The dI/dV spectra are pre-filtered in accordance with the methodology described earlier in section 2.4.

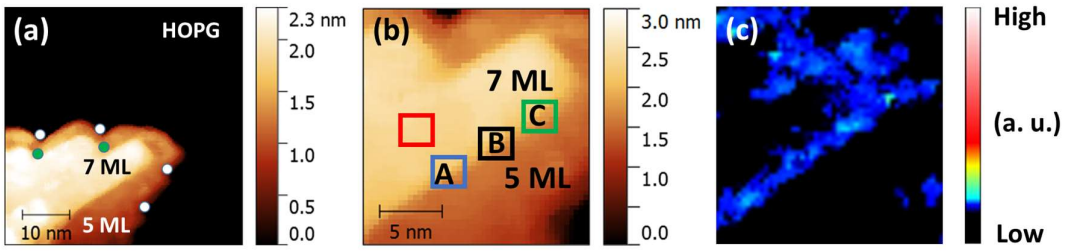


*Figure 5-7 (a) STM image of a $Bi_{0.76}Sb_{0.24}$ island with a 5 ML base chosen for 50 K CITS measurement. (b) Shows the 7 ML stripe topography, focussed upon during the CITS data set acquisition. (c) Shows the corresponding conductance map at 120 mV indicating higher conductance along the 7 ML stripe edges. Experimental parameters: ±0.4 V, 1 nA.*

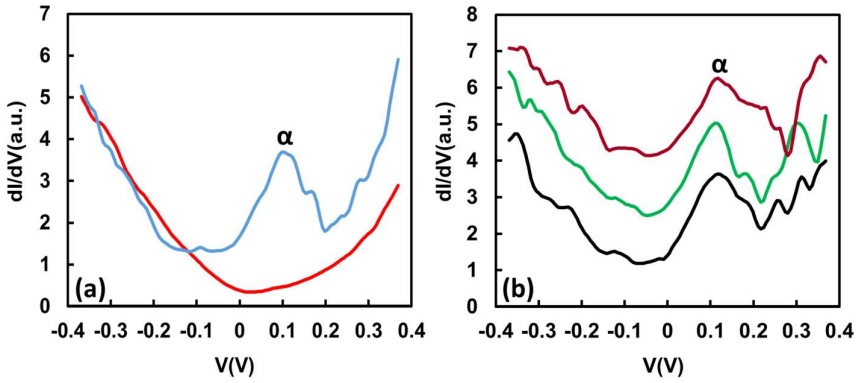


*Figure 5-8 (a) Plot showing a comparison between the dI/dV spectra extracted from the 7 ML stripe edge (blue) with the dI/dV spectra extracted from a region inside the 7 ML stripe (red). (b) Plot showing a comparison between the dI/dV spectra extracted from different regions of the same 7 ML stripe edge demonstrating the reproducibility of the +0.1 V (α) LDOS feature.*

In addition, a red square marks a region inside the 7ML stripe from where the corresponding dI/dV spectra [spatially averaged 8 dI/dV spectra] is extracted and shown in Figure 5-8 (a). Figure 5-7 (c) shows the corresponding conductance map (120 mV) of Figure 5-7 (b) in which the regions inside the 5 ML base and 7 ML stripe are darker and depict lower conductance in comparison to the higher conductance along the straight and curved (top end) regions of the 7 ML stripe edge. The apparent absence of edge states around the top end of the 7 ML stripe is not well understood and the discussion is focused upon the edge states along the straight 7 ML stripe edges.

Figure 5-8 (a) shows a comparison between a representative dI/dV spectra of the straight 7 ML stripe edge and that of the bulk region of the 7 ML stripe, as shown in Figure 5-7 (b). The red dI/dV spectrum does not comprise any peak in the measured experimental bias range (±0.4 V) and is the cause of darker 7 ML stripe region of Figure 5-7 (c). On the contrary, the blue dI/dV spectrum shows a distinct peak at +0.1 V, which corresponds to the higher edge conductance at 120 mV, as seen earlier in Figure 5-7 (c).

Hereafter, the +0.1 V feature will be referred to as 'α' to distinguish the edge states' LDOS characteristics from that of the bulk $Bi_{1-x}Sb_x$ island regions. Representative dI/dV spectra corresponding to three different regions of 7 ML stripe edge, marked in Figure 5-7 (b) are shown in Figure 5-8 (b). The strong intensity of the 'α' feature is identified in all the three spectra and highlights the data sets' reproducibility. The discussion till now gives the impression that 'α' feature is unique to the straight 7 ML stripe edges of $Bi_{1-x}Sb_x$ islands, a result similar to the previous reports on the edges of Bi (110) islands by Lu et al[45] and Mahapatra et al[124]. Both the reports claim to have observed a

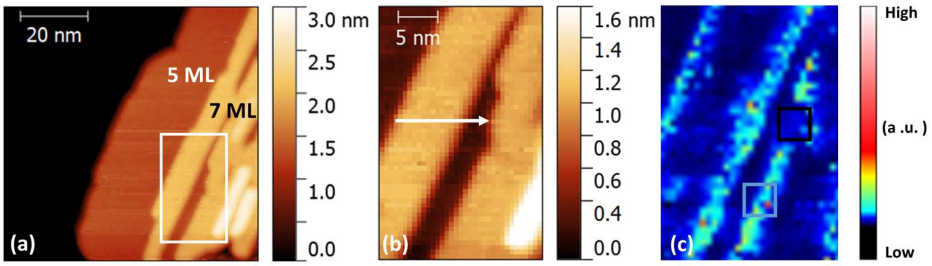


*Figure 5-9 (a) Topography of a $Bi_{0.87}Sb_{0.13}$ island with a 5 ML base, shosen for CITS measurement (+0.9 V, 1 nA). (b) 7 ML stripe region where CITS measurement is done (+0.9V, 1 nA). (c) Corresponding conductance map (120 mV) highlighting bright edge states along regular stripe edges and absence of edge states along the facetted stripe edges.*

distinct dI/dV peak for Bi (110) island edges around +0.1 V, which further highlights the significance of 'α'. A comparison between the edge states of $Bi_{1-x}Sb_x$ and Bi (110) islands on HOPG is discussed later in section 5.5.

Having shown that the straight 7 ML stripe edges have a distinct dI/dV feature (α), a major portion of this section is focused on understanding the dependence of 'α' on experimental parameters (section 5.3) and the extent of 'α' into the island's bulk (section 5.4). The next section discusses the absence of edge states (discussed earlier in Figure 5-3 (a-b)) along the facetted edges of 7 ML stripes.

#### 5.2.2.2 Facetted regions on 7 ML stripe edges

Figure 5-9 (a) shows the topography of a $Bi_{0.87}Sb_{0.13}$ island with a 5 ML base, two 7 ML and 9 ML stripes on top. The 5 ML base has a flat topography with the presence of two kinks along the edge. A white rectangle in Figure 5-9 (a) marks the region chosen for CITS measurement whose magnified view is shown in Figure 5-9 (b). The 7 ML stripe edges are fairly straight, apart from a facetted region (white arrow). Figure 5-9 (c) shows the conductance map (120 mV) corresponding to the topography of 7 ML stripe shown in Figure 5-9 (b). Distinct edge states are observed along the straight 7 ML stripe edge as compared to their absence along the edge facet in Figure 5-9 (c). The conductance map thus clearly demonstrates the variation in the conductance along the facetted 7 ML stripe edges, an observation that is verified by comparison of the corresponding dI/dV spectra.

A straight region and facetted region of the 7 ML stripe edge are marked by a blue and black square in Figure 5-9 (c) respectively. The marked regions represent the areas from where the corresponding dI/dV spectra are extracted and shown in Figure 5-10. The comparison shows that the 'α' LDOS feature is absent in the dI/dV spectra extracted from the facetted region, effectively

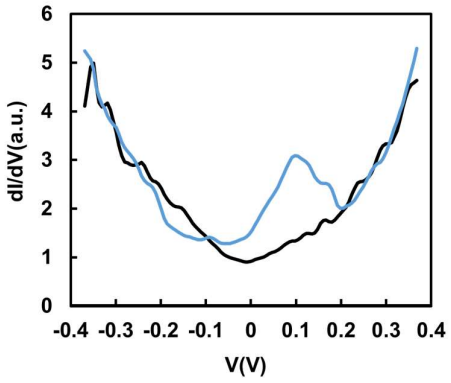


*Figure 5-10 Comparison of the dI/dV spectra extracted from a facetted 7 ML stripe edge and a straight 7 ML stripe edge. The blue spectra corresponds to the straight edge and the black spectra corresponds to the facetted edge region.*

distinguishing it from the dI/dV spectra extracted from the straight 7 ML stripe region (blue), which shows the characteristic 'α' feature.

Figure 5-11 shows a schematic ball and stick model which compares the atomic arrangement along a facetted 7 ML stripe edge with that of a straight 7 ML stripe edge, in which blue spheres denote Bi atoms and red spheres denote Sb atoms in the lattice. The $[\bar{1}10]$ fast growth direction[86] along the straight zig zag edges is denoted by a red arrow. For simplicity, edge reconstructions are not considered in this schematic ball and stick model. A zig zag atomic arrangement of the Bi-Sb bonds is

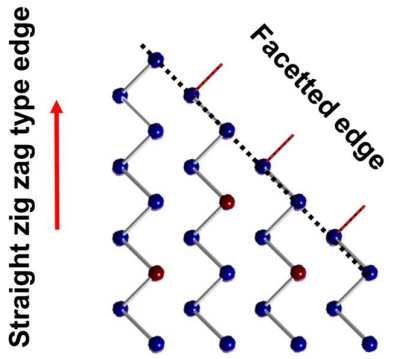


*Figure 5-11 A schematic ball and stick model showing a different atomic arrangement along the facetted edge for a $Bi_{1-x}Sb_x$ stripe edge. Alternating in plane dangling bonds differentiate the facetted edge from the zig-zag type straight edge. The red spheres denote Sb atoms and blue spheres denote Bi atoms.*

along the straight edge is consistent with the atomic arrangement of the lattice (strong zig zag bonds). A dashed line at the facetted edge is drawn to highlight the edge atomic arrangement. The presence of in-plane dangling bonds at every alternate atom on the facetted edge differentiate it from the straight (zigzag) type edge. This difference in terms of the in-plane dangling bonds is speculated to be one of the reasons for the absence of edge states along the facetted edges of 7 ML stripes.

Missing edge states along the facetted edges of 7 ML stripes bear resemblance to the anomalous edge states reported along the differently terminated edges of graphene[136]. On the basis of different atomic arrangements (armchair and zigzag) for graphene[157], different electronic properties of the edges are reported. A lower conductance along zigzag type edges for graphene[136] indicates a similarity to the above-discussed results of missing edge states along the facetted edges of 7 ML stripes on $Bi_{1-x}Sb_x$ islands.

The section is concluded by stating that different conductance is observed along differently terminated 7 ML stripe edges of $Bi_{1-x}Sb_x$ islands. Considerable focus in future experiments will be on acquiring higher resolution CITS data sets along the facetted 7 ML stripes edges for a confirmation of the above discussed results. The next section verifies the presence of edge states along straight 7 ML stripe edges as a function of experimental parameters.

## 5.3 Dependence of edge states on experimental parameters

The impact of experimental CITS parameters such as bias range of the data set, scan direction of the STM tip, and spatial resolution on dI/dV spectra of edges is discussed in this section.

### 5.3.1 Bias range

To understand the impact of bias range on the dI/dV spectra of edges, it is important to consider the experiments in which data acquisition is done with different bias ranges on the same island. Figure 5-12 (a-f) shows an experimental result in which 3 different, 50 K CITS datasets with a 128×128 grid points are acquired on the same 5 ML base $Bi_{0.87}Sb_{0.13}$ island, consecutively in different bias range values. Figure 5-12 (a, c, e) show the topographies of the island for three different bias ranges (±2V, ±1V and ±0.3 V) respectively. The island comprises a flat 5 ML base with a 7 ML stripe on the top. Edges of the 5 ML base and the 7 ML stripe are straight and devoid of any noticeable irregularity. The primary reason for selecting this island is the smooth and straight morphology of 7 ML stripe edges, which reduces the need to understand complex physics at defected and facetted edges.

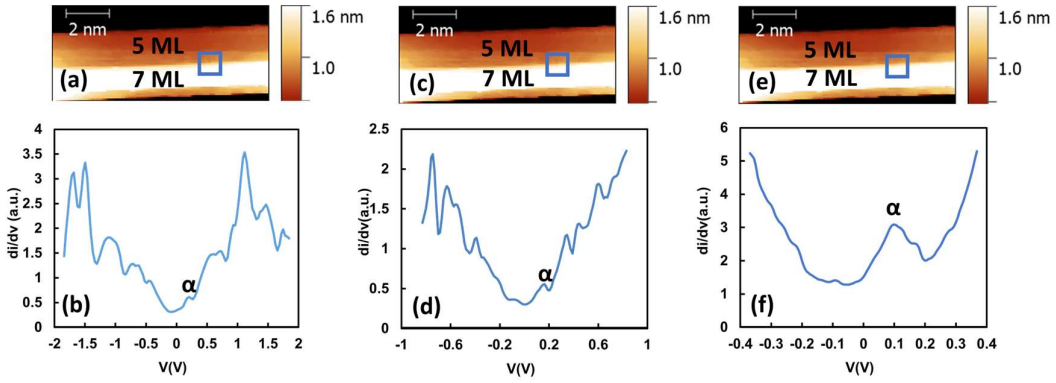


*Figure 5-12 (a) STM image of a 5 ML base $Bi_{0.87}Sb_{0.13}$ island, on which a 50 K CITS measurement is acquired in ± 2 V, setpoint current (1 nA) (b) Shows a plot of dI/dV spectra along the region of 7 ML stripe marked by a blue square in the topography (c) STM image of the same 5 ML base $Bi_{0.87}Sb_{0.13}$ island, on which a 50 K CITS measurement is acquired in ± 1 V and a setpoint current of 1 nA in immediate succession (d) Shows a plot of dI/dV spectra along the region of 7 ML stripe marked by a blue square in the topography (e) STM image of the same 5 ML base $Bi_{0.87}Sb_{0.13}$ island, on which a 50 K CITS measurement is acquired in ± 0.3 V and with a setpoint current of 1 nA on the same day (f) Shows a plot of dI/dV spectra along the region of 7 ML stripe marked by a blue square in the topography.*

Figure 5-12 (a, c, e) clearly depicts that the island morphology does not change during the course of this experiment. In each dataset, same region (i.e. blue squares) of the 7 ML stripe edge is focused upon to extract the corresponding dI/dV spectra. Figure 5-12 (c, e, f) shows the corresponding dI/dV spectra of the marked 7 ML edge regions in different bias (±2 V, ±1 V, ±0.4 V) ranges respectively. The other dI/dV features observed at higher bias values are a result of the interaction of the tip with the island's edge and can vary from region to region within a CITS data set (section 2.4) and therefore are not considered for analysis here. The intensity of 'α' is noted to be considerably weaker in Figure 5-12 (b) which increases slightly in the bias range of ±1V as seen in Figure 5-12 (d). Figure 5-12 (f) shows edge dI/dV spectra corresponding to the ±0.3V bias range in which a marked increase in the intensity of 'α' is seen as compared to the corresponding dI/dV intensities in the ± 2V and ± 1V bias ranges.

The above experiment demonstrates that the acquisition of CITS datasets along island edges with a better energy resolution and within lower bias ranges ensures better current and dI/dV resolution. Apart from the bias range, a few other CITS experimental factors that can impact the interpretation of results on island edges are considered in the next two sections.

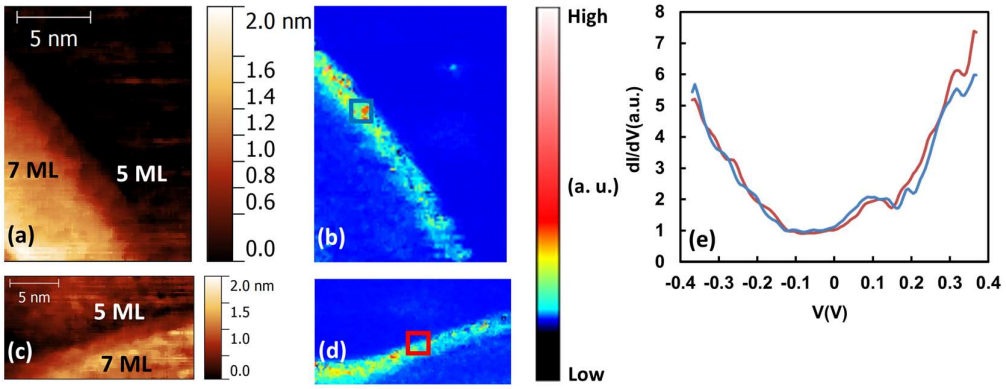


*Figure 5-13 (a-e) 50 K CITS datasets acquired on a 5 ML base $Bi_{0.94}Sb_{0.06}$ island, demonstrating the impact of STM tip scan direction on edge states, where (a-b) Show the topography and conductance map of a CITS dataset acquired by scanning approximately perpendicular to the edge and (c-d) represent the topography and conductance map of same CITS dataset which is acquired by scanning parallel to the edge (e) Demonstrates the similarity in the corresponding dI/dV spectra of the edge acquired with scan direction, in which 'α' feature is seen clearly. The blue spectra corresponds to the dataset shown in (a-b) and the red spectra corresponds to the dataset shown in (c-d).*

### 5.3.2 Scan direction

During CITS measurements, the striped morphology of $Bi_{1-x}Sb_x$ islands (as explained in chapter 3) makes it imperative to consider the impact of STM tip's scanning direction towards the island. The key question considered here is - does scanning perpendicular or parallel to an island's edge result in the acquisition of different dI/dV spectra? To answer this question, the scanning direction of the STM tip towards an island's edge is altered in successive CITS datasets and the dI/dV spectra corresponding to the same region of an edge is compared. Figure 5-13 (a-b) shows a 50 K CITS data set acquired by scanning perpendicular to a 7 ML stripe edge. Figure 5-13 (a) shows the topography of the 7 ML stripe and Figure 5-13 (b) shows the corresponding conductance map at 120 mV.

Figure 5-13 (b) shows the distinct edge states along the straight 7 ML stripe edge, consistent with the results discussed in the previous section. Figure 5-13 (c-d) shows a 50 K CITS data set acquired along the same 7 ML stripe edge immediately after the acquisition of the previous dataset. The key difference is the scanning direction of the STM tip in this dataset as it is acquired by rotating the scan direction by 90 degrees with respect to the scan direction of the first CITS dataset shown in (a-b). Figure 5-13 (c) shows morphology of the 7 ML stripe edge and Figure 5-13 (d) shows the corresponding conductance map at 120 mV. Importantly, the 7 ML stripe edge states are observed again in this dataset which shows that edge states are observed irrespective of the STM tip scanning direction. Figure 5-13 (e) shows a comparison between the dI/dV spectra (spatially averaged 8 curves)

corresponding to the perpendicularly scanned dataset (blue) and the horizontally scanned dataset (red). The spectra are extracted from regions marked by coloured squares in Figure 5-13 (b, d). Both the dI/dV spectra show the presence of 'α' with comparable intensities.

This experiment concludes that the observation of distinct edge states along the 7 ML stripe edges is independent of STM tip's scanning direction.

### 5.3.3 Spatial resolution

Figure 5-14 (a) shows the topography of a 50 K CITS data set with a real space size of (30×30) $nm^2$. The data set is acquired on a $Bi_{0.76}Sb_{0.24}$ island with a 5 ML base consisting of one 7 ML stripe. The 5 ML base and 7 ML stripe edges are straight and devoid of any noticeable irregularity. The corresponding conductance map (120 mV) in Figure 5-14 (b) shows distinct edge states along the straight 7 ML stripe edge. The curved edge at the top of the stripe is marked by a decrease in the edge states' intensity and is not analysed in more detail here. Furthermore, the 5 ML base edge does not show the presence of consistent and distinct edge states and is not analysed in detail in this data set. A white rectangle marks the region in Figure 5-14 (a) where a higher spatial resolution 50 K CITS data set is acquired and shown in Figure 5-14 (c-d).

Figure 5-14 (c) shows the topography of the same 7 ML stripe edge with a real space size of 10×10 $nm^2$ . The straight edge morphology is seen clearly here and allows for a consistent analysis of the edge dI/dV spectra. Four lines (A, B, C, D) correspond to the respective STS intensity maps which are discussed later in section 5.4. The corresponding conductance map (120 mV) shown in Figure 5-14 (d) shows the distinct 7 ML stripe edge states, similar to the edge states observed in the lower resolution conductance map of Figure 5-14 (b). As seen in the conductance map, the edge states evolve smoothly over the entire length of the edge and are devoid of any inconsistency.

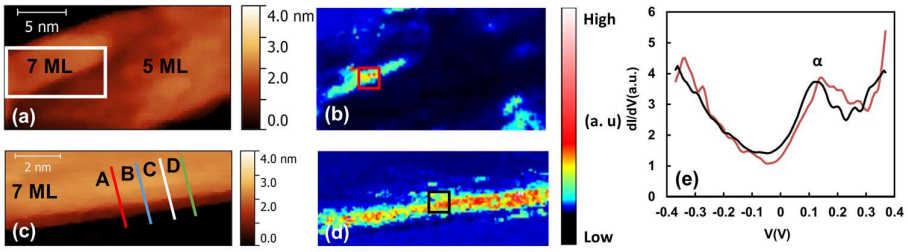


*Figure 5-14 (a-b) 50 K CITS dataset on a $Bi_{0.76}Sb_{0.24}$ island with a 5 ML base. (c-d) Higher resolution 50 K CITS dataset acquired on the same island, with a focus on the straight 7 ML stripe edge. (e) Comparison of representative edge state dI/dV spectra, where red corresponds to the lower resolution dataset and black corresponds to the higher resolution dataset. Bias range (±0.4 V), setpoint current (1 nA).*

Figure 5-14 (e) shows a comparison between the representative edge dI/dV spectra [spatially averaged 8 curves] of the two data sets. The red spectrum is extracted from the region marked by the red square in the lower resolution data set of Figure 5-14 (b) and the black spectrum is extracted from the region marked by a black square in Figure 5-14 (d). Both the dI/dV spectra are noted with the presence of 'α' with comparable intensities. Two important inferences are made from this experiment, firstly that the spatial resolution of the CITS datasets does not affect the LDOS characteristics of the edges and secondly no difference is observed in the intensity of the 'α' state.

The discussion till now establishes that 'α' state of the 7 ML stripe edges is not affected by the spatial resolution of the CITS datasets as well as the scan direction of STM tip. The bias range of the CITS datasets although, has a significant impact, which emphasizes the importance of acquiring CITS datasets in smaller bias ranges. Keeping this in perspective, rest of the CITS datasets on 7 ML stripe edges are shown in (±0.4 V) bias range. The next section discusses the edge states' reproducibility and extent into the islands' bulk by means of STS intensity maps.

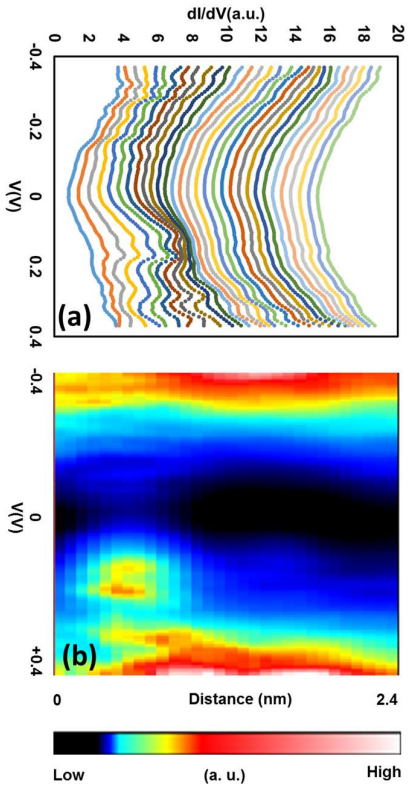


*Figure 5-15 (a) A stacked plot showing successive dI/dV spectra extending from the edge of a 7 ML stripe of a $Bi_{0.76}Sb_{0.24}$ island into the bulk. (b) An STS intensity map representing the dI/dV spectra of (a). Bias range: (±0.4 V), setpoint current 1 nA.*

## 5.4 STS intensity maps

An STS intensity map is a 3-dimensional representation of dI/dV spectra as a function of position, as shown in Figure 5-15 (a-b). Figure 5-15 (a) is a stacked plot of successive dI/dV spectra extracted perpendicular to a 7 ML stripe edge of the $Bi_{0.76}Sb_{0.24}$ island. The plot shows dI/dV spectra intensity along the horizontal axis and the CITS bias range on the left vertical axis. The 'α' feature is clearly identified to peak in the first few dI/dV spectra, with an eventual decrease in the intensity as the dI/dV spectra of the bulk 7 ML region are approached.

Figure 5-15 (b) shows an STS intensity map analogous to the stacked dI/dV spectra plot of Figure 5-15 (a). The horizontal axis in Figure 5-15 (b) denotes distance and the vertical axis on the left denotes CITS bias range and the dI/dV spectra values are represented by different colour intensities. The presence of 'α' can be easily identified in the STS map as a bright yellow feature, which shows an extent into the stripe from the start of the edge. The STS intensity maps in principle, provide the possibility of mapping the edge states' extent from an edge into the island, consistently.

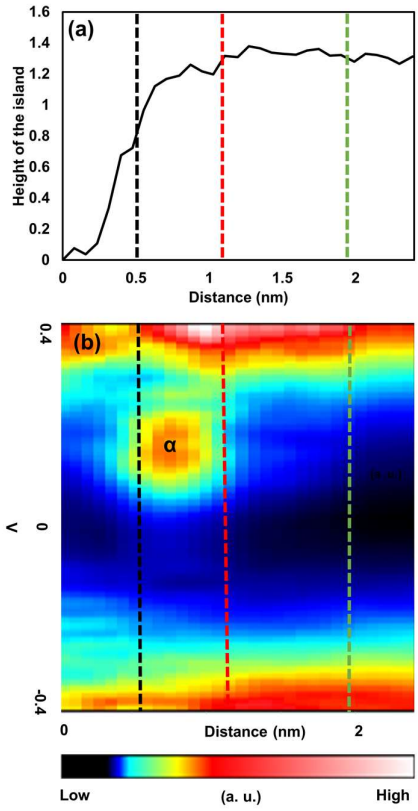


*Figure 5-16 (a) A height profile along the red line drawn in Figure 5-14 (b). The corresponding STS intensity map is shown in (b), which gives an estimate about the extent of 'α' from the 7 ML stripe edge of a $Bi_{0.76}Sb_{0.24}$ island. (±0.4 V, 1 nA).*

### 5.4.1 Extent and reproducibility of edge states

Figure 5-16 (a) shows a height profile across a 7 ML stripe edge and corresponds to the red line of Figure 5-14 (c). The line profile spans an approximate distance of 2.5 nm into the 7 ML stripe. A black dashed line acts as a guide to the eye, indicating the start of the stripe edge. Red and green dashed lines indicate the distances inside the stripe up to which features related to the edge states are identified. Figure 5-16 (b) clearly shows that the edge states' intensity peaks at the stripe edge slope and it remains sharp for an approximate distance of 1 nm into the bulk of the stripe. A gradual decrease in the intensity of edge states is observed which vanishes completely approximately 2 nm into the bulk (green dashed lines).

The gradual decrease in the intensity of 'α' is reminiscent of the exponential decay of Bi[45] (110) edge states with an extent of approximately 2 nm into the island's bulk. The fact that edge states along the 7 ML stripes of $Bi_{1-x}Sb_x$ islands are observed for an approximate distance of 1 nm from the stripe's edge indicates that edge dangling bonds cannot be the only reason for the presence of distinct edge states as shown in Ref[47], but a definitive and clear explanation cannot be given at the moment.

Figure 5-17 shows STS intensity maps extracted from different regions of the same 7 ML stripe edge to understand the dI/dV features' reproducibility. The maps are extracted from the four regions (A-D) marked by the coloured lines in Figure 5-14 (c). All the four STS maps show that the edge states' intensity remains strong for approximately 1 nm from the edge. The energy position of 'α' does not change as well and highlights the reproducibility of the data set.

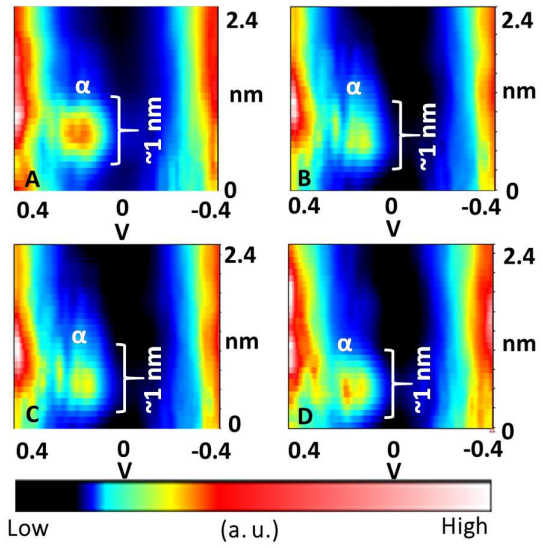


*Figure 5-17 LDOS intensity plots corresponding to four different regions (A, B, C, D) drawn perpendicular to the 7 ML stripe of Figure 5-14 (c).*

The origin of 'α' state along the 7 ML stripe edges of $Bi_{1-x}Sb_x$ islands can be understood in more detail by comparing with the band structure calculations of similar edge states. Having shown earlier in chapter 3 that the general morphology and lattice structure of $Bi_{1-x}Sb_x$ islands on HOPG is similar to that reported for pure Bi[45,98,99] (110) islands on HOPG, a comparison of the experimental dI/dV results on $Bi_{1-x}Sb_x$ island edges with band structure calculations for the edges of pure Bi (110) islands is discussed briefly in the next section.

## 5.5 Thickness dependence and comparison with Bi (110) edge states

This section presents the comparison between the edge states for different thicknesses of $Bi_{1-x}Sb_x$ islands with the experimental results for pure Bi[124,45] (110) islands on HOPG. The discussion is started by comparing the edge state results obtained for 7 ML stripe edges, followed by brief discussions on the edge states of 5 ML bases and concluded with a short discussion on 3 ML $Bi_{1-x}Sb_x$ edge states.

### 5.5.1 7 ML edge states

The unavailability of experimental results and band structure calculations for the edge of a 6 ML thick Bi (110) island prevents a direct comparison of the 7 ML edge states of $Bi_{1-x}Sb_x$ islands and the results are instead compared with the band structure results of 2 ML edge states of pure Bi (110) islands reported in Ref[45]. Figure 5-18 (a-b) shows a comparison between the experimental dI/dV spectrum of a 7ML stripe edge of a $Bi_{1-x}Sb_x$ island and band structure calculations corresponding to an

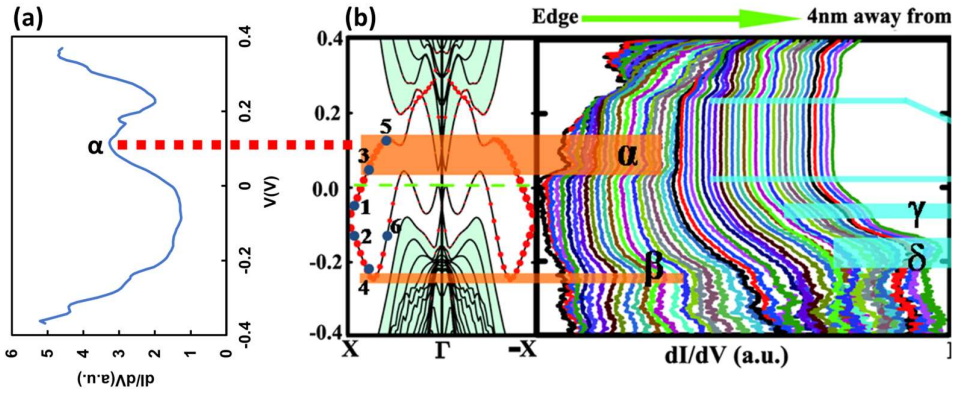


*Figure 5-18 (a) A plot showing dI/dV spectrum extracted from a 7 ML stripe of a $Bi_{0.76}Sb_{0.24}$ island. (b) DFT calculated band structure calculations and experimentally acquired dI/dV spectra for a 6 nm wide Bi (110) nanoribbon along with the experimental dI/dV spectra, both of which are reproduced from[45].*

edge of a 2 ML thick Bi (110) island, reported in Ref[45]. Figure 5-18 (a) is a dI/dV spectrum corresponding to a 7 ML stripe edge of a $Bi_{0.76}Sb_{0.24}$ island shown earlier in Figure 5-14 (c). Figure 5-18 (b) consists of two separate panels, in which the left panel shows the DFT[138] calculated band structure calculated for a 6 nm wide Bi (110) nanoribbon and the right panel of Figure 5-18 (b) shows successive dI/dV spectra extracted perpendicular to a 2 ML Bi (110) edge, spanning a distance of 4 nm into the bulk of the island. The edge states in the band structure in the left panel are indicated by red circles and the bulk electronic states are shaded in green. The odd number of crossings of the edge states between X and Γ point is consistent with the idea of non-trivial[18,25] topological nature of edge states.

The dI/dV spectra in the right panel of Figure 5-18 (b) comprises four distinct LDOS features, namely, 'α', 'β', 'γ' and δ which correspond to high LDOS in the electronic band structure. The 'α' state has a high intensity closest to the island edge and vanishes completely at an approximate distance of 4 nm into the island. The 'β' state is weak and merges with the bulk bands with increasing distance from the edge. The 'γ' and 'δ' states appear approximately 4 nm away from the edge and correspond to the bulk bands and is different to the extent of 2 nm observed for $Bi_{1-x}Sb_x$ 'α' state (Figure 5-16 (a)).

The results from Ref[45] in Figure 5-18 (b) shows that the 'α' feature in the experimental results of Bi (110) islands on HOPG arises as a result of edge states in the band structure. Having established earlier that the 'α' state corresponding to the 7 ML stripe edges of $Bi_{1-x}Sb_x$ islands is a distinct feature, a red dashed line is drawn in Figure 5-18 (a-b) to compare the energy positions of the two different (Bi and $Bi_{1-x}Sb_x$) 'α' states, both of which clearly show a good agreement. The weak intensity of rest of the dI/dV spectra features of $Bi_{1-x}Sb_x$ edges prevents a detailed comparison with the β', 'γ' and 'δ' features of Bi[45] (110) edges.

### 5.5.2 5 ML edge states

Figure 5-19 (a) and (b) show topographies of $Bi_{1-x}Sb_x$ islands with 5 ML high bases, acquired during 50 K CITS measurements in the bias range of ±1 V and ±0.4 V respectively. Both the islands comprise narrow 7 ML stripes at the bottom of the images and in general have the typical wedding cake (Chapter 3) like structures. The coloured squares mark five different regions along the 5 ML base edges, from where, dI/dV spectra are extracted, analysed and shown in Figure 5-20 (a-b).

Figure 5-20 (a) shows the representative, vertically offset dI/dV spectra extracted from the regions marked by coloured squares in Figure 5-19 (a). All the five dI/dV spectra are a result of 8 spatially averaged individual curves and pre-filtered with the methodology described earlier in section 2.4. All the five spectra show a weak dI/dV feature (shoulder) around +0.1 V, a feature that is speculated to be characteristic of 7 ML edge states. The reproducibility of the remaining features, both

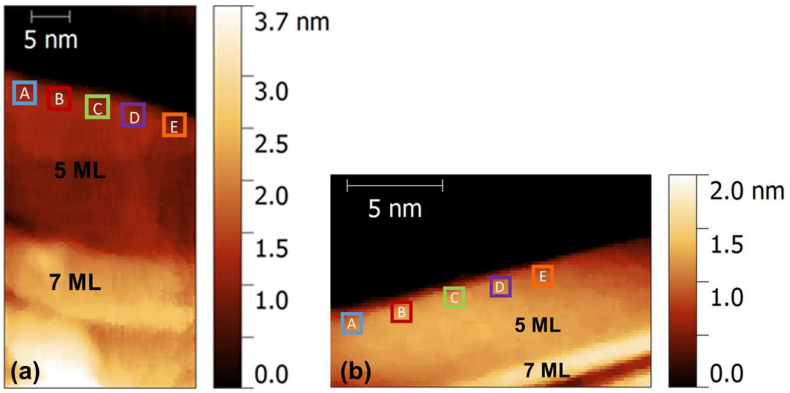


*Figure 5-19 (a) Topography of a $Bi_{0.87}Sb_{0.13}$ island with a 5 ML base acquired during a 50 K CITS measurement in ±1 V bias range (b) Topography of a $Bi_{0.76}Sb_{0.24}$ island acquired during a 50 K CITS measurement in ±0.4 V bias range. The coloured squares on each of the two islands represent the regions along the 5 ML base edges from where dI/dV spectra corresponding the edges are extracted and shown in Figure 5-20.*

in the positive and negative bias regions is debatable and difficult to establish at the moment. A better understanding of 5 ML edge states will be developed by comparing with the results reported for the 5 ML base edges of pure Bi[45] (110) islands in Figure 5-21.

Figure 5-20 (b) shows representative, vertically offset dI/dV spectra extracted from the regions marked by coloured squares in Figure 5-19 (b). All the dI/dV spectra are representative of the 5 ML edge dI/dV spectra acquired in ±0.4 V bias range. The feature around +0.1 V is again not distinctly identifiable in any of the spectra, much in contrast, to the strong 'α' feature identified for the 7 ML

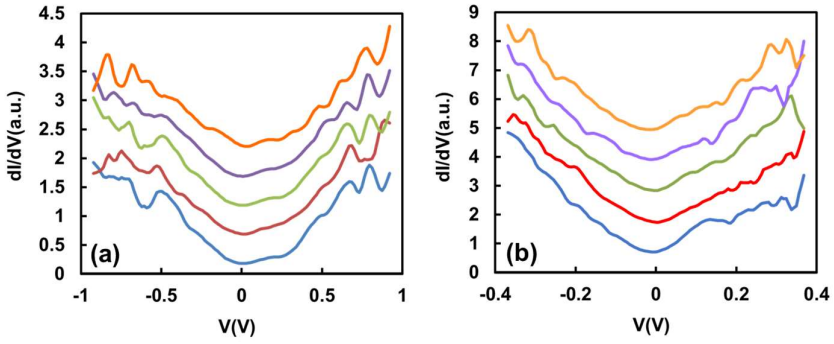


*Figure 5-20 (a) shows vertically offset (+0.5) dI/dV spectra corresponding to edge states of a 5 ML base for the island shown in Figure 5-19 (b) shows vertically offset (+1) dI/dV spectra corresponding to the edge states of the 5 ML base island shown in Figure 5-19.*

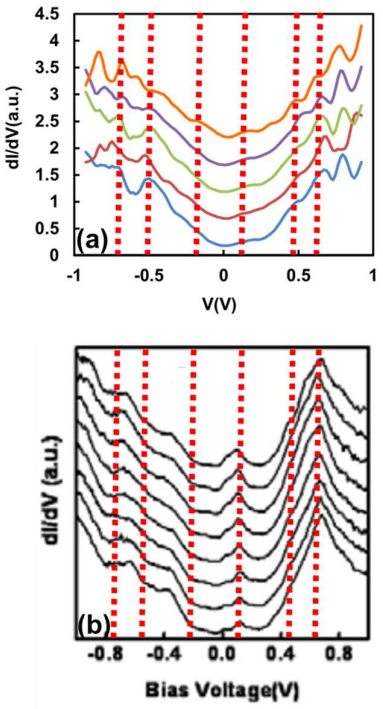


*Figure 5-21 shows a comparison between the 5 ML base edge states of (a) $Bi_{1-x}Sb_x$ islands and that of (b) pure Bi (110) islands, reproduced from[45]. The major dI/dV features are aligned by red dashed lines, which show a reasonable agreement.*

stripe edges in ±0.4 V bias range. In addition to the low intensity of 'α', all the five dI/dV spectra show differences in the positions of the key dI/dV features, rendering it difficult to judge data set's reproducibility.

Figure 5-21 (a-b) shows a comparison between the representative dI/dV spectra of 5 ML base edge states of $Bi_{1-x}Sb_x$ and pure Bi (110) islands (reproduced from Ref[45]), both of which are acquired in the same bias range of ±1 V. Figure 5-21 (a) is the same plot as shown previously in Figure 5-20 (a) and Figure 5-21 (b) shows the reproduced[45] plot of 5 ML edge states of pure Bi (110) islands. Red dashed lines drawn on top of each of the plots indicate positions of the major features for both of the dI/dV spectra plots. Three major features (+0.1, +0.5 and +0.7) V are identified in the positive bias region and three major features (-0.3, -0.6 and -0.8) V in the negative bias region as well in both the plots. As demonstrated by the red lines, a reasonable agreement is noted in the positions of the major features of 5 ML edge states of pure Bi and $Bi_{1-x}Sb_x$ islands, although a more detailed investigation is required and will be pursued in the future.

### 5.5.3 3 ML edge states

The 3 ML bases of $Bi_{1-x}Sb_x$ islands did not show the presence of distinct and identifiable edge states, a result consistent with the discussion about the low conductance along the 3 ML edges as described earlier in the conductance maps (section 5.2.1). The reason for low conductance along the 3 ML base edge states is not well understood at the moment and will be addressed in future CITS measurements.

## 5.6 Anomalous states

Apart from the typical edge states, additional electronic states have been observed in the CITS conductance maps of a select few $Bi_{1-x}Sb_x$ islands. The additional states tend to localize inside the 5 ML bases and in close proximity to the 7 ML stripe edges. To understand the characteristics of the additional states, CITS datasets acquired in different bias ranges on a select few $Bi_{1-x}Sb_x$ islands are discussed in the next two sections.

### 5.6.1 Anomalous states in ±0.4 V bias range

Figure 5-22 (a-b) shows one such 50 K CITS result acquired on a $Bi_{0.76}Sb_{0.24}$ island with a 5 ML base. It is clarified here that the data set is the same one as shown earlier in Figure 5-19 (b). Figure 5-22 (a) shows the island's topography, comprising one straight 7 ML stripe (bottom right corner) on top of a flat 5 ML base. A green line is drawn across the island topography in (a) to indicate the region from where the STS intensity map (shown later in Figure 5-24 (a)) and bias dependent line profiles (shown later in Figure 5-27) are extracted and analysed.

Figure 5-22 (b) shows the corresponding conductance map (120 mV) of the island in which a distinct additional state (red arrow) is identified. The 5 ML base edge states are difficult to distinguish from the higher background conductance of HOPG and are consistent with the conductance maps

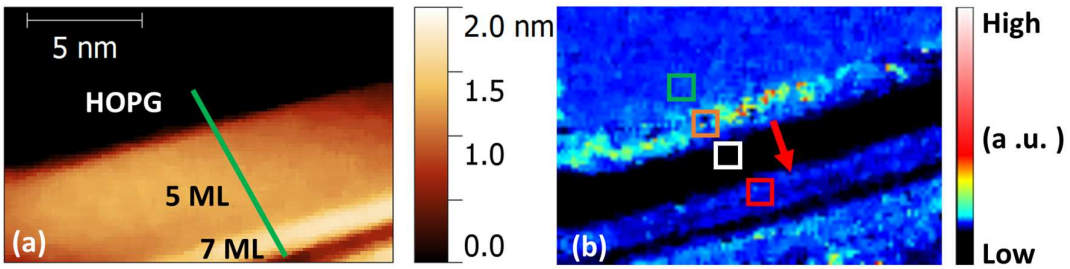


*Figure 5-22 (a) Topography of a 50 K CITS result obtained on a 5 ML base $Bi_{0.76}Sb_{0.24}$ island, in which anomalous high conductance is observed in close proximity to the 7 ML stripe edge as seen in the corresponding conductance map of (b) Imaging parameters: bias range (±0.4 V), setpoint current (1 nA).*

shown earlier in section 5.5.2. The 7 ML stripe edge states are observed to continue along the entire length of the 7 ML stripe; although the edge state tends to extend further away from the stripe's topographic edge. This extent of edge states beyond the topographic edge is not well understood at the moment and is not focused upon further here.

The darker region inside the island corresponds to lower conductance of the 5 ML base. It is inside this region that the additional bright state (red arrow) is observed a few (~2) nm away from the 7 ML stripe edge. This additional state is called anomalous primarily because of the location, as it is not associated with an edge and instead is localized inside the 5 ML base; an interesting result in itself.

### 5.6.2 Anomalous states in ±1 V bias range

Figure 5-23 (a-b) shows the topography and conductance map of a 50 K CITS dataset of a $Bi_{0.87}Sb_{0.13}$ island, where (a) is the island's topography and (b) is the corresponding conductance map. The island topography has been shown earlier in Figure 5-19 and therefore, not described again. The conductance map shows the presence of the typical 5 ML base and 7 ML stripes edge states, which are consistent with the previous descriptions of 5.2.1. In addition to the typical edge states, an additional, anomalous state (red arrow) is again observed inside the 5 ML base and in close proximity to the 7 ML stripe edge. At first sight, the nature of the anomalous state of the (±1 V) CITS data set appears similar to that observed in the data set of Figure 5-22 (a-b).

### 5.6.3 Location of the anomalous state

Figure 5-24 (a) shows the height profile corresponding to the green line drawn in Figure 5-22 (a) demonstrating the typical wedding cake like structure observed for $Bi_{1-x}Sb_x$ islands (Chapter 3). The

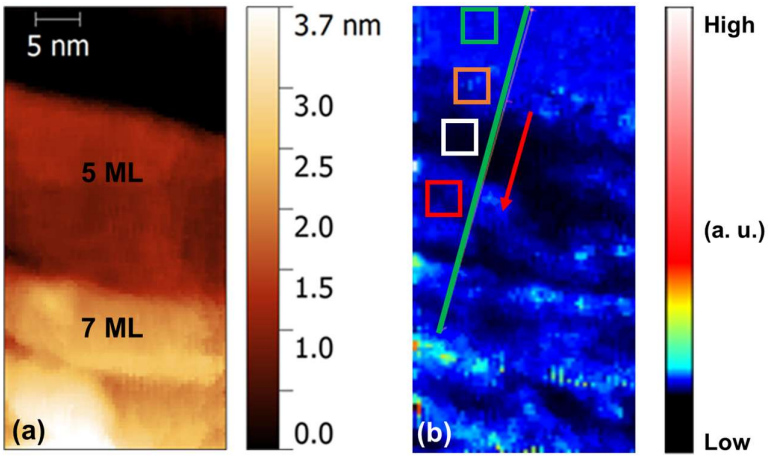


*Figure 5-23 (a) Topography of a $Bi_{0.87}Sb_{0.13}$ island, acquired during a 50 K CITS measurement in ± 1 V bias range. (b) Shows the corresponding conductance map (120 mV) in which an anomalous electronic state (red arrow) is observed in addition to the typical 5 ML and 7 ML edge states. Bias range (±1 V), setpoint current (1 nA).*

dashed red line corresponds to the 5 ML base edge, the dashed green line to the location of the anomalous state and the dashed black line to the 7 ML stripe edge. Figure 5-24 (b) shows the corresponding STS intensity map to the red line of Figure 5-22 (a). Dashed lines in the STS intensity map correspond to the corresponding states described in Figure 5-24 (a).

High conductance is observed along the 5 ML base edge (red dashed line), much of which is indistinguishable from HOPG and is followed by the low conductance region of the 5 ML base up to 6 nm into the island. At this point inside the 5 ML base, higher conductance corresponding to the anomalous state is observed. As seen in Figure 5-24 (b), the anomalous state (green dashed line) does not correspond to any topographic feature in Figure 5-24 (a), indicating clearly that it is not associated with an edge and therefore, has a different origin. Moving further along in the STS map, the characteristic 'α' feature is identified again whose position corresponds with the 7 ML stripe edge (black dashed line) and is consistent with the discussion of section 5.4.

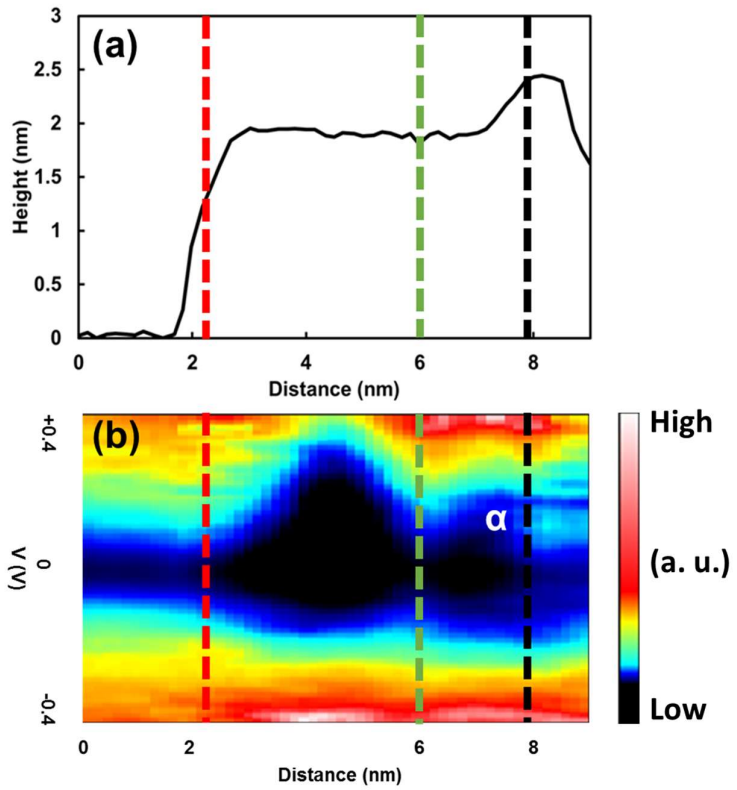


*Figure 5-24 (a) A height profile across the 5 ML base $Bi_{0.76}Sb_{0.24}$ island, showing the typical wedding cake like structure (b) An STS intensity map corresponding to the height profile of (a).*

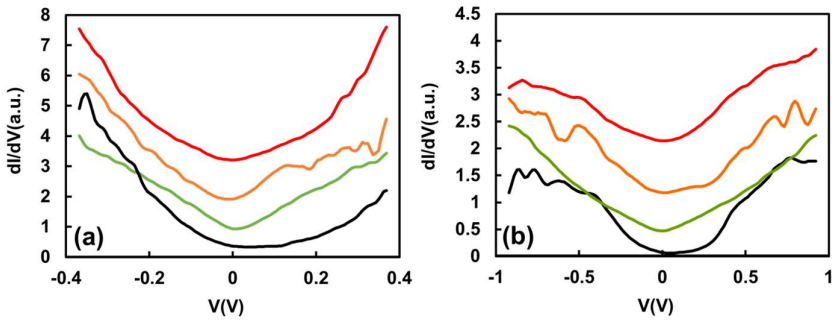


*Figure 5-25 (a) Vertically offset (+0.2) dI/dV spectra extracted from the CITS dataset (±0.4 V) shown in Figure 5-22 (b), where black represents 5 ML base, green represents HOPG, orange represents the 5 ML base edge state and red represents the anomalous state. (b) Vertically offset dI/dV spectra extracted from the CITS dataset (±1V) shown in Figure 5-23 (b), where the different colours represent the same regions as that described for (a). Each of the dI/dV spectra shown here are a result of spatially averaged 8 individual curves.*

The discussion is summarized by stating that the anomalous state is observed inside the 5 ML base in both the CITS datasets and in close proximity to the straight 7 ML stripe edges (see Figure 5-23 (b) and Figure 5-24 (b)) for reference.

## 5.6.4 dI/dV spectra analysis

### 5.6.4.1 Anomalous state in ±0.4 V bias range

Figure 5-25 (a) shows a comparison between the dI/dV spectra [spatially averaged 8 individual curves] extracted from the areas of interest (marked) in the CITS dataset shown in Figure 5-22 (a-b). All the spectra are vertically offset (+0.2) for clarity and as seen clearly, the dI/dV spectra of HOPG (green) shows the typical 'V-shape' reported for HOPG[158], the 5 ML base dI/dV spectra (black) shows a wider valley and is essentially devoid of any distinct dI/dV features. The dI/dV spectra of the 5 ML base edge state (orange) shows a weak feature around +0.1 V, consistent with the earlier discussion of Figure 5-20 (b) in section 5.5.2. In contrast, a weak dI/dV feature is observed at approximately +0.3 V for the anomalous state (red) with the rest of the spectra being largely featureless.

### 5.6.4.2 Anomalous state in higher bias range (±1 V)

Figure 5-25 (b) shows a comparison between the dI/dV spectra [spatially averaged 8 individual curves] corresponding to the CITS data set acquired in ±1 V bias as shown in Figure 5-23 (a-b). All the spectra are vertically offset (+0.2) for clarity and extracted from the regions marked by coloured squares in Figure 5-23 (b). As can be seen clearly from the plot, the 5 ML base spectra (black) again

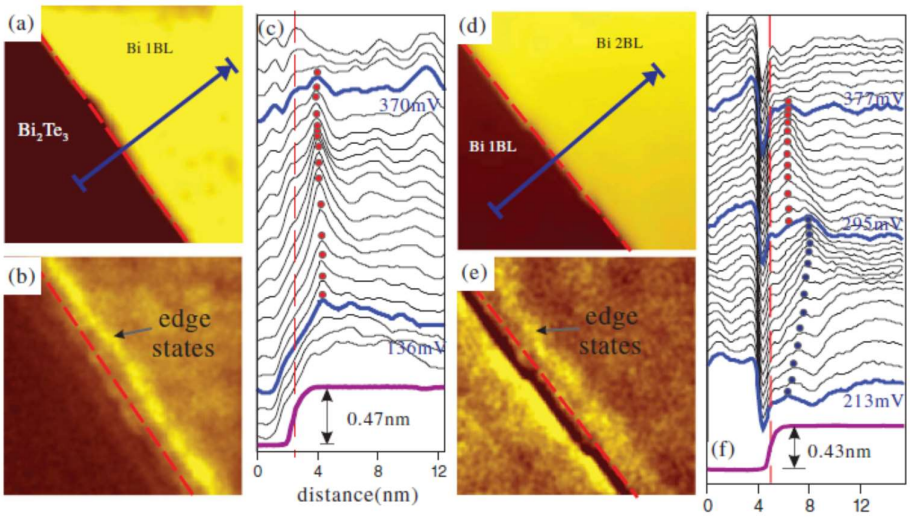


*Figure 5-26 (a) STM image of a step edge of Bi (111) 1 BL on $Bi_2Te_3$ (b) shows the corresponding conductance map at +283mV (c) Bias dependant line profiles of the conductance map drawn along line profile (blue) (d) STM image of a step edge between 1 BL of Bi (111) and 2 BL of Bi (111). ($V_t$ = 1V, $I_t$ = 300pA). (e) STS map at +338mV corresponding to (d). (f) Profiles of STS maps together with a STM line scan taken along the arrowed blue line in (d) Images reproduced from[47].*

shows a wide valley near the Fermi level as noted for the spectra in the ±0.4 V bias range. The HOPG dI/dV spectra (green) shows the typical V-shape associated with HOPG and is again consistent with the spectra of ±0.4 V CITS dataset (Figure 5-22). The 5 ML base edge state dI/dV spectra (orange) is extracted from Figure 5-23, which has previously been shown to be similar and consistent with the characteristics of 5 ML edge states of pure Bi (110) islands on HOPG. The anomalous state dI/dV spectra (red) is essentially featureless, although two weak shoulders at approximately +0.4 and -0.5 V are identified.

The low intensity of the dI/dV features for the anomalous state in either of the two bias ranges discussed in this section renders it difficult to conclude about their dI/dV characteristics and acquisition of more CITS datasets is considered necessary to reliably map anomalous states' spectroscopic nature, although, a different analysis approach for the anomalous states is presented in the next subsection by comparing the results reported[47] for Bi (111) islands.

### 5.6.5 Comparison with literature

Yang et al[47] report the observation of electronic states localized in close proximity to the edges of Bi (111) islands, when grown on $Bi_2Te_3$. Figure 5-26 (a) shows the topography of a 1 BL Bi (111) layer grown on $Bi_2Te_3$. A red dashed line marks the boundary of the Bi island and is used to correlate the

location of the edge states observed in the conductance map of Figure 5-26 (b). The conductance map (+283 mV) clearly demonstrates the presence of an edge state away from the island's step edge and is indicated by a blue arrow. As can be seen from the conductance map, the edge state does not align with island's step edge and is rather localized further inside the island, a result confirmed by the bias dependent line profiles shown in Figure 5-26 (c). The red dots mark the position of the edge state localized away from the island edge, which does not show any shifts in the peak position as a function of bias, i.e. it is a bias independent edge state. The independent nature of the above described edge states is argued in Ref[47] as an experimental evidence for a protected edge state.

Observation of similar edge states is evidenced on a 2 BL Bi (111) island, when grown on a 1 BL Bi (111) island as shown in Figure 5-26 (d-e). The results are confirmed by the corresponding bias dependent line profiles shown in Figure 5-26 (f), in which two different types of edge states are identified. The peak positions of the two edge states are indicated by blue and red dots. The edge state marked by blue dots shows shifts in the peak positions as a function of bias, in contrast to the edge state marked by the red dots, which shows no noticeable shift as a function of bias.

#### 5.6.5.1 Bias dependent line profiles for $Bi_{1-x}Sb_x$ anomalous states

To analyse the characteristics of the anomalous state in more detail, bias dependent line profiles, similar to that for Bi (111) islands shown in Figure 5-26 are extracted from the two CITS data

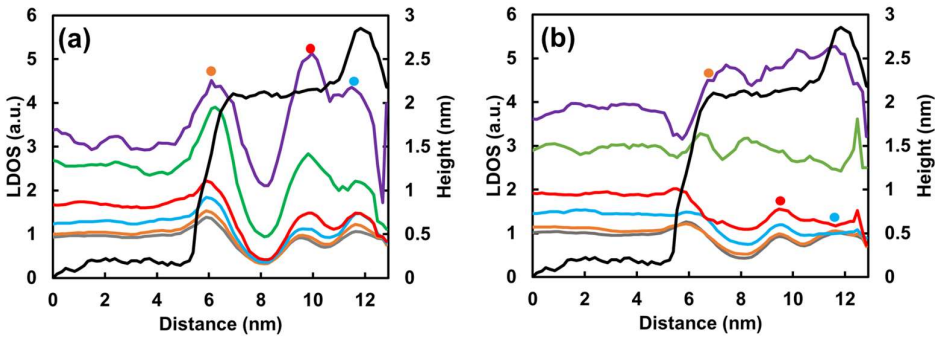


*Figure 5-27 (a) Bias dependent (positive) line profiles plotted as a function of distance along the 5 ML edge of the $Bi_{0.76}Sb_{0.24}$ island shown in Figure 5-22 and correspond to (15, 35, 75, 120, 250 and 350) mV from bottom to top (b) Bias dependent (negative) line profiles plotted as a function of distance along the 5 ML edge of the $Bi_{0.76}Sb_{0.24}$ island shown in Figure 5-22 and correspond to (-15, -35, -75, -120, -250, -350) mV from bottom to top. In both the plots, orange dots indicate 5 ML base edge states, red dots indicate anomalous states and blue dots indicate the 7 ML stripe edge states. The black profile in each of the two plots ((a) and (b)) represents height of the selected regions and are plotted on right-hand side y axes.*

sets discussed earlier in this section. Figure 5-27 (a-b) shows the bias dependent line profiles, plotted as a function of distance, corresponding to the green line in Figure 5-22 (a). Figure 5-27 (a) shows positive bias line profiles and Figure 5-27 (b) shows bias dependent line profiles corresponding to the negative bias range. The corresponding heights of the edges are plotted on the right hand side vertical axes and denoted by black lines in each of the two plots. In both the plots, orange dots indicate 5 ML base edge states, red dots indicate anomalous states and blue dots indicate the 7 ML stripe edge states

The line profiles corresponding to the positive bias (Figure 5-27 (a)) demonstrate that the intensity of the anomalous state (red dot) remains high within the bias range [15 (grey) to 350 (purple)] mV as compared to the intensity of 7 ML stripe edge states (blue dot), which demonstrates an increase in the intensity up to 120 mV (red) and decreases up to 350 mV (purple). The intensity of the 5 ML edge state is low up to 120 mV (red) and the conductance appears to submerge with the background conductance of HOPG. The line profiles corresponding to 250 (light green) and 350 mV (purple), on the other hand, demonstrate an increased conductance intensity, a result that is not well understood. Importantly, no movement in the peak positions of the anomalous state is observed as a function of bias, within the above-discussed bias range.

The line profiles corresponding to the negative bias (Figure 5-27 (b)) on the other hand demonstrate weak intensity for the 7 ML edge state within the bias range [-15 (grey) to -350 (purple)] mV, consistent with the dI/dV spectra described earlier in 5.2.2. The overall conductance intensity of the anomalous state is observed to be low within the chosen bias range and diminishes completely at -250 mV (light green). The conductance intensities of 5 ML base edge states remain considerably low up to -120 mV (red) and thereafter, show a slight increase in the intensity around -250 mV (light green) and -350 mV (purple) and the trend is not understood well.

Figure 5-28 (a-b) shows bias dependent line profiles corresponding to the green line drawn in Figure 5-23. Figure 5-28 (a) shows positive bias line profiles and Figure 5-28 (b) shows negative bias line profiles. The corresponding heights (black profile) of each of the edges is plotted on the secondary vertical axes The line profiles corresponding to the positive bias in Figure 5-28 (a) demonstrate that the intensity of the anomalous state is relatively low between 35 mV (dark green) and 75 mV (orange) and thereafter, shows an increase in the intensity up to 350 mV (brown), eventually fading away completely around 500 mV (maroon). The 7 ML stripe edge state again shows high intensity up to approximately 120 mV (light blue), before submerging with the conductance of the 7 ML stripe, rendering it difficult to distinguish. The 5 ML edge states, on the other hand, do not demonstrate a clearly defined pattern. The intensity of the 5 ML edge states is higher as compared to the bulk 5 ML region up to 350 mV (brown), although, it remains indistinguishable from the conductance of HOPG

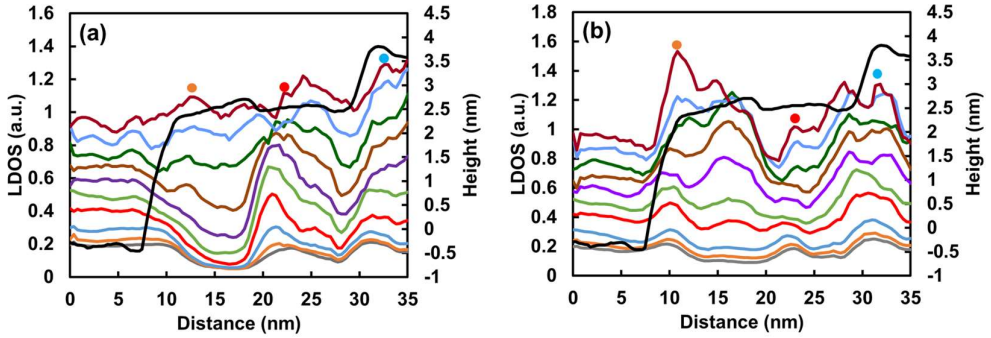


*Figure 5-28 (a) Positive bias dependent line profiles plotted as a function of distance along the 5 ML edge of the $Bi_{0.87}Sb_{0.13}$ island shown in Figure 5-23 and correspond to (35, 75, 120, 200, 250, 300, 350, 400, 450 and 500) mV from the bottom to the top. (b) Negative bias dependent line profiles plotted as a function of distance along the 5 ML edge of the $Bi_{0.87}Sb_{0.13}$ island shown in Figure 5-23 and correspond to (-35, -75, -120, -200, -250, -300, -350, -400, -450 and -500) mV. In both the plots, orange dots indicate 5 ML base edge states, red dots indicate anomalous states and blue dots indicate the 7 ML stripe edge states. The black profile in each of the two plots ((a) and (b)) represents the height of the selected region and are plotted on right-hand side y axes.*

within the discussed bias range. The peak of the 5 ML edge state shows slight shifts and does not align perfectly with the island edge.

The line profiles corresponding to the negative bias in Figure 5-28 (b) demonstrate that the intensity of the anomalous state shows subtle variations and a clearly defined pattern is missing. The line profiles up to -120 mV (light blue) show a weak conductance peak which tends to weaken further with increasing bias, in addition to an extra peak whose intensity increases steadily up to -450 mV (blue). The 7 ML edge states show a similar and consistent pattern with the lower bias (± 0.4 V) data set of Figure 5-27 (a-b), where the conductance increases steadily up to -120 mV (light blue) and decreases thereafter. The line profiles corresponding to 5 ML base edge states are more distinct as the peaks can be distinguished clearly up to -250 mV (light green), although, without a clear pattern.

Higher-resolution CITS experiments and complimentary band structure calculations are required to understand the nature of the anomalous states in a better manner. The primary focus of future experiments will be on identifying the precise location of anomalous states and mapping their evolution as a function of island's topology. A significant focus will be on understanding the impact of Sb content on the nature of the anomalous states of $Bi_{1-x}Sb_x$ islands.

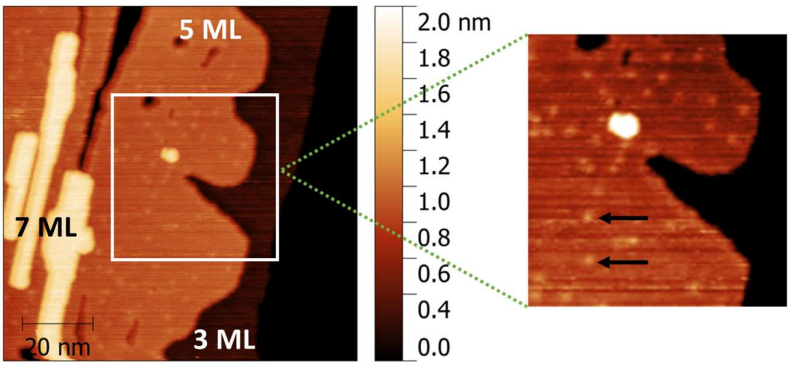


*Figure 5-29 STM image of a 3 ML base $Bi_{0.87}Sb_{0.13}$ island acquired at a low tip sample bias (+0.2 V). Bright spots (black arrows) are observed inside the 5 ML stripe. Imaging parameters: (+0.2 V,1 nA). The inset shows an image of the 5 ML stripe region marked by a white square, where the bright spots can be identified easily.*

## 5.7 Bright spots

This section discusses room temperature STM images and 50 K CITS results of $Bi_{1-x}Sb_x$ islands, in which localized regions of peculiar brightness are identified inside the 5 ML regions (bases and stripes). The presence of these bright regions is noted both in STM images and the CITS conductance maps. The result is interesting as such peculiar bright regions do not appear in pure Bi (110) islands on HOPG[97-99] and are unique to $Bi_{1-x}Sb_x$ alloys. The next two sections describe the morphology and distribution of bright spots.

### 5.7.1 Morphology and distribution of bright spots

Figure 5-29 shows a room temperature STM image of a $Bi_{0.87}Sb_{0.13}$ island with a 3 ML high base. The STM image is acquired with a tip-sample bias of +0.2V and a set point current of 1 nA. The 3 ML high base island comprises a bulgy 5 ML stripe and three small 7 ML stripes (left corner). The edge of 3 ML base is fairly straight but the 5 ML stripe edges are irregular, which is a common feature (section 3.2.2.2) of 5 ML stripes on $Bi_{1-x}Sb_x$ islands. The 7 ML stripes, on the other hand, are more regular and relatively straight.

The inset clearly shows that the 5 ML stripe has randomly distributed bright spots; two such bright regions are indicated by black arrows. The low resolution of the STM image does not allow measurement of the exact size and shape of the bright spots, although it is evident that the spots lack a defined geometry. In addition, the brightness of the spots is not uniform and is similar to the varying spread of LDOS around lattice defect sites[149,159]. It is interesting to note that the 3 ML base and the three 7 ML stripes do not show any noticeable bright spots and they are primarily seen inside the 5

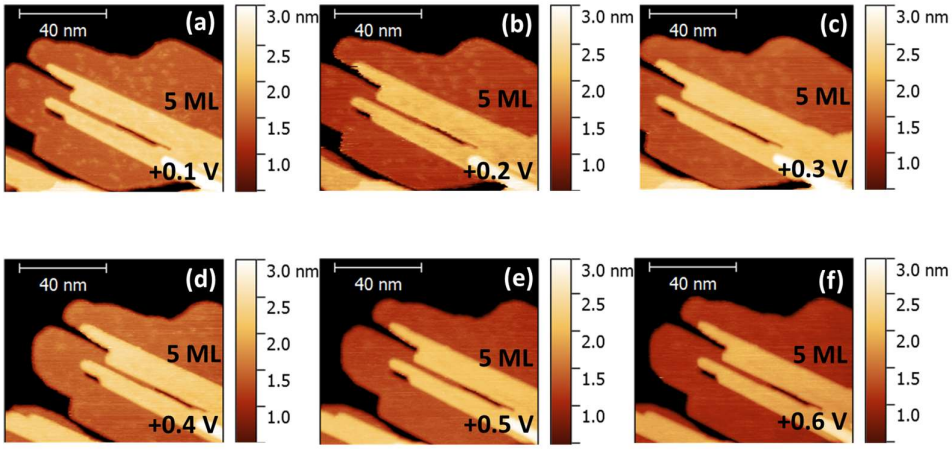


*Figure 5-30 (a-f) The presence of bright spots inside the 5 ML base of a $Bi_{0.87}Sb_{0.13}$ island is verified by altering the tip-sample bias. Lower (+0.1 to +0.4) V tip-sample bias RT-STM images (a-d) show the presence of bright spots which gradually disappear with increasing bias (+0.5 to +0.6) V (e-f). Setpoint current: 1 nA.*

ML stripe. The discussion on bright spots, therefore, is kept limited to 5 ML regions from here on and their observation is verified by bias dependent imaging in the next section.

### 5.7.2 Bias dependence of bright spots

Figure 5-30 (a-f) shows RT-STM images acquired in quick succession on a $Bi_{0.87}Sb_{0.13}$ island with different tip sample bias values. The 5 ML island has an overall compact shape, with a flat base and two straight 7 ML stripes on top. The large area of the 5 ML base allows for a reasonable analysis of the bright spots. Figure 5-30 (a) shows the STM image acquired at a tip sample bias of +0.1 V. The bright spots are present on both the sides of the 5 ML base.

As the tip sample bias is gradually increased, the intensity of the spots starts to decrease as seen in the STM image acquired at +0.2 V (Figure 5-30 (b)), without a decrease in density of the spots. This decrease in the intensity of the spots continues and is clearly evidenced in Figure 5-30 (c) and (d) acquired at +0.3 and +0.4 V respectively. Moreover, the spots' density appears to have reduced considerably in (c) and (d). Figure 5-30 (e) and (f) show STM images acquired at higher bias values of +0.5 V and +0.6 V respectively and clearly the bright spots are no longer seen. The experiment therefore, illustrates that the observation of 5 ML bright spots in STM images is bias dependent and an electronic effect.

A high LDOS centered around +0.1 V for the bright spots can be inferred from the above-discussed results. Low temperature (50 K) CITS measurements are discussed in the next section which further help in verifying this inference.

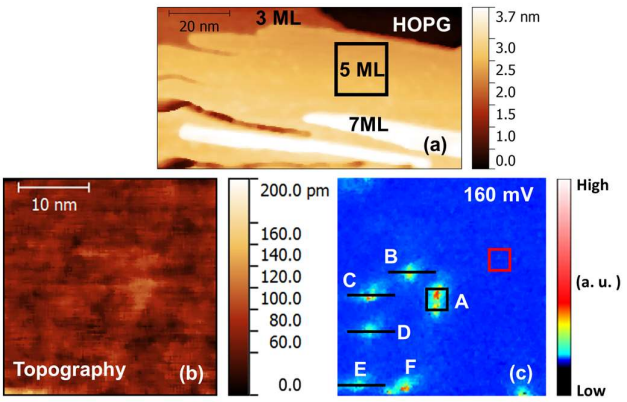


*Figure 5-31 (a) A 3 ML base $Bi_{0.87}Sb_{0.13}$ island with a large 5 ML stripe and two 7 ML stripes on top. A black square marks a region inside the 5 ML stripe, where 50 K CITS data set is acquired. (b) Topography of the 5 ML region acquired during CITS acquisition. (c) Corresponding conductance map at 160 mV showing bright spots. CITS parameters: (±0.3 V, 1 nA).*

### 5.7.3 CITS measurements

Figure 5-31 (a) shows the topography of a large 3 ML base $Bi_{0.87}Sb_{0.13}$ island chosen for a 50 K CITS measurement. The large area of the 5 ML stripe allows the possibility of performing higher resolution CITS measurements (± 0.3 V) on a region with a high density of bright spots and a small region inside the 5 ML stripe (black square) is focused upon. Figure 5-31 (b) shows the topography of the flat 5 ML stripe region. The topography is acquired simultaneously during the CITS data set acquisition with a tip sample bias maintained at -0.3 V and hence it is difficult to locate any bright spots. Figure 5-31 (c) shows the corresponding conductance map at 160 mV in which distinct high conductance is observed at different bright spots labelled as A, B, C, D, E and F.

All the six bright spots show a different spread of the LDOS and the observations are consistent with their irregular morphology (Figure 5-29). The rest of the 5 ML stripe region shows comparatively lower conductance as compared to that of the bright spots. A black square marks the bright spot A and a red square marks a region inside the 5 ML stripe. The two squares highlight the regions from where corresponding dI/dV spectra [spatially averaged 8 curves] are extracted and shown later in Figure 5-35 (b). Four coloured lines are drawn across the different spots (B, C, D and E) and indicate the spots from where STS intensity maps are extracted and shown later in Figure 5-33.

Figure 5-32 (a-f) shows conductance maps at different bias for the data set described earlier in Figure 5-31 (b, c). The first two conductance maps at -120 mV and -35 mV are noisier as compared to the other conductance maps and this is attributed to tip-sample interactions during the measurements. The conductance maps at higher bias, although, clearly show that the brightness of

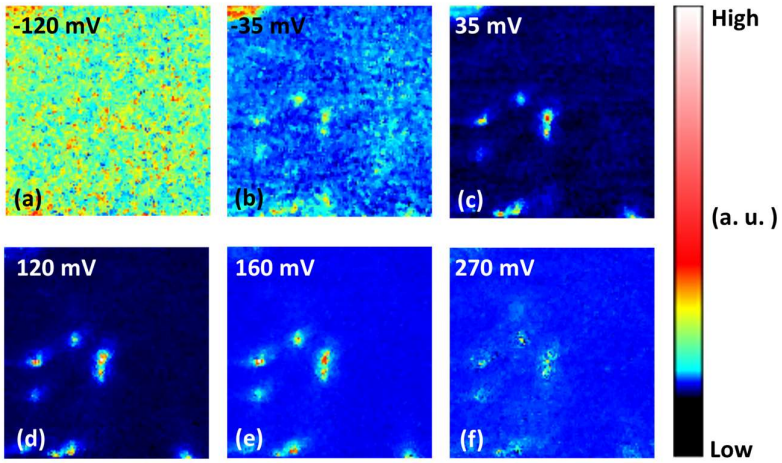


*Figure 5-32 Conductance maps at different bias corresponding to the CITS result on 5 ML spots shown in Figure 5-31 (a-c). CITS parameters: (±0.3 V, 1 nA)*

the spots peaks around 160 mV, complementing the results shown in section 5.7.2, highlighting the high LDOS around +0.16 V for the bright spots. The next two sub sections confirm this result by analyzing the representative dI/dV spectra and the corresponding STS intensity maps.

#### 5.7.3.1 dI/dV spectra

Figure 5-33 (a) shows a comparison between the dI/dV spectra [spatially averaged 8 curves] extracted from spot A (marked by a black square) in Figure 5-31 (c) and the dI/dV spectra [spatially averaged 8 curves] extracted from the bulk 5 ML region (marked by a red square) in Figure 5-31 (c). A strong dI/dV peak at approximately +0.16 V characterizes the spot's dI/dV spectra. The dI/dV spectra of the 5 ML base does not show any distinct features and is essentially featureless. The dI/dV peak at approximately +0.16 V thus confirms the inference (high LDOS around 0.1 V) of sections 5.7.2 and 5.7.3. The dI/dV peak around +0.1 V for the bright spots has a stark similarity to the 'α' state discussed earlier for the 7 ML stripe edges (section 5.2.2).

Figure 5-33 (b) compares the representative dI/dV spectra of bright spots with that of 7 ML stripe edges (section 5.2.2). It is clear that that the two dI/dV spectra are similar to the dI/dV peak around +0.1 V. The slight differences in the two spectra are the respective energy values at which the dI/dV peak is observed. The next section discusses the reproducibility of the +0.1 V state associated with the bright spots by comparing the corresponding STS intensity maps.

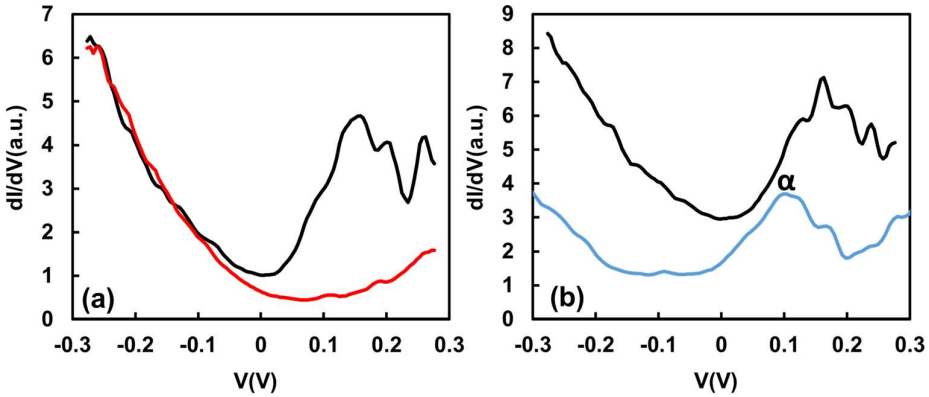


*Figure 5-33 (a) Comparison between the dI/dV spectra corresponding to a bright spot (black) with the corresponding dI/dV spectra of the bulk 5 ML region (red) (b) Comparison of the dI/dV spectra corresponding to a bright spot (black) and that of a 7 ML stripe edge (blue). The spectra in (b) are vertically offset (+2) for clarity.*

#### 5.7.3.2 STS intensity maps

Figure 5-34 shows four STS intensity maps that correspond to the black lines drawn across the bright spots (B, C, D and E) in Figure 5-31 (c). The length of each line is 5 nm, where a bright feature between +0.1 and +0.2 V (high colour intensity) in all the maps corresponds to the peak in dI/dV spectra around +0.16 V is identified. The regions away from the bright spots are considerably darker;

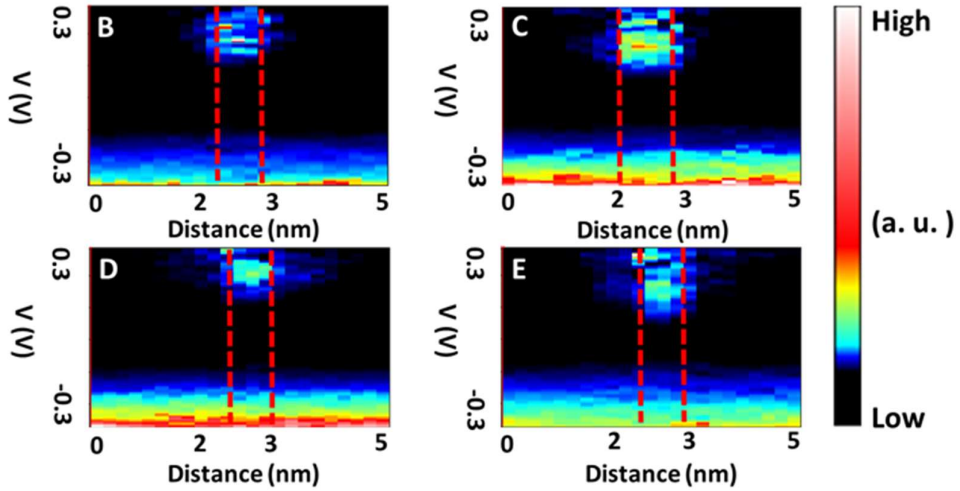


*Figure 5-34 STS intensity plots corresponding to the different spots (B and C) marked in Figure 5-32 (c). A strong intensity at (+160 mV) is observed in all the maps.*

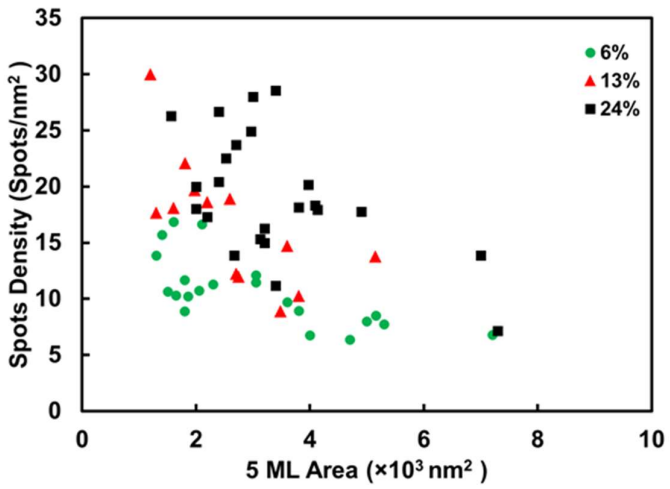


*Figure 5-35 Number density of bright spots plotted for different concentrations of $Bi_{1-x}Sb_x$ islands as a function of the 5 ML area.*

reminiscent of the low conductance of 5 ML regions (section 5.7.3.1). In addition, high conductance is noted near the negative bias values (-0.3 V) in all four maps, however, these features are present in all the CITS measurements for 5 ML regions and are not focused upon further from here on.

Red dashed lines are drawn in the four maps, highlighting the regions up to which the highest intensity of conductance is observed. This representation indicates that a distinct feature appears for the bright spots around +0.1 V. This difference in conductance intensities is attributed to local LDOS perturbations around defect sites[132,160]. The results shown in this section establish that the bright spots observed inside 5 ML regions of $Bi_{1-x}Sb_x$ islands are dependent on the tip sample bias (i.e. electronic effect) and show a peak around +0.1 V in the dI/dV spectra; similar to that for the 7 ML stripe edges (section 5.2.2). The next subsection builds on this knowledge and discusses the impact of Sb and the 5 ML area on the bright spots.

### 5.7.4 Concentration dependence

This section briefly shows the analysis on the evolution of bright spots for different $Bi_{1-x}Sb_x$ concentrations as a function of the 5 ML area. The motivation for this analysis is primarily to understand the role of Sb in the manifestation of bright spots. The approach involves statistical analysis (number density) of the bright spots.

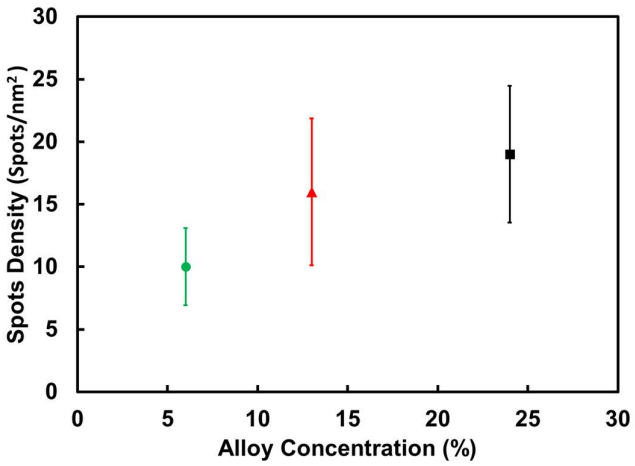


*Figure 5-36 Average number density of bright spots as a function of Sb content in $Bi_{1-x}Sb_x$ islands, where the colours of the three datapoints is kept the same as that for different concentrations in Figure 5-35.*

#### 5.7.4.1 Number Density

Figure 5-35 shows the number of bright spots per unit area (number density) for different $Bi_{1-x}Sb_x$ concentrations as a function of the 5 ML region. Both, 5 ML stripes and bases are included in this analysis and the data sets are extracted only from the STM images acquired with a low tip sample bias (+0.2 V). The analysis shows that the number density increases slightly with increasing Sb content, however, no clear and definitive dependence of the bright spots is observed as a function of the area of 5 ML region.

The trend is summarized in Figure 5-36 which shows that the spot's number density increases by approximately a factor of 2 when the Sb concentration is increased by a factor of 4, but these changes are barely larger than the uncertainties in the number densities and does not clearly indicate the role of Sb in the cause of bright spots. The next section builds on this analysis and discusses the relevant literature studies.

### 5.7.5 Discussion

This discussion aims to understand the appearance of bright spots in $Bi_{1-x}Sb_x$ islands by comparing with the relevant literature. Two key STM results of the recently published[159] work on $Bi_2Se_3$ nanostructures are discussed.

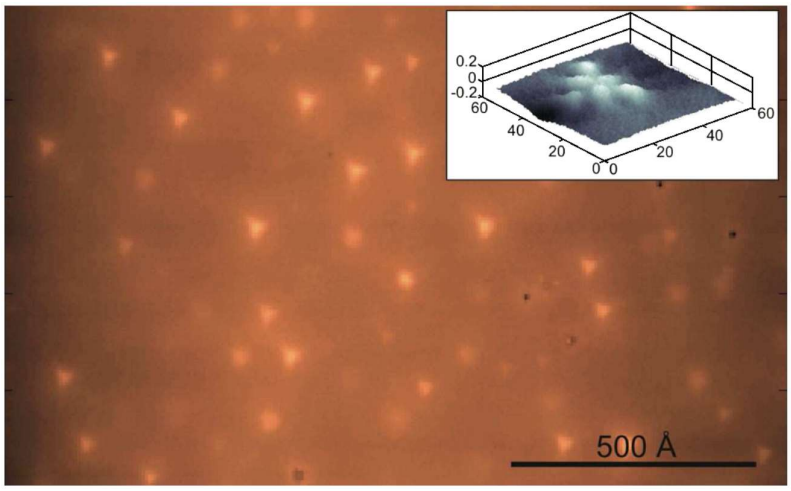


*Figure 5-37 Topography of an undoped $Bi_2Se_3$ surface showing triangular shaped defect sites, expected to be sub-surface Se vacancies. The intensity of the defect sites is not uniform and show a variation from region to region. Inset shows a three dimensional STM image of one of the triangular shaped defects. Image reproduced from[159].*

#### 5.7.5.1 Vacancy defect sites: Un-doped $Bi_2Se_3$

Isolated and randomly distributed bright triangular regions were observed[159] on the surface of un-doped $Bi_2Se_3$, as seen in the STM image of Figure 5-37. The triangular defects have different brightness which is argued[159] to be the response of Se vacancy defect sites buried in different layers beneath the top $Bi_2Se_3$ surface. The result at first sight, is similar to that observed for $Bi_{1-x}Sb_x$ bright spots (section 5.7.1) as both the results demonstrate a random spatial distribution.

Figure 5-38 (a-d) shows STM measurements[159] on a small region of the $Bi_2Se_3$ surface which is populated with triangular defects with different intensities. Figure 5-38 (a) shows the topography in which, analysis is concentrated upon two triangular defects of different intensities (white squares). Figure 5-38 (b) shows the corresponding conductance map at 90 meV (bulk conduction band) in which enhanced LDOS intensity is observed at both the triangular defect sites. Figure 5-38 (c) shows the corresponding conductance map at -180 meV (bulk valence band) showing reduced LDOS intensity around the two triangular defects, where, instead, additional LDOS features (resonance states)[161] are observed around the defects (marked). The last conductance map at -400 meV (bulk valence band) shows that the LDOS intensity around the triangular defects is completely suppressed. It is argued in Ref[159] that the increase in LDOS intensity of the triangular defects inside the bulk conduction band (Figure 5-38 (c)) renders the defects as positively charged. In addition, the compact shape of triangular defects is used to infer the results as a local LDOS lattice perturbation[6].

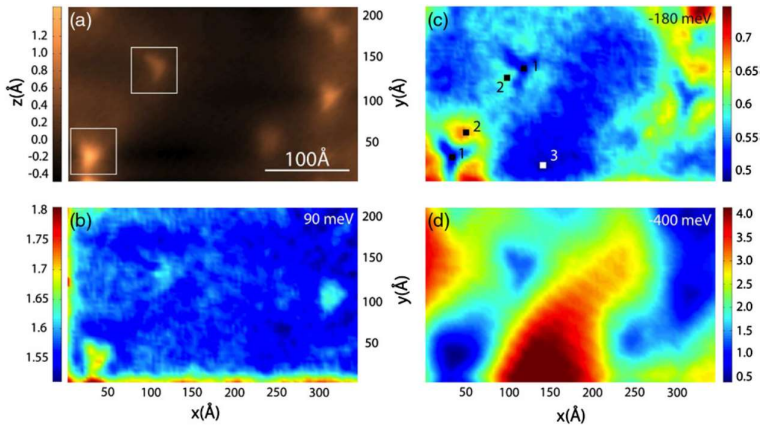


*Figure 5-38 (a) Topography of a small region on the $Bi_2Se_3$ surface, populated with triangular defects of different intensities. (b-d) Selected conductance maps at different bias showing variation in conductance around the defect sites. Image reproduced from[159].*

The varying LDOS intensities of the Se vacancy defects (STM images and conduction maps) for $Bi_2Se_3$ are in principle, similar to the spatially varying LDOS intensities of $Bi_{1-x}Sb_x$ bright spots, indicating that the vacancy type defects might be a probable cause of the $Bi_{1-x}Sb_x$ bright spots.

#### 5.7.5.2 $Sb_4$ Clusters: Sb doped $Bi_2Se_3$

The impact of Sb doping on the $Bi_2Se_3$ surface[159] is shown in Figure 5-39 (a-d). The presence of a bright protruding feature in the topography (Figure 5-39 (a)), assumed to be a $Sb_4$ cluster[133,162,163] is identified. As it can be seen, the shape of the $Sb_4$ cluster is not compact like that of the triangular Se vacancy defects discussed previously and is rather an extended defect. Figure 5-39 (b-d) show the bias dependent conductance maps showing the LDOS intensity variation associated with the $Sb_4$ cluster, where (b) and (d) are the conductance maps acquired at 75 meV (bulk conduction band) and -440 meV (bulk valence band) respectively. A careful look shows suppressed LDOS intensities are noted around the vicinity of $Sb_4$ cluster site in both the conductance maps of (b) and (d). It is clearly visible that there are suppressed conductance intensities (dark blue) in (b) and (d) panels of Figure 5-39, which correspond exactly with the $Sb_4$ cluster site (light brown) shown in panel (a) of Figure 5-39.

Figure 5-39 (c) shows conductance map at -225 meV (inside bulk band) which is characterized by a greater spatial LDOS spread around the $Sb_4$ cluster and it is seen clearly that the conductance intensity decreases with increasing distance from the cluster's centre. This broad LDOS spread related with $Sb_4$ clusters is not well understood in Ref[159], although it is argued to unlikely to be a lattice defect induced LDOS perturbation.

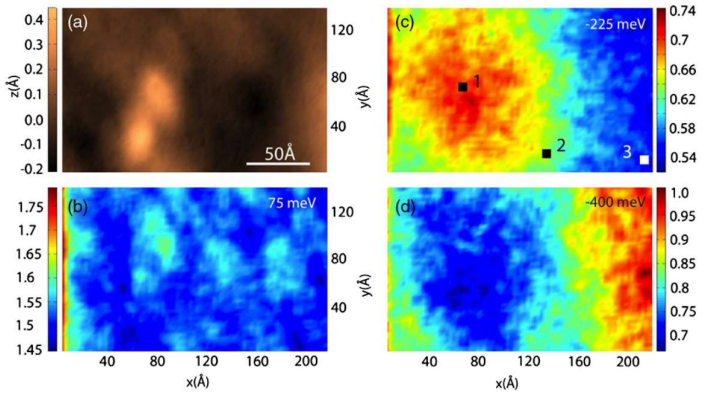


*Figure 5-39 (a) Topograph of an Sb doped $Bi_2Se_3$ surface imaged with a bias of 400 mV and a setpoint current of 70 pA. (b-d) Show corresponding conductance maps acquired at different bias. Image reproduced from[159].*

The variation in LDOS intensity corresponding to the $Sb_4$ clusters at different bias is similar to that for $Bi_{1-x}Sb_x$ bright spots (Figure 5-31), but the difference lies in the shape and spatial extent of LDOS. The spatial extent of LDOS for $Sb_4$ clusters is greater as compared to the Se defect sites and to the bright spots of $Bi_{1-x}Sb_x$ islands. This difference tentatively indicates that $Sb_4$ clusters cannot be the cause of $Bi_{1-x}Sb_x$ bright spots. In addition, $Sb_4$ clusters occupy a larger area as compared to a single Sb atom and therefore with increasing Sb content, a significant portion of $Bi_{1-x}Sb_x$ island area is expected to be occupied by $Sb_4$ clusters, which is not seen in the experimental results and it contradicts the number density analysis (section 5.7.4.1). The discussion presented till now thus indicates that vacancy like defect sites are a more probable and likely cause of bright spots in $Bi_{1-x}Sb_x$ islands.

The discussion is concluded by stating that distinct bright spots are observed most prominently in 5 ML regions (stripes and bases) of $Bi_{1-x}Sb_x$ islands in STM images. The non-observation of bright spots inside 3 ML bases and 7 ML stripes is not understood well and is subject to further experimentation and analysis. Bright spots are understood primarily to be an electronic effect (bias dependent) and the number density analysis of spots hints towards a weak Sb dependence, therefore, speculated to be a vacancy type defect. Vacancy defects with dangling bonds show pronounced LDOS in STM images and conductance maps. The distinct peak in the dI/dV spectra of the bright spots is thus attributed to dangling bonds around vacancy defect sites.

## 5.8 Summary

Observation of distinct edge states along the edges of $Bi_{1-x}Sb_x$ islands in 50 K CITS conductance maps, in particular, along the straight and regular edges of 7 ML stripes prompted an in depth characterisation by means of high resolution STM imaging and 50 K CITS measurements. In contrast,

the facetted edges of the 7 ML stripes show an absence of edge states, a result speculated to arise out of different atomic arrangements, similar to the results on armchair and zigzag type edges of graphene[136,157]. The 7 ML stripe edge states show a distinct peak in the corresponding dI/dV spectra, when acquired in the bias range of ±0.4 V, a result which is strikingly similar to the published[45] results on the edges of pure Bi (110) islands. In contrast, the 5 ML edge states demonstrated the presence of a weak dI/dV peak around +0.1 V. The 3 ML bases on the other hand, did not show a clear evidence of edge states. The observation of 7 ML edge states is interesting, although, a clear and definitive trend as a function of Sb concentration could not be mapped and will be the focus upon of future CITS experiments.

In addition to the typical edge states, an anomalous electronic state localized in close proximity to the straight 7 ML stripe edges in a select few CITS results is identified as another key result as STM studies in the past have revealed the presence of similar anomalous states, which are argued to be as manifestations of standing waves[23,164] or topologically protected edge states[47] and thus merit future experiments.

Apart from edge states, bright spots are observed inside the 5 ML stripes and bases of $Bi_{1-x}Sb_x$ islands which are speculated to be vacancy type defect sites. 50 K CITS measurements show a dI/dV peak around +0.1 V, similar to that observed for the straight 7 ML edges. Recent research demonstrates the presence of topologically protected states around defect sites of $Bi_2Te_3$[165] and $Bi_{1-x}Sb_x$ (111)[137] films, meriting future studies on $Bi_{1-x}Sb_x$ bright spots.

# 6 Conclusions and outlook

The self-assembly of nanostructures on weakly interacting substrates like HOPG gives an opportunity to study adatoms' diffusion and aggregation and at the same time provides a rich platform to engineer and study different nanostructure morphologies[17]. A balance between diffusion and nucleation can be used to manipulate the final nanostructure geometries and prepare different morphologies, for example the fingered, 3-dimensional Sb[53] islands and ordered, 2-dimensional Bi[52] islands on HOPG. This knowledge and experience[52,53,99] of synthesizing different Bi and Sb island morphologies was utilized to grow nanostructured islands of the 3-D topological insulator, $Bi_{1-x}Sb_x$ on HOPG. Motivated by the predictions[12,41] and consequent experimental demonstrations[10,11] of topologically protected surface states in bulk $Bi_{1-x}Sb_x$ alloy films within a certain ($0.07<x<0.22$) Sb concentration range, an (x) dependent (x=0.06, 0.13 and 0.24) study of $Bi_{1-x}Sb_x$ islands on HOPG was pursued. The synthesis and characterisation (morphological and electronic) of $Bi_{1-x}Sb_x$ islands was undertaken in a UHV-STM (Omicron VT AFM) system.

High resolution RT-STM images revealed that the morphology of $Bi_{1-x}Sb_x$ islands on HOPG is similar to the that of pure Bi (110) islands[98,99] on HOPG, i.e. the islands comprise a paired layer (BP[91] like) structure, with similar islands heights. Apart from the overall similarity, there were a few noticeable differences in the $Bi_{1-x}Sb_x$ island morphology, in particular, the irregular 5 ML stripe edges and fingered 3 ML bases. It was observed that an additional 1 ML structure nucleated adjacent to the irregular 5 ML stripe edges and on top of flat 3 ML bases for a select few $Bi_{1-x}Sb_x$ islands, a region referred to as the (3+1) ML region. In addition, the probability of finding a (3+1) ML region increased as a function of Sb concentration. The (3+1) ML will be studied in more detail by higher resolution CITS measurements and corresponding band structure calculations in the future.

50 K CITS measurements performed on the paired layers (3, 5 and 7) ML of $Bi_{1-x}Sb_x$ islands revealed a good agreement with the reported CITS results obtained[98,124] on pure Bi (110) islands. The dI/dV spectra analysis was complemented by spectral histograms[123] which show the reproducibility of the key features and distinguish them from experimental artefacts. Furthermore, dI/dV spectra of each of the paired layers (3, 5 and 7) ML demonstrated no identifiable difference as the Sb content (x) was tuned and varied between x=0.06 and x=0.24, in agreement with the corresponding DFT calculated band structures.

The edges of $Bi_{1-x}Sb_x$ islands showed the presence of distinct edge states. The CITS conductance maps acquired along the straight 7 ML stripe edges, in particular, showed edge states clearly at +120 mV. The facets of the 7 ML stripes, on the other hand, showed an absence of any edge states, a result speculated to arise out of a different atomic arrangement.

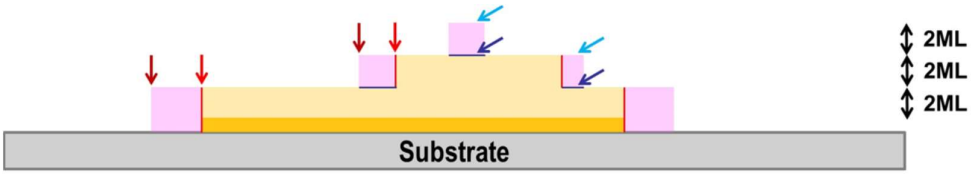


*Figure 6-1 A schematic drawing showing the possible nanostructures that can be engineered by growing materials ($Bi_{1-y}Sb_y$) sequentially on top of an already grown $Bi_{1-x}Sb_x$ island.*

The edges of the 5 ML stripes and bases showed comparatively lower edge state intensity as compared to that of the 7 ML stripe edges and the 3 ML base edge states could not be characterised. Evidence for the evolution of edge states' characteristics as a function of Sb concentration (x) for each of the paired layers could not be mapped and will be a focus of future CITS measurements.

The distinct dI/dV peak around +0.1 V for the edge states on 7 ML stripes of $Bi_{1-x}Sb_x$ islands showed remarkable agreement with the dI/dV peak ('α' state) reported[45] in the experimental dI/dV spectra of 2 ML and 4 ML high, pure Bi (110) islands, where, the 'α' state is argued to have topologically non-trivial characteristics as evidenced in the corresponding band structure calculations. The similarity between $Bi_{1-x}Sb_x$ and Bi edge states, therefore, makes a strong case for pursuing band structure calculations for $Bi_{1-x}Sb_x$ nano-ribbons in the near future.

An additional electronic state, localized in close proximity to the straight 7 ML stripe edges were also observed and the origin of these states needs further investigation. In addition, bright (high LDOS) spots were observed inside the 5 ML stripes of $Bi_{1-x}Sb_x$ islands, a result speculated to arise out of vacancy like defect sites, similar to Ref[159].

Motivated by the experimental results of $Bi_{1-x}Sb_x$ islands on HOPG, future experiments will be centred on addressing the challenges outlined in each of the three results chapters and considerable focus will be on the synthesis and growth of hetero-structure islands. Such islands, in principle, can be synthesized by sequential deposition of any alloy on any other already deposited alloy ($Bi_{1-x}Sb_x$) island.

As $Bi_{1-x}Sb_x$ islands grow via diffusion and aggregation, the second material deposited will aggregate at the edges of already grown islands, which will result in the creation of stripes of materials with dis-similar edges (red arrows, Figure 6-1, left). As new material lands on an existing island, it will tend to aggregate and result in the formation of stripes. This will create layers of materials in which the upper and lower surfaces are different (blue arrows, Figure 6-1, right). It is expected that the island stripes of the second material on top of the first material will create profound differences in the edge states due to coupling[166] of the electronic states and thus open new avenues of research. Importantly, coupling with the islands bases is expected to have an impact on the island's edge states, therefore

the states in the underlying island provides an important route to engineering new nanostructures with interesting electronic properties[43,167].

# 7 References


1 Moore, G. E. in *SPIE's 1995 Symposium on Microlithography.* 2-17 (International Society for Optics and Photonics).

2 Schaller, R. R. Moore's law: past, present and future. *IEEE spectrum* **34**, 52-59 (1997).

3 Sze, S. M. & Devices, S. Physics and Technology. (1985).

4 Keyes, R. W. Fundamental limits of silicon technology. *Proceedings of the IEEE* **89**, 227-239 (2001).

5 Jones, M. G. *et al.* Nanotechnology and nanoscale science: Educational challenges. *International Journal of Science Education* **35**, 1490-1512 (2013).

6 Kittel, C. & McEuen, P. *Introduction to solid state physics*. Vol. 8 (Wiley New York, 1976).

7 Hook, J. R. & Hall, H. E. (John Wiley and Sons Ltd, 2000).

8 Kane, C. L. & Mele, E. J. Z 2 topological order and the quantum spin Hall effect. *Physical Review Letters* **95**, 146802 (2005).

9 Kuroda, K. *et al.* Experimental realization of a three-dimensional topological insulator phase in ternary chalcogenide TlBiSe 2. *Physical Review Letters* **105**, 146801 (2010).

10 Hirahara, T. *et al.* Topological metal at the surface of an ultrathin $Bi_{1-x}Sb_x$ alloy film. *Physical Review B* **81**, 165422 (2010).

11 Hsieh, D. *et al.* A topological Dirac insulator in a quantum spin Hall phase. *Nature* **452**, 970-974 (2008).

12 Nakamura, F. *et al.* Topological transition in $Bi_{1-x}Sb_x$ studied as a function of Sb doping. *Physical Review B* **84**, 235308 (2011).

13 Binnig, G. & Rohrer, H. Scanning tunneling microscopy—from birth to adolescence. *Reviews of Modern Physics* **59**, 615-625 (1987).

14 Binnig, G. & Rohrer, H. Scanning tunneling microscopy. *IBM Journal of Research and Development* **44**, 279-293 (2000).

15 Binnig, G., Rohrer, H., Gerber, C. & Weibel, E. Tunneling through a controllable vacuum gap. *Applied Physics Letters* **40**, 178-180 (1982).

16 Whitesides, G. M. & Grzybowski, B. Self-assembly at all scales. *Science* **295**, 2418-2421 (2002).

17 Zhang, Z. & Lagally, M. G. Atomistic processes in the early stages of thin-film growth. *Science* **276**, 377-383 (1997).

18 Manoharan, H. C. Topological insulators: A romance with many dimensions. *Nature Nanotechnology* **5**, 477-479 (2010).

19 Alivisatos, A. P. Semiconductor clusters, nanocrystals, and quantum dots. *Science* **271**, 933 (1996).

20 Crommie, M., Lutz, C., Eigler, D. & Heller, E. Quantum corrals. *Physica D: Nonlinear Phenomena* **83**, 98-108 (1995).

21 Dekker, C. Carbon nanotubes as molecular quantum wires. *Physics today* **52**, 22-28 (1999).

22 Geim, A. K. & Novoselov, K. S. The rise of graphene. *Nature Materials* **6**, 183-191 (2007).

23 Crommie, M., Lutz, C. & Eigler, D. Imaging standing waves in a two-dimensional electron gas. *Nature* **363**, 524-527 (1993).

24 Kane, C. L. & Mele, E. J. Quantum spin Hall effect in graphene. *Physical Review Letters* **95**, 226801 (2005).

25 Hasan, M. Z. & Kane, C. L. Colloquium: topological insulators. *Reviews of Modern Physics* **82**, 3045 (2010).

26 Chang, C.-Z. & Li, M. Quantum anomalous Hall effect in time-reversal-symmetry breaking topological insulators. *Journal of Physics: Condensed Matter* **28**, 123002 (2016).

27 Berger, C. *et al.* Electronic confinement and coherence in patterned epitaxial graphene. *Science* **312**, 1191-1196 (2006).

28 Brar, V. W. *et al.* Scanning tunneling spectroscopy of inhomogeneous electronic structure in monolayer and bilayer graphene on SiC. *Applied Physics Letters* **91**, 122102 (2007).

29 Brihuega, I. *et al.* Quasiparticle chirality in epitaxial graphene probed at the nanometer scale. *Physical Review Letters* **101**, 206802 (2008).
30 De Parga, A. V. *et al.* Periodically rippled graphene: growth and spatially resolved electronic structure. *Physical Review Letters* **100**, 056807 (2008).
31 Deshpande, A., Bao, W., Miao, F., Lau, C. N. & LeRoy, B. J. Spatially resolved spectroscopy of monolayer graphene on SiO 2. *Physical Review B* **79**, 205411 (2009).
32 Klusek, Z. *et al.* Local electronic edge states of graphene layer deposited on Ir (111) surface studied by STM/CITS. *Applied Surface Science* **252**, 1221-1227 (2005).
33 Neto, A. C., Guinea, F., Peres, N. M., Novoselov, K. S. & Geim, A. K. The electronic properties of graphene. *Reviews of Modern Physics* **81**, 109 (2009).
34 Pan, M. *et al.* Topographic and spectroscopic characterization of electronic edge states in CVD grown graphene nanoribbons. *Nano Letters* **12**, 1928-1933 (2012).
35 Ritter, K. A. & Lyding, J. W. The influence of edge structure on the electronic properties of graphene quantum dots and nanoribbons. *Nature Materials* **8**, 235-242 (2009).
36 Suenaga, K. & Koshino, M. Atom-by-atom spectroscopy at graphene edge. *Nature* **468**, 1088-1090 (2010).
37 Yang, H. *et al.* Quantum interference channeling at graphene edges. *Nano Letters* **10**, 943-947 (2010).
38 Damascelli, A. Probing the electronic structure of complex systems by ARPES. *Physica Scripta* **2004**, 61 (2004).
39 Bernevig, B. A., Hughes, T. L. & Zhang, S.-C. Quantum spin Hall effect and topological phase transition in HgTe quantum wells. *Science* **314**, 1757-1761 (2006).
40 König, M. *et al.* Quantum spin Hall insulator state in HgTe quantum wells. *Science* **318**, 766-770 (2007).
41 Teo, J. C., Fu, L. & Kane, C. Surface states and topological invariants in three-dimensional topological insulators: Application to $Bi_{1-x}Sb_x$. *Physical Review B* **78**, 045426 (2008).
42 Zhang, H.-J. *et al.* Electronic structures and surface states of the topological insulator $Bi_{1-x}Sb_x$. *Physical Review B* **80**, 085307 (2009).
43 Bian, G., Wang, X., Liu, Y., Miller, T. & Chiang, T.-C. Interfacial protection of topological surface states in ultrathin Sb films. *Physical Review Letters* **108**, 176401 (2012).
44 Lee, C.-H. & Yang, C.-K. Topological states of Sb thin films contacted by a single sheet of heterogeneous atoms. *New Journal of Physics* **16**, 093006 (2014).
45 Lu, Y. *et al.* Topological Properties Determined by Atomic Buckling in Self-Assembled Ultrathin Bi (110). *Nano Letters* **15**, 80-87 (2014).
46 Drozdov, I. K. *et al.* One-dimensional topological edge states of bismuth bilayers. *Nature Physics* **10**, 664-669 (2014).
47 Yang, F. *et al.* Spatial and energy distribution of topological edge states in single Bi (111) bilayer. *Physical Review Letters* **109**, 016801 (2012).
48 Neupane, M. *et al.* Observation of quantum-tunnelling-modulated spin texture in ultrathin topological insulator Bi2Se3 films. *Nature Communications* **5** (2014).
49 Zhang, H. *et al.* Topological insulators in Bi2Se3, Bi2Te3 and Sb2Te3 with a single Dirac cone on the surface. *Nature Physics* **5**, 438-442 (2009).
50 Burkov, A. & Balents, L. Weyl semimetal in a topological insulator multilayer. *Physical Review Letters* **107**, 127205 (2011).
51 Scott, S. A., Kral, M. V. & Brown, S. A. Growth of oriented Bi nanorods at graphite step-edges. *Physical Review B* **72**, 205423 (2005).
52 Scott, S. A., Kral, M. V. & Brown, S. A. Bi on graphite: Morphology and growth characteristics of star-shaped dendrites. *Physical Review B* **73**, 205424 (2006).
53 Scott, S. & Brown, S. Three-dimensional growth characteristics of antimony aggregates on graphite. *The European Physical Journal D-Atomic, Molecular, Optical and Plasma Physics* **39**, 433-438 (2006).

54 Scott, S. A. *Self-assembly of Sb and Bi nanostructures on graphite* Ph.D. thesis, University of Canterbury, (2005).
55 Anton, R. & Schneidereit, I. In situ TEM investigations of dendritic growth of Au particles on HOPG. *Physical Review B* **58**, 13874 (1998).
56 Arthur, J. & Cho, A. Adsorption and desorption kinetics of Cu and Au on (0001) graphite. *Surface Science* **36**, 641-660 (1973).
57 Koma, A., Sunouchi, K. & Miyajima, T. *Fabrication of ultrathin heterostructures with van der Waals epitaxy*, AVS, (1985).
58 Tseng, A. A. & Notargiacomo, A. Nanoscale fabrication by nonconventional approaches. *Journal of Nanoscience and Nanotechnology* **5**, 683-702 (2005).
59 Milanil, P., Iannotta, S., Biasioli, F., Piseri, P. & Barborini, E. in *MRS Proceedings.* 283 (Cambridge Univ Press).
60 Pacholski, C., Kornowski, A. & Weller, H. Self-assembly of ZnO: from nanodots to nanorods. *Angewandte Chemie International Edition* **41**, 1188-1191 (2002).
61 Volmer, M. & Weber, A. Keimbildung in übersättigten Gebilden. *Z. phys. Chem* **119**, 277-301 (1926).
62 Volmer, M. & Weber, A. Novel growth mechanism in heteroepitaxial semiconductor growth. *Z. phys. Chem* **119**, 277 (1926).
63 Kaiser, B., Stegemann, B., Kaukel, H. & Rademann, K. Instabilities and pattern formation during the self-organized growth of nanoparticles on graphite. *Surface Science* **496**, L18-L22 (2002).
64 Koch, R., Winau, D., Führmann, A. & Rieder, K. Intrinsic stress of polycrystalline and epitaxial Ag, Cu and Au films on mica (001). *Vacuum* **43**, 521-523 (1992).
65 Frank, F. & van der Merwe, J. H. in *Proceedings of the Royal Society of London A: Mathematical, Physical and Engineering Sciences.* 205-216 (The Royal Society).
66 Frank, F. & Van der Merwe, J. in *Proceedings of the Royal Society of London A: Mathematical, Physical and Engineering Sciences.* 216-225 (The Royal Society).
67 Kramer, H. Epitaxial growth of rare gas solids. *Journal of Crystal Growth* **33**, 65-76 (1976).
68 Stranski, I. N. & Krastanow, L. v. Sitzungsber. Akad. Wiss. Wien, Math. *Naturwiss. Kl., Abt. B* **2**, 797 (1938).
69 Brune, H., Röder, H., Boragno, C. & Kern, K. Strain relief at hexagonal-close-packed interfaces. *Physical Review B* **49**, 2997 (1994).
70 Cho, W. *et al.* Atomic structure of Ag grown on Si (001)(2× 1) at high temperature. *Surface Science* **439**, L792-L798 (1999).
71 Olsen, G. Interfacial lattice mismatch effects in III–V compounds. *Journal of Crystal Growth* **31**, 223-239 (1975).
72 McCarthy, D. N., Robertson, D., Kowalczyk, P. J. & Brown, S. A. The effects of annealing and growth temperature on the morphologies of Bi nanostructures on HOPG. *Surface Science* **604**, 1273-1282 (2010).
73 Jensen, P. Growth of nanostructures by cluster deposition: Experiments and simple models. *Reviews of Modern Physics* **71**, 1695 (1999).
74 Anisimov, M. A., Rabinovich, V. A. & Sychev, V. V. *Thermodynamics of the critical state of individual substances*. (CRC press, 1995).
75 Roder, H., Hahn, E., Brune, H., Bucher, J.-P. & Kern, K. Building one-dimensional and 2-dimensional nanostructures by diffusion-controlled aggregation at surfaces. *Nature* **366**, 141-143 (1993).
76 Schinzer, S., Kinne, M., Biehl, M. & Kinzel, W. The role of step edge diffusion in epitaxial crystal growth. *Surface Science* **439**, 191-198 (1999).
77 Jensen, P., Barabási, A.-L., Larralde, H., Havlin, S. & Stanley, H. Deposition, diffusion, and aggregation of atoms on surfaces: A model for nanostructure growth. *Physical Review B* **50**, 15316 (1994).

78 Witten Jr, T. & Sander, L. M. Diffusion-limited aggregation, a kinetic critical phenomenon. *Physical Review Letters* **47**, 1400 (1981).
79 Witten, T. A. & Sander, L. M. Diffusion-limited aggregation. *Physical Review B* **27**, 5686 (1983).
80 Eden, M. A two-dimensional growth process. *Dynamics of Fractal Surfaces* **4**, 223-239 (1961).
81 Stegemann, B., Ritter, C., Kaiser, B. & Rademann, K. Crystallization of antimony nanoparticles: Pattern formation and fractal growth. *The Journal of Physical Chemistry B* **108**, 14292-14297 (2004).
82 Langer, J. & Müller-Krumbhaar, H. Theory of dendritic growth—I. Elements of a stability analysis. *Acta Metallurgica* **26**, 1681-1687 (1978).
83 Mullins, W. W. & Sekerka, R. F. Morphological stability of a particle growing by diffusion or heat flow. *Journal of Applied Physics* **34**, 323-329 (1963).
84 He, Y. & Borguet, E. Effect of local environment on nanoscale dynamics at electrochemical interfaces: Anisotropic growth and dissolution in the presence of a step providing evidence for a Schwoebel–Ehrlich barrier at solid/liquid interfaces. *Faraday Discussions* **121**, 17-25 (2002).
85 Schwoebel, R. L. & Shipsey, E. J. Step motion on crystal surfaces. *Journal of Applied Physics* **37**, 3682-3686 (1966).
86 Scott, S., Kral, M. & Brown, S. A crystallographic orientation transition and early stage growth characteristics of thin Bi films on HOPG. *Surface Science* **587**, 175-184 (2005).
87 Scott, S., Kral, M. & Brown, S. Growth of nanorods and mesoscale stars prior to an orientation transition in thin Bi films on graphite. *Applied Surface Science* **252**, 5563-5567 (2006).
88 Venables, J. A. Atomic processes in crystal growth. *Surface Science* **299**, 798-817 (1994).
89 Joy, D. C. *Scanning electron microscopy*. (Wiley Online Library, 2006).
90 McCarthy, D. N. Nucleation and Equilibration via Surface Diffusion: An Experimental Study. *University of Canterbury* (2008).
91 Nagao, T. *et al.* Nanofilm Allotrope and Phase Transformation of Ultrathin Bi Film on S i (111)-7× 7. *Physical Review Letters* **93**, 105501 (2004).
92 Girifalco, L., Hodak, M. & Lee, R. S. Carbon nanotubes, buckyballs, ropes, and a universal graphitic potential. *Physical Review B* **62**, 13104 (2000).
93 Stegemann, B., Ritter, C., Kaiser, B. & Rademann, K. Characterization of the (0001) cleavage surface of antimony single crystals using scanning probe microscopy: Atomic structure, vacancies, cleavage steps, and twinned interlayers. *Physical Review B* **69**, 155432 (2004).
94 Yokoyama, E. & Kuroda, T. Pattern formation in growth of snow crystals occurring in the surface kinetic process and the diffusion process. *Physical Review A* **41**, 2038 (1990).
95 Binnig, G., Quate, C. F. & Gerber, C. Atomic force microscope. *Physical Review Letters* **56**, 930 (1986).
96 Kowalczyk, P. *et al.* Anisotropic oxidation of bismuth nanostructures: Evidence for a thin film allotrope of bismuth. *Applied Physics Letters* **100**, 151904 (2012).
97 Kowalczyk, P., Mahapatra, O., Brown, S., Bian, G. & Chiang, T.-C. STM driven modification of bismuth nanostructures. *Surface Science* **621**, 140-145 (2014).
98 Kowalczyk, P. *et al.* Electronic size effects in three-dimensional nanostructures. *Nano Letters* **13**, 43-47 (2012).
99 Kowalczyk, P. *et al.* STM and XPS investigations of bismuth islands on HOPG. *Surface Science* **605**, 659-667 (2011).
100 Sandomirskii, V. Quantum size effect in a semimetal film. *Sov. Phys. JETP* **25**, 101 (1967).
101 Morse, P. M., America, A. S. o. & Physics, A. I. o. *Vibration and sound*. Vol. 2 (McGraw-Hill New York, 1948).
102 *Omicron VT AFM XA Manual*.
103 Hofmann, P. The surfaces of bismuth: Structural and electronic properties. *Progress in Surface Science* **81**, 191-245 (2006).

104 Liu, Y. & Allen, R. E. Electronic structure of the semimetals Bi and Sb. *Physical Review B* **52**, 1566 (1995).
105 Donohue, J. Structures of the Elements. (1974).
106 McCracken, G. & Pashley, N. Titanium filaments for sublimation pumps. *Journal of Vacuum Science and Technology* **3**, 96-98 (1966).
107 Gupta, A. & Leck, J. An evaluation of the titanium sublimation pump. *Vacuum* **25**, 362-372 (1975).
108 Ikeda, T. *Piezoelectricity*. (Oxford university press, 1990).
109 Glawe, G. E., Simmons, F. S. & Stickney, T. M. Radiation and recovery corrections and time constants of several chromel-alumel thermocouple probes in high-temperature, high-velocity gas streams. (Lewis Flight Propulsion Lab., Cleveland, 1956).
110 Turner, R. S. Laminar air flow. *J Bone Joint Surg Am* **56**, 430-435 (1974).
111 O'sullivan, C. & Guilbault, G. Commercial quartz crystal microbalances–theory and applications. *Biosensors and bioelectronics* **14**, 663-670 (1999).
112 Livingston, M. S., Blewett, J. P. & Stickley, E. Particle accelerators. *American Journal of Physics* **30**, 940-941 (1962).
113 Domon, B. & Aebersold, R. Mass spectrometry and protein analysis. *Science* **312**, 212-217 (2006).
114 Fisher, J. & Giaever, I. Tunneling through thin insulating layers. *Journal of Applied Physics* **32**, 172-177 (1961).
115 Wiesendanger, R. & Güntherodt, H.-J. *Scanning tunneling microscopy III: theory of STM and related scanning probe methods*. Vol. 29 (Springer Science & Business Media, 2013).
116 Nagahara, L., Thundat, T. & Lindsay, S. Preparation and characterization of STM tips for electrochemical studies. *Review of Scientific Instruments* **60**, 3128-3130 (1989).
117 Feenstra, R. M. Scanning tunneling spectroscopy. *Surface Science* **299**, 965-979 (1994).
118 Swartzentruber, B. Direct measurement of surface diffusion using atom-tracking scanning tunneling microscopy. *Physical Review Letters* **76**, 459 (1996).
119 Sumetskii, M. & Kornyshev, A. Noise in STM due to atoms moving in the tunneling space. *Physical Review B* **48**, 17493 (1993).
120 Weisman, A. D., Dougherty, E. R., Mizes, H. A. & Miller, R. D. Nonlinear digital filtering of scanning-probe-microscopy images by morphological pseudoconvolutions. *Journal of Applied Physics* **71**, 1565-1578 (1992).
121 Arenhold, K., Surnev, S., Coenen, P., Bonzel, H. & Wynblatt, P. Scanning tunneling microscopy of equilibrium crystal shape of Pb particles: test of universality. *Surface Science* **417**, L160-L165 (1998).
122 Wang, Z. & Zhang, D. Progressive switching median filter for the removal of impulse noise from highly corrupted images. *IEEE Transactions on Circuits and Systems II: Analog and Digital Signal Processing* **46**, 78-80 (1999).
123 Kowalczyk, P. J. Investigation of STM tip influence on the recorded position of the Shockley surface state on Au (111). *Surface Science* **603**, 747-751 (2009).
124 Mahapatra, O. *A scanning probe microscopy (SPM) study of Bi (110) nanostructures on highly oriented pyrolytic graphite (HOPG)* Ph.D. thesis, University of Canterbury, (2013).
125 Feenstra, R. M., Ramachandran, V. & Chen, H. Recent developments in scanning tunneling spectroscopy of semiconductor surfaces. *Applied Physics A: Materials Science & Processing* **72**, S193-S199 (2001).
126 Feenstra, R. M., Stroscio, J. A. & Fein, A. Tunneling spectroscopy of the Si (111) 2× 1 surface. *Surface Science* **181**, 295-306 (1987).
127 Ritter, C., Heyde, M., Stegemann, B., Rademann, K. & Schwarz, U. D. Contact-area dependence of frictional forces: moving adsorbed antimony nanoparticles. *Physical Review B* **71**, 085405 (2005).

128 Kowalczyk, P. *et al.* Origin of the moiré pattern in thin Bi films deposited on HOPG. *Physical Review B* **91**, 045434 (2015).
129 Novoselov, K. *et al.* Two-dimensional gas of massless Dirac fermions in graphene. *Nature* **438**, 197-200 (2005).
130 Kara, A. *et al.* A review on silicene—new candidate for electronics. *Surface Science Reports* **67**, 1-18 (2012).
131 Dávila, M., Xian, L., Cahangirov, S., Rubio, A. & Le Lay, G. Germanene: a novel two-dimensional germanium allotrope akin to graphene and silicene. *New Journal of Physics* **16**, 095002 (2014).
132 Kondo, T. *et al.* Atomic-scale characterization of nitrogen-doped graphite: Effects of dopant nitrogen on the local electronic structure of the surrounding carbon atoms. *Physical Review B* **86**, 035436 (2012).
133 Kumar, V. Electronic and atomic stuctures of Sb 4 and Sb 8 clusters. *Physical Review B* **48**, 8470 (1993).
134 Kobayashi, K. Moiré pattern in scanning tunneling microscopy: Mechanism in observation of subsurface nanostructures. *Physical Review B* **53**, 11091 (1996).
135 Kim, S. H. *et al.* Edge and interfacial states in a two-dimensional topological insulator: Bi (111) bilayer on Bi 2 Te 2 Se. *Physical Review B* **89**, 155436 (2014).
136 Li, Y. *et al.* Absence of edge states in covalently bonded zigzag edges of graphene on Ir (111). *Advanced Materials* **25**, 1967-1972 (2013).
137 Roushan, P. *et al.* Topological surface states protected from backscattering by chiral spin texture. *Nature* **460**, 1106-1109 (2009).
138 Gross, E. K. & Dreizler, R. M. *Density functional theory*. Vol. 337 (Springer Science & Business Media, 2013).
139 Feenstra, R. Tunneling spectroscopy of the (110) surface of direct-gap III-V semiconductors. *Physical Review B* **50**, 4561 (1994).
140 Feenstra, R. M. & Stroscio, J. A. Tunneling spectroscopy of the GaAs (110) surface. *Journal of Vacuum Science & Technology B* **5**, 923-929 (1987).
141 Bian, G., Miller, T. & Chiang, T.-C. Electronic structure and surface-mediated metastability of Bi films on Si (111)-7× 7 studied by angle-resolved photoemission spectroscopy. *Physical Review B* **80**, 245407 (2009).
142 Winkler, R., Papadakis, S., De Poortere, E. & Shayegan, M. *Spin-Orbit Coupling in Two-Dimensional Electron and Hole Systems*. Vol. 41 (Springer, 2003).
143 Märkl, T. *et al.* Engineering multiple topological phases in nanoscale Van der Waals heterostructures: realisation of α-antimonene. *2D Materials* **5**, 011002 (2017).
144 Mead, C. & Spitzer, W. Fermi level position at metal-semiconductor interfaces. *Physical Review* **134**, A713 (1964).
145 Bihlmayer, G., Koroteev, Y. M., Chulkov, E. V. & Blügel, S. Surface-and edge-states in ultrathin Bi–Sb films. *New Journal of Physics* **12**, 065006 (2010).
146 Chun-Lei, G., Dong, Q., Can-Hua, L., Jin-Feng, J. & Feng, L. Topological edge states and electronic structures of a 2D topological insulator: Single-bilayer Bi (111). *Chinese Physics B* **22**, 067304 (2013).
147 Giunta, P. & Kelty, S. Direct observation of graphite layer edge states by scanning tunneling microscopy. *The Journal of Chemical Physics* **114**, 1807-1812 (2001).
148 Klusek, Z. *et al.* Observations of local electron states on the edges of the circular pits on hydrogen-etched graphite surface by scanning tunneling spectroscopy. *Applied Surface Science* **161**, 508-514 (2000).
149 Kondo, T., Honma, Y., Oh, J., Machida, T. & Nakamura, J. Edge states propagating from a defect of graphite: Scanning tunneling spectroscopy measurements. *Physical Review B* **82**, 153414 (2010).

150 Niimi, Y. *et al.* Scanning tunneling microscopy and spectroscopy of the electronic local density of states of graphite surfaces near monoatomic step edges. *Physical Review B* **73**, 085421 (2006).
151 Wang, Z., Chen, L. & Liu, F. Tuning topological edge states of Bi (111) bilayer film by edge adsorption. *Nano Letters* **14**, 2879-2883 (2014).
152 Chen, Y. *et al.* Experimental realization of a three-dimensional topological insulator, $Bi_2Te_3$. *Science* **325**, 178-181 (2009).
153 Hsieh, D. *et al.* Observation of time-reversal-protected single-Dirac-cone topological-insulator states in $Bi_2Te_3$ and $Sb_2Te_3$. *Physical Review Letters* **103**, 146401 (2009).
154 Pons, S., Mallet, P. & Veuillen, J.-Y. Electron confinement in nickel and copper nanostructures on Cu (111). *Physical Review B* **64**, 193408 (2001).
155 Sun, J.-T. *et al.* Energy-gap opening in a Bi (110) nanoribbon induced by edge reconstruction. *Physical Review Letters* **109**, 246804 (2012).
156 Kowalczyk, P., Belić, D., Mahapatra, O. & Brown, S. Grain boundaries between bismuth nanocrystals. *Acta Materialia* **60**, 674-681 (2012).
157 Kobayashi, Y., Fukui, K.-i., Enoki, T., Kusakabe, K. & Kaburagi, Y. Observation of zigzag and armchair edges of graphite using scanning tunneling microscopy and spectroscopy. *Physical Review B* **71**, 193406 (2005).
158 Li, G., Luican, A. & Andrei, E. Y. Scanning tunneling spectroscopy of graphene on graphite. *Physical Review Letters* **102**, 176804 (2009).
159 Alpichshev, Z. *et al.* STM imaging of impurity resonances on Bi 2 Se 3. *Physical Review Letters* **108**, 206402 (2012).
160 Fujimoto, Y. & Saito, S. Formation, stabilities, and electronic properties of nitrogen defects in graphene. *Physical Review B* **84**, 245446 (2011).
161 Biswas, R. R. & Balatsky, A. V. Impurity-induced states on the surface of three-dimensional topological insulators. *Physical Review B* **81**, 233405 (2010).
162 Rayane, D. *et al.* Evaporation of tetramers in Sb4n clusters and conditions for the formation of Sb2n+ 1 clusters. *Zeitschrift für Physik D Atoms, Molecules and Clusters* **12**, 217-219 (1989).
163 Bardotti, L., Jensen, P., Hoareau, A., Treilleux, M. & Cabaud, B. Experimental observation of fast diffusion of large antimony clusters on graphite surfaces. *Physical Review Letters* **74**, 4694 (1995).
164 Kanisawa, K., Butcher, M., Yamaguchi, H. & Hirayama, Y. Imaging of Friedel oscillation patterns of two-dimensionally accumulated electrons at epitaxially grown InAs (111) A surfaces. *Physical Review Letters* **86**, 3384 (2001).
165 Zhang, T. *et al.* Experimental demonstration of topological surface states protected by time-reversal symmetry. *Physical Review Letters* **103**, 266803 (2009).
166 Fatemi, V. *et al.* Electrostatic coupling between two surfaces of a topological insulator nanodevice. *Physical Review Letters* **113**, 206801 (2014).
167 Bian, G. *et al.* First-principles and spectroscopic studies of Bi (110) films: Thickness-dependent Dirac modes and property oscillations. *Physical Review B* **90**, 195409 (2014).

# 8 Poster and Oral presentations from the thesis

- I.V. Mahajan, P.J. Kowalczyk, G. Bian, 4, T.C. Chiang, S.A. Brown. Scanning tunnelling microscopy studies of nanostructures of the topological insulator $Bi_{1-x}Sb_x$. Poster presentation at Advanced Materials and Nanoscience Conference (AMN 7 2015).
- I.V. Mahajan, P.J. Kowalczyk, G. Bian, 4, T.C. Chiang, S.A. Brown. Edge states in $Bi_{1-x}Sb_x$ nanostructures probed with scanning probe microscopy. Poster presentation at International Conference on nanoscience and Nanotechnology Conference (ICONN 2016).
- I.V. Mahajan, T. Maerkl, P.J. Kowalczyk, G. Bian, 4, T.C. Chiang, S.A. Brown. Exotic electronic states in $Bi_{1-x}Sb_x$ nanostructures. Oral Presentation at Advanced Materials and Nanoscience (AMN 8 2017).
- T. Maerkl, I.V. Mahajan, P.J. Kowalczyk, G. Bian, 4, T.C. Chiang, S.A. Brown. Morphology of $Bi_{1-x}Sb_x$ islands on HOPG. Oral Presentation at Advanced Materials and Nanoscience (AMN 8 2017).
- S.A. Brown, I.V. Mahajan, H.Pirie, P. J. Kowalczyk, T. C. Chiang, G. Bian, 'Topological Edge States and Lateral Quantum Size Effects in $Bi_{1-x}Sb_x$. Gordon Research Conference on Topological & Correlated Matter: Advances in Topological Phases of Matter in Crystalline Solids and Cold Atom Systems, The Hong Kong University of Science and Technology Hong Kong, China, June 28 - July 3, 2015. Poster Presentation.

# 9 Acknowledgements

The completion of this project would have been impossible without paying my gratitude to the people who guided and supported me throughout this journey.

Firstly, I am thankful to my supervisor, Prof. Simon Brown for giving me the opportunity to work on the project and for being a great guide. His inputs and feedback into the project are highly appreciated and have been instrumental in tackling the challenges encountered during the project.

I am ever thankful to Dr. Pawel Kowalczyk, firstly for being a wonderful person whose company I really enjoyed. Secondly, for teaching me well the nuances of STM, analysis methods and the insightful discussions which often felt overwhelming at first, but made a lot of sense afterwards..:). Lastly, for being connected throughout over email, whenever I had problems during the course of the project and guiding me well.

Heartfelt thanks to Dr. Saurabh Bose, without whose constant support as a friend, elder brother and a teacher, completion of this project seemed difficult. I really appreciate your words of wisdom, especially the times when you have criticized me, for it has always made me understand something deeper not only about science, but life in general. Your practical inputs and teachings are like 'root 2 salvation'! and they remain forever ingrained in me.

I thank a wonderful person and a dear friend Dr. Rodrigo Martinez Gazoni, for being one of my pillars of strength, a great friend and someone I look upto, both as a person and as a researcher. The numerous discussions over lunch and walks have often helped me to imagine, 'light' at the end of tunnel, when there was none. Again, with your friendship and support, the days have often seemed more positive. Thanks a lot.

The support of the technical staff at the Department of Physics in undertaking challenging experiments is really appreciated, in particular that of Stephen Hemmingson, Graeme McDonald who have not only provided solid technical input, but have been wonderful people to talk to and spend time with. Thanks a lot to Rosalie for helping with the numerous administrative tasks I needed help with and always helping me with some mundane task I needed to complete. Thanks to Ross and Hardie, whose cheerful morning conversations provided the best possible starts to the days.

I am thankful to Dr. Tobias Maerkl, Maxime Le Ster for the useful, insightful conversations and inputs on the project. Thanks to Shota Shirai, for being a good friend and again for having wonderful conversations that have varied from watching stars to eating bananas. The friendly and often fact filled conversations with Dr. Sebastian Horvath and Dr. Mohammad Ziedan made my work, post the normal working hours possible. Your friendships and guidance about the system are highly valued and appreciated.

I thank the Macdiarmid institute of Advanced materials and nanotechnology for providing me with the full scholarship covering my tuition fees and living expenses and I am grateful to the University of Canterbury for allowing me to pursue my Phd degree in Physics.

My lab members from Indian Institute of Science, India, in particular, Professor Ramesh Mallik are thanked wholeheartedly for encouraging me in the first place to consider the option of acquiring expertise at University of Canterbury and aiming for a Phd.

I thank my 'Friday night buddies' and friends, Dr. Amol Nande, Arvind, Nilanjana for being the people they are and often lightening the heavy mood by their interesting conversations and acts, some of which are local legends and have had us in splits so often. My flatmates, Gokul, Prahlad and Issac are thanked for making the life livelier by their interesting acts and conversations.

To Isha and Dhiraj, for their wonderful friendship and company. New Zealand has been more exciting due to you both. I thank you both for often motivating me to come out of my self imposed shell and asking me to enjoy more. Of course, Isha, I have thoroughly enjoyed being a guinea pig to your successful and not so successful food experiments. Thanks a lot.

Thinking about studying abroad is never easy, and it is here that the role of my school and university friends is to be appreaciated. Aashutosh, Ashish and Nikhil, I have been far, yet your friendship and support over the years has encouraged me to aim for greater challenges. Dr. Arjun seth, Dr. Manpreet Bariana, Ketan Warikoo, Arnab, Greeshma chandan, I can only relish looking back at the fun university days and can't wait to meet you soon and hear about your own success stories.

Saying a mere thanks to Ambika might be an insult to the level of patience, support, love and guidance she has showered on me over the course of these years of study. As much as I appreciate and thank you for being my eternal support system, I have often admired in silence, your ability to point the flaws in a no non-sense manner, the result of which has been the improvement of my efficiency and me being focussed onto my ultimate goals. Therefore, I say to the super Marvin, $(\text{Thanks})^{\text{infinity}}$ !!!!

Thanks a ton to my sister, Alisha, for being there with me always. You know that you are my first born and best friend and without your nagging sibling love, I wouldn't have been here in the first place. Last, but not the least, thanks to my parents, for all the sacrifices that you have done over the

years, for making sure that I get the best possible education and for never ever letting me give up. You are my world. Much Love.:)